THESE DE DOCTORAT DE

L'UNIVERSITE DE NANTES

COMUE UNIVERSITE BRETAGNE LOIRE

ECOLE DOCTORALE N° 601
Mathématiques et Sciences et Technologies de l'Information et de la Communication
Spécialité : *Signal, Image et Vision*

Par

Shreedhar Savant TODKAR

Suivi de l'endommagement des structures de chaussées par technique radar Ultra-large bande

Application to debonding detection

Thèse présentée et soutenue à Nantes, le 27 Novembre 2019

Unité de recherche : Évaluation Non-Destructive des Structures et des Matériaux (Cerema)
Département Composants et Systèmes - Laboratoire Structure et Instrumentation Intégrée (IFSTTAR)

Thèse N° :

Rapporteurs :

M. Pascal LARZABAL Professeur des universités, ENS Cachan – Cachan
Mme. Atika MENHAJ Professeur des universités, Université Polytechnique Hauts-de-France

Composition du Jury :

Président :	**M. François AUGER**	Professeur des Universités, Université de Nantes
Examinateurs :	**M. Pascal LARZABAL**	Professeur des Universités, ENS Cachan – Cachan
	Mme. Atika MENHAJ	Professeur des Universités, Université Polytechnique Hauts-de-France
	M. Emmanuel TROUVE	Professeur des Universités, Université Savoie Mont-Blanc
	M. Emanuel RADOI	Professeur des Universités, Université Bretagne Occidentale
	M. François AUGER	Professeur des Universités, Université de Nantes
Dir. de thèse :	**M. Amine IHAMOUTEN**	IDTPE – HDR (ENDSUM), Cerema - Angers
Invité(s)		
	M. Cédric LE BASTARD	Co-directeur de thèse, Chargé de Recherches HDR, Cerema - Angers
	M. Vincent BALTAZART	Co-directeur de thèse, Chargé de Recherches, IFSTTAR – Nantes
	M. Xavier DEROBERT	ITPE – HDR (GERS-GeoEND), IFSTTAR – Nantes

The hardest choices require the strongest wills

-Thanos

Acknowledgements

To my life-coach, my beloved father and my life-support, my lovely mother. I owe it all to you.

First of all, I am indebted to my Thesis director, Dr. Amine IHAMOUTEN and my co-director Dr. Vincent BALTAZART for his great support and invaluable advice throughout the course of my research. I extend my gratitude to Dr. Cédric LE BASTARD for his guidance throughout the course of my research and for his invaluable comments that helped me improve the manuscript.

I am grateful to Dr. LE BASTARD and Dr. BALTAZART for their insights and sharing their knowledge and experience in Signal Processing and Machine Learning. I also thank Dr. BALTAZART for his crucial remarks that shaped my final dissertation. A special thanks to Dr. Xavier DEROBERT for sharing his knowledge and experience in GPR and Geophysics.

A very special gratitude goes out to all the members of '*Comite de Suivi de Thèse*', Prof. Emanuel RADOI and Dr. Christophe BOURLIER for providing me their valuable feedback and suggestions to improve my work.

A personal note of thanks to my dissertation rapporteurs: Prof. Pascal LARZABAL and Prof. Atika MENHAJ for taking their valuable time in providing me a speedy response. I extend my gratitude towards the thesis committee members Prof. Emmanuel TROUVE and Prof. Emanuel RADOI and the president of the jury, Prof. François AUGER for their presence during the defense and their comments that helped me improve the final version of the manuscript.

And at last but by no means least, a special thanks to all my colleagues at Cerema and IFSTTAR for directly or indirectly sharing their experience with me throughout the course of the thesis.

Last but not least, I would like to express my deepest gratitude to my family and friends. This dissertation would not have been possible without their warm love, continued patience, and endless support.

Thanks one and all for your encouragement!

Contents

List of Figures

List of Illustrations

List of Tables

List of Algorithms

ABSTRACT
AND
RÉSUMÉ ÉTENDU

Résumé étendu

Le réseau routier français est principalement constitué de routes nationales, dont la plupart a été achevée il y a plus de 30 ans. Les routes se dégradent à l'usage, sous l'influence du trafic, ainsi que des conditions météorologiques et des phénomènes associés (infiltrations d'eau). La dégradation de la chaussée est visible par le phénomène d'orniérage et de fissuration de surface (voir Figure. 1). Les deux phénomènes peuvent révéler des défauts de structure, incluant entre autres, les défauts de collage ou de délamination aux interfaces entre couches de chaussée. Des fissures peuvent ainsi remonter en surface (*reflexive cracks*) de chaussée et favoriser l'infiltration d'eau. Dans ce contexte, la détection précoce de décollement entre couches permettrait d'améliorer la gestion et l'entretien du réseau routier.

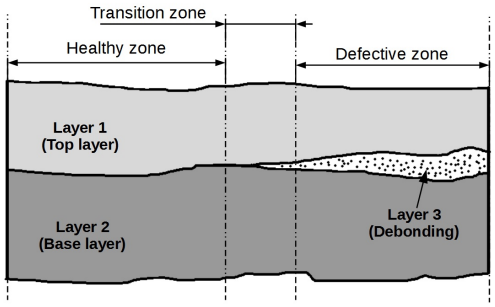

Figure 1: *Schéma simplifié d'un décollement entre couches de chaussée*

Dans le cadre de cette thèse, nous nous focalisons sur la détection de décollements entre les deux premières couches de la structure de chaussée. Le premier chapitre présente la problématique de la détection du décollement et les travaux existants dans la littérature sur cette problématique. La plupart des travaux utilisent des essais destructifs, qui présentent l'inconvénient d'être ponctuels et limités en nombre de mesures. En comparaison, les traitements développés dans cette thèse sont basés sur des méthodes d'évaluation non-destructive (END ou Non-destructive Testing), qui permettent une auscultation exhaustive de la subsurface.

Au Chapitre 2, nous discutons de l'état de l'art des méthodes END pour l'auscultation des chaussées. Nous présentons en particulier les travaux destinés à détecter les délaminations entre les interfaces de la structure de chaussée. Le dépouillement des mesures des méthodes existantes nécessite généralement l'intervention d'opérateurs compétents.

Parmi les méthodes END, les systèmes GPR (Ground Penetrating Radar) sont utilisés depuis une vingtaine d'années en génie civil pour réaliser des opérations d'auscultation des chaussées à vitesse de trafic. Ils utilisent les propriétés de propagation des ondes

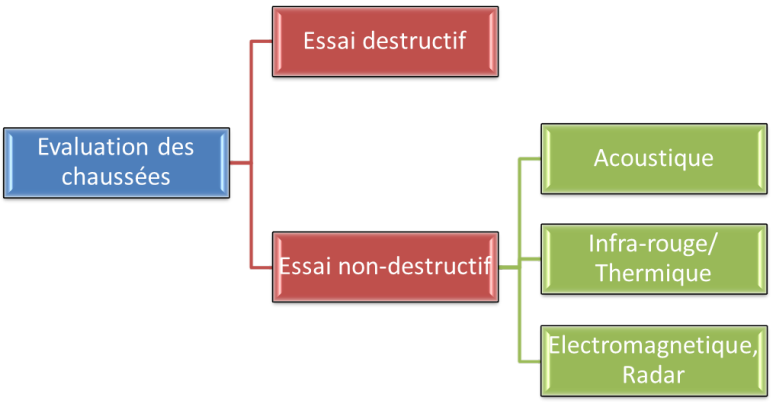

Figure 2: *Méthodes END pour l'auscultation des chaussées*

électromagnétiques pour sonder la chaussée, et déterminer la géométrie et les propriétés diélectriques des couches. Le radar présente l'avantage d'être une technique non destructive à grand rendement et sans contact. En outre, des travaux de la littérature ont également développé des méthodes de détection de décollements centimétriques. En comparaison, l'objectif de cette thèse est la détection des décollements millimétriques entre les deux premières couches de chaussé par des techniques radar. Pour atteindre cet objectif, nous combinons l'utilisation d'un radar GPR Ultra-Large Bande (ULB) à des techniques de traitement de données. Nous cherchons à améliorer la détection du décollement par rapport aux autres méthodologies existantes dans la littérature.

Les méthodes par apprentissage (Machine Learning) est une famille de méthodes de traitement de données. Nous la développons dans cette thèse pour la détection de décollements à partir de données GPR. En particulier, nous détaillons au Chapitre 3 la mise en œuvre de ces méthodes pour la détection du décollement. Ainsi, pour atteindre cet objectif, nous avons mené une étude comparative de quatre méthodes par apprentissage. Une méthode non supervisée (*k-means*) et trois méthodes par apprentissage supervisée (deux méthodes de classification à vaste marge (SVM) et une méthode par forêt d'arbres décisionnels) ont été étudiées. La Figure 3 présente le synoptique général de la mise en œuvre de ces quatre méthodes de traitement pour la détection de décollement d'interfaces de chaussées.

Dans ce travail, la méthode des rapports d'amplitude (ART pour Amplitude Ratio Test) sert de référence pour comparer les performances de méthodes étudiées. La méthode ART est une méthode opérationnelle utilisée par la communauté GPR pour détecter la présence de défauts d'interfaces dans la chaussée, et tester l'intégrité des chapes d'étanchéité des tabliers de ponts.

Au Chapitre 3, nous présentons les quatre méthodes de traitement de données par apprentissage qui sont utilisées dans la thèse pour détecter les décollements d'interface de chaussées. La méthode de clustering classique non-supervisée *k-means* est d'abord présentée. Une modification de l'initialisation de cette méthode a permis d'améliorer

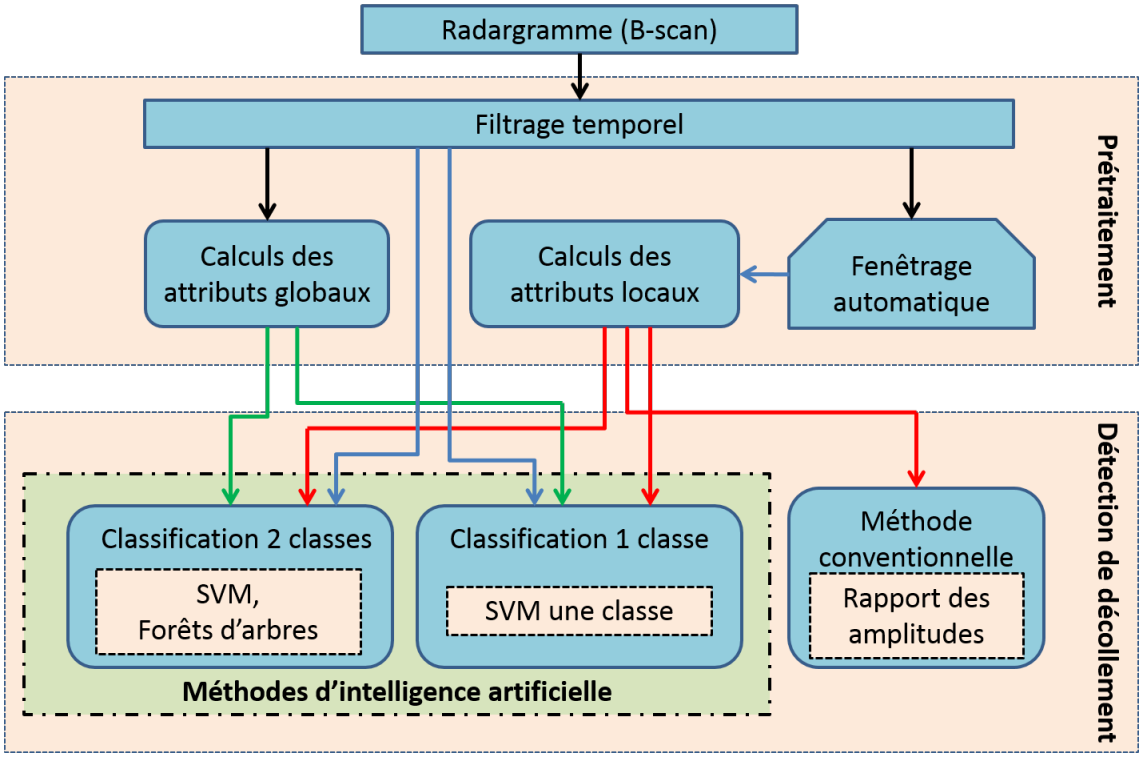

Figure 3: *Synoptique général des méthodes de traitement de données étudiées dans cette thèse pour la détection de décollement entre couches de chaussées*

ses performances. Nous présentons ensuite deux méthodes par apprentissage supervisée, une méthode paramétrée (séparateur à vaste marge ou *Support Vector Machine*) et une dernière, non paramétrée (forêts d'arbres décisionnels). La méthode SVM a été utilisée de deux manières. La méthode SVM conventionnelle consiste à réaliser la détection à partir d'une classification binaire (en deux classes) des données (décollement, sans décollement). La variante One-class SVM, que nous introduisons ensuite, cherche à détecter les décollements comme des anomalies (*outliers*) dans le signal. Enfin, la méthode non-paramétrée des forêts d'arbres décisionnels (*Random forests*), est introduite. La Figure. 4 présente une classification des méthodes étudiées.

Le principe de chaque méthode est illustré au Chapitre 3 par le traitement des échantillons temporels des signaux radar sans pré-traitement, *i.e.*, donnée brutes. Les signaux correspondent à des données radar bruitées simulées avec des hypothèses simplificatrices (le modèle est détaillé en annexe). Chaque méthode supervisée a permis de détecter des décollements d'interfaces de permittivités différentes à moyen rapport signal à bruit ($\approx$ 30 dB). La méthode non-supervisée (k-means) se distingue par des résultats de classification moins précis.

Toutefois, cette mise en œuvre des méthodes par apprentissage, bien qu'immédiate et intuitive, présente quelques inconvénients, qui sont susceptibles d'en limiter les performances : redondance des informations, base de données volumineuse, temps de calcul et complexité calculatoire importantes.

Une alternative consiste à représenter les échantillons temporels des signaux par un nombre réduit d'attributs (ou descripteurs). Le Chapitre 4 présente une sélection d'attributs

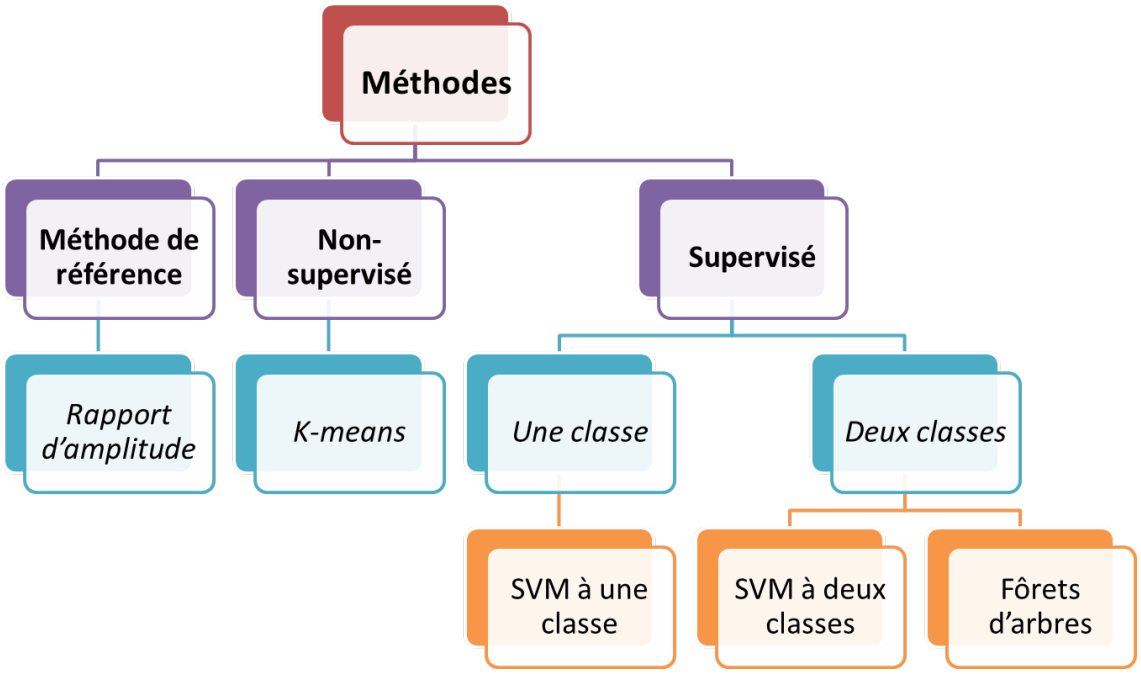

Figure 4: *Classification des méthodes de traitement de données étudiées dans cette thèse*

du signal temporel, qui peut être utilisée pour la classification des signatures GPR. On distingue les attributs locaux et globaux. Les attributs locaux décrivent le signal sur une fenêtre temporelle localisée à l'interface de la chaussée où le décollement survient. Les attributs globaux décrivent le signal GPR sur un intervalle temporel plus étendu, incluant les échos des deux premières interfaces de la chaussée. Les attributs les plus sensibles au décollement sont mis en évidence par la séparation de leurs densités de probabilité respectives.

Les performances des méthodes sont évaluées quantitativement à partir des résultats de classification des signaux de chaque A-scan, soit en bonne détection (vrai positif; TP), absence de défauts (ou vrai négatif; TN), fausse alarme (faux positif; FP) et non détection (faux négatif; FN). Ces valeurs permettent d'établir des courbes ROC, et de calculer les indices de performances de type DSC (Dice score) et MCC (Matthew's correlation coefficient), dont le principe est rappelé en Annexe C.

En termes de classification, l'influence du type d'attributs (attributs locaux, globaux avec /sans réduction par l'ACP) sur les performances de classification des méthodes de traitement a été mise en évidence à partir de signaux GPR simulés. Dans le cas de la SVM, les meilleures performances de classification sont obtenues à partir des attributs locaux; elles sont très proches de celles obtenues au Chapitre 3 à partir des échantillons temporels du signal GPR. L'ACP permet de réduire quelque peu le nombre d'attributs, mais sans observer de différence significative sur les performances de classification.

Après le choix du type de données, nous présentons au Chapitre 5, l'optimisation des

paramètres des méthodes supervisées paramétrées, *i.e.*, SVM. En résultat du Chapitre 4, les paramètres des deux variantes de la méthode SVM sont optimisés à partir des attributs locaux des signaux. L'optimisation est analysée par le biais d'une étude de sensibilité des performances des méthodes vis-à-vis de la taille des données d'apprentissage, de l'optimisation des hyper-paramètres, du choix du noyau, et des techniques de validation croisée (Cross Validation ou CV en anglais); cette dernière étant jugée comme la plus importante. La sensibilité des performances des méthodes de traitement est illustrée sur des données simulées.

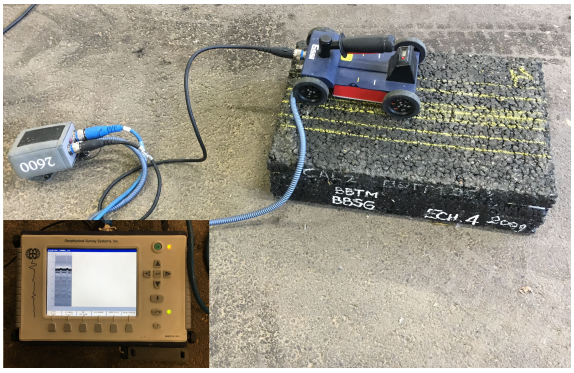

Figure 5: *Acquisition de données radar GSSI SIR-3000 sur des dalles de béton bitumineux au Cerema-Angers*

(a) Sans décollement

(b) Décollement de $t_{deb} = 0.5\,\text{cm}$

(c) Décollement de $t_{deb} = 1\,\text{cm}$

Figure 6: *Illustration des trois décollements artificiels entre dalles de bétons bitumineux.*

Enfin, les méthodes de traitement présentées dans la thèse sont testées au Chapitre 6 sur deux bases de données expérimentales de signaux radar. Les données radar ont été collectées au-dessus de décollements artificiels respectivement, sur des dalles bitumineuses (Cerema-Angers) et sur une structure de chaussée du manège de fatigue de l'IFSTTAR-Nantes. Le descriptif de ces bases est disponible dans l'Annexe B.

Au Cerema, le radar utilisé est un radar impulsionnel commercial GSSI (modèle SIR-3000), couplé au sol, et de fréquence centrale 2.6 GHz. Il a servi à collecter des mesures sur des dalles de béton bitumineux, composées de 2 couches séparées par un vide d'air variable de 0.5 cm cm à 1.0 cm d'épaisseur (voir Figures B.4 et B.5).

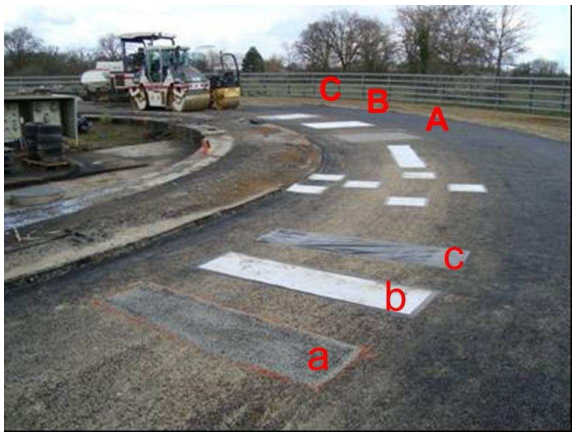

Figure 7: *Zone du manège de fatigue de l'IFSTTAR-Nantes où ont été placés des défauts artificiels sur la couche de base. Les zones [A], [B] et [C] représentent les zones des trois plus grands défauts (sable, géotextile et non-collé, respectivement) introduits à la construction entre la couche de base et la couche de roulement.*

(a) Radar GSSI SIR-3000 (2.6 GHz couplé au sol) (b) Radar ULB à sauts de fréquences (4.5 GHz couplé à l'air)

Figure 8: *Acquisition des deux types de données radar sur le manège de fatigue, IFSTTAR-Nantes*

Le manège de fatigue de l'IFSTTAR-Nantes permet de simuler de manière accélérée l'effet du trafic routier sur la durabilité des infrastructures de chaussée. Pour simuler un décollement entre couches, trois types de défauts artificiels ont été intégrés à la structure de chaussée lors de la construction d'une portion de piste. Comme illustré Figure B.9, il s'agit d'une zone Géotextile (décollement très fort), une Sable (décollement intermédiaire) et une zone non-collée (décollement faible). Les données ont été acquises à plusieurs étapes de chargement (10, 50, 100, 200, 250 et 300 kilo-chargements) à l'aide des deux configurations et technologies radar existantes: le radar GSSI SIR-3000 déjà évoqué, fonctionnant à 2.6 GHz (voir Figure B.15), et un système experimental de radar à sauts de fréquences (SFR) couplé à l'air, fonctionnant à 4.5 GHz (voir Figure B.11). Seules les résultats obtenus à l'aide des données radar SFR sont présentés dans cette thèse.

Les résultats de traitement du Chapitre 6 ont été obtenus après optimisation des méthodes par apprentissage pour chacun des jeux de données, selon la procédure explicitée aux Chapitres 4 et 5. Sur les données GSSI du Cerema (radar couplé au sol, vide d'air), on observe que la méthode SVM à deux classes et la méthode de forêts d'arbres décisionnels atteignent le meilleur taux de détection. La méthode SVM à une classe, affiche une plus faible précision. Pour les données SFR sur le manège de fatigue (défauts artificiels insérés à la construction entre la couche de roulement et la couche de base), les résultats de classification à chaque cycle de chargement sont rassemblés en Annexe. Les trois méthodes de classification détectent facilement les défauts les plus marqués (géotextile et sable). Mis à part les données à 200K et 250K, les trois méthodes détectent également le défaut le moins marqué (tack free) avec précision.

Finalement, les résultats de classification des méthodes SVM et de forêt d'arbres décisionnels sont formulés en termes d'estimation de la probabilité d'apparition d'un décollement (voir Figure 9) par l'intermédiaire des deux indices DPR (*debonding prediction rate*) et NPR (*Non-debonding prediction rate*). Les tests expérimentaux semblent montrer que ces deux nouveaux indices permettraient de fournir une aide à la décision plus concrète que les indices de classification binaire DSC et MCC utilisés conventionnellement.

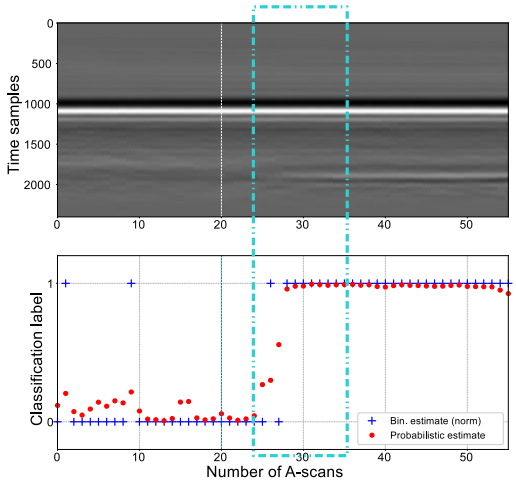

(a) [SVM à une classe

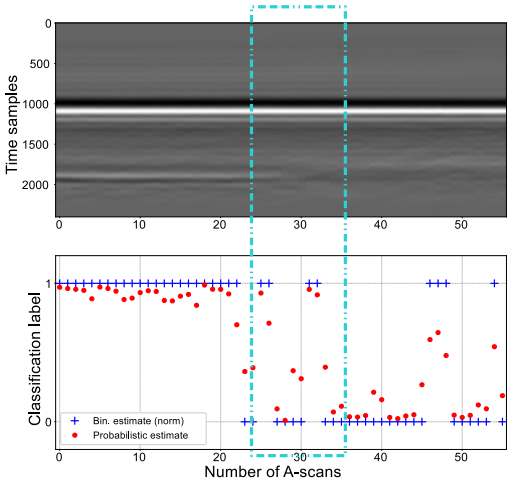

(b) SVM à deux classes

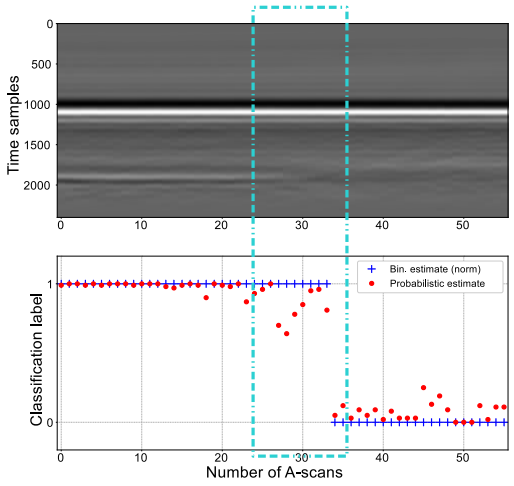

(c) Forêts d'arbres décisionnels

Figure 9: *Exemple de résultats de classification des signaux radar SFR méthodes en terme de classification binaire et d'estimation de la probabilité d'apparition d'un décollement pour le zone non-collé (décollements faible) à 10K de chargements*

Extended Abstract

The network of French roadways consist mainly of national roads (or auto-routes), most of which were completed over three decades ago. Over the passage of time, the influence of traffic, weather conditions and various phenomena such as water seepage, the degradation of the pavement structure is inevitable. This degradation is visible on the pavement surface by cracks. Additionally, surface cracks may also reveal structural defects within the pavement, including, among other things, uncoating or delamination defects at the interfaces between the pavement layers. Internal delaminations can give rise to surface cracks with time, namely, reflexive cracks. In this context, the early detection of such type of internal defects (debondings) can improve the management and maintenance of the road network.

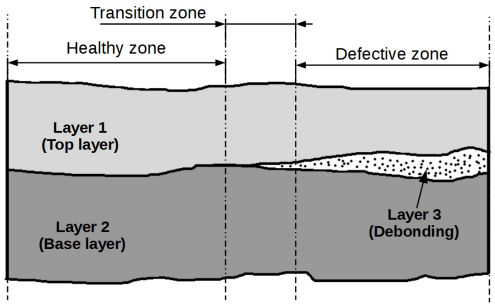

Figure 10: *Illustration of a pavement structure with a debonding between layers*

During the thesis, we primarily focused on the detection of interlayer debondings between the top two layers of the pavement structure. The first chapter presents the problem statement and the global objectives of the thesis. Various works are already available in the literature on this issue. However, most of these applications use destructive tests, which are limited to a few number of spatial measurements and also specific to a time of test. In comparison, in this thesis, we develop data processing methods to detect debondings by means of Non-Destructive Testing (NDT) which allow a dense spatial sensing of the subsurface.

In Chapter 2, we discuss the State of the Art and the progress made in the field of NDT with the emphasis on radar imaging of pavement structures. To support the work in this thesis, various research has been found to implement NDT delaminations between the interfaces of the pavement structure. However, most of these methods require specific human skills for data interpretation purposes.

In this context, Pulse radar systems, called Ground Penetrating Radar (GPR) have been in use for over twenty years in civil engineering to conduct pavement survey at traffic

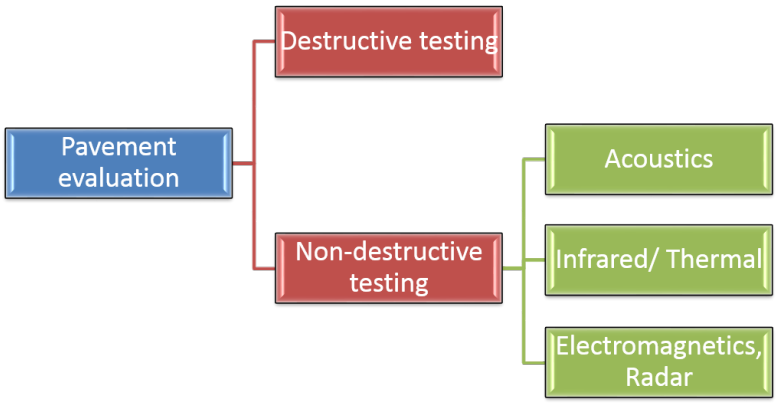

Figure 11: *NDT ascultation methods for pavement evaluation*

speed. GPR uses the properties of electromagnetic waves to probe the pavement material in order to determine the characteristics of the structure (e.g, geometry and dielectric properties). The advantage of GPR is from the fact that it is a non-invasive, contact-less technique with high efficiency. In addition, some research already exist in the literature that provide the thickness of layers in the order of a few centimeters. In contrast, the objective of this thesis is detecting debondings of the order of a few millimeters between the first two layers of pavement by radar techniques. To achieve this goal, it is required to improve the time resolution by combining the use of Ultra-Wide Band (UWB) GPR technology with suitable data processing techniques. Moreover, we aim to improve the debonding detection efficiency compared to other existing methodologies in the literature.

To achieve this goal, in this thesis, we develop machine learning methods for debonding detection from GPR data. In Chapter 3, we detail the implementation of these machine learning methods for our application. A comparative study of four machine learning methods is conducted, which included both unsupervised and supervised methods. An unsupervised method based on clustering technique, namely, k-means, and three supervised learning methods (Two-class SVM, One-class SVM and Random forests) were studied. Figure 12 presents the global approach of the data processing methods used for the detection of interlayer debondings.

In this research, a conventional method, namely Amplitude Ratio Test (ART) is used as a reference to compare the performance of the methods studied. ART is an operational-level method used in the GPR community to detect the presence of defects in the pavement structure and to probe waterproofing screeds on bridge decks. The following chapters detail the different data processing methods studied in this thesis.

In Chapter 3, we present the four machine learning methods studied during the thesis to detect interlayer debondings from radar data. An unsupervised classical clustering method (called k-means) is first introduced. The initialization step of the clustering method is modified to improve its performance. We then present two supervised learning methods, a parametric method namely Support Vector Machines (SVM) and a non-parametric method

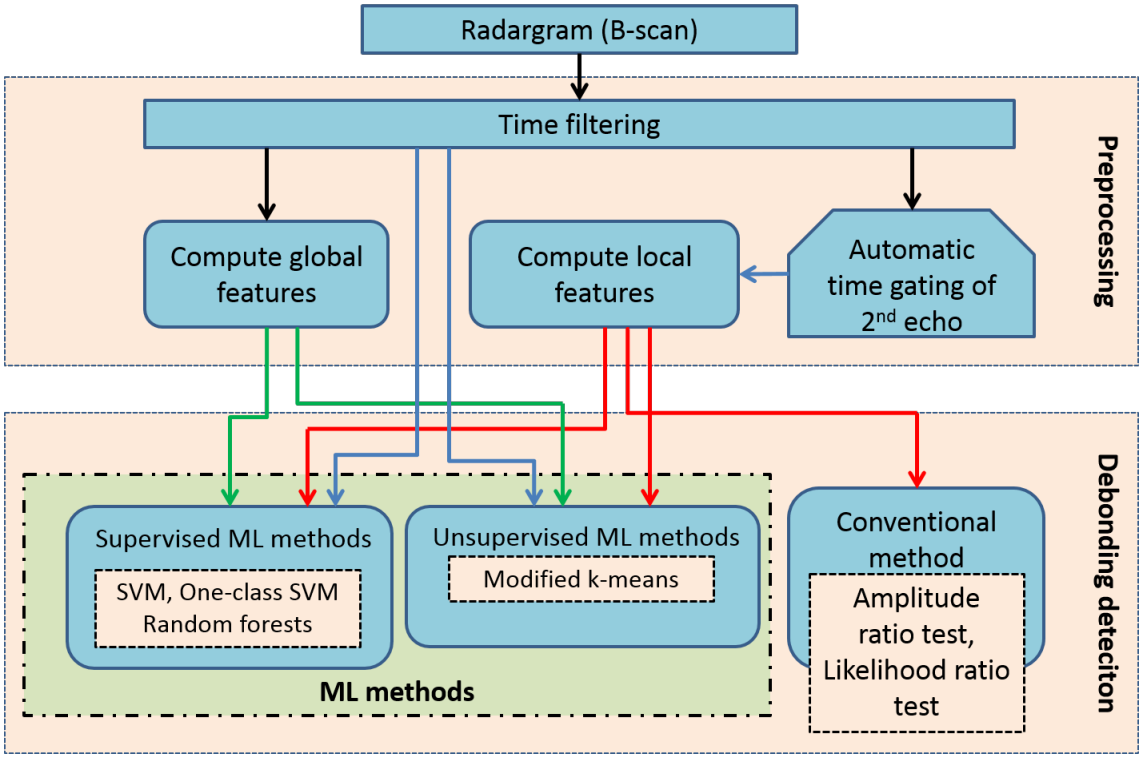

Figure 12: *General synopsis of the processing methods studied in the thesis for the detection of thinf interlayer debondingd*

namely, Random forests. The conventional SVM is used to detect debondings as binary SVM (Two-class SVM) and as an anomaly detection method (One-class SVM). The One-class SVM is a variant that is used to detect debondings as anomalies (outliers) in the signal. Finally, Random forests was introduced. Figure. 13 presents a classification of the studied methods.

The implementation of each machine learning method is illustrated in Chapter 3 by direct processing of the temporal GPR data (*i.e*, raw GPR data). In the initial phase, the simplified analytic data model presented in Appendix A was used. Each supervised method showed good qualitative results as they were able to detect debondings (of thicknesses 2 mm) of different permittivities with medium signal-to-noise ratio (≈ 30 decibels). Nevertheless, the unsupervised method (k-means) is shown to not perform as well as the supervised methods (SVM, Random forests).

Although the implementation of machine learning methods using raw GPR data is intuitive and easy, redundant data, computational complexity and burden may likely limit the performance of said methods.

One possible alternative would be to represent the temporal samples as a reduced number of signal attributes (or signal features). Chapter 4 presents the selection of time signal features, which can be used for the classification of GPR A-scans. Here, we categorize the GPR data attributes as local and global features. Local signal features describe the signal within a limited time window located at the interface of the pavement where the debonding is supposed to occur. As a result, these signal features, which focus on the sought-out information (*i.e*, second echo) are expected to be optimal for best classifica-

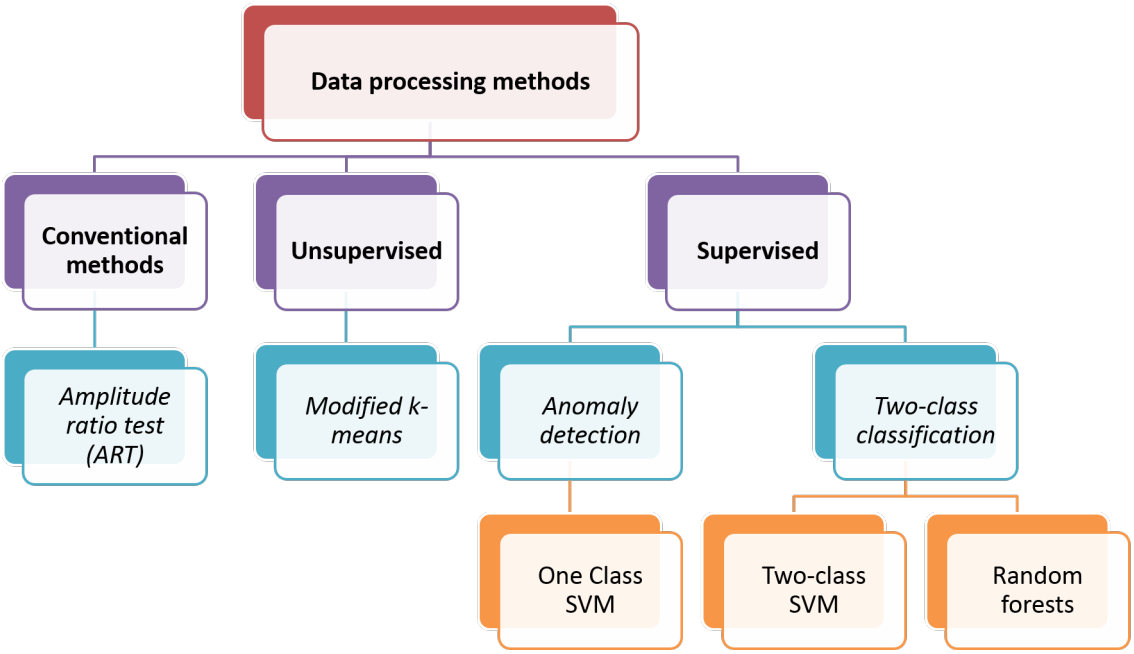

Figure 13: *Classification of data processing methods studied during the thesis*

tion. Global attributes describe the GPR signal over a longer time interval, that includes the first two echoes (*i.e*, surface and the interface reflections) of the pavement. The most sensitive signal features to the debonding are highlighted by using their probability density distributions. Finally, Principal Component Analysis (PCA) attempts to reduce the number of signal features by an additional factor.

The performances of the methods are evaluated quantitatively using classification results of each A-scan as one of the four possible outcomes, namely, good detection (True Positive, TP), absence of defects (or True Negative TN), false alarm (False Positive; FP) and non-detection (False Negative; FN). These values are used to establish ROC curves, and to calculate the Performance indexes namely, DSC (Dice score) and MCC (Matthew's correlation coefficient), which are presented in Appendix C.

As part of the initial analyses, the influence of the feature type (local, global features with/without PCA reduction) on the classification performance of the data processing methods was evidenced from simulated GPR signals (Appendix A). The results were compared with the performances observed in Chapter 3 obtained using the raw GPR data. In the case of SVM, the best classification performance is obtained from the set of local features. Although PCA somewhat reduced the number of global and local features, no significant difference in classification performance was observed.

However, the robustness of machine learning methods also depends on other parameters, such as the size of the learning data, method hyper-parameters, method kernels, cross validation techniques, *etc.* It is therefore necessary to identify the 'best' parameters that can be used to achieve improved efficiency in terms of detecting fine interlayer debondings.

Once the optimal feature data set is chosen, in Chapter 5, we present the optimization of parameters for the parametrized supervised methods, *i.e.*, SVM. Strictly speaking, the optimization depends on the type of data processed. Also, from Chapter 4, the parameters

of the two variants of SVM are optimized from the local signal features. The CV is seen to undoubtedly be the most important step of optimization. The results are illustrated for simulated analytic data (detailed in Appendix A).

Chapter 5 primarily consists of the approach aimed at optimizing methods that includes the Model-fitting using cross validation techniques and kernel functions. In addition, to make the method more operational, the optimization of the parameters is performed on various debonding permittivity values.

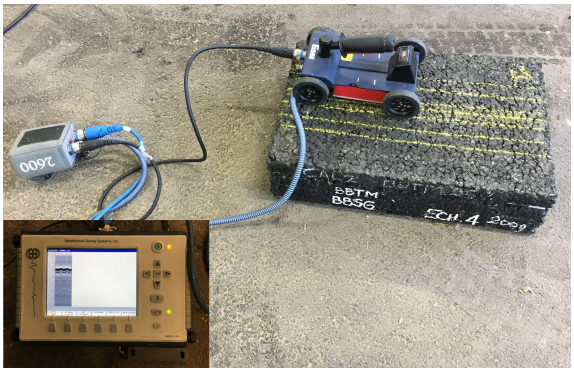

Figure 14: *GSSI SIR-3000 experimental setup for data acquisition on the bituminous test bench at Cerema-Angers*

(a) Non-debonding

(b) Debonding thickness $t_{deb} = 0.5\,\text{cm}$

(c) Debonding thickness $t_{deb} = 1\,\text{cm}$

Figure 15: *Test bench configuration at Cerema-Angers with air-void as debonding layer*

Finally, the machine learning methods presented in the thesis are tested in Chapter 6 on two experimental GPR databases. The radar data were collected over artificial debondings respectively on bituminous slabs (Cerema-Angers), and on a test pavement structure (Fatigue carousel at IFSTTAR-Nantes). The description of these databases is available in Appendix B.

At Cerema, a commercial impulse radar, namely GSSI (SIR-3000 model) operating in ground-coupled configuration at 2.6 GHz is used. It was used to collect GPR data on asphalt concrete slabs, composed of 2 layers with an air-void acting as a debonding layer of thickness 0.5 cm and 1.0 cm (see Figures 14 and 15).

On the other hand, the IFSTTAR's fatigue carousel in Nantes is used to simulate road

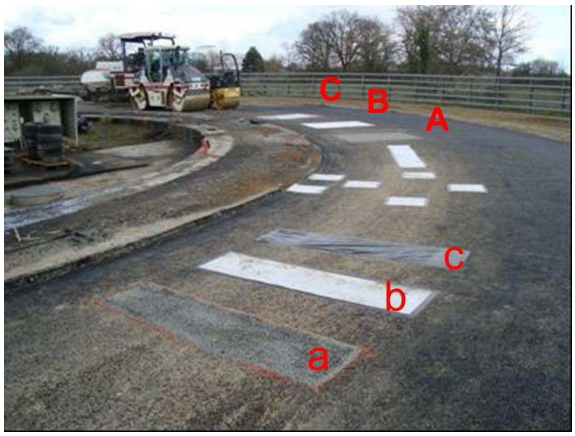

Figure 16: 25 m *track with artificial defects at the fatigue carousel before laying the wearing course layer. Areas 'A,a', 'B,b' and 'C,c' indicate Sand, Geotextile and Tack-free based defects respectively between the base and the top layer*

traffic in order to carry out accelerated durability tests. Three types of artificial defects were incorporated into the pavement structure during the construction of a 25 m section of the track to simulate a separation between layers. As shown in Figure 16, these defects are respectively Geotextile-based (very strong debondings), sand-based (weaker debondings) and tack-free based (weak debondings). The data was collected at several loading stages (10, 50, 100, 200, 250 and 300 K-loadings) using the two existing configurations of radar technologies. The ground-coupled GSSI SIR-3000 radar (presented earlier), operating at 2.6 GHz (see Figure 17(a)) and an experimental system of air-launched stepped-frequency radar operating at 4.5 GHz (see Figure 17(b)) were used. Only the results obtained using the SFR radar data are presented in this thesis.

(a) Using ground-coupled commercial GSSI SIR-3000 (b) Using air-launched UWB radar

Figure 17: *Data acquisition at the fatigue carousel, IFSTTAR-Nantes*

The results presented in Chapter 6 were obtained after the optimization of the machine learning methods for each dataset, following the procedures explained in Chapters 4 and 5. On the Cerema GSSI data (ground coupled radar, air-void), it is observed that Two-class SVM and Random forest methods achieved the best detection rate. One-class SVM,

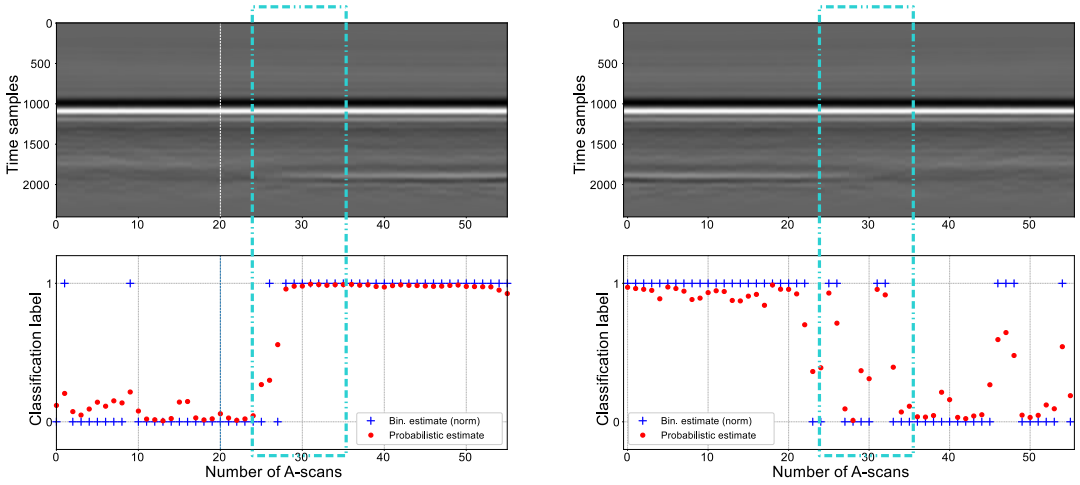

(a) One-class SVM

(b) Two-class SVM

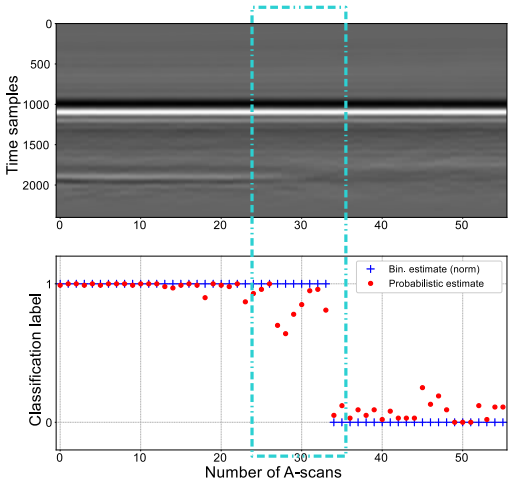

(c) Random forests

Figure 18: *Some illustrations of results for the classification of GPR data using machine learning methods as binary classification and probability estimates for Tack-free based defects at 10K loading*

displays a lower precision. For SFR data on the fatigue carousel (artificial defects inserted between the wearing course and the base layer), the classification results for each loading stage are collated in Appendix E. The three classification methods easily detect the strong defects (Geotextile and Sand). Apart from the data at 200K and 250K, the three methods were also able to detect the weak defects (Tack-free) with precision.

Finally, the classification results of the three machine learning methods are formulated in terms of estimating the probability of occurrence of a detachment (see Figure 9) through the two indexes: DPR (*Debonding Prediction Rate*) and NPR (*Non-debonding Prediction Rate*). Experimental tests seem to show that these two new indexes would provide more concrete decision support than conventionally used DSC and MCC binary classification indexes.

List of Publications

International Conference Publications

- S. S. Todkar, C. Le Bastard, V. Baltazart, A. Ihamouten, X. Dérobort, C. Fauchard, D. Guilbert and F. Bosc, "*Detection of debondings with Ground Penetrating Radar using a machine learning method*", 2017 **9th International Workshop on Advanced Ground Penetrating Radar (IWAGPR)**, Edinburgh, 2017, pp. 1-6.(DOI: 10.1109/IWAGPR.2017.7996056)

- S. S. Todkar, C. Le Bastard, V. Baltazart, A. Ihamouten and X. Dérobort, "*Comparative Study of Classification Algorithms to Detect Interlayer Debondings within Pavement Structures from Step-Frequency Radar Data*", IGARSS 2018 - 2018 **IEEE International Geoscience and Remote Sensing Symposium**, Valencia, 2018, pp. 6820-6823. (DOI: 10.1109/IGARSS.2018.8518959)

- A. Ihamouten, X. Derobert, F. Bosc, D. Guilbert, J.N. Gaudin, S. S. Todkar, F. Bernardin and J.L. Bicard., '*Monitoring of water imbibition of a particular porous pavement structure by impulse and step-frequency radar*'. 2018 **17th International Conference on Ground Penetrating Radar (GPR)**, June 2018, Rapperswil, France. DOI: 10.1109/ICGPR.2018.8441526

Journal Publications

- Shreedhar Savant Todkar, Cédric Le Bastard, Vincent Baltazart, Amine Ihamouten, Xavier Dérobert, "*Performance assessment of SVM-based classification techniques for the detection of artificial debondings within pavement structures from stepped-frequency A-scan radar data*", **NDT & E International**, Volume 107, 2019, 102128, ISSN 0963-8695, DOI: https://doi.org/10.1016/j.ndteint.2019.102128.

- C. Le Bastard, J. Pan, Y. Wang, M. Sun, S. S. Todkar, V. Baltazart, N. Pinel, A. Ihamouten, X. Dérobert and C. Bourlier , '*A Linear Prediction and Support Vector Regression-Based Debonding Detection Method Using Step-Frequency Ground Penetrating Radar*', in IEEE Geoscience and Remote Sensing Letters, vol. 16, no. 3, pp. 367-371, March 2019. DOI: 10.1109/LGRS.2018.2873045

Publications under writing/ready for submission

- Shreedhar Savant Todkar, Cédric Le Bastard, Vincent Baltazart, Amine Ihamouten and Xavier Dérobert, '*One-class SVM based outlier detection strategy to detect thin interlayer debondings within pavement structures using Ground Penetrating Radar data*', **IEEE Journal Of Selected Topics In Applied Earth Observations And Remote Sensing (JSTARS)**; *under writing.*

- Shreedhar Savant Todkar, Vincent Baltazart, Cédric Le Bastard, Xavier Dérobert, Amine Ihamouten and Jean-Michel Simonon, '*Performance assessment of supervised machine learning methods on GPR data to detect interlayer debondings within pavement structures*'; accepted at the **6th international conference on Accelerated Pavement Testing (APT)**; *full-text under writing.*

Miscellaneous

- Poster presentation at the '*Journées Téchniques des Routes (JTR) 2018*' conducted at Cité des Congres de Nantes in February 2018

- Video presentation of thesis as a part of '*Ma thèse au Cerema*' on 26th April 2019, published on 24th May 2019 (Video link: https://dai.ly/x797kgp)

- Thesis presentation under 3 minutes: '*Ma thèse en 180 seconds*' in April 2019 (Presentation link: https://www.cerema.fr/fr/actualites/ma-these-au-cerema-suivi-endommagement-structures-chaussees)

- Thesis work presented at **IFSTTAR, Site: Marne la Vallée** during the 'Journées doctoriales COSYS' on 4th July 2018

- Oral thesis presentation entitled '*Suivi de l'endommagement des structures des chaussées par technique radar ultra-large bande*' at the '*Journées des Doctorants MathSTIC*' conducted at Université de Nantes in May 2018

- Paper presentation entited 'Detection of debondings with GPR using machine learning methods' at Cerema, Site: Angers as a part of ECODEM; on 3rd July 2017

Part I

INTRODUCTION

Chapter 1

Introduction

Contents

1.1 Introduction

1.1.1 Context of the Thesis

This thesis was conducted during the period 2016 - 2019 within both the Laboratory *Evaluation Non-Destructive des Structures et des Matériaux (ENDSUM)* at the Centre d'Etudes et d'Expertise sur les Risques, l'Environnement, la Mobilité et l'Aménagement (**Cerema**) and the Laboratory *Composants et Systèmes / Structure et Instrumentation Intégrée (COSYS-SII)* at the Institut Français des Sciences et Technologies des Transports, de l'Aménagement et des Réseaux (**IFSTTAR**).

IFSTTAR and Cerema are two recent French public institutes affiliated to the Ministry of Ecology, Sustainable Development and Energy, which have been created in 2011 and 2014, respectively. They both collaborate to conduct applied research activities and expert appraisals in the fields of transport, civil engineering infrastructures, natural hazards and urban issues with the aim of improving the living conditions and promoting the sustainable development of our societies. They support public policies at different scales.

Within this scope, IFSTTAR and Cerema have been both involved in the survey of civil engineering structures, namely, road network and bridges mainly, by Non-Destructive Techniques (NDT) and Structural Health Monitoring (SHM) methods. Such survey contributes to minimize the risk of collapse, help at planning, maintenance and repairs, and, at extending the life cycle of civil engineering infrastructures.

1.1.2 Problem statement: Monitoring structural pavement conditions

France has a large network of roads that stretch for over a million kilometers reaching to every part of the country. According to the research conducted by 'The World Factbook' of the CIA in 2010, France stands 8th in the ranking of the world's largest network of roadways. A major portion of these roads are made up of bituminous concrete (also sometimes referred to as Hot-mix asphalt) and were laid about three decades ago.

Since the beginning of human settlements, one of the major transportation media has been the use of roads. With the change in times, the roadways proved to be one of the most efficient and convenient means of transportation within a mainland until the invention of the airplanes at the beginning of the 20th century.

Today, roads are the most widespread means for transportation. And depending on the environmental situations, a wide variety of materials have been used to construct these pavements. Based on the type of material used, roads can be classified as:

- Earthen roads
- Gravel roads
- Water bound Macadam (WBM) and Wet Mix Macadam (WMM) roads
- Bituminous concrete (Hot-Mix asphalt or HMA) roads
- Concrete roads

From the various types of materials mentioned above, bituminous is the most widely used material for roads. They are low-cost and are excellent for driving conditions over all types of weather conditions. The bituminous pavements are multi-layered (generally two or three layers) pavement structures. The thickness of each layer depend on the mechanical characteristics to achieve for the pavement structure. According to [19], the pavement surfacing materials (*i.e.*, the top layer) could be as high as half of the entire pavement costs. Thus, the selection of proper materials plays an important role in the lifespan of the pavement and the user comfort.

However irrespective of the material quality, with the passage of time, these pavements undergo deterioration. The cause can be environmental (rain, weather, erosion *etc.*), the excessive use by the traffic or even the use of average quality construction material. The damage to the pavement structures can be either external, *e.g.*, visible surface cracks, or internal, *e.g.*, delamination between layers. Be it may, both damages equally pose a threat to the lifespan of the pavement. Additionally, the road surface defects are caused mainly by underground defects that can occur long before visible degradation occurs on the surface. As a result, the evaluation and monitoring of pavement structure damage is of utmost importance for the sustainable management of roads.

The monitoring of pavement structures has been carried out for over quite a few decades. The methods can be broadly classified as Destructive testing (DTs) and Non-destructive testing (NDTs). Under DTs, a small section of the structure is drilled and the specimen is used to analyze the structure. On the other hand, NDT involves no

such disturbance to the structure. It uses various methods to determine the properties of the materials without damaging the structure whatsoever. Ground Penetrating Radar is one of the most widely used method under NDT. The use of GPR Systems have been one of the major achievements in the NDT for roads and bituminous pavements. GPR systems are used to probe the structural pavement conditions, which include the detection of subsurface defects and the determination of the geometric subsurface structure.

1.1.3 Objectives: GPR data processing for debonding detection

Pulse radar systems have been used over two decades to perform NDT operations on pavements. They not only provide continuous measurements of pavement layer thickness, but also allow the detection of significant discontinuities (cracks, debondings *etc.*) between layers providing a large enough dielectric contrast between layers/discontinuities. However, their use depends on the skills of users to perform the interpretation of radar images. The debonding can be defined as the horizontal delamination or break at the interface between two pavement layers, as illustrated in Figure 2.1. Debondings may initiate reflexive cracks up to the pavement surface and greatly reduce the lifespan of the structure. It is thus recommended to detect such defects at an early stage to avoid the degradation of the structure.

Within this scope, the objective is to map the coating condition at the interface between the top two pavement layers, with the help of both Ground Penetrating Radar (GPR) at microwave range and suitable data processing methods. Debonding if any, is assumed to be a few mm in thickness, *i.e.*, to represent a small fraction of the dominant radar wavelength. The objective will then rely on the use of Ultra wide-band (UWB) capabilities at S and C bands on the one hand, and on the other hand, on advanced data processing techniques to detect the millimetric debondings within said pavements.

On one hand the UWB systems provide better time resolution, but may reduce the penetration depth of microwaves within pavement structure in a limited way. Using a combined effort of better time resolution and advanced signal processing techniques, we aim to improve GPRs ability to detect even thinner defects (in the order of a few mm). The heterogeneity of civil engineering materials imposes an upper limit on the frequency that can be used, where we will attempt to quantify using experimental approaches.

The data processing is integrated within a more general framework including a two-step strategy to process radar B-scan images. At first, some data processing techniques will be used to detect debondings within the radar profiles, then, as a second step, time delay estimation techniques may be performed on the selected A-scans to further characterize the defects, *e.g.*, thickness and permittivity. However, the PhD will focus on the first-step, namely, the detection, and the results may be used later on for the ongoing ANR research project, called **ACIMP** (https://anr.fr/Projet-ANR-18-CE22-0020).

For debonding detection, the thesis will focus on a specific data processing family techniques, called Machine Learning Methods (MLMs). In this thesis, a comparative study of various MLMs, namely, unsupervised and supervised methods, is carried out. The performance of these methods is compared with the conventional method which is

routinely used by the GPR community for the qualitative assessment of the pavement subsurface conditions and sealing screeds over bridges.

The performance assessment of the studied methods is based on both simulated and field data. Simulated models are created with the help of analytical models and two numerical methods, namely, Method of moment (MoM) and Finite Differential Time Domain (FDTD) methods). Field data are collected using the two main radar technologies, namely, air-coupled step-frequency radar and ground-coupled pulse radars.

1.2 Thesis Structure

The thesis is categorized into six chapters with three parts:

In Part-A, Chapter. 2 presents the debonding survey in the pavement structures. It discusses the state of the art in destructive and non-destructive testing and the process to detect debondings. Finally, a reference debonding detection method namely, Amplitude Ratio Test (ART) is presented with qualitative results from a simulated data model.

Chapter. 3 introduces the concept of Machine Learning. This chapter discusses the family of machine learning and its types. An unsupervised methods based on k-means clustering is presented along with three supervised methods, namely Support vector machines (Two-class SVMs and One-class SVMs) and Random forests are presented. Qualitative results using the raw GPR data obtained from analytic simulated data are also presented.

Under Part-B, beginning with the need for preprocessing and feature selection, Chapter. 4 introduces the signal feature analyses and the feature selection. Various approaches such as A-scan *vs.* B-scan feature selection, temporal and spectral, and, global and local signal features are presented. Two major feature selection techniques namely distribution basesd (PDF) based feature selection and PCA-based feature reduction techniques are presented. A preliminary test is conducted using simulated data to compare the performance of the machine learning methods using various input feature sets.

Part-C proceeds with the Data processing for debonding detection. In Chapter. 5, the performance measurement criteria are presented. The chapter also introduces the various optimized parameter selection techniques used to in the detection of thin debondings. The robustness of the machine learning methods *w.r.t* the input parameters and the pavement medium are discussed.

Chapter. 6 finally presents the various results using machine learning methods application for decision support to detect debondings from experimental data. These experimental data are acquired at the test sites at both Cerema and IFSTTAR using ground and air-coupled radar configurations. The results presented are in two categories: binary detection and probabilistic estimation.

The final chapter draws the conclusions of the thesis and provides perspectives to the direction where the GPR NDT work is heading in the near future.

In addition, five appendices are added at the end of the manuscript. Appendix. A presents the simulated data modeling using analytic method (Fresnel model), MoM (GPILE) and FDTD (GprMax) methods. These databases are used to qualitatively represent the performance of the machine learning methods in Chapter. 3. Appendix. B presents the ex-

perimental data collected using two radar configurations (air-coupled and ground-coupled) at IFSTTAR's fatigue carousel and ground-coupled GSSI at test bench setup at Cerema. Appendix. C presents the various performance indexes that are used throughout the manuscript to indicate the performance of the machine learning methods. Appendix. D explains the automatic time gating used to isolate the second echo of the GPR A-scan in order to obtain the local signal features used in Chapter. 4 to Chapter. 6. The final appendix (Appendix. E) provides additional illustrative results for experimental data from Chapter. 6.

1.3 Conclusions

In this chapter, we presented the problem statement that led us to the objectives to pursue this research. The overview of the manuscript was also presented here.

The next chapter discusses the state of the art presented the various research, both ongoing, and completed in the field of NDT&E and their advantages and limitations.

Chapter 2

Debonding Survey in Pavement Structures

Contents

Over the past few decades, several technologies have been developed to survey the surface and subsurface conditions of the pavement. Additionally, these techniques have been improved in sensitivity and performance. In this chapter, we present the existing Non-destructive testing techniques for pavement survey with a large focus on the subsurface radar techniques, namely, GPR-based techniques.

Within this scope, the conventional method, Amplitude Ratio Test (ART) is introduced. This method will serve as a reference method to detect debonding within B-scan radar data. It will additionally be used in the subsequent chapters as a performance benchmark for other data processing methods.

2.1 Existing methods for structural pavement survey

Roadways are one of the most widely spread network of transportation across the world. As of 2014, in France alone, roadways stretched over a million kilometers. Most of these roads are made up of multi-layered bituminous concrete and were laid over three decades ago.

The condition of the pavement structures depend on the proper mixture, bituminous content and its characteristics (such as aggregate size, compaction *etc.*), the construction method used, traffic and weather conditions en suite [20]. Additionally, the bonding strength between pavement layers depends on various factors, including emulsion quality and quantity of tack, grading mixture of each layer *etc.* [21, 22, 23]. The occurrence of fatigue cracking in pavements has been observed due to repeated loading [24] and has been recognized as an important reoccurring issue in pavement structures [25]. In fact, [23] provides a study on the effect of pavement interlayer bonding quality of asphalt layers on the performance of these pavement structures.

Over time, traffic and environmental factors such as water seepage, seismic activities, seasonal temperature variations may lead to sub-surface cracks at the interface between two stratified layers. These horizontal cracks are called *debondings*. Figure 2.1 presents an example of one such debonding occurring between the first two layers. Since these precarious defects occur sub-superficially, they tend to go unnoticed for some time. However, the defects may continue to grow underneath until being visible on the pavement surface condition, *e.g.*, reflexive cracks, and causing further severe degradations. Thus, it is of great importance for early detection of these defects.

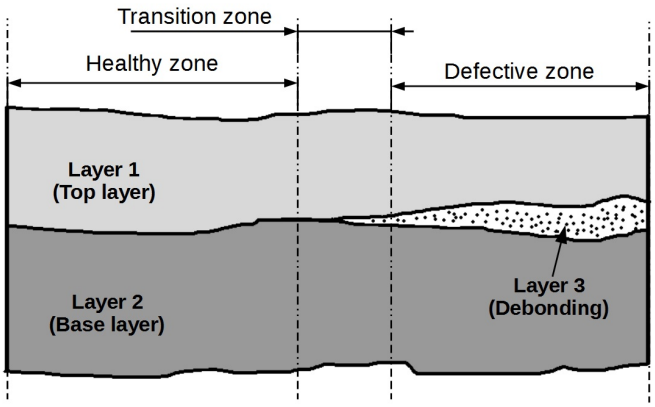

Figure 2.1: *Representation of debonding occurring in a pavement structure*

Over the past decades, different methods have been proposed to monitor the pavement structures. They can be broadly categorized into Destructive Testing (DT) and Non-destructive Testing (NDT) [7]. In DT, a small section of the structure is extracted and analyzed for anomalies. Although DT provides accurate information about the structure, it has several disadvantages. To overcome the drawbacks in destructive testing, NDT has been widely adopted to monitor structures. NDT is the process of testing and monitoring the properties of a material without damaging the material under test (MUT) in any way.

Due to its non-damaging ability, NDT is used in numerous applications including (but not restricted to) monitoring in monument degradation [26, 27], structural integrity tests [28], mechanical equipment testing [29] and pavement monitoring [7, 30, 31].

2.2 Common methods of Structural health evaluation

Structural health evaluation (SHE), sometimes also referred to as Structural health monitoring (SHM) is process of implementing a damage detection and characterization strategy for civil engineering structures [32]. SHE aims to enhance the performance of an existing structure by:

- integrating sensors (such as Piezo-ceramic transducers [33] or embedded wireless sensors [32, 34, 35]), smart materials, data transmission and processing inside the structure
- monitoring the structures affected by external and internal factors
- development of statistical models to estimate the longevity of the structure

Evaluation and Monitoring of a pavement structure can be broadly categorized as Destructive Testing and Evaluation (DTE or simply DT) and, Non-Destructive Testing and Evaluation (NDT&E or simply NDT).

2.2.1 Destructive Testing

Destructive testing (DT) methods are defined as the methods used to evaluate the condition of a material, normally, by extracting a small sample of the overall material under test (MUT) [4]. The MUT is procured through a process wherein the characteristics of the material under survey is mostly altered in some way (physical or chemical alterations). Although DTs

DTs have also been used for pavement survey in some cases. These pavement tests can be performed at regular distance intervals. Three well-known DT methods in pavement survey are briefly presented hereafter.

Pavement Coring (PC)

Pavement coring (or simply known as Coring) is a well-known approach of pavement testing by means of DT. In coring, a cylindrical drill is used to excavate a portion of the pavement structure for further analysis, as shown in Figure 2.2. The objective of coring is to collect information at *in-situ* conditions [36]. Coring provides vital information about the structure that is unavailable from other tests such as log measurements or productivity tests [36]. With the help of pavement coring, it is possible to determine:

1. Pavement thickness and various layer thicknesses [37]
2. Bonding/debonding between pavement layers [38, 39] and,

3. Granular material characterization (such as soil, rubble *etc.*) under the pavement structure

Figure 2.2: *Coring equipment in [1]: the core cylinder is up to* 200 mm *in diameter and the complete setup can weigh up to* 110 kg.

Dynamic cone penetration test (DCPT)

The Dynamic Cone Penetration Test (DCPT) on the other hand is a light-weight, cheaper, considerably faster approach to pavement survey compared to the former method [2, 40]. It was originally developed as an alternative to evaluate the properties of pavements [41] and subgrade soil.

According to [2], DCPT is used to measure the fatigue on a part of the pavement by using an 8 kg 'hammer' and a *Scala penetrometer* (named after its inventor in 1956) [42]. The 'hammer' is dropped on the pavement from a specific height. The pavement is then pierced with the penetrometer to estimate the penetration depth and to analyze the structural pavement condition. Figure. 2.3 shows the DCP test setup for pavement fatigue evaluation used in [2].

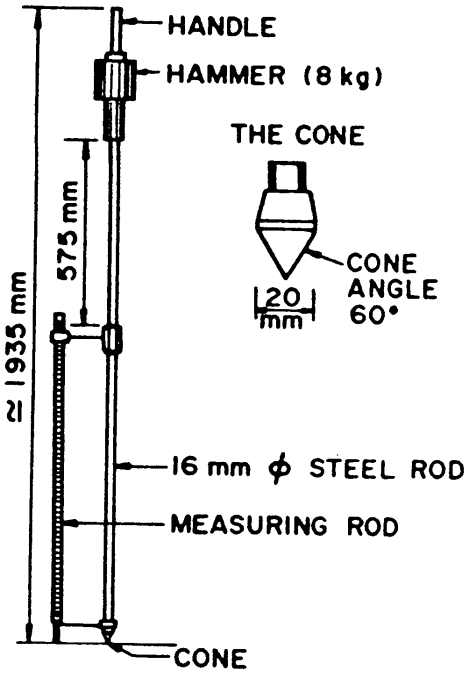

Figure 2.3: *DCPT setup for pavement fatigue evaluation [2]*

Falling Weight Deflectometer (FWD)

The Falling Weight Deflectometer (FWD) test is an impulsive load test is applied on the road surface [43]. The FWD is a device designed to 'simulateâ the effect of a vehicle of specific weight passing over a pavement and it is used to measure the vertical deflection of the pavement *w.r.t* the load [44]. It is used to estimate the elastic moduli of the pavement layers and the subgrades [45]. In the pavement testing community, the FWD test is now a standard approach to characterize these subsurface properties to estimate the remaining life of the pavement [44]. Figure.2.4 shows an FWD test mounted behind a vehicle.

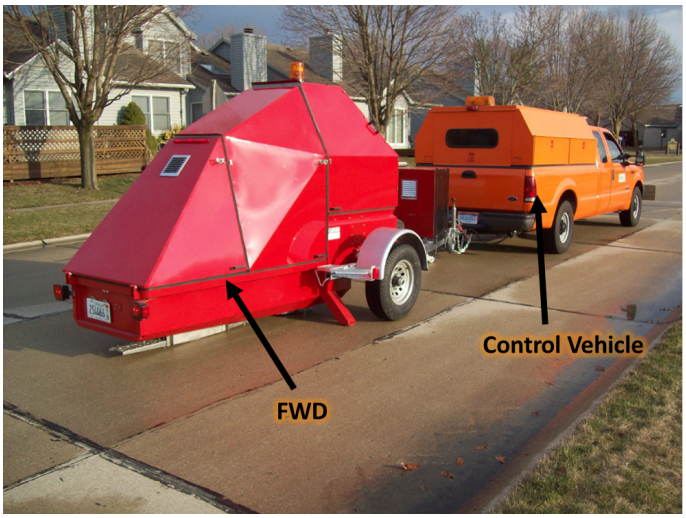

Figure 2.4: *An FWD double-mass (KUAB) setup mounted behind a control unit vehicle [3]*

Advantages and Drawbacks of Destructive testing

DTs have been in use for over sixty years and they have several advantages. Some of its key benefits are listed below:

1. Provides reliable and accurate information about the test material
2. Are extremely useful data for design purposes
3. Are useful to predict the durability of the material
4. Provide information of the test material that can be used to create a benchmark for further tests
5. Usually provide quantitative results

DTs provide sparse spatial information on the pavement structure through a limited data samples. To be reliable, it is assumed that the extracted test samples represent the "average" material in terms of condition and characteristics. However, in reality, it cannot be ascertained that this assumption will hold true. Thus, we now list some of its drawbacks:

1. Provides localized information *i.e.* specific to the examined zone at a particular instant of time
2. Most DT samples cannot be reused once the test is complete since it presents a single-state of the structure [46]
3. DTs sometimes require bulky and expensive equipment
4. Cannot be performed at all places (*e.g*, pavements cannot be cored that have sub-surface embedded sensors)

To overcome these drawbacks, Non-destructive testing is used. As mentioned in [47], NDT approaches are also recommended by enterprises as the best technique in the evaluation of pavement structural capacity.

2.2.2 Non-destructive Testing

The concept of Non-destructive testing (NDT), sometimes also referred to as Non-destructive Examination (NDE), Non-destructive Evaluation (NDE) or Non-destructive Inspection (NDI), can be defined as a type of test performed on a material without altering or changing its physical, chemical and geometrical characteristics in any way. These are the methods that use indirect means to do the structure health evaluation [4].

Within the scope of the thesis, NDTs are conducted to probe subsurface conditions within pavement structures, especially, disbonding. It can be also used to further characterizing the pavement structure in thickness and material composition.

NDT has seen significant innovations and growth over the past few years. Today, NDT is considered to be one of the fastest growing technologies from the standpoint of uniqueness and innovation. A number of NDT methods that are used to inspect the

materials has been growing since the past few decades. Researchers continue to find new ways of applying physics and other scientific disciplines to either improve existing NDT methods or to develop new ones.

Several NDT methods are already available depending on the application such as Visual Testing, Magnetic Particle Testing, Eddy Current Testing, Radiography, Ultrasonic Testing, Acoustic Testing, Electromagnetics etc.

Within our scope, the structural evaluation was conducted using the wave signal. There are primarily two classes of waves: mechanical and electromagnetic [4].

2.2.2.1 Mechanical wave

The mechanical wave is defined as the oscillation of matter that transfers energy through a medium [4, 48]. Ultrasonics is one such type of mechanical wave used in the field of NDT. Figure. 2.5 shows the sound wave spectrum used in ultrasonic NDT. The human ear is sensitive to sound frequencies averagely between 20 Hz to 20 kHz. Thus, as the name suggests, ultrasonics use sound frequencies above 20 kHz which has proved to be efficient in various NDT applications [49].

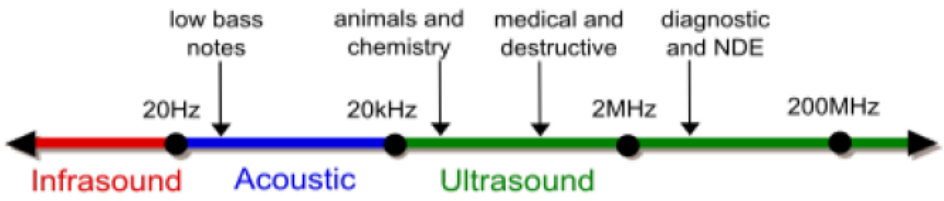

Figure 2.5: *Sound wave spectrum [4]*

Since its invention in 1943 [4], ultrasonics have been used in various applications such as: damage detection in asphalt [50, 51], defects in concrete [52], buried object detection [53, 54], welding cracks [55, 56] and several other NDT applications.

2.2.2.2 Electromagnetic (EM) wave

EM waves propagates in straight lines at the speed of light in vacuum. Electromagnetic wave consists in both electric and magnetic field components, which synchronously propagate perpendicular to each other and perpendicular to the direction of energy and wave propagation, namely, TEM wave propagation. According to [57], a large group of NDT community uses the EM for non-invasive tests including X-rays (used in radiographic testing), Ultraviolet rays (for dye penetrant inspection and liquid penetrant testing), infrared and thermal (for visual/optical testing). The EM frequency band used mainly depends on the application. However, in case of structural evaluation, the commonly chosen band is microwaves and radio waves [4, 57] which is also the band used by Ground Penetrating Radar.

For illustration, Figure. 2.6 shows the EM spectrum.

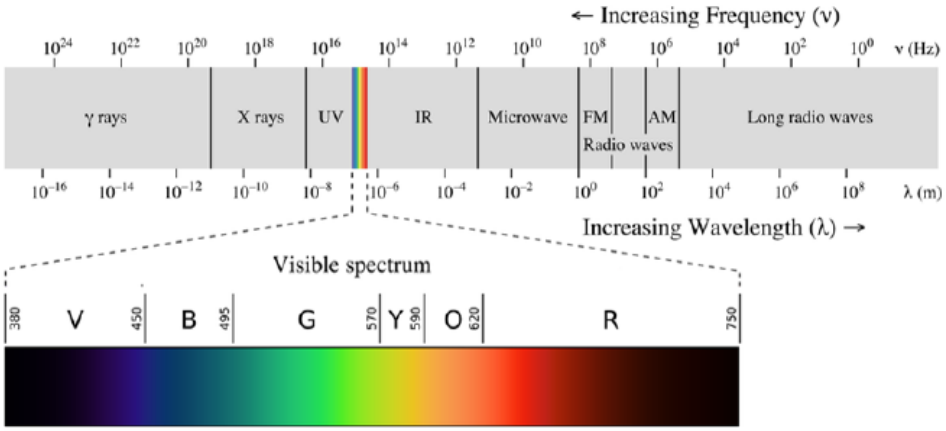

Figure 2.6: *Electromagnetic spectrum [4]*

Within the scope of the thesis, GPR is used as the means for non-destructive evaluation of pavement structures. GPR has been used in numerous NDT applications. The following sections and chapters discuss the concept of GPR in detail.

2.3 Radar-based NDT techniques

Radar (or Radio Detection and Ranging) is one of the application of the theory of electromagnetism. Radar systems use radio waves to probe any dielectric media and to determine the range of the objects which reflect radio waves back to the receiver. Eventually, the size of the object may be estimated as well as the wave velocity of the probed media.

Within the scope of the thesis, we focus on Ground Penetrating Radar (GPR), which is also known as Ground Probing Radar (GPR), Subsurface Radar or Geophysical Radar, is a non-destructive method that uses electromagnetic waves to probe the subsurface structure. GPR provides a cross-sectional profile of subsurface features without drilling, probing, or digging. As electromagnetic waves can propagation within dielectric materials, GPR is able to find target or interfaces embedded within the subsurface [58].

GPR stands out as one of the most popular electromagnetic NDT&E methods since the past few decades. It responds to both metallic and non-metallic objects. Besides, the GPR antennas are easy to be operated and can be moved rapidly above the ground.

Due to this diversity, in the field of civil engineering, GPR has been involved in the estimation of various sub-material characteristics such as its dielectric properties, determination of layer thicknesses and identification of subsurface objects etc. As [4] reiterates, these indicators are important observables linked to the structure evaluation, namely monitoring.

Additionally, the applications of GPR evolved as electronic systems gradually improved in frequency center and frequency bandwidth. While it was initially devoted to probe soils and large targets for geophysical applications, shorter wavelengths allowed to extend GPR applications to depth-limited civil engineering structures, such as concrete and pavement

structures.

Within the scope of this thesis, to probe the layered pavement structures for thin interlayer debonding detection, the microwave spectrum from the range of roughly around 1 GHz to 10 GHz was used.

2.3.1 GPR System

A generic GPR system has three main components: a transmitter- receiver (Tx-Rx) and a control unit [58]. When a GPR pulse is emitted a reflected signal is received at each encounter of dielectric contrast. The velocity (v_m) of the pulse within a material is inversely proportional to the square root of the material permittivity and is given by [59, 60]:

$$v_m = \frac{c_0}{\sqrt{\epsilon_r}} \tag{2.1}$$

where,

- c_0 is the velocity of the EM wave in vaccum
- ϵ_r is the dielectric constant of the layer

Let us consider the case of a layered pavement structure. When the EM wave enters the ground, it travels through the material at a velocity expressed in Equation.2.1. The wave then spreads out and travels downward until it encounters a layer whose properties differ from its preceding material. At each such encounter, a part of the signal is reflected back and the remainder enters the succeeding layer (subject to Fresnel equations; see Appendix.A.2). This process continues until a certain depth where the signal completely fades out (the penetration depth being a factor of the frequency of operation and pavement material properties as mentioned before).

Finally, the received signal by the GPR system consists of:

1. Coupling induced by transmitting and receiving antennas (also called direct coupling)
2. Reflection from the ground surface (first echo)
3. Interference either from GPR system itself or from environment (clutter, discussed later)
4. Reflection by subsurface targets and/or pavement interface
5. Reflection by the underground inhomogeneity (roughness etc.).

2.3.2 GPR Data Acquisition

To probe the subsurface structure, the GPR antennas can be pulled over the ground along a scanning direction. The configuration of the Transmitter (Tx) and Receiver (Rx) antennas will determine the capability to perform different kinds of data collection with

the radar [61]. Three primary antenna configurations are available for GPR namely, mono-static, quasi-mono static and bi-static configurations.

Mono-static radar is the term given to the radar antenna configuration in which the Tx and Rx are collocated, namely, zero-offset configuration. However, radar instruments that have both transmitting and receiving antenna housed within the same box are normally considered to be coincident and mono-static because they cannot be separated.

On the contrary, a bi-static radar is a configuration where the Tx and Rx are physically separated so that the reflected echo does not take the same path as the transmitted signal [62].

A bi-static radar is one in which the receiver is physically separated from the transmitter so that the echo signal does not travel over the same path as the transmitted signal. A setup of bi-static antennas can be set on a frame that allows the operator to control the unit to move over the surface to acquire data (refer Figure. 2.7).

Figure 2.7: *Data collection at the fatigue carousel at IFSTTAR using a pair of robot-controlled bistatic antennas*

Finally, the quasi-mono static is a configuration where the Tx and Rx antennas have a small offset to each other. Thus, such an antenna configuration can be assumed to act in mono-static at far-field condition and as bi-static in case of near-field conditions.

To summarize, Figure. 2.8 illustrates the three configurations.

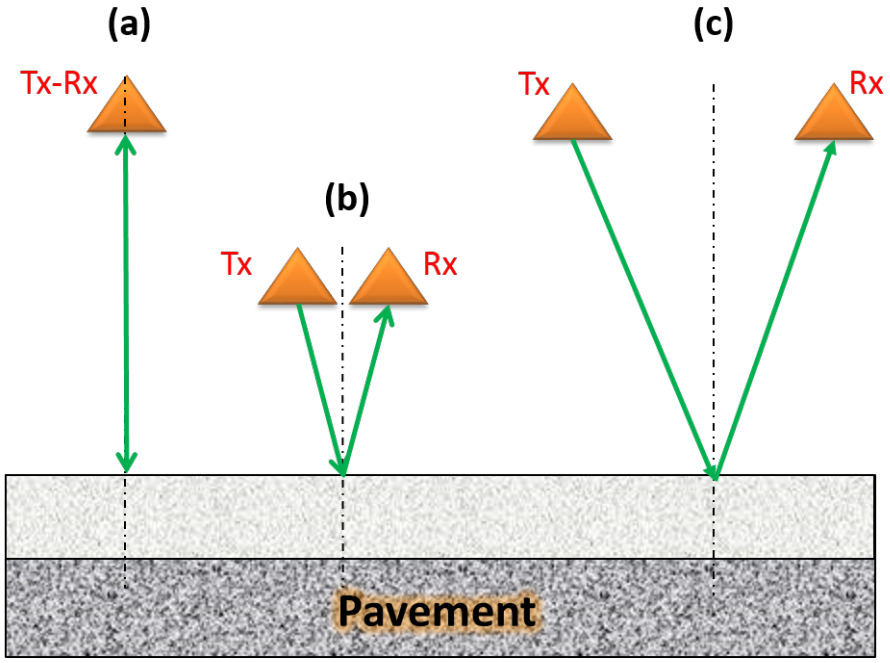

Figure 2.8: *An illustration of the three antenna configurations: (a) Mono-static (b)Quasi-mono static and (c) Bi-static*

Within the scope of the thesis, two radar antenna configurations (bi-static and quasi-mono static) were used. In case of quasi-mono static, the commercial GPR was used in the acquisition of data over various experimental sites, namely GSSI SIR-3000 (see Appendix. B.1 for details). On the other hand, an experimental stepped-frequency radar (SFR) in bi-static configuration developed at IFSTTAR is also used to collect the pavement data over similar experimental sites (see Appendix. B.2 for details). The GSSI SIR-3000 was a ground-coupled GPR whereas the experimental SFR was configured to collect data in air-coupled configuration. In the following sections under data collection modes, we briefly present the two radar configurations, namely, ground-coupled and air-coupled.

2.3.2.1 Data collection modes

Figure. 2.9 [5] illustrates the air and ground-coupled GPR modes for data collection.

Ground-coupled radar (GC-GPR)

Ground-coupled systems operate at near-field with either the antennas directly in contact with the pavement or the antennas are a few centimeters above the surface. This configuration provides better energy coupling than air-coupled antennas, resulting in a better penetration depth of waves. As a counterpart, the shape of the received signal is more complex to model and the data interpretation may be more qualitative rather than quantitative.

The ground-coupled technology has been widely used for a variety of geophysical applications, including mapping and detection of ground water [63, 64], bedrock [65, 66], and soil layers, detecting pipes [67], buried containers [68] and several other applications.

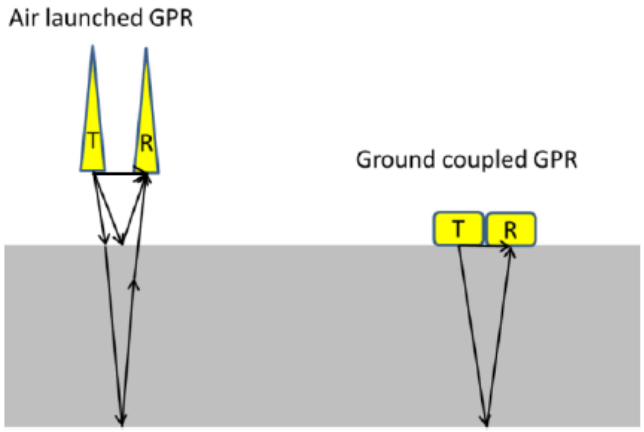

Figure 2.9: *Illustration of air-launched and ground-coupled GPR systems [5]*

For these radar systems, the energy transfer can be further improved by some top-shielding (on both Tx and Rx antennas) to reduce the back lobes of antennas. These antennas are available with center frequencies ranging from 80 MHz to over 3.0 GHz providing a wide range of penetration depths and resolutions. [69]. (see Figure 2.10).

Figure 2.10: *Example of ground coupled GPR [6]*

Air-coupled radar (AC-GPR)

Most of GPR layer thickness studies have been carried out with air-coupled antenna, since these can be implemented at traffic speed without lane closures. The antennas are usually located in far-field above ground, *i.e.* the height of antenna above the ground is beyond the Fraunhoffer limit, defined as $(2 * D^2)/\lambda$, where D is the lateral dimension of the antenna and λ is the free space dominant wavelength [70], as shown in Figure 2.11.

Figure 2.11: *Example of a commercial Air-coupled GPR [6]*

Despite their applications, some GPR experts consider ground-coupled GPR to be more effective since, by raising the antennas off the surface degrades the lateral spatial resolution of the measured data [5, 71]. However, on the other hand some experts counter-argue that air-coupled GPRs are faster and can be easily deployed on vehicles moving at highway speeds [5, 72]. Nevertheless, the two configurations present their own advantages and thus, in this thesis, we study both configurations for our application.

2.3.3 GPR Performance Specifications

GPR data are site-specific and vary depending on various factors such as the measurement surface and subsurface conditions. The performance specifications that govern the data acquired over a zone include the requirements for information about reflected signals (from interfaces, objects *etc.*), depth of penetration, and resolution (which relies on the material characteristics and frequency of operation of the GPR) [60, 73].

2.3.3.1 Reflections

Reflection in an electromagnetic wave occurs when a change in the electrical and magnetic properties of the traveling medium is encountered. However in most situations, magnetic effects are negligible.

In case of layered pavement structures, the GPR reflections are observed due to dielectric contrast (small or large) between layers. Per Fresnel equations (presented in Appendix. A.2), the greater the change in properties, the more is the amplitude of the echo. Additionally, the amplitude also depends on other material characteristics such as the interface roughness, dispersion and scattering angle.

A decay in frequency of the interface echo is observed due to dispersion and material roughness. These frequency variations of the radar magnitude introduce some distortions in the shape and form on the reflected signals [74]. However, as mentioned in [75], the dispersion can be usually neglected for pavement materials. On the other hand, the influence

of surface and interface roughness on the reflected signal is studied in Appendix. B.

2.3.3.2 Penetration depth

The penetration depth of GPR waves reduces with increasing electrical conductivity of the ground, higher transmitting frequency, and decreasing transmitting power.

In practice, GPR system designer must make a trade-off between vertical time resolution and penetration depth. A lower frequency (and limited bandwidth) provides greater penetration depth but lower resolution, while a higher frequency antenna (and large frequency bandwidth) provides less depth penetration but has better time resolution [76]. The latter solution is better matched to probe the layered pavement structure.

2.3.3.3 Vertical Resolution (or Time Resolution)

The definition of resolution, as described in [77, 78] is the capability of the GPR to discriminate individual scatterers in the subsurface. Without any further processing, the time resolution $\Delta\tau$ is limited by the bandwidth Bw of the radar system, *i.e.* $\Delta\tau \approx 1/Bw$ at the most [69]. It corresponds to the minimum time shift for which two successive echoes can be separated in time. The vertical resolution of GPR, Δz, is with respect to the material permittivity, $\Delta z = c_o \Delta\tau / 2\sqrt{\epsilon_r}$.

Various frequency antennas (*i.e*, from 25 MHz to 2.0 GHz or more) can be selected so that the resulting data can be optimized to the application requirements. In practice, radar geophysical survey requires to reach a trade-off between penetration depth and time resolution as pointed in the previous section [79, 80, 81, 58].

Within the scope of this thesis, the probing of layered pavement structures requires a vertical resolution of a few millimeters. This implies to use ultra wide band GPR systems, and as a result, higher dominant frequency. Better time resolution also provides a larger dynamic range of the isolated echoes [82].

2.3.4 Clutter

The definition of clutter is quite versatile according to the radar configuration and the application under consideration. In practice however, clutter is generally considered to be any signal other than the useful one.

Within the scope of the application, useful echoes are the backscattered signals from the sub-surface targets one is looking for. Clutter is the direct coupling of the Tx-Rx signal between the antennas for air-launched radars. In case of ground-coupled configuration, the clutter is the combination of direct coupling between Tx and Rx overlapping with reflected wave from the surface [83].

Compared to the useful echoes, clutter usually shows different shape and lower dominant frequency. Besides, clutter and useful echoes usually overlap to each other on the radar display. As a result, the resolution of images is degraded. Clutter reduction technique have been developed in the literature, e.g., [83, 84, 85].

The ability of any radar system to cancel clutter depends on the purity (stability) of the transmitted waveform. [86]. The clutter may sometimes vary with dielectric characteristics and/or surface roughness subsequently leading to uncertainty in the measurements [83, 87].

As mentioned previously, in this thesis both air-launched and ground-coupled GPRs have been used. Since the zone-of-interest for processing is limited to the top two pavement layers, certain clutter removal methods are implemented for the two configurations.

In case of ground-coupled radar, the clutter reduction technique implemented is simply based on an automatic time gating window (presented in Appendix. D) to process local data concentrated at the interface of interest where the debonding may occur.

In case of air-coupled GPR, since the direct Tx-Rx coupling is well-separated from the surface reflection, similar automatic windowing is used to eliminate the clutter and the reflections from the subsequent pavement interfaces which do not require our interest.

2.4 GPR Data formats

The GPR data has three common representation formats namely: A-scan, B-scan and C-scan. They are respectively one (temporal; X-axis), two (spatio-temporal; X-Y plane) and three (spatio-temporal planar; X-Y-Z region) dimensional representations of the GPR data. Figure. 2.12 from [7] provides a visual representation of the GPR signal in 1,2 and 3 dimensions.

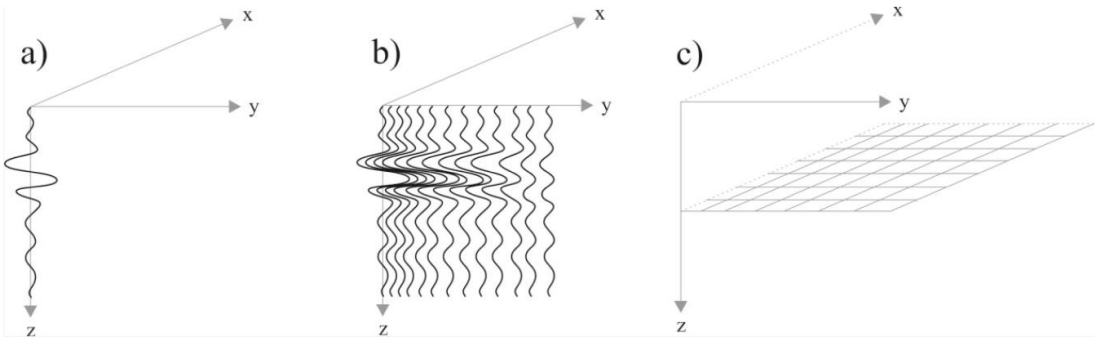

Figure 2.12: *Visualization of GPR signal as (a) A-scan, (b) B-scan, and (c) C-scan [7]*

The first form of GPR data representation is the one dimensional A-scan. It is the representation (or vertical profile) display of the backscattered received signal as a function of time. Reflector depth can be determined by the position of the echoes, *i.e*, the extrema in signal amplitude, on the horizontal sweep. Figure. 2.13 illustrates an example of a one-dimensional A-scan signal.

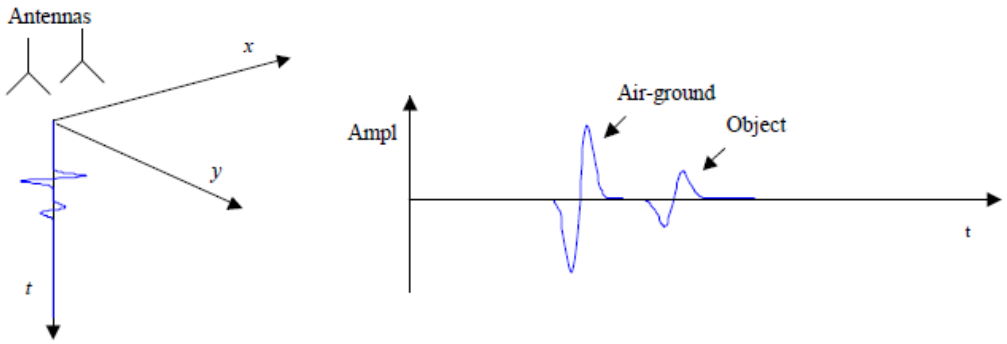

Figure 2.13: *Configuration and representation of an A-scan (or 1D signal) [8]*

A collection of 1D A-scans along the scanning direction (*i.e*, Y-axis) is used to obtain a two-dimensional image representation called B-scan. To display this data matrix, the travel time is displayed along the vertical axis, and the scanning direction is displayed along the horizontal axis. Figure. 2.14 illustrates an example of a B-scan image.

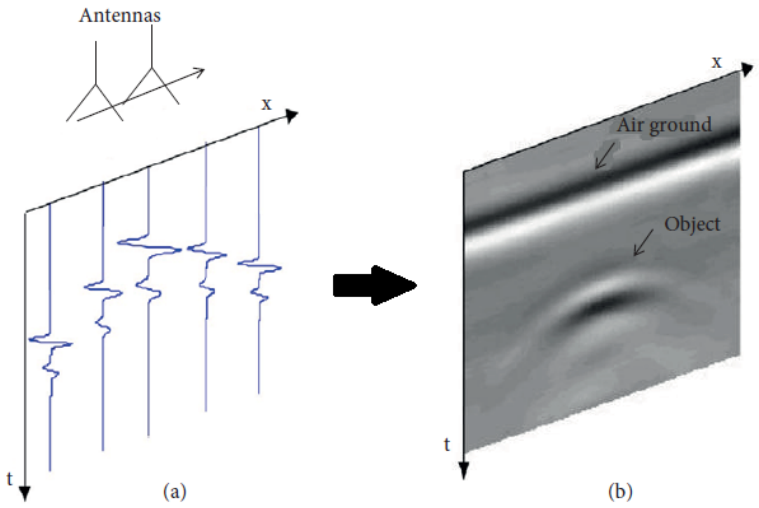

Figure 2.14: *B-scan (or 2D representation) of a GPR image [8, 9]*

The third type of representation of GPR data is the C-scan (i.e, 3-dimensional data representation). C-scan illustrates the amplitude variation of the radar signal over the X-Y probed surface *w.r.t* the round-trip time (*i.e*, B-scans). An ensemble of several parallel B-scans along the plane (*i.e*, Z-axis) is used to obtain the C-scan. These 3D images an be useful for interpreting specific targets. Figure. 2.15 illustrates an example of a C-scan image.

Both B and C-scans are generally represented using gray-scale levels or different colors indicating the signal amplitude or intensity. Specific image features characterize the subsurface situation. *For e.g*, perfect horizontal features may represent clutter, stratified image structure may represent subsurface layered structures, hyperbolas represent point-like targets or edges of stratified layers.

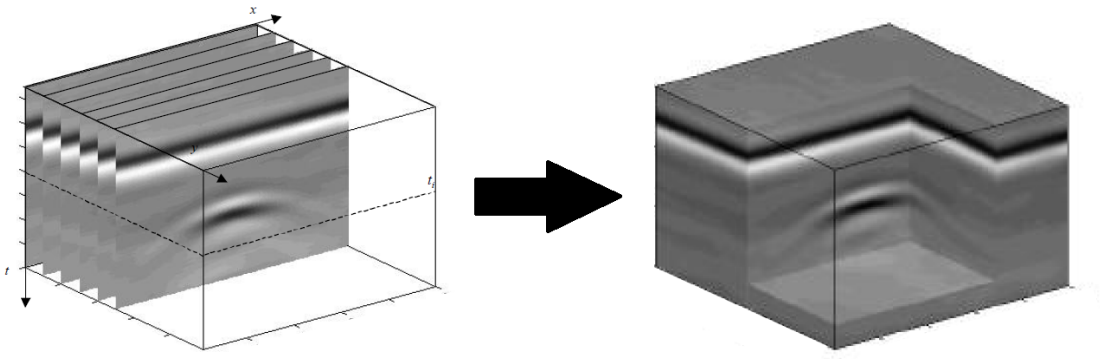

Figure 2.15: *C-scan (or 3D representation) as a collection of several B-scan images [8, 9]*

Within the scope of this thesis, the detection of debondings will be carried out for individual A-scans; however, the results will be presented for a section of the pavement (*i.e.* B-scan) as a whole; see Chapter. 3.1.3 for detailed description.

2.5 Data processing techniques for debonding survey

The data processing for debonding survey aims at detecting the defected pavement areas by selecting the proper A-scan vectors, and then if possible, at characterizing the interlayer debonding in terms of both permittivity and thickness by estimation techniques.

This section reviews some potential data processing techniques which may be used to both purposes. They are herein categorized broadly into: Data driven and Model-based processing techniques. The data processing method to be developed for debonding detection is then integrated within a more general framework including a two-step processing strategy.

2.5.1 Data-driven methods

Data-driven methods are a broad family of processing techniques which is based entirely on experimental data without the support of any physical model that may represent accurately the data variations. Additionally, such methods do not require the knowledge about the data; instead they recognize the patterns of each class by themselves [88].

The methods presented in Chapter. 3, namely, supervised Machine Learning methods, belong to this family. Such methods have been already used by the GPR community for detecting various subsurface objects, *e.g.*, voids [89, 90], landmine [91, 92, 93, 94] and other buried objects [95], subsurface defects [96, 97], underground utilities [98]. They are mostly applied for classification purposes, either as binary and/or multi-class classification.

Following the work in [99], among the machine learning family techniques, Support Vector Regression (SVR) method may show the potential to fill both purposes. But, SVR is likely encounter some limited performance over thin debonding, smaller than $\lambda_{mat}/4$.

Thus, it is believed that data-driven methods can be only used for detection purpose (binary classification) within the scope of the thesis. Besides, per our knowledge, the

machine learning methods (especially supervised), have not yet been used in the literature to detect horizontal interface debondings.

2.5.2 Model-based or Model-driven methods

By contrast to the previous subsection, model-driven methods rely on a physical model to process data. As detailed in the next section, the conventional GPR method, namely Amplitude Ratio Test (ART) relies on the thin-bed analytical data model (see Appendix. A.2). ART has been used for binary classification of A-scan data within the GPR community [100, 18]. However, no attempt has been made to interpret ART values in terms of thickness (on the condition that the layer permitivities are known).

Time Delay Estimation (TDE) techniques are data processing techniques that may potentially fulfill both purposes, namely, detection and characterization of debonding. It has been initially developed for GPR pavement survey to control the thickness pavement layers.

However, TDE tends be more difficult and challenging is GPR pavement applications when: the backscattered echoes from the thin debonding interface are too close to each other (*i.e*, overlapping echoes) or, they are highly correlated (which is usually the case for GPR data) [101].

To overcome this issue, super-resolution TDE techniques have been introduced to measure thin and ultra thin pavement layers [102], *i.e*, TAS and UTAS (*i.e*, Thin and Ultra-thin Asphalt Surface), respectively. At medium to high levels of SNR, they can achieve about 10 (resp. 20) times better time resolution than the conventional FFT-based TDE techniques. In other words, they can distinguish between overlapping echoes, which the differential time shift $\Delta\tau$ is up to $(10 \times \mathrm{Bw})^{-1}$ (resp. $(20 \times \mathrm{Bw})^{-1}$). The latter time resolution capability matches to the detection of debonding larger than a few millimeter in thickness for the UWB step-frequency radar [103]. This may be not sufficient enough within the scope of the thesis for thin debonding within the range $[0, \lambda_{mat}/4]$. Besides, super-resolution TDE techniques rely on a single scattering signal model (see Appendix. A.2) which is not always true in practice.

Therefore, model-based TDE techniques are likely not expected to manage the debonding survey problem on its own.

2.5.3 Proposed two-step strategy for debonding survey

Following the previous subsections, we can conclude that no unique data processing technique exists that can fulfill the two described purposes of debonding survey. The characterization step requires some physical model while the detection step may not.

Therefore, the data processing method to be developed for debonding survey is integrated within a more general framework including a two-step strategy to process radar B-scan images. At first, some data-driven processing techniques will be used to select the A-scan data vectors which debondings within the B-scan data. Then, as a second step, super TDE techniques may be performed on the selected A-scans to further characterize the defects in thickness and permittivity.

The thesis will focus on the detection step, namely, the detection, and the results may be used later within the ongoing ANR research project, called ACIMP (https://anr.fr/Projet-ANR-18-CE22-0020).

2.6 Reference data processing method for debonding detection: Amplitude Ratio Test

ART is a conventional NDT method to detect subsurface delamination from GPR data [100, 18]. The ART method is usually carried out at the operational level for two kinds of qualitative diagnosis: the debonding detection within pavement structures and the control of sealing screed over bridge decks. ART allows selecting the areas where some coring is performed to verify the NDT diagnosis.

In this section, we present the basis of the ART method for debonding detection within a more rigorous framework. This method relies on a simple data modeling of A-scan data, which is detailed in Appendix. A.2. For detection purpose, the decision threshold is determined using the conventional likelihood ratio test on the basis of each A-scan data vector.

2.6.1 ART Principle

Any delamination/debonding can be seen as a thin-bed structure []. In case of thin beds, two reflections from respectively the upper and lower interface are recieved [104, 105, 106, 107]. Similarly, in case of a debonding occurring within the top two pavement layers, (as illustrated in Figure 2.16 and Figure. 2.17), two echoes are received: the first echo ($A_s(t)$) is the surface echo, and the second one ($A_{T/H_{0,1}}(t)$) is the echo from the interface between the top two layers to be monitored by NDT techniques. Healthy and debonding structures are referred as H_0 and H_1 assumptions, respectively. The t is simply to indicate that the signals are in time domain.

According to the data modeling in Appendix. A.2, $A_{T/H_0}(t)$ is conventionally assumed to be a shifted and attenuated copy of the top echo $A_s(t)$. Whereas in case of debonding, $A_{T/H_1}(t)$ is a *composite signal* made of the overlapping of two echoes from the upper and the lower interfaces of the debonding along with multiple echoes occurring within the debonding region (as shown in Figure. 2.16). As detailed in Appendix A1, the latter echoes interact constructively with each other, assuming limited thickness of the debonding interface and providing $\varepsilon_{r,deb} > \varepsilon_{r,1,2}$. The resulting composite echo usually shows a larger signal strength compared to the echo over the non-debonding interface.

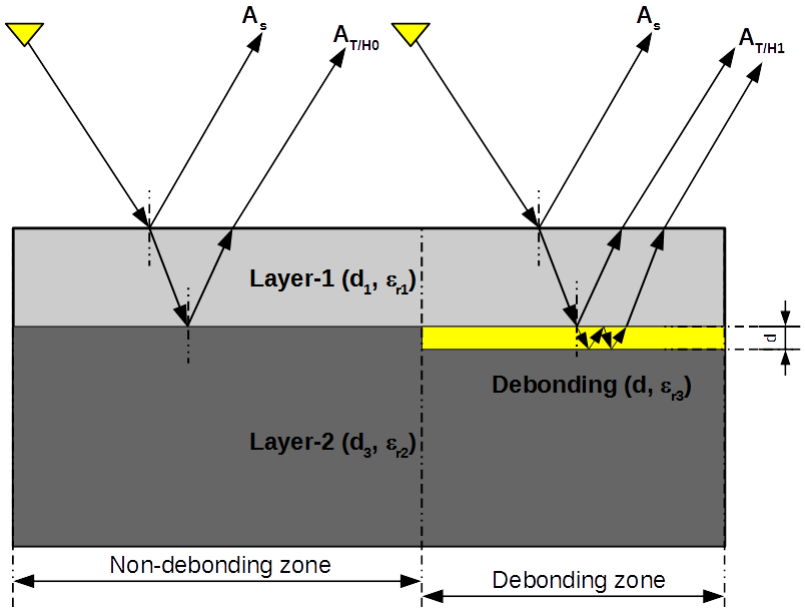

Figure 2.16: *Synthetic pavement structure showing the signals received from the healthy (left) and defective zones (right). On the left, A_s is the surface echo and A_{T/H_0} is the second echo for non-debonding zone. In case of debonding (right), A_{T/H_1} is the composite signal with multiple scattering accounted for*

2.6.2 ART Computation

ART is defined as the ratio between the signal strength of the two latter echoes, namely, $A_S(t)$ and $A_{T/H_{0,1}}(t)$. In the following, the signal strengths are labeled A_S and $A_{T/H_{0,1}}$, respectively. They can be computed from the local extreme values of either the signal magnitude (MAG) or the Maximum Absolute Amplitude Deviation ($MAAD$), where $MAAD$ value of the surface ($A_S(t)$) and second $A_{T/H_{0,1}}$ echoes are written as follows:

$$MAAD(A_S) = |max(A_S(t)) - min(A_S(t))| \tag{2.2}$$

$$MAAD(A_{T/H_{0,1}}) = |max(A_{T/H_{0,1}}(t)) - min(A_{T/H_{0,1}}(t))| \tag{2.3}$$

where $|...|$ represents the absolute value.
Similarly, we express the MAG for the two echoes as:

$$MAG(A_S) = max(|\mathcal{H}(A_S(t))|) \tag{2.4}$$

$$MAG(A_{T/H_{0,1}}) = max(|\mathcal{H}(A_{T/H_{0,1}}(t))|) \tag{2.5}$$

where $\mathcal{H}(s(t)))$ represents the analytical signal of the amplitude signal $s(t)$, which is computed by Hilbert transform.
For representation, $MAAD(A_S)$ and $MAAD(A_{T/H_{0,1}})$ are shown in Figure. 2.17(a) and $MAG(A_S)$ and $MAG(A_{T/H_{0,1}})$ are shown in Figure. 2.17(b) for the debonding and non-debonding A-scans. In practice, an automatic time gating window is used to isolate both echoes and to compute the MAG and $MAAD$ values as detailed in Appendix. D.

The ART values are usually computed for each A-scan data vector from the $MAAD/MAG$

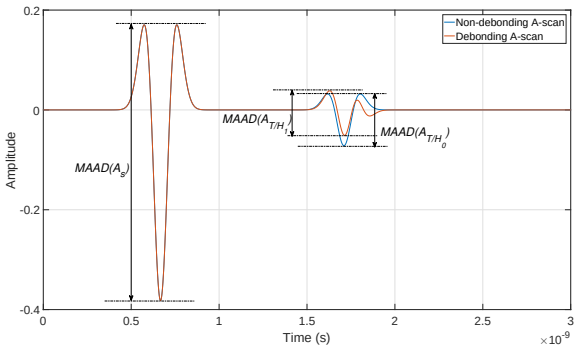

(a) $MAAD$ trace

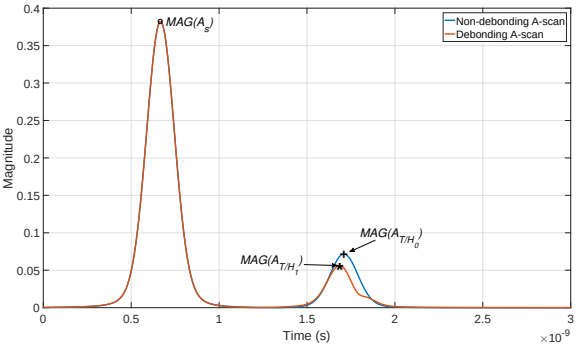

(b) MAG trace

Figure 2.17: *Simulated backscattered (noiseless) signal over healthy and debonding interface (top layer:* $\varepsilon_{r1} = 5$, $t_1 = 7\,\mathrm{cm}$, *base layer: :* $\varepsilon_{r2} = 7$, $t_2 = \inf$*; debonding layer: :* $\varepsilon_{r,deb} = 6$, $t_{deb} = 0.2\,\mathrm{cm}$*); the maximum absolute amplitude difference (MAAD) and magnitude (MAG) for each echo, namely,* $A_S, A_T/H_0$ *and* A_T/H_1*, are shown for comparison of amplitudes* A_S*;* A_T/H_0 *(non-debonding case) and* A_T/H_1 *(debonding case)*

values of both echoes, as follows:

$$ART = \frac{A_{T/H_{0,1}}}{A_S} \tag{2.6}$$

$$\tag{2.7}$$

Finally, for classification purposes, the following normalized ratio ART_{norm} is introduced:

$$ART_{norm} = \frac{ART_{test}}{ART_{ref}} \tag{2.8}$$

where ART_{test} is the ART value over the pavement area to test (under either H_0 or H_1 hypothesis) and ART_{ref} is the one for a reference data set over the healthy pavement zone (*i.e.* Non-debonding A-scan or H_0 hypothesis).

Following the ART principle in Chapter. 2.6.1, for noiseless condition and limited debonding thickness ($< \lambda_{mat}/4$), we can express ART_{norm} as:

$$ART_{norm} \begin{cases} = 1 \text{ for Healthy case } (H_0) \\ > 1 \text{ for Debonding case } (H_1) \text{ if } \varepsilon_{r,deb} > \varepsilon_{r,1,2} \\ < 1 \text{ for Debonding case } (H_1) \text{ if } \varepsilon_{r1} < \varepsilon_{r,deb} < \varepsilon_{r2} \end{cases} \tag{2.9}$$

Then, the debonding detection relies on the decision threshold η_{ART}, which is established by the likelihood ratio test (presented later in the next section).

The magnitude of echoes (MAG) can be theoretically expressed *w.r.t* the dielectric contrast between layers through the Fresnel coefficients as discussed in Appendix. A.2. The latter correspondence is more difficult to establish with $MAAD$ values. However, it can be shown that both definitions of ART_{norm} take larger values when the debonding material shows a larger dielectric contrast compared to the surrounding pavement material layers.

In [100], ART_{ref} is theoretically computed using MAG values from the prior knowledge of the permittivity attached to the two first underlying layers. By contrast, it is experimentally established in [15, 108]. In [10], $MAAD$ values were selected to compute ART because they provided a slightly larger contrast in ART_{norm} values (by a few dB) compared to MAG values, as shown on Figure. 2.18.

2.6.3 Decision threshold

The decision threshold relies on the statistical distribution (*i.e*, PDF) of ART values over both healthy and defective areas. PDFs are established from the collection of ART values, which are computed for each A-scan vector along the scanning direction. Figure. 2.19 presents an example of the PDFs for simulated analytic data in Appendix. A.2. As seen in Figure 2.19(a), due to destructive interference, the PDF for debonding case is lower than that of non-debonding. Figure. 2.20 presents the ART_{norm} for experimental data. As seen, we can say that in practice, destructive interference (as seen in Figure 2.19(a))

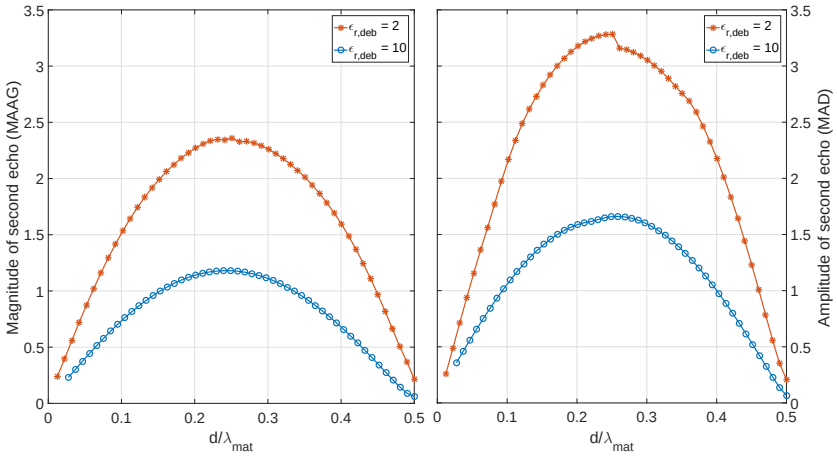

Figure 2.18: *MAG (left) and MAAD (right) as functions of debonding layer thickness for* $\varepsilon_{r,deb} = 2, 10$ *using noiseless simulated analytic Fresnel data; parameters for layers 1 and 2 are as specified in Table. A.1*

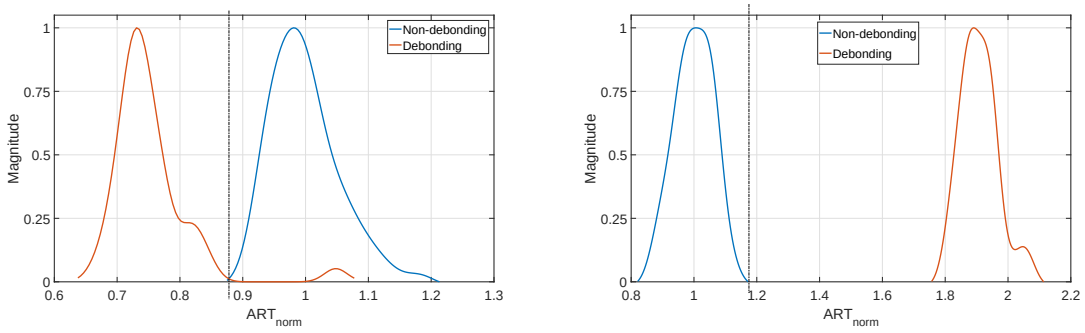

(a) $\varepsilon_{r,deb} = 6$ (b) $\varepsilon_{r,deb} = 2$

Figure 2.19: *PDF for* ART_{norm} *over defective and healthy areas computed from noisy simulated analytic data with* $SNR = 30\,\text{dB}$ *(Appendix. A.2),* $\varepsilon_{r1} = 5$, $\varepsilon_{r2} = 7$ *and* $t_{deb} = 0.3\,\text{cm}$. *The dashed vertical line depicts the decision threshold for debonding detection*

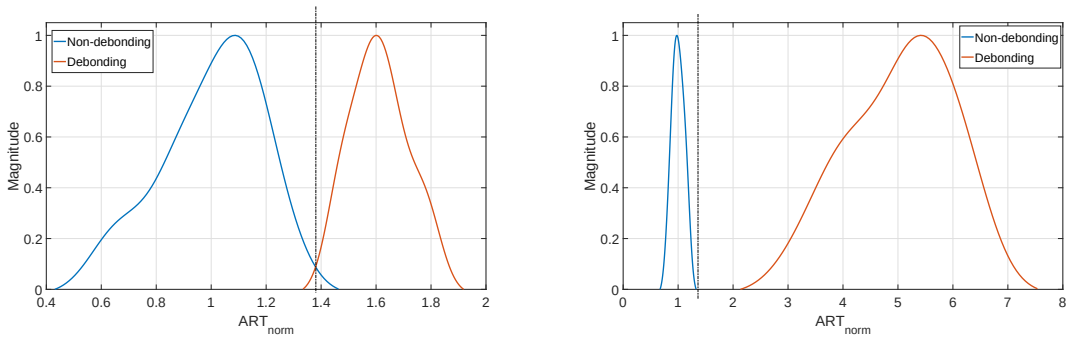

(a) Tack-free defects (weak contrast) (b) Sand based defects (strong contrast)

Figure 2.20: *PDF for* ART_{norm} *over defective and healthy areas computed from experimental data (see Appendix B). The dashed vertical line depicts the decision threshold for debonding detection*

is not observed.

Following Equation. 2.9, for noisy GPR A-scan data, ART_{norm} values are expected to be normally distributed around a mean value, which is different for healthy and debonding areas, as follows:

$$\text{Hypothesis H0: } ART_{norm/H_0}(x) = 1 + n_{H_0}(x)$$
$$\text{Hypothesis H1: } ART_{norm/H_1}(x) = \mu_{H_1} + n_{H_1}(x)$$

where,

- $\mu_{H_0} = 1$ and $\mu_{H_1} > 1$ are the mean ART values, which is assumed steady along the scanning direction x over each area, namely, healthy (H_0) and defective areas (H_1);
- $n_{H_0}(x)$ and $n_{H_1}(x)$ are the noise attached to each case

The noises are assumed to be of zero mean with different standard deviations, namely, σ_{H_0} and σ_{H_1}. Besides, they are assumed to be decorrelated between A-scans and also to each other.

The decision threshold for debonding detection depends on the following two classification strategies: Two-classed and One-classed decision thresholds.

Two-class decision threshold

The conventional approach to distinguish between two classes of data with normal distribution consists in finding the point of intersection of the two PDFs [10]. The following likelihood ratio test (LRT) is used to this aim:

$$\lambda(ART_{norm}) = \frac{p(ART_{norm}|\mu_{H_1}, \sigma_{H_1})}{p(ART_{norm}|\mu_{H_0}, \sigma_{H_0})} \underset{H_0}{\overset{H_1}{\gtrless}} 1 \tag{2.10}$$

where $p(x|\mu, \sigma)$ represent the gaussian PDF with mean μ and standard deviation σ. It can be easily shown that the log-Likelihood is expressed as follows:

$$\Lambda(ART_{norm}) = 2ln\{\sigma_{H_0}/\sigma_{H_1}\} + \frac{(ART_{norm} - \mu_{H_0})^2}{2\sigma_{H_0}^2} - \frac{(ART_{norm} - \mu_{H_1})^2}{2\sigma_{H_1}^2} \underset{H_0}{\overset{H_1}{\gtrless}} 0 \tag{2.11}$$

Finally, the test for debonding detection (H1) becomes :

$$\frac{(ART_{norm} - \mu_{H_0})^2}{2\sigma_{H_0}^2} - \frac{(ART_{norm} - \mu_{H_1})^2}{2\sigma_{H_1}^2} \underset{H_0}{\overset{H_1}{\gtrless}} 2ln\{\sigma_{H_1}/\sigma_{H_0}\} \tag{2.12}$$

Equation. 2.12 requires to have some estimation (or prior knowledge) of both the mean and standard deviation of the two-class data, that means a collection of ART values over healthy (H_0) and defected areas (H_1). This scenario is difficult to hold in practice. Thus, the second approach using one-class decision threshold is proposed.

One-class decision threshold

This scenario is better tailored to the operational level, where the operator has no prior information on the location of defective areas. Here, the operator has access to a reference non-circulated area, where the interface layer is assumed to be perfectly coating, *i.e.*, healthy with no possible occurrences of debondings.

ART values are then collected over the reference area to compute σ_{H_0} (recalling, $\mu H_0 = 1$). The following decision threshold then serves to detect the outlier ART values over the area under test:

$$ART_{norm} \underset{H_0}{\overset{H_1}{\gtrless}} \mu_{H_0} + K\sigma_{H_0} \tag{2.13}$$

where K is a constant value, usually within the interval $[2, 3]$, which allows tuning the true negative rate (see Chapter. 3.3.2 for One-class SVM for further explanation) and makes the outlier detection more robust.

Illustration

Figure. 2.21, Figure. 2.22 and Figure. 2.23 present the debonding detection using the two-class decision classification on simulated noisy analytic Fresnel data (SNR = 30 dB). Three configurations with debonding thickness $t_{deb} = 0.2$ cm and permittivity values of respectively $\varepsilon_{r,deb} = 2$, 6 and 10. To present detailed information on the false classification (if any), we also present the curve-smoothed PDFs and the threshold observed for each configuration.

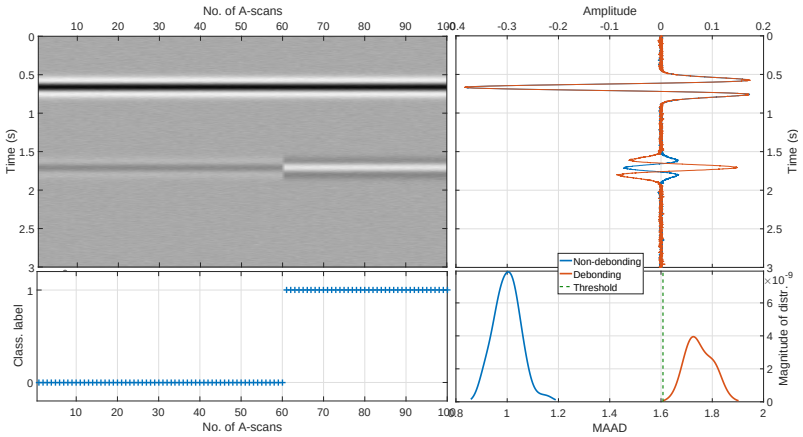

Figure 2.21: *Results for the detection of debondings on noisy simulated analytical data two-class decision classification. Permittivities of top and base layers are respectively* $\varepsilon_{r1} = 5$ *and* $\varepsilon_{r2} = 7$, $f_c = 4.2$ GHz, $SNR = 20$ dB*; with* $\varepsilon_{r,deb} = 2$

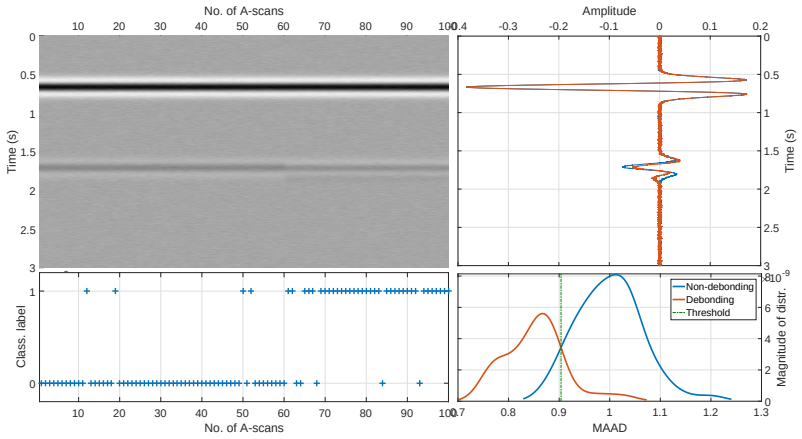

Figure 2.22: *Results for the detection of debondings on noisy simulated analytical data two-class decision classification. Permittivities of top and base layers are respectively* $\varepsilon_{r1} = 5$ *and* $\varepsilon_{r2} = 7$, $f_c = 4.2\,\mathrm{GHz}$, $SNR = 20\,\mathrm{dB}$*; with* $\varepsilon_{r,deb} = 6$

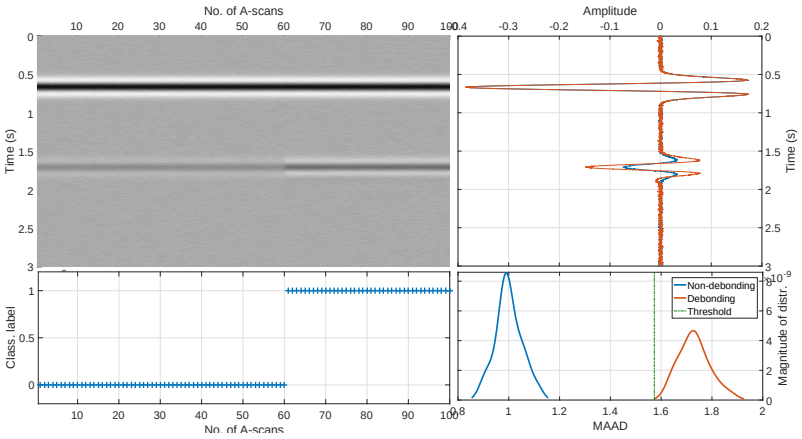

Figure 2.23: *Results for the detection of debondings on noisy simulated analytical data two-class decision classification. Permittivities of top and base layers are respectively* $\varepsilon_{r1} = 5$ *and* $\varepsilon_{r2} = 7$, $f_c = 4.2\,\mathrm{GHz}$, $SNR = 20\,\mathrm{dB}$*; with* $\varepsilon_{r,deb} = 10$

As done for the two-class decision classification, Figure. 2.24, Figure. 2.25 and Figure. 2.26 present the results for one-class classification for the same simulated data model configurations.

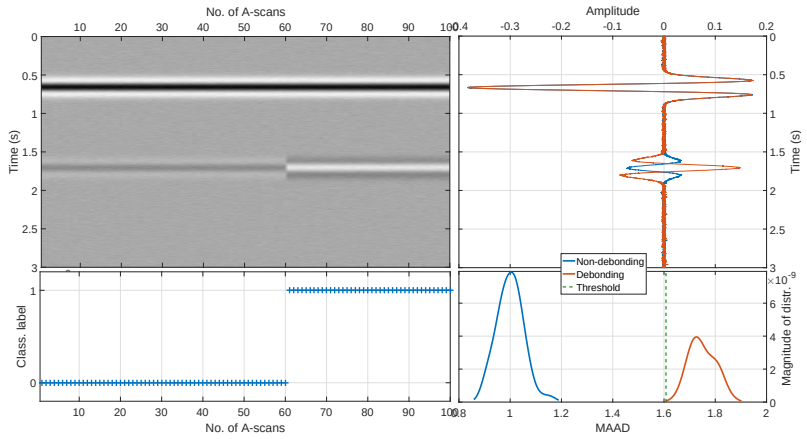

Figure 2.24: *Results for the detection of debondings on noisy simulated analytical data one-class decision classification. Permittivities of top and base layers are respectively* $\varepsilon_{r1} = 5$ *and* $\varepsilon_{r2} = 7$, $f_c = 4.2\,\mathrm{GHz}$, $SNR = 20\,\mathrm{dB}$; *with* $\varepsilon_{r,deb} = 2$

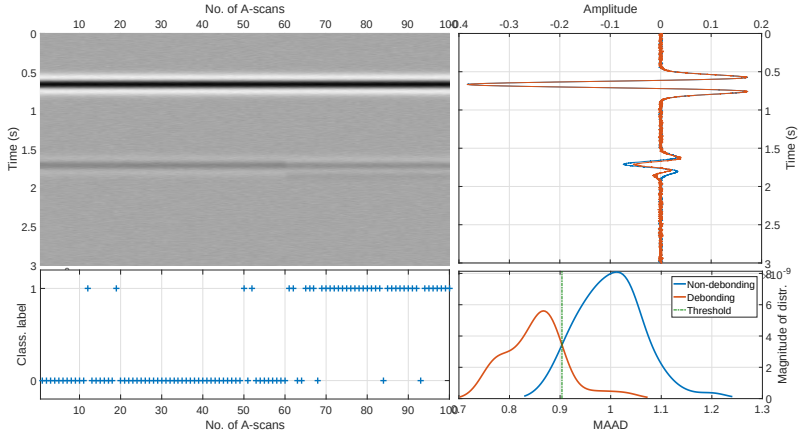

Figure 2.25: *Results for the detection of debondings on noisy simulated analytical data using one-class decision classification. Permittivities of top and base layers are respectively* $\varepsilon_{r1} = 5$ *and* $\varepsilon_{r2} = 7$, $f_c = 4.2\,\mathrm{GHz}$, $SNR = 20\,\mathrm{dB}$; *with* $\varepsilon_{r,deb} = 6$

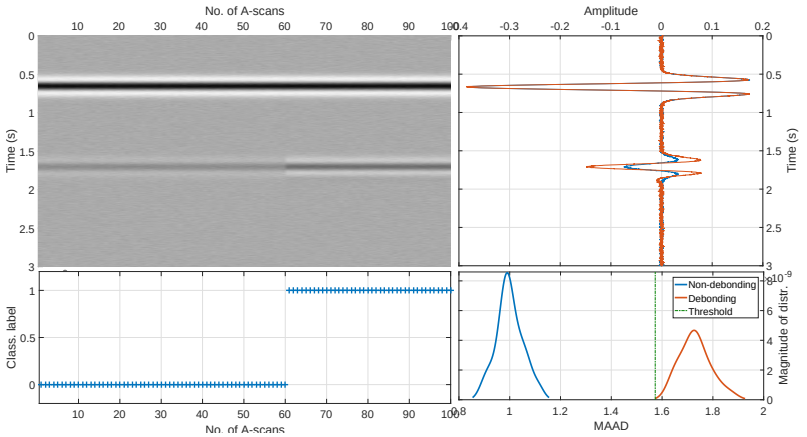

Figure 2.26: *Results for the detection of debondings on noisy simulated analytical data using one-class decision classification. Permittivities of top and base layers are respectively* $\varepsilon_{r1} = 5$ *and* $\varepsilon_{r2} = 7$, $f_c = 4.2\,\mathrm{GHz}$, $SNR = 20\,\mathrm{dB}$; *with* $\varepsilon_{r,deb} = 10$

2.7 Conclusion

We begin this chapter by presenting the existing techniques for pavement evaluation. These techniques were categorized broadly into Destructive and Non-destructive techniques. A review on the various aspects of destructive testing was presented along with its limitations. We then presented the pavement evaluation methods in the field non-destructive testing scopes along with the various existing methods to detect debondings. We then focused on the GPR tool, which is used in the thesis for pavement imaging and survey.

A reference method, namely, ART for Amplitude Ratio Test, was then presented. ART is routinely used by the GPR community for qualitative trace debondings within pavement structures. In this chapter, this method was presented within a more rigorous framework. The ART is selected to serve as a reference method to assess the performance of the classification methods to be presented in the next chapter for debonding detection.

However, the reference method depends on a single feature of the GPR A-scan signal, namely $MAAD$ or MAG. As such, it may achieve limited performance compared to the data-driven methods mentioned in section 2.5.

In the next chapter, we study three machine learning methods, namely unsupervised (k-means clustering) and supervised (Support vector machines and Random forests) in the context of debonding detection.

Part II

MACHINE LEARNING METHODS AND DATA PREPROCESSING FOR DEBONDING DETECTION

Chapter 3

Machine Learning Methods

Contents

The concept of Machine Learning (ML) is a rapidly growing field due to its immense range of applications. Machine learning is a subset of Artificial Intelligence that focuses on making predictions based on its experience. The goal of machine learning is to be able to predict and perform classification or regression tasks based on historical relationships between data [109]. The ML algorithms can be broadly classified into unsupervised learning, semi-supervised learning and Supervised learning family groups [110, 111, 112].

Among the existing ML methods in the literature, we select in this chapter three relatively mature ML methods that can be used within the scope of the thesis, namely,

the Support Vector Machine (SVM), Random Forest (RF) and k-means clustering. The methods based on "deep learning" were not selected in this thesis since the GPR databases are too limited in size. ML methods are expected to improve the performance of debonding detection in comparison with the reference ART method which was presented in Chapter. 2 (Section. 2.6). It should also be noted that, in contrast to the reference method, the ML methods do not use the same number of signal features (ART uses only one signal feature).

The ML techniques have been already used by the GPR community for various applications. Among others, SVM methods have been applied for the detection of voids in concrete [89, 90], landmine detection [91, 92, 93, 94], detection of subsurface defects [96, 97], railway ballast classification [113], underground utilities [98], buried objects [95] *etc.* One-class SVM has been used to detect landmines [93, 114]. Pavement surface cracks have been investigated using GPR in [115, 116, 117]. However, to the extent of our knowledge, ML methods have not yet been used to detect interface debondings.

This chapter provides an overview of three different machine learning families from an applied perspective. We then present the principle of one unsupervised ML method (k-means clustering) and three supervised ML methods (Support Vector Machines, One-class SVM and Random forests). For illustration, the latter methods are used to process simulated raw A-scan data vectors.

Finally, Figure. 3.1 presents the family of data processing methods studied in this thesis.

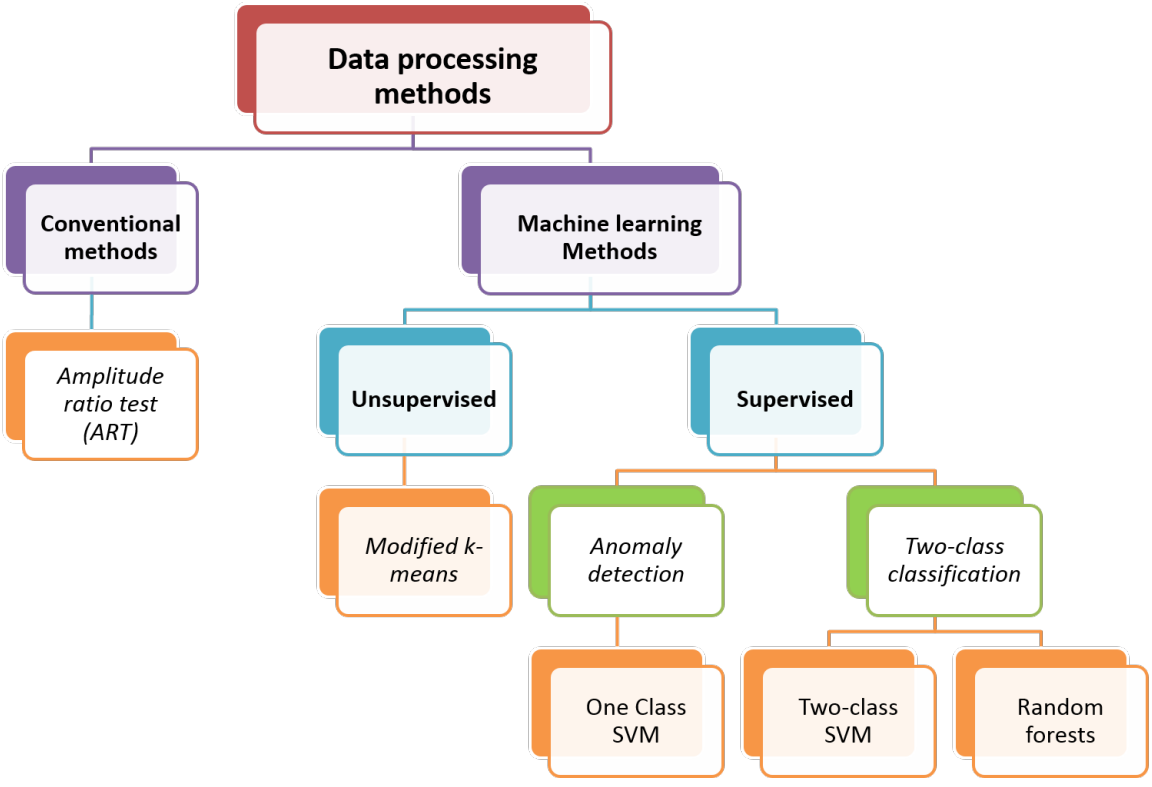

Figure 3.1: *Data processing methods which are tested in this thesis*

3.1 Elements of Machine Learning

Each ML algorithm possesses its own approach towards making predictions. However, a key common element for each algorithm is the use of Learning data and in some cases, the use of feature extraction/transformation step. The learning data is used by the ML to create a prediction (or classification) model [111, 118]. This model is the basis for the prediction. When a new input is introduced to the ML algorithm, it makes a prediction using the said model.

The ML algorithms can be broadly classified into three major groups amely, unsupervised learning, semi-supervised learning and Supervised learning [110, 111, 112]. One unsupervised method, namely k-means clustering [119], and two supervised methods, namely Support Vector Machines (SVM) [120] and Random Forests [121] are presented hereafter. The semi-supervised learning (SSL) would have practical interest within the scope of the thesis [122, 123]. However, the potential interest is canceled by the drawbacks listed in [124, 125, 126, 127]. Thus, only supervised and unsupervised methods were studied in the thesis.

3.1.1 Unsupervised Machine Learning

As mentioned in [128] (Chap. 5), the unsupervised learning methods do not require any guidance making them rely only on the data instances [112], namely, data labeling. Such methods 'learn' through observation and attempt to find structures in the data [128, 112]. Here, the prediction model automatically finds the patterns and relationships between data and clusters them into individual groups that present similar characteristics and it does not require the use of predefined labels [129]. The unsupervised learning aims to assign the data into subsets (also referred to as clusters) which possess certain similarities in characteristics.

Various unsupervised machine learning methods have been studied in the literature, including Self-organizing Maps (which is based on unsupervised Neural networks) [130], k-means [131, 130, 132], expectation maximization [132], C-means and hierarchical clustering [131], *etc.* Additionally, [133] presents and compares the performance of six unsupervised ML methods (k-means, DBSCAN, OPTICS, Agglomerative, Divisive and COBWEB) on the basis of number of iterations, clusters used, computational time *etc.*

The motivation behind using k-means as a reference for unsupervised methods is that it is one of the most commonly used unsupervised learning method [131] due to its simplicity in comparison to other clustering approaches [134]. Moreover, for a large number of variables, k-means can be computationally faster than other unsupervised methods such as hierarchical clustering [134].

Unsupervised clustering methods have several advantages:

1. They significantly reduce the computational costs [135]
2. They are flexible to deal with various datatypes: temporal data [135], spectral data [136] (using fuzzy clustering or even time-frequency data) [137] (by means of hierarchical clustering)

3. They are known for their simplicity [135], ease of implementation and real-time capability [138, 139, 140]

4. They do not require the operator intervention for labeling the data (except during the performance assessment stage). This is also the key difference between supervised and unsupervised ML methods.

By contrast, the lack of prior information may bring certain drawbacks to unsupervised methods:

1. Lower accuracy of the results: this is also because the input data is not known and not labeled by the operator in advance.

2. Although unsupervised clustering focuses more on being real-time, it is sometimes a time-consuming in case of large data [141]

3. May sometimes result in loss of information conveyed by the original data for clustering [135]

4. Different algorithmic approaches may lead to drastic changes in the results [142]

5. Since the numbers of classes are also not known, it could lead to the inability to ascertain the results generated by the analysis.

These drawbacks in unsupervised learning approach demands the need of an approach to overcome by the use of supervised machine learning.

3.1.2 Supervised Machine Learning

According to [143, 144], the most common form of ML relies on supervised learning. In contrast to the unsupervised methods, the Supervised learning methods is based on a training data model to classify and/or perform prediction. It is a two-step method where, the training data is used to create a classification model controlled by various parameters (discussed later). This model is then fed with test data and the model performs the classification.

In case of supervised learning, the data is divided into two groups namely, learning and testing data. Figure 3.2 shows the data division. The learning data is sub-divided into Training data and Validation data. During the learning stage, a method as for example Cross validation [145, 146] is used. The training data is used to 'train' the model while the validation data is used to optimize the model-parameters for the given application (*i.e.* debonding detection). Once the optimal parameters (for a certain method) are obtained, the testing data uses this model to predict the presence or absence of debondings.

In Section. 3.3, three supervised ML techniques are selected for the application. They are categorized into parameterized (SVM-based) and non-parameterized (Random Forest) techniques. The first method requires to adjust its internal parameters on the learning data set.

Supervised machine learning has many advantages:

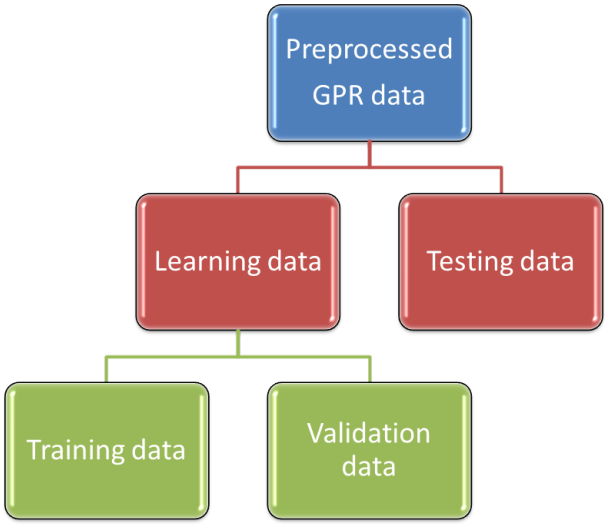

Figure 3.2: *GPR data grouping for supervised ML methods*

1. The learning step (which creates the classification model) allows achieving better classification performance

2. It allows the user to be very specific: the user has the freedom to set the decisional boundaries to distinguish between classes (*i.e.* benchmarking)

3. The results produced by the supervised method are known to be more accurate and reliable in comparison to the results produced by the unsupervised techniques of machine learning. This is mainly because the input data in the supervised algorithm is well known and labeled [147]

4. As mentioned in [148, 149], supervised learning method such as decision trees and self-organizing neural networks can be suitable for real-time with very fast testing speed. SVM has also been readapted to be used in real-time for hyperspectral image classification [150], emotion recognition [151], trojan-horse detection [152] *etc.*

5. Since the number and the type of classes are set at the labeling stage and are included in the classification model, no ambiguous results can occur.

However, besides all the advantages, supervised ML methods has a few drawbacks:

1. Supervised learning can sometimes be a complex method both in terms of modeling and computational time compared to the unsupervised method.

2. The necessity to label the inputs in supervised learning adds to the overhead and is not always accurately done

3. It may or may not be applicable in real time since the learning stage demands computational time thereby making supervised learning quasi-real time at the most. On the other hand, unsupervised learning can be implemented in real-time, constrained by the data size.

4. For dynamic and large data sets, it is a huge challenge to pre-define the labels.

Nevertheless, the efficiency and robustness of supervised learning is expected to achieve the detection of thin debondings with high accuracy.

3.1.3 Implementation of ML algorithms

According to Maxwell et al. [153], the implementation of ML methods is not straightforward, and the literature may provide conflicting advice. The implementation of algorithms helps to understand the mathematical approach and the practical considerations behind the method. It could supposedly improve the ML method's efficiency, reduce its computational time and perform at low costs.

In this subsection, we explore some practical considerations regarding the use of ML methods within the perspective of debonding/non-debonding classification of radar data. We then broadly categorize the implementation of ML methods into the feature-space selection and reduction, and the possible impact on computer burden and (specific) limitation/difficulties reported in the literature.

Signal *vs.* Image data processing

According to Section. 2.3, the most conventional processing formats for GPR data are B-scan (2D image) and A-scan (1D data vector). We initially represent each B-scan radar data by a spatio-temporal image, *i.e.*, a $N \times M$-dimensional matrix, where M is the number of data samples in an A-scan, and N is the number of A-scans along the scanning direction. B-scan radar data matrix are arranged column wise, each column, namely, A-scan, representing 1D time data vector. As an example, Figure. 3.3(a) illustrates two 1D A-scan signals while Figure. 3.3(b) shows the collection of adjacent A-scan signals to form the 2D GPR B-scan image.

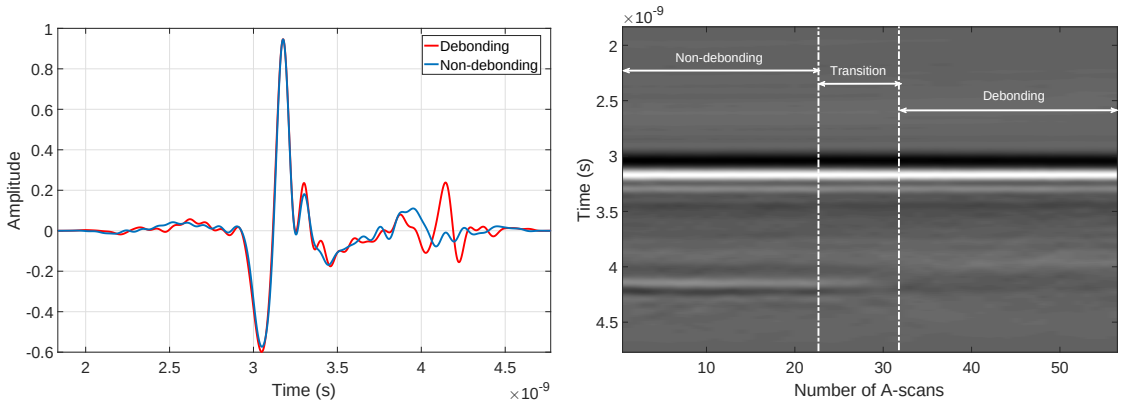

(a) 1D signal (A-scan) over debonding and non-debonding areas

(b) 2D GPR image (Bscan)

Figure 3.3: *GPR data collected over artificial embedded debonding at the IFSTTAR's fatigue carousel (Tack-free defect at 10kcycles loading stage); see Appendix. B for more information*

ML methods can theoretically process the two data formats in either independent signal-by-signal 1D analysis basis or in image based 2D analysis. Theoretically, the image data brings more information than independent data vectors due to its possible spatial coherency of the overall data.

Within the GPR community, the choice of the data format to be processed usually depends on the application under scope. The 2D image processing are required for detecting point-like scatterers within subsurface, provided a dense enough spatial sampling of GPR data collection is available. In this case, the spatial sampling is required to be smaller than the footprint of the antenna beams, introducing some useful spatial overlapping between successive A-scan profiles.

By contrast, for GPR pavement surveys at traffic speed, the latter condition on spatial sampling does not hold (since the acquisition rate of the electronic system is limited, and the sampling spatial interval increases with traffic speed). In addition, in case of 2D B-scan data, radar clutter demonstrates a strong spatial coherency, which may disturb the analysis of the subsequent stratified pavement layers. Thus, in case of GPR pavement survey, B-scan data are usually processed on a scan-by-scan basis.

Similarly, in this thesis, radar data are processed on a scan-by-scan (individual A-scan at a time) basis to keep the processing closer to the operational level. (Note: Although the data collection in Appendix. A provides dense enough spatial sampling.)

Raw data *vs.* Signal features

ML techniques were initially applied to process data in their raw form. However, according to LeCun et al., 2015 [143], this conventional implementation of ML techniques is supposed to limit their ability to process data. Then, feature extractor have been introduced to transform the raw data into a suitable internal representation or feature vector, on which the ML techniques then perform classification.

For the GPR application under scope, the 'raw' data is the collected GPR data in time/frequency domain without introducing any alteration or modifications into the data. Feature vector on the other hand refers to some selected signal characteristics extracted from the raw data, that well-represent the actual data but with reduced data size. ML systems required careful engineering to design a feature extractor. The feature set will be extensively explored in the later chapters and the two implementation ways of ML techniques will be quantitatively compared.

To implement the machine learning methods using feature sets, an initial preprocessing step is used wherein the signal features (or characteristics) that strongly represent the data are extracted. This will be later discussed in detail in Chapter. 4.2 and the performance between the two implementations of ML techniques, *i.e.*, raw-based data and features-based processing, will be compared in Chapter. 5.

Limitations and difficulties

Despite of various approaches of ML methods, they have certain limitations. In case of supervised learning, one such problem is over-fitting. It is generally referred in machine

learning where a model produced by the method (in the learning stage) is unable to make proper predictions for the new (test) data [154, 155, 156]. On the other hand, under-fitting is another issue wherein the method is unable to produce a model based on the learning data [157, 158].

A survey on ML methods is conducted in [159]. It presents a detailed list of individual limitations of various supervised machine learning methods (such as SVM, Decision trees, k-nearest neighbors *etc.*) and unsupervised clustering methods. Moreover, the computational burden and complexity may increase due to the large size of the raw data sets.

However, solutions to overcome some of these limitations have already been proposed in the literature. These include signal feature selection and extraction, feature dimensionality reduction and cross validation techniques, which are discussed in detail in Chapter. 4 and Chapter. 5 respectively.

3.2 Data Clustering method

The clustering algorithm is one of the most simple unsupervised method to categorize data into N different clusters. Such algorithms are useful in classifying the raw data and possibly identify any hidden patterns that exist within the datasets. The method presented thereafter is a modified iterative clustering of the conventional k-means algorithm, which is explained hereafter.

3.2.1 Principle

The clustering algorithm works on the principle of 'grouping' the datasets into various categories based on their statistical parameters and distance . In this algorithm, the primary step is to choose the number of clusters N required by the user. This is a user-defined parameter. Once the number of clusters is decided, an iterative process is conducted until convergence is met or defined by the user.

Within the scope of the thesis, the primary focus of the clustering methods and processes is to determine the presence (or absence) of debondings occurring at the interface between the first two layers of the pavement structure from GPR A-scan data. According to Chapter. 4.2), signal features may be different on Healthy (unbonded) and Defective (debonded) regions and then, can be used to cluster the data as debonding or non-debonding groups.

Thus, the value of initial cluster is $N = 2$. [160] describes the k-means approach using an algorithm. For the debonding detection applications, the number of clusters $k = 2$; these initial cluster centroids are chosen at random. We then form 2 clusters by assigning the remaining points to their nearest cluster.

A proximity measure, namely Euclidean (L2) distance (d), is used to quantify the 'nearest' points to a cluster defined by:

$$d(C_i, x_j) = \sqrt{(s_i - s_j)^2 + (k_i - k_j)^2} \tag{3.1}$$

where,

- $C_i = (s_i, k_i)$ is the ith centroid with $i \in \{1, 2\}$ indicating each cluster, and $j \in \{1, 2 \dots N\}, j \neq i$,
- s and k are respectively the skewness and kurtosis computed for each A-scan vector,
- $x_j = (s_j, k_j)$ is associated to the jth A-scan

The A-scan x_j is then assigned to the cluster based on:

$$x_j \in \begin{cases} C_{deb} \text{ if } d_{1,j} < d_{2,j} \\ C_{ndeb} \text{ if } d_{1,j} > d_{2,j} \end{cases} \tag{3.2}$$

where $d_{1,j} = d(C_{deb}, x_j)$ and $d_2 = d(C_{ndeb}, x_j)$ are the Euclidean distances of x_j from respectively debonding (C_{deb}) and non-debonding (C_{ndeb}) centroids.
Iteratively, new centroids are recomputed until no such reassignment is possible (*i.e.* convergence is met) using the now clustered data as follows [128]:

$$C_{i,new} = \frac{1}{card(C_{i,old})} \sum_{(s_j,k_j) \in C_{i,old}} \begin{bmatrix} s_j \\ k_j \end{bmatrix} \tag{3.3}$$

where,

- $C_i \in \{C_{deb}, C_{ndeb}\}$
- $[s_j \ k_j]^T$ is associated to the jth A-scan point in the cluster $C_{i,old}$
- $card(C)$ is the cardinality of C

However, since the initial seed step in the conventional approach is chosen at random, the choice of a wrong centroid may lead to a high misclassification rate.

3.2.2 Modified clustering algorithm

By contrast to the conventional method, the modified clustering approach proposed to introduce an initial seed step wherein the first k centroids are predetermined by the user as follows.

In the modified clustering approach, we select two signal characteristics, namely, signal kurtosis and signal skewness to construct the 2D cluster-space. We modify Equation. 3.1 to get the 2 farthest points in this cluster-space as follows:

$$d_{max} = \max_{i,j,i \neq j} \left\{ \sqrt{(s_i - s_j)^2 + (k_i - k_j)^2} \right\} \tag{3.4}$$

Each A-scan is then assigned to its nearest centroid (as shown in Equation. 3.3) and the process is then repeated until convergence is met as done in the conventional k-means approach. Figure. 3.4 presents the schematic for the implementation of the modified clustering approach and also compares it with the conventional k-means.

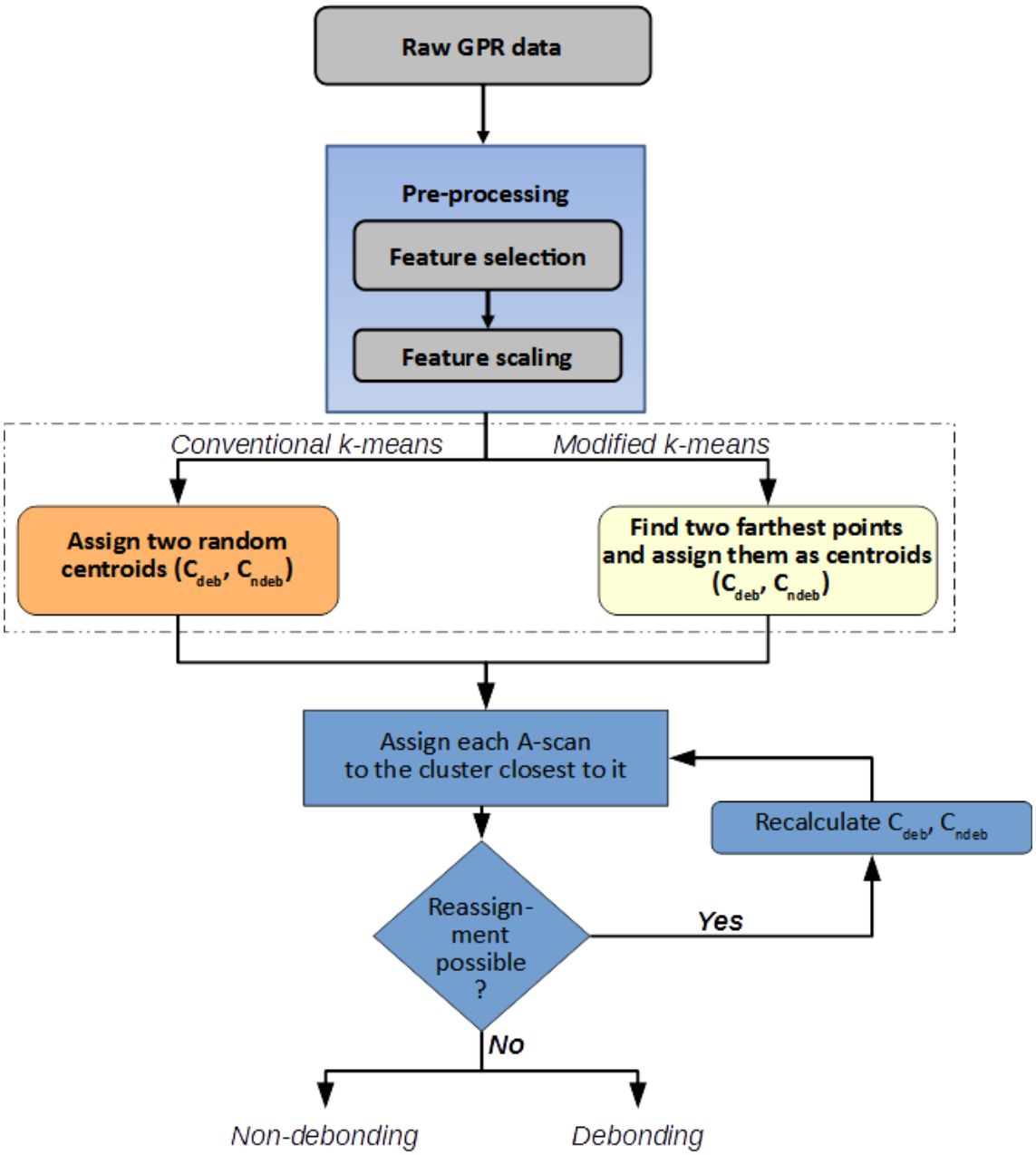

Figure 3.4: *Implementation of the unsupervised clustering algorithm to detect debondings presenting the difference in the initial seed point w.r.t. conventional k-means*

The conventional k-means approach and the modified clustering approach are used to process noisy simulated B-scan radar data (see Appendix. A.2). Figure. 3.5 compares the final clustering results using the global skewness and kurtosis computed from raw A-scan data. The proposed modified approach achieves a more relevant data grouping with less misclassification.

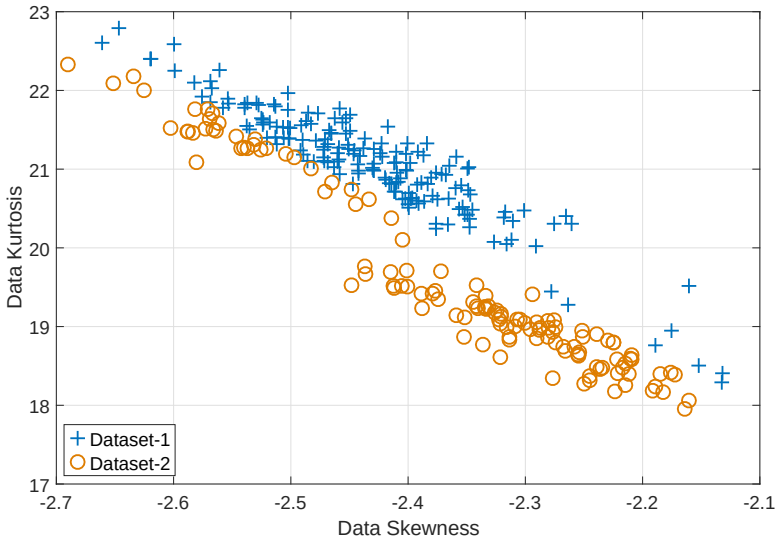

(a) Clustering by conventional k-means

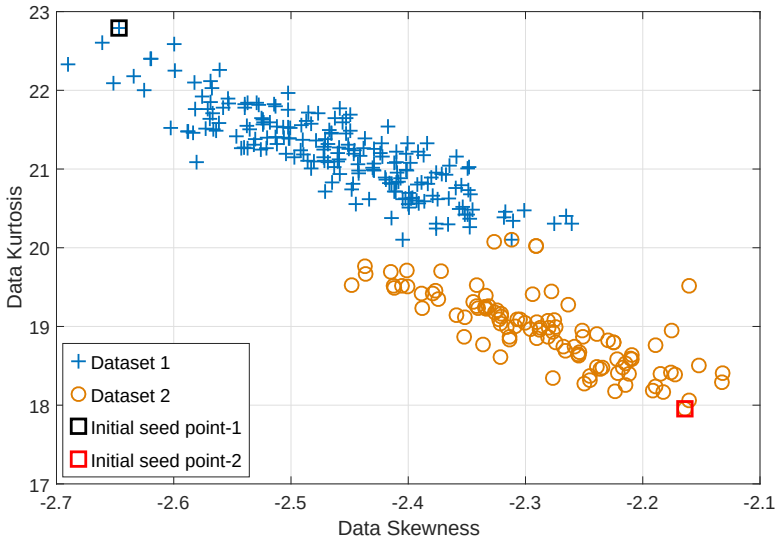

(b) Clustering by modified k-means

Figure 3.5: *Comparison of clustering methods on noisy simulated analytic raw data (with* $SNR = 20\,\mathrm{dB}$*) using two signal features, namely, Kurtosis and Skewness*

3.3 Parameterized Supervised machine learning: Support Vector Machines

Support Vector Machines (SVM) have been extensively researched in the data mining and machine learning communities for the two last decades due to its robustness and easiness to implement. It actively applied to applications in various domains such as handwriting recognition [161, 162], facial detection [163], learning of cancer genomics [164]. SVM can be typically implemented for both classification (classifying SVM or C-SVM) and regression (Support Vector Regression) problems. In the field of NDT, SVM has been used for the detection of buried objects [95, 165]. We have also implemented SVM in the detection of thin inter-layer debondings in pavement structures in [13], [166], [10].

The precursor to SVM was first introduced by Vladimir Vapnik and Alexey Chervonenkis in 1963 [167, 168]. In 1992, Boser et al. [169] suggested a way to create nonlinear classifiers by applying the kernel trick to maximum-margin hyper-planes. The current standard incarnation (soft margin) was proposed by Cortes and Vapnik in 1995 [120].

SVM is usually applied for multi-class classification in the literature. However, within the scope of the thesis, SVM is first focused on the two-class classification in Section 3.3.1 to distinguish between radar A-scan data over debonding and non-debonding areas. Later on in Section 3.3.2, SVM is implemented as an outlier detection methods namely, One-Class SVM to detect debonding A-scan data as an outlier class.

For representation, in this section, each B-scan radar data is represented by an $N \times M$-dimensional matrix $\mathbf{X} = [\mathbf{x}_1, \mathbf{x}_2 \dots \mathbf{x}_N]$, where N is the number of A-scans and M may be either the number of time samples or the number of signal features. In the following, the conventional way of applying SVMs to data is presented; it consists in processing data in their raw form, i.e., the time samples of Ascan in our case. By contrast, signal features will be used in Chapters 4 and 5 to implement SVMs.

3.3.1 Two-Class SVMs for binary classification

Binary SVMs are classifiers which discriminate data points of two categories. To classify data into two classes, we initially represent each B-scan data by an $N \times M$-dimensional matrix, where M is the number of data samples in an A-scan, and N is the number of A-scans. Each of the A-scans belongs to only one of two classes (*i.e* non-debonding or debonding). A classification boundary is used to separate the two classes; such boundaries are called hyper-planes. In theory, to separate the data into two classes, several hyper-planes can be traced. However, in order to avoid misclassifications, an optimal hyper-plane must be found that provides the maximum separation of the data. In order to achieve this, SVM picks the hyper-plane which has the largest margin [170] as shown in Figure. 3.6.

SVM can be implemented differently depending on the application requirements and the data. The two general types SVM based on the kernel are linear SVM and non-linear (kernel) based SVM.

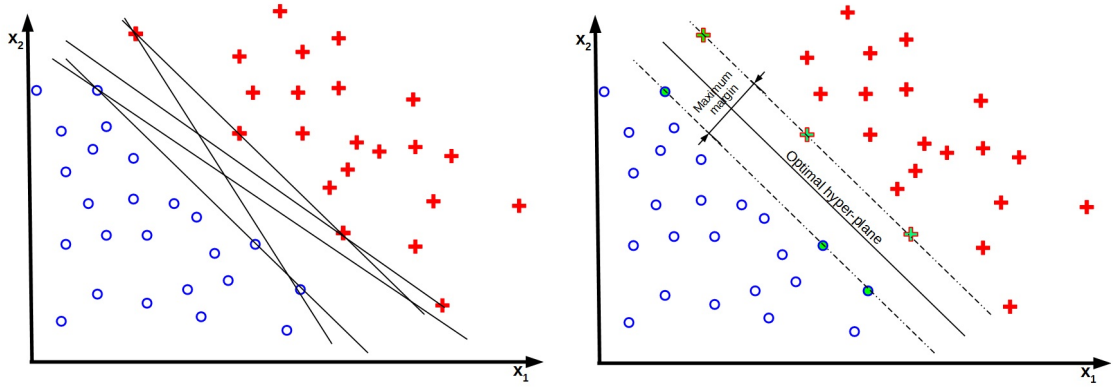

(a) All possible hyper-planes (b) Optimal hyper-plane for classification

Figure 3.6: *SVM Hyper-planes. x_1 and x_2 are the the axes of the feature-planes [10]*

3.3.1.1 Linear SVM

Given a learning data set $\mathbf{X} = [\mathbf{x}_1, \mathbf{x}_2 \dots \mathbf{x}_N]$ of the order $M \times N$ (where M is the number of time samples and N is the number of A-scans), the aim is to find the maximum-margin hyper-plane that divides the learning data A-scans $\mathbf{X}$ into two separate classes, namely, Non-debonding (labeled as -1) or debonding (labeled as +1). Additionally, the margin between the separation is expected to be maximized as much as possible in order to have a better classification.

Each hyper-plane can be expressed as a linear equation that depends on the learning data as follows [171]:

$$\mathbf{w}^T\mathbf{x} + b = 0 \tag{3.5}$$

where $\mathbf{w}$ is the normal vector to the hyper-plane (the distance between $\mathbf{x}$ and the hyper-plane)). The parameter b is the bias (offset from the origin [172]) introduced and $\frac{b}{||\mathbf{w}||}$ determines the offset of the hyper-plane from the origin along the normal vector $\mathbf{w}$.

In case of linearly separable data, two parallel hyper-planes to Equation. 3.5 can be selected that separate the two classes of data, so that the distance between them is as large as possible. The distance bounded by these two hyper-planes is called the 'margin' and the maximum-margin hyper-plane is the hyper-plane that lies halfway between the two hyper-planes. These hyper-planes can be described by the equations [10]:

$$\mathbf{w}^T\mathbf{x}_i + b = 1 \text{ for debonding; } y_i = 1 \tag{3.6}$$

$$\mathbf{w}^T\mathbf{x}_i + b = -1 \text{ for non-debonding; } y_i = -1 \tag{3.7}$$

where $\mathbf{x}_i$ is the ith learning A-scan and y_i is its associated classification label.

The decision function $D(\mathbf{x})$ for linearly separable data is expressed using Equation. 3.6 and Equation. 3.7 as [10]:

$$D(\mathbf{x}_i) = sgn(\mathbf{w}^T\mathbf{x}_i + b) \tag{3.8}$$

where, *sgn* is the sign function.
Geometrically speaking, the distance between the two hyper-planes from Equation. 3.6 and Equation. 3.7 would be $\mathbf{2}/||\mathbf{w}||$. As mentioned earlier, in order to obtain better classification, the margin must be maximized. Thus, the weight vector should be minimized. Additionally, to prevent the data points from being falsely classified, constraints are added to 'force' each learning data to remain on the designated side of the margin. To do so, we combine Equation. 3.6 and Equation. 3.7 to obtain a single condition as:

$$y_i.(\mathbf{w}^T\mathbf{x}_i + b) \geq 1, \ \forall \ 1 \leq i \leq n \tag{3.9}$$

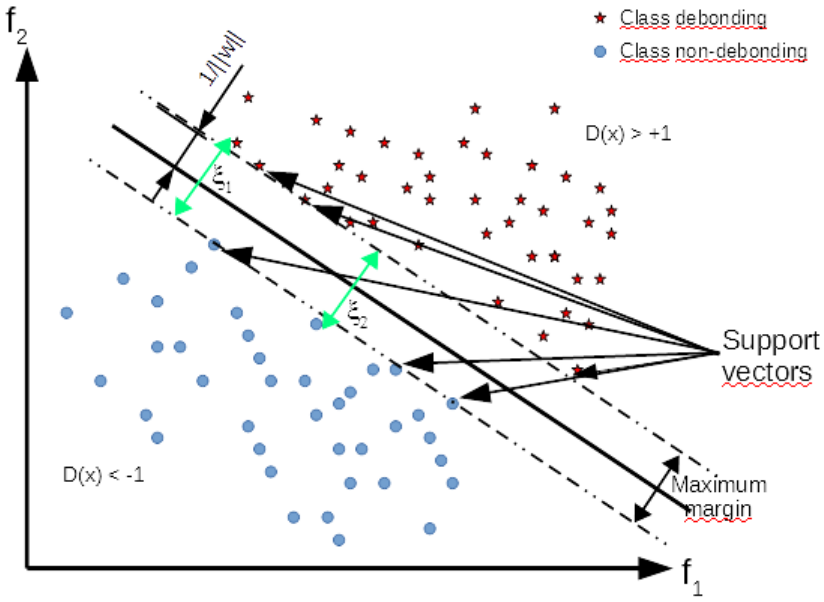

Figure 3.7: *Example of a principal scheme of Soft SVM on a 2-dimensional feature space. Axes f_1 and f_2 indicate the feature space*

The GPR data in practice are noisy data. So even if there is a linear relationship between the data and their classes, a linear classifier may result in false classifications. To deal with such cases, it is reasonable to permit a relaxation parameter for such noise. In the context of SVM this amounts to release the constraint imposing that all the examples are many classes. In order to 'loosen' the constraint variables, called spring or relaxation deviations denoted ξ_i were introduced, as shown in Figure 3.7 To ensure that the number of outliers is reasonable, the gap variables are included in the objective function. The new

formulation of the optimization problem can thus be written as [10]:

$$\text{Minimize } \frac{1}{2}||\mathbf{w}||^2 + C\sum_{i=1}^{N}\xi_i \tag{3.10}$$

where C is called the Cost function or compromise constant. The parameter C is important in the learning model as it controls the tolerance level of the classifier. For larger values of C, only low ξ values are permitted thereby reducing the margin. Conversely, low C values result in larger margins. Finally, if C is undetermined (*i.e.* $C = \inf$), the classifier is a hard margin SVM. In short, C is used to indicate the importance given to errors on the training set against the attempt to maximize the margin. To express the formulation of flexible margins (*i.e*, with slack variable ξ_i), the Lagrangian of the problem of minimizing associated to the Equation. 3.6 - Equation. 3.10 can be expressed as [173]:

$$L(\mathbf{w}, b, \xi, \alpha, \beta) = \frac{1}{2}||\mathbf{w}||^2 + C\sum_{i=1}^{N}\xi_i + \sum_{i=1}^{N}\alpha_i\Big\{1 - \xi_i - y_i(\mathbf{w}^T\mathbf{x}_i + b)\Big\} \tag{3.11}$$

where α_i is the Lagrangian associated with the hyperplane and β_i is the Lagrangian associated with slack variable ξ_i. Next, we use the Karush-Kuhn Tucker (KKT) conditions in order to obtain the saddle point for Equation. 3.11. These conditions are necessary in general, and sufficient for convex optimization problems [174]. These conditions are defined as the as [171]:

$$\frac{\partial L}{\partial \mathbf{w}} = \mathbf{w} - \sum_{i=1}^{N}\alpha_i\ y_i\ \mathbf{x}_i = 0 \tag{3.12}$$

$$\frac{\partial L}{\partial b} = \sum_{i=1}^{N}\alpha_i\ y_i = 0 \tag{3.13}$$

$$\frac{\partial L}{\partial \xi_i} = C - \alpha_i - \lambda_i = 0 \tag{3.14}$$

$$\alpha(y_i(\mathbf{w}, \mathbf{x}_i) + b) - 1 + \xi_i = 0\ \forall\ i = 1 \ldots N \tag{3.15}$$

The dual classification problem can thus be written as [171, 175]:

$$\text{Maximize } W(\alpha) = \sum_{i,j=1}^{N}\alpha_i + \frac{1}{2}\sum_{i,j=1}^{N} y_i\ y_j\ \alpha_i\ \alpha_j\langle \mathbf{x}_i, \mathbf{x}_j\rangle \tag{3.16}$$

constrained by,

$$\sum_{i=1}^{N} \alpha_i \; y_i = 0 \tag{3.17}$$

$$0 \leq \alpha_i \leq C \; \forall \; i = 1 \ldots N \tag{3.18}$$

The decision function $D(\mathbf{x})$ from Equation. 3.8 for a linear kernel can thus be expressed as [10]:

$$D(\mathbf{x}) = sgn\Big\{ \sum_i \mathbf{w}^T \alpha_i \langle \mathbf{x}_i, \mathbf{x} \rangle + b \Big\} \tag{3.19}$$

An advantage of the flexible margins is that the solution of the problem is often 'hollow', *i.e.* a large proportion of α_i is zero. The geometric interpretation is given by the Figure. 3.8:

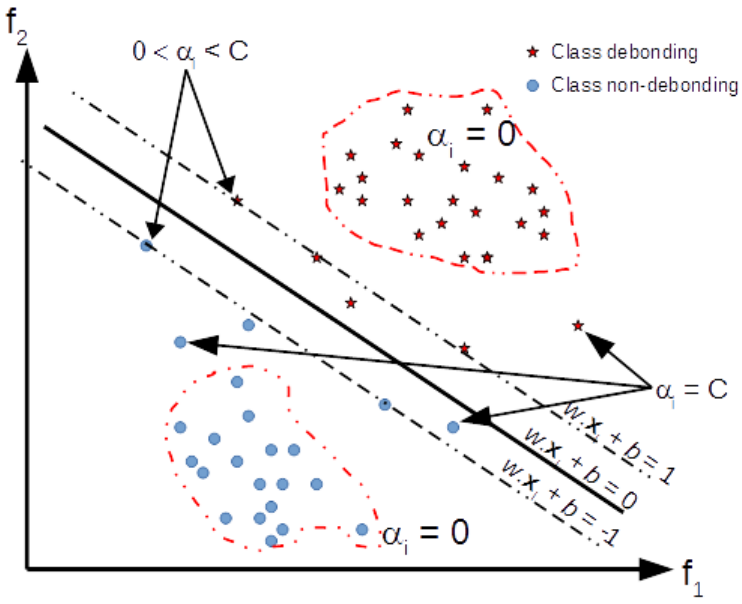

Figure 3.8: *Geometrical representation of Figure. 3.7. Axes f_1 and f_2 indicate the feature space*

3.3.1.2 Non-linear SVM

When there is no available possibility to classify the data by Linear classification, non-linear methods by applying Kernel tricks can be used. This methodology was suggested by Vapnik, Boser and Guyon in 1992 [169]. This method maximizes the hyper-plane margins that allow to fit the maximum-margin hyper-plane in a transformed feature space. The transformation may be nonlinear and the transformed space high dimensional. Although the classifier is a hyper-plane in the transformed feature space, it may be nonlinear in the original input space [176].

The SVM classifier method consists of a maximum margin in which the scalar product (in Equation. 3.19) was replaced by the kernel. Extending the linear SVM from Equation. 3.16, we get [171, 175]:

$$\text{Maximize } W(\alpha) = \sum_{i=1}^{N} \alpha_i - \frac{1}{2} \sum_{i,j=1}^{N} y_i.y_j.\alpha_i.\alpha_j \kappa(\mathbf{x}_i, \mathbf{x}_j) \tag{3.20}$$

once again under the constraints of Equation. 3.17 and Equation. 3.18.

The decision function for a kernel-based non-linear SVM can thus be expressed as [10]:

$$D(\mathbf{x}) = sgn\left\{ \sum_{i=1}^{N} \alpha_i y_i \kappa(\mathbf{x}, \mathbf{x}_i) + b \right\} \tag{3.21}$$

It can be seen that the term $\kappa(\mathbf{x}, \mathbf{x_i})$ in the latter equation replaces the term $\langle \mathbf{x}, \mathbf{x}_i \rangle$ in Equation. 3.19 for the Linear SVM.

NOTE: Kernel classifiers were described as early as the 1960s, with the invention of the kernel perceptron. They rose to great prominence with the popularity of SVMs in the 1990s, when the SVM was found to be competitive with neural networks on tasks such as handwriting recognition. Some of the well-known kernel functions include:

1. **Gaussian Radial basis function (RBF)** [171, 177]:

$$\kappa(\mathbf{x}_i, \mathbf{x}_j) = exp(-\gamma ||\mathbf{x}_i - \mathbf{x}_j||^2) \tag{3.22}$$

for all positive values of γ.

2. **Polynomial kernel** [171, 177]:

$$\kappa(\mathbf{x}_i, \mathbf{x}_j) = ({\mathbf{x}_i}^T \mathbf{x}_j + 1)^d \tag{3.23}$$

where d is the degree of the polynomial.

3. **Sigmoid kernel** [177]:

$$\kappa(\mathbf{x}_i, \mathbf{x}_j) = \tanh(\alpha {\mathbf{x}_i}^T \mathbf{x_j} + c) \tag{3.24}$$

with α being the degree of the sigmoid and c is the kernel coefficient.

Under Kernel based classification, the Radial Basis Function (or commonly called the RBF kernel) is a popular and most commonly used kernel function in SVM classifications [177, 178].

Figure 3.9 shows the flowchart of SVM classification for our application. The GPR data is divided into Learning and Testing data sets after initial preprocessing steps. With the help of suitable performance indication method, an optimal SVM model is constructed in the learning step. These model parameters are then applied on the Testing data set to

validate the overall performance of the method.

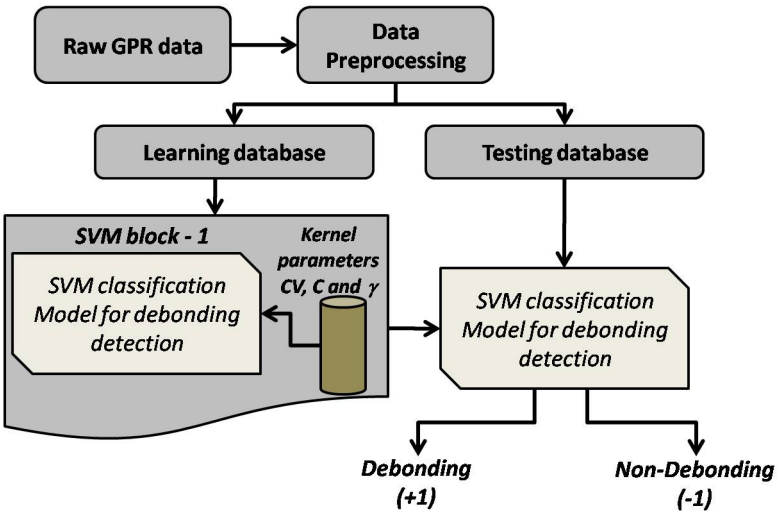

Figure 3.9: *Flowchart for SVM classification*

Figure. 3.10 illustrates the application of the binary SVM (with a non-linear RBF kernel) to process noisy simulated A-scan data (see Appendix. A.2) for test data only. A B-scan consisting of 200 A-scan vectors is created (using the analytic Fresnel model; see Appendix. A.2). The desired noise is then added to the B-scan (see Appendix. A.5). One half of the B-scan (*i.e.* 100 A-scans) is then used for the learning step to create an SVM classification model. The remainder is used for the testing step. We can see that the two-class SVM classification is able to identify the presence of debondings of various interlayer permittivities.

3.3.2 One-Class SVMs for anomaly detection

One-class SVM was suggested by Schölkopf [179] in the late 1990's as a method of adapting SVM to a one-class classification problem (as anomaly detection or outlier detection). This approach can be considered as a conventional two-class SVM where the training data consists only non-debonding data and the origin is the only member of the debonding data set (in contrast to the previous method, where, the training data comprises of both debonding and non-debonding data). It has been used in many applications such as image retrieval [180], document classification [181] *etc.*
Figure 3.11 shows the geometrical interpretation of One-class SVM. It is worth to noting that the labeling convention is the opposite to the one for the binary SVM: -1 refers to debonding and $+1$ to non-debonding.

One-class SVM can be obtained using the support vector data description (SVDD) [182] method wherein the data-points are mapped onto a higher dimension circumscribed by a sphere. This sphere acts as the limiting factor and aim would be to find the sphere with minimal radius that encompasses the positive data in the hyper-space.

To begin with, we first define a closed sphere around our data-points in the hyperplane (also referred to as the hyper-sphere). This sphere is defined by its radius $R > 0$ and

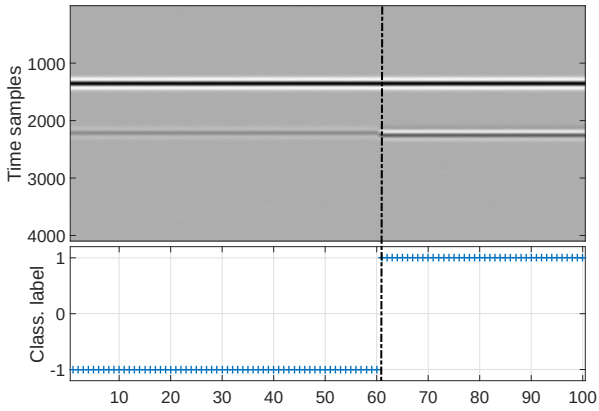

(a) Config. 1: B-scan with $t_{deb} = 0.3\,\text{cm}$ and $\varepsilon_{r,deb} = 2$

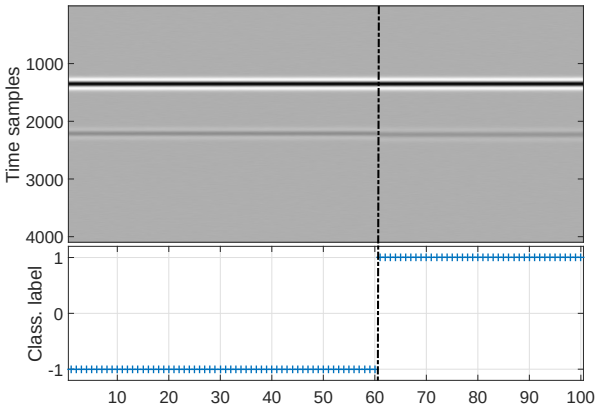

(b) Config. 2: B-scan with $t_{deb} = 0.3\,\text{cm}$ and $\varepsilon_{r,deb} = 6$

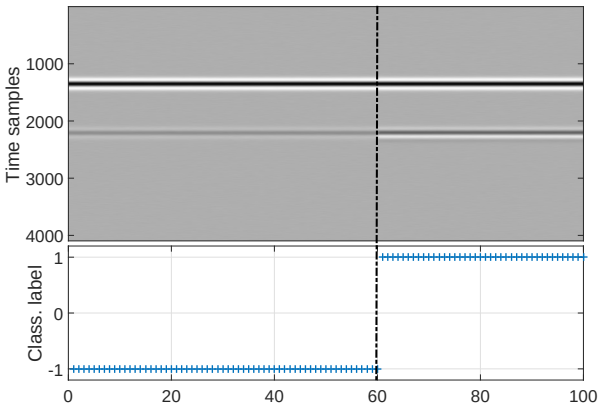

(c) Config. 3: B-scan with $t_{deb} = 0.3\,\text{cm}$ and $\varepsilon_{r,deb} = 10$

Figure 3.10: *Binary SVM applied on simulated noisy raw Ascan data (see Appendix A) for the detection of debondings using non-linear RBF kernel. Permittivities of top and base layers are respectively* $\varepsilon_{r1} = 5$ *and* $\varepsilon_{r2} = 7$, $f_c = 4.2\,\text{GHz}$, $SNR = 20\,\text{dB}$. *The dashed line differentiates the non-debonding and debonding zones*

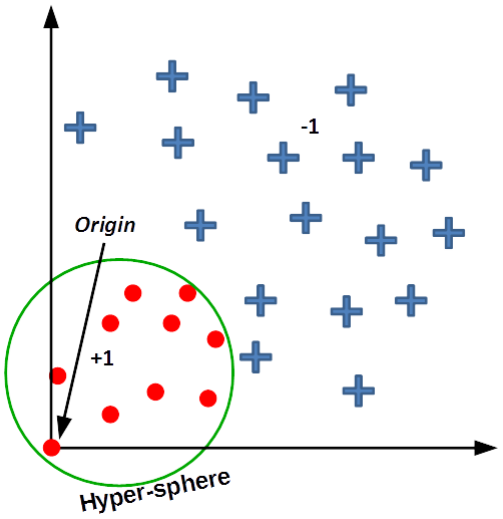

Figure 3.11: *Geometrical representation of a One-class SVM*

centered at b. As done in the previous section, the training data matrix $\mathbf{X}$ strictly consists of N A-scans of the non-debonding class and is given by : $\mathbf{X} = [\mathbf{x}_1, \mathbf{x}_2 \ldots \mathbf{x}_N\ ]$. The aim is to minimize the volume of this hyper-sphere by minimizing the radius R keeping in mind that all the training non-debonding points are embedded within this hyper-sphere. The error function for minimization, according to the Support vector classifier proposed by Vapnik is given by [182]:

$$f(R, b) = R^2 \tag{3.25}$$

with constraints:

$$||\mathbf{x}_i - b||^2 \leq R^2 \ \forall\ i;\ \ i \in 1 \ldots N \tag{3.26}$$

Now, to allow all possibilities of the outliers into the training set, the distance between the data-point $\mathbf{x}_i$ and the center of the hyper-sphere b should be less than R^2. An A-scan where the result goes beyond the radius R should be considered to be an debonding (*i.e.* outlier). If this condition is not satisfied, the distances larger than this should be penalized.

To do so, we introduce a slack variable ξ_i (where $\xi_i \geq 0$). The minimization problem thus becomes:

$$\text{Minimize}_{R,\xi,b} = f(R, b, \xi) = R^2 + \frac{1}{\nu N} \sum_{i=1}^{N} \xi_i \tag{3.27}$$

such that, $||\kappa(\mathbf{x}_i) - b||^2 \leq R^2 + \xi_i,\ \forall i = 1, 2, \ldots N$
where ν is a user designed parameter that is used to determine the amount of admitted

slack, $\kappa(\mathbf{x})$ is the kernel function (either linear or non-linear), R is the radius of the hyper-sphere and ξ is the introduced slack variable.

We now introduce the Lagrangian multipliers α and β to obtain the Lagrange function ($\mathcal{L}$) as follows:

$$\mathcal{L}(R, \xi, b, \alpha, \beta) = R^2 + \frac{1}{\nu N} \sum_{i=1}^{N} \xi_i + \sum_{i=1}^{N} \alpha_i \{(\kappa(\mathbf{x}_i) - b)^T (\kappa(\mathbf{x}_i) - b) - R^2 - \xi_i\} - \sum_{i=1}^{N} \beta_i \tag{3.28}$$

Now, to obtain the values for the saddle point, we partially differentiate $w.r.t$ the Lagrangian multipliers and after calculation we obtain:

$$\mathcal{L}(R, \xi, b, \alpha, \beta) = \sum_i \alpha_i \kappa(\mathbf{x}_i, \mathbf{x}_i) - \sum_i \sum_j \alpha_i \alpha_j \kappa(\mathbf{x}_i, \mathbf{x}_j) \tag{3.29}$$

such that, $0 \leq \alpha_i$, $\beta_i \geq 0$ and $\alpha_i + \beta_i = \frac{1}{\nu N}$
NOTE: For simplicity, henceforth $\sum_{i=1}^{N}$ and $\sum_{j=1}^{N}$ are simply written as $\sum_i$ and $\sum_j$ respectively.

The boundary condition is defined by the radius R of the hyper-sphere and is given by:

$$||\kappa(\mathbf{x}_i) - b||^2 = R^2 \tag{3.30}$$

where, $\mathbf{x}_i$ is any support vector with $0 < \alpha_i < \frac{1}{\nu N}$
The decision function $D(\mathbf{x})$ is given as : $D(\mathbf{x}) = sgn(\kappa(\mathbf{x}_i) - b)$

$$D(\mathbf{x}) = \begin{cases} +1, & \text{for } f(\mathbf{x}) \\ -1, & \text{for } \bar{f}(\mathbf{x}) \text{ is odd} \end{cases}$$

Substituting the value of b in Equation 3.30, we obtain the optimal radius of the hyper-sphere which is also the boundary condition to separate the anomalous data. It is given as:

$$R^2 = \kappa(\mathbf{x}_i, \mathbf{x}_i) - 2 \sum_j \alpha_j \kappa(\mathbf{x}_i, \mathbf{x}_j) + \sum_i \sum_j \alpha_i \alpha_j \kappa(\mathbf{x}_i, \mathbf{x}_j) \tag{3.31}$$

Once the boundary conditions are obtained, it is possible to classify the data and identify if they belong to the class non-debonding (*i.e.* inliers within the hyper-sphere) or class debonding (*i.e.* outliers). However, a major step of optimizing said boundary should be done to increase the efficiency and avoid the false detection of any outliers. The radius

given in the previous section (Eq. 3.31) provides the boundary condition. To optimize this boundary, it is necessary to obtain the minimum value for R. The optimization problem is thus presented as:

$$\text{argmin}_{\alpha}\left\{\sum_{i}\alpha_i\kappa(\mathbf{x}_i,\mathbf{x}_i)-\sum_{i}\sum_{j}\alpha_i\alpha_j\kappa(\mathbf{x}_i,\mathbf{x}_j)\right\} \tag{3.32}$$

Considering the Translation Invariant Kernel [183], we get that the kernel function for the same data is a constant *i.e.*, $\kappa(x,x) = const$, and it can be omitted. Similarly, from before, we have $\sum_i \alpha_i = 1$. Hence we can simplify Equation 3.32 to:

$$\text{argmin}_{\alpha}\left\{\sum_{i}\sum_{j}\alpha_i\alpha_j\kappa(\mathbf{x}_i,\mathbf{x}_j)\right\} \tag{3.33}$$

Figure. 3.12 presents an overall anomaly detection approach using OCSVM. During the learning stage, the data used is made sure to be of only one type (*i.e.* non-debonding zone). As done previously in case of two-class SVM, the raw GPR data is used here. Using the OCSVM, a classification model is generated. The unknown B-scan is then 'tested' to identify the anomalies (debondings).

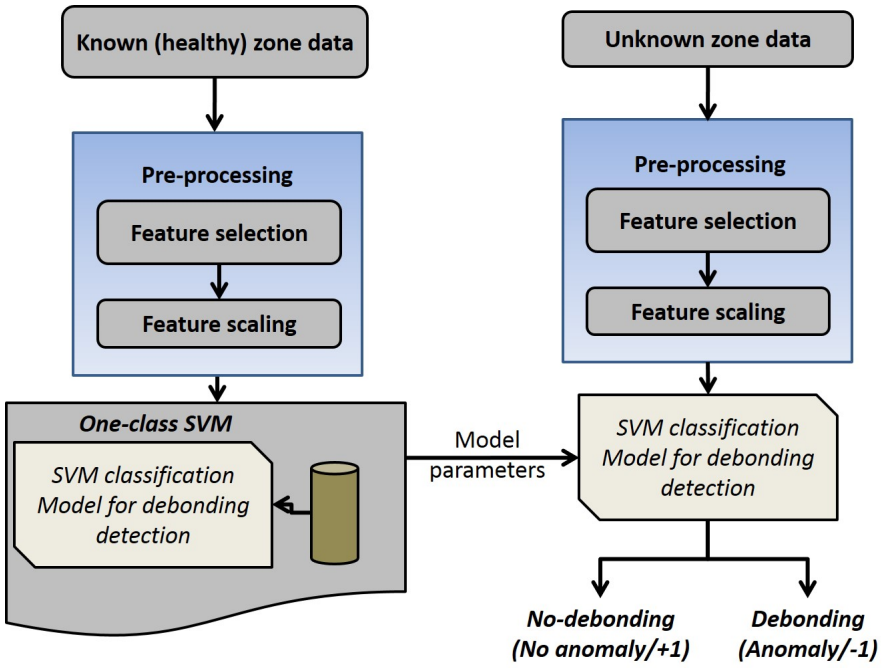

Figure 3.12: *Implementation of One-class SVM to detect a debonding as an anomaly*

Figure. 3.13 illustrates the application of OCSVM (using RBF kernel) to process the same noisy simulated A-scan data as in Figure. 3.10. The 20 initial non-debonding A-scans are used for the learning step. The remainder part of the B-scan is assumed to be the unknown data that comprise both debonding and non-debonding A-scans. Compared to the two-class SVM results in Figure. 3.10, OCSVM provides some false detection (false alarm) for all cases and misses some true debonding (false negative) rate for the intermediate interlayer permittivity (Figure. 3.13(b)).

3.4 Non-Parameterized Supervised learning: Random Forests

3.4.1 Background

Decision trees are a class of non-parameterized supervised machine learning methods. They are widely used due to their high execution speed and low complexity [184]. By definition, decision trees are a map (or branching) of all possible outcomes for a set of data.

Initially, the decision tree starts at one node and branches into a set of possible outcomes [185, 186, 187]. Each outcome further leads to additional nodes until there is no longer a possibility of branching (or the user-defined limit is reached).

Over the past two decades, there have been numerous methods studied under decision trees. One of the well known type are the Classification and regression trees (CART) which include the Random forests. Random Forests (RF) was first proposed by Tin Kam Ho [121] in 1995. It is a supervised machine learning algorithm that works on classification and regression by branching the data into nodes and possible outcomes (decisions). Due to its versatility, RF has been used in several applications including: image segmentation and classification [188, 189, 190], disease identification [11, 191, 192, 193], facial classifcation [194], crack detection in concrete structures [195, 196], text categorization [197], pavement crack detection [198] and numerous other applications. Most recently, we have also used RF to detect debondings [166]. Although RF seems to be underused for binary 1D signal classification in our application, due to its advantages (listed in Table. 3.6), this method was studied during the thesis.

Random Forests gain their strength from the combination of a large number of individual possibly weak models. Since the models are generated by a random process, with random selection of data and partially random selection of predictors, we can be sure of an adequate supply of substantially different decision trees. These substantially different trees are then combined through a voting process. Figure. 3.14 shows the RF approach.

3.4.2 Principle

Before diving into RF, we present two terms widely used with RF namely, Bootstrapping and Bagging. Bootstrapping is an approach of drawing subsets at random from a larger dataset. It is mainly used to estimate 'how good' the parameters perform in order to control the complexity of the method. In actuality, bootstrapping is an alternative to cross-validation technique implemented by other machine learning methods (such as SVM, One-class SVM *etc.*). Bagging, on the other hand, is the combination of several estimators/trees obtained after the bootstrapping process.

The main difference between RF and the previous methods is that they are intended to design and apply good standalone models. Random Forests, on the other hand, is different in that aspect as it introduces an entirely new way of generating individual component models by combining several weaker standalone models (or trees) to perform together

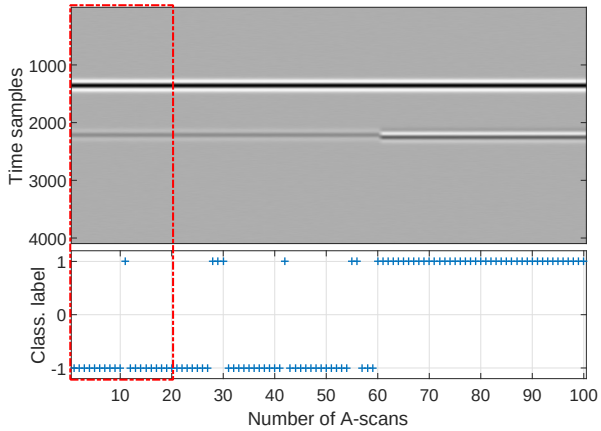

(a) Config. 1: B-scan with $t_{deb} = 0.3\,\text{cm}$ and $\varepsilon_{r,deb} = 2$

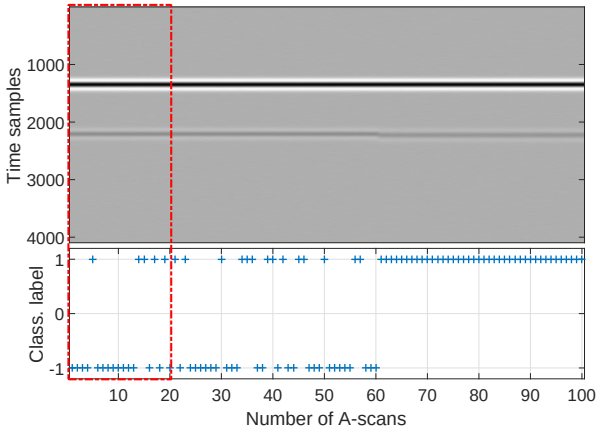

(b) Config. 2: B-scan with $t_{deb} = 0.3\,\text{cm}$ and $\varepsilon_{r,deb} = 6$

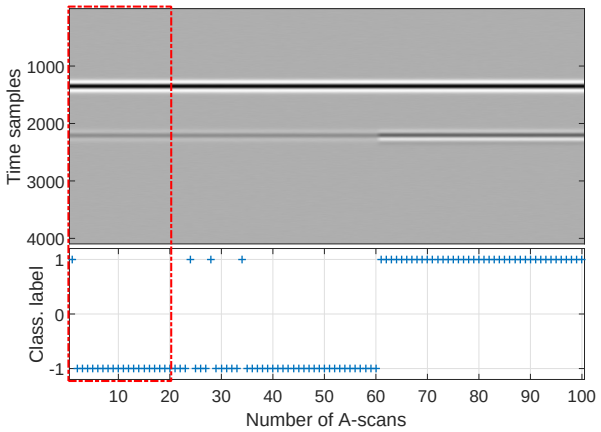

(c) Config. 3: B-scan with $t_{deb} = 0.3\,\text{cm}$ and $\varepsilon_{r,deb} = 10$

Figure 3.13: *OC-SVM applied on simulated noisy raw A-scan data (see Appendix. A) for the detection of debondings. Permittivities of top and base layers are respectively* $\varepsilon_{r1} = 5$ *and* $\varepsilon_{r2} = 7$, $f_c = 4.2\,\text{GHz}$, $SNR = 20\,\text{dB}$. *The blue dashed box indicates the learning data set. The dashed box indicates the learning database*

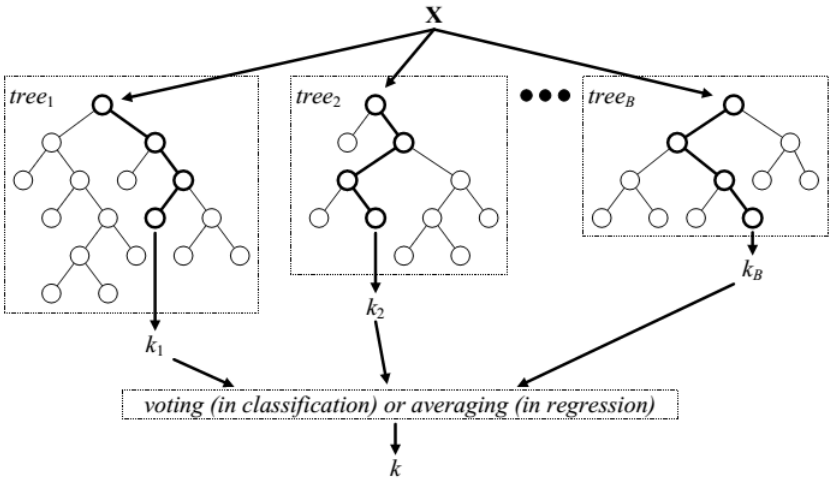

Figure 3.14: *Random Forests voting approach for classification and regression problems [11]*

effectively to obtain better results. Random forests uses various performance metrics to perform the classification of data into different nodes. We have, for example: Information gain, Entropy, Gini Impurity or Gini Index (GI) and Variance reduction.

The Gini impurity or Gini Index (GI) is one the most commonly used metric for classification in RF. It refers to the probability of 'dissimilarity' between two elements that are chosen at random from a given dataset. In other words, GI is the sum of probabilities of an item 'i' being chosen multiplied by the sum of the probabilities of the same item 'i' being misclassified.

Let $\mathbf{X}$ be a 2D B-scan matrix of size $M \times N$, where M is the number of data points (or number of features) and N is the number of A-scans. The GI is computed as follows. Initially, the data is split into learning ($\mathbf{X}_L$) and testing data ($\mathbf{X}_T$). the training data is bootstrapped into subsets such that each subset is disjoint (*i.e.* do not contain the same data-points or features). An example is as shown in Figure. 3.15.

In general, the GI for a K-class classification is given by []:

$$GI = \sum_{i=1}^{K} p_i(1 - p_i) \tag{3.34}$$

where,

- K is the number of classes in which the data is to be classified
- p_i is the probability of belongingness to class i computed using all the data points (or features) randomly chosen from respective subset

Once the split is carried out, a single node can be visualized as shown in Figure. 3.16.

After the split, the question now arises if the node can further be split or, it is a leaf. A leaf is defined as the terminal node which cannot be further split.

To verify this, the node is initially split and the GI is once again computed at both nodes using Equation. 3.34. If the GI after the split is less than the GI before the split, the

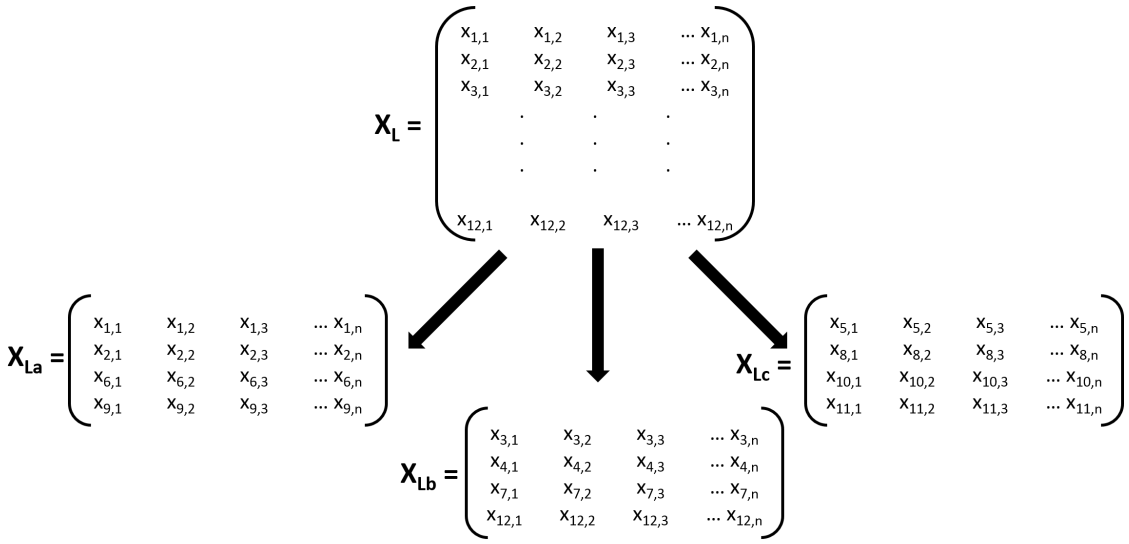

Figure 3.15: *Example of randomly splitting the data into three subsets.* $\boldsymbol{X}_L$ *is the learning data set;* $\boldsymbol{X}_L a$, $\boldsymbol{X}_L b$ *and* $\boldsymbol{X}_L c$ *represent one possibility of bootstrapped data*

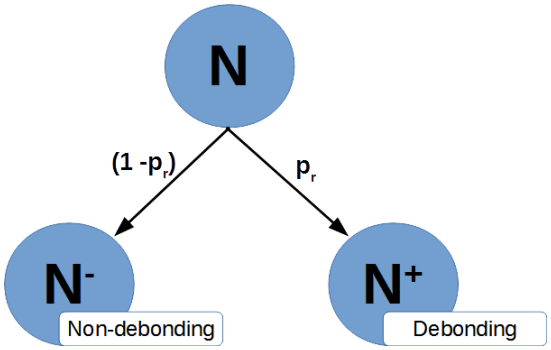

Figure 3.16: *Node splitting at a specific node N based on Gini impurity index*

node-splitting is retained; otherwise, it is rejected and the specific node is now considered as a leaf (further splitting not possible). This is one tree. The process is repeated for T trees with each tree having the same number of subsets obtained randomly. After obtaining all the trees in the forest, the forest would resemble somewhat as shown earlier in Figure. 3.14.

The test data is then validated using each of the decision trees. In case of classification, Majority voting (or sometimes called majority ranking [197]) is used. Here, the highest number of 'decisions' are considered to be the final result.

3.4.3 Application to binary classification for debonding detection

In case of binary classification to classify the data as debonding or a non-debonding, implies that $K = 2$. Thus Equation. 3.34 can be simplified to get []:

$$GI_{(s,N)} = 1 - \{p_{deb}^2 + p_{ndeb}^2\} \tag{3.35}$$

where, for a particular node,

- p_{deb} is the probability of belongingness to class debonding given by $\frac{TP}{(TP+TN)}$
- p_{ndeb} is the probability of belongingness to class non-debonding given by $\frac{TN}{(TP+TN)}$

Initially, a bootstrap learning data set sampled from $\mathbf{X}$ with replacement [199, 200], and containing p random data samples ($p \leq m$) each with n instances (A-scans) are generated. Although RF trees can work with even one data point, as described in the literature by Breiman et al. [201], the optimal data size for each subset is $p \times n$ where $p = \sqrt{m}$. The number of trees we thus obtain are $T \approx \frac{m}{p}$. The GI is computed then for each subset as a whole using Equation. 3.35 and the split is obtained.

Iteratively, the GI is computed for each node until either no further splitting is possible, or, the GI of the node before split is less than the GI of the individual nodes after the split. The process is then repeated for T trees and majority voting is used to 'decide' the presence or absence of debondings. Figure. 3.17 illustrates an example of a forest. The nodes marked in green represent the 'leaves'.

The initial step of RF implementation are similar to the SVM. The B-scan data (either raw or feature set) is divided into learning and test data sets. The learning data set is used to generate individual trees (and subsequently, a forest). As mentioned earlier, the number of trees is a function of the number of A-scan vectors (or features).

However, as mentioned in [200], there is no such limit on the number of trees; however, by increasing the number of trees, we subsequently increase the computational time. As mentioned in [200, 202], the optimal number if trees in the forest can be between 64 to 128. Thus, in case of raw GPR data, we follow this approach and use $T = 100$ trees with each tree having the same number of observation samples. The value for the subset size (p) is fixed as mentioned before.

Figure. 3.18 presents an illustration of the implementation of RF.

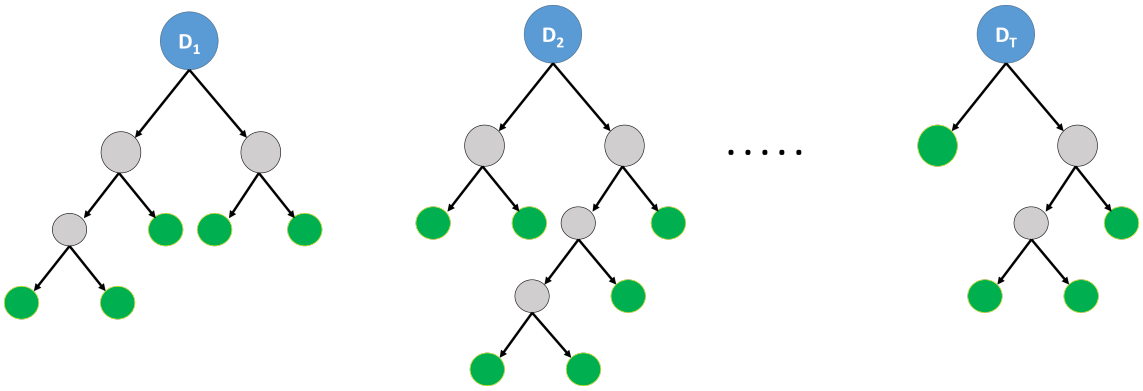

Figure 3.17: *Illustration of a forest with T trees. The final nodes marked in green represent the 'leaves' (i.e. no further splitting possible)*

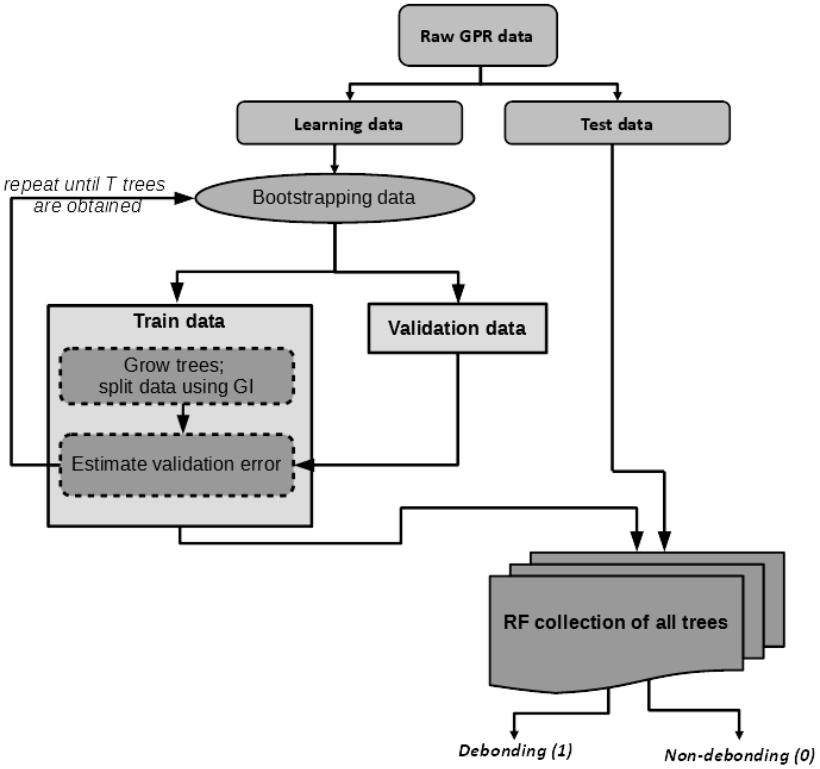

Figure 3.18: *Random Forests implementation for the detection of debondings using raw GPR data*

Figure. 3.19 illustrates the application of RF to process the same noisy simulated A-scan data as in Figure. 3.10 and Figure. 3.13. Here, the ratio between learning and testing data is 1:1 with 4096 time samples in each A-scan. The number of data points in each subset $p = \sqrt{4096} = 64$. The number of trees is fixed to $T = 100$, as mentioned earlier (the data is bootstrapped with repetitions).

By observing the performance for raw GPR data, we see that RF provided equivalent results compared to the binary SVM results in Figure. 3.10. It is observed that RF is capable of identifying debondings of various interlayer permittivities ($\varepsilon_{r,deb} = 2, 6, 10$).

In the following chapters, the performance of RF will be tested on experimental data collected at various test sites.

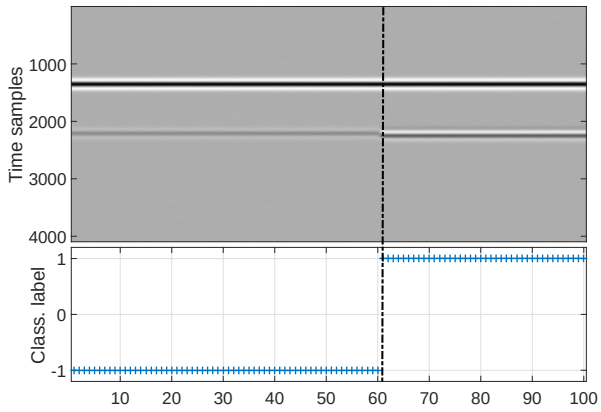

(a) Config. 1: B-scan with $t_{deb} = 0.3\,\text{cm}$ and $\varepsilon_{r,deb} = 2$

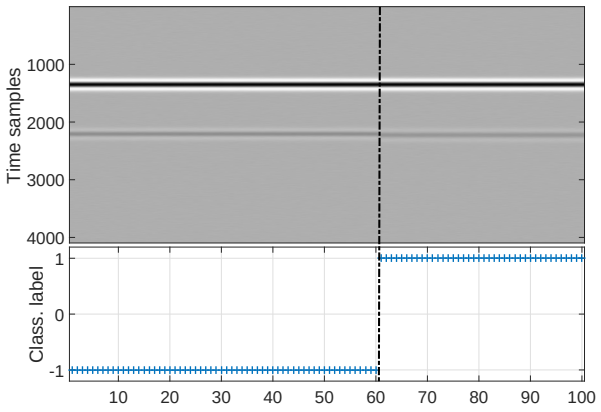

(b) Config. 2: B-scan with $t_{deb} = 0.3\,\text{cm}$ and $\varepsilon_{r,deb} = 6$

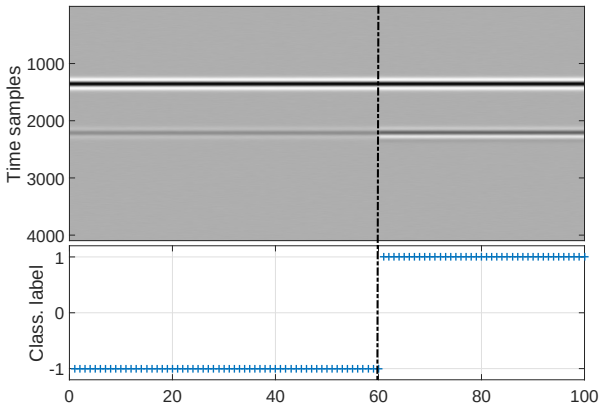

(c) Config. 3: B-scan with $t_{deb} = 0.3\,\text{cm}$ and $\varepsilon_{r,deb} = 10$

Figure 3.19: *RF applied on simulated noisy raw A-scan data (see Appendix. A) for the detection of debondings. Permittivities of top and base layers are respectively* $\varepsilon_{r1} = 5$ *and* $\varepsilon_{r2} = 7$, $f_c = 4.2\,\text{GHz}$, $SNR = 20\,\text{dB}$

3.5 Decision making: Probabilistic estimates

The previous section presented the classification of GPR B-scans into two classes, namely, debonding and non-debonding as binary indicators. While the binary classification

methods can be used to provide a discrete label, by means of probability estimations, it is possible to predict outputs that are continuous. In other words, the prediction is made in terms of quantity rather than being confined to a specific set of labels.

3.5.1 Introduction

Probabilistic estimation is quite interesting as it has quite some advantages. Firstly, many machine learning models are designed with the probabilistic framework. For e.g., Random forests are primarily used for regression problems via probability estimations as mentioned in Chapter. 3.4. Additionally, probability estimations can be used to simplify the machine learning model. By providing a flexible range of values rather that rigid (*i.e*, between 0 and 1 rather than 0 or 1 for example), the model is free to take ambiguous data into consideration. This could also help the model to reduce the amount of outliers.

Finally, one of the most interesting characteristic of probabilistic estimation is that they act as a measure of their own assessment. For e.g., suppose, for an A-scan, the model predicts a debonding with probability of 0.2. This means that this prediction is only 20% accurate, thereby indicating that the error rate for the A-scan is 0.8. Therefore, by using probabilities, the operator can express the decisions at various confidence levels, in contrast to binary values 0 and 1 (or +1 and -1) as done by classical classification techniques.

All the three machine learning methods studied in this thesis have been used for probabilistic estimation; as in, Two-class SVM [203, 204, 205, 206, 207], Random Forests [208, 209, 210, 211, 212, 213] and One-class SVM [214, 215, 216].

3.5.2 Probabilistic estimation for SVMs: Platt scaling

Probability estimation using SVM has been implemented for multi-class classification [207], in medicine for leukaemia data [217], risk prediction of rheumatoid arthritis [218] *etc.* Since standard SVMs do not provide probabilistic estimates, it can be achieved by simply mapping the outputs of a single SVM into posterior probabilities [219]. These estimations for SVMs can be achieved in two ways: by using regression, proposed by Drucker et al. [220] or Platt scaling (similar to logistic regression) introduced by John C. Platt [221, 219].

In case of SVMs for binary classification, one of the commonly used approach for estimating the probability is Platt scaling. Another approach is the Isotonic regression as presented in [222]. However, as mentioned in [222], a learning curve analysis showed that Isotonic regression is more prone to over-fitting than Platt scaling and therefore, has a lower performance. Thus, in the thesis, we implement the probability estimation using Platt scaling. The Platt scaling is implemented for both Two-class and One-class SVMs.

In general terms, Platt scaling can be defined as an approach used to transform the binary outputs of a machine learning classification model into a distribution of probability values. Platt scaling assumes that the posterior probability of the debonding class given the classification scores takes form of a sigmoidal function [223]. Platt scaling for SVMs was first introduced in [221].

As studied in [217, 218, 224, 225], supervised learning using SVM have also been proven to provide consistent probability estimates.

Principle

In case of pavement monitoring, the probabilities can be estimated in two ways, *i.e,* probability of occurrence of debondings (P_{deb}) or probability of occurrence of non-debondings (P_{ndeb}). It should be noted that, for any A-scan, $P_{deb} + P_{ndeb} = 1$. As the focus is to predict debondings, we focus on the former *i.e*, debonding probability.

In order to calculate the '*probability of occurrence of debondings*' (denoted by $P(y = 1|f)$ or P_{deb}), the estimation is given using Platt scaling as [221, 222]:

$$P_{deb} = P_i(y = 1|f) = \frac{1}{1 + exp\{A.f + B\}} \tag{3.36}$$

where,

- P_{deb} is the probability of occurrence of debonding (*i.e*, $y = 1$)
- f is the signed distance from the optimal hyperplane $\mathcal{H}$
- A and B are two values that are determined during the learning step

The parameters A and B from Equation. 3.36 are computed by maximum likelihood estimation from the learning data set (f_i, y_i); where y_i is the classification label ($\in \{-1, +1\}$) for the ith A-scan vector and f_i is its signed distance from the optimal hyperplane $\mathcal{H}$ [221].

In case of binary classification using labels $y_i = \{-1, +1\}$, an intermediate value t_i (called target probability) is introduced in [221] such that:

$$t_i = \frac{y_i + 1}{2}$$

This transforms the binary labels from $y = \{-1, +1\}$ to $t = \{0, +1\}$. Now, the parameters A and B can be determined as follows [221, 222]:

$$\arg\min_{A,B} \left\{ -\sum_i t_i log(p_i) + (1 - t_i) log(1 - p_i) \right\} \tag{3.37}$$

where,

$$p_i = \frac{1}{1 + exp\{A.f_i + B\}}$$

NOTE: In cases where the classification label used are positive, *i.e,* $y = \{0, +1\}$, t_i in Equation. 3.37 can be replaced by y_i (as presented in [222]).

However, over-fitting/over-learning may very well be encountered in Platt scaling as well. As mentioned in [221], complex learning models can introduce unwanted bias leading to poor results. This is overcome by splitting the data into training and validation sets (as done for the conventional binary SVMs). As [222] mentions, k-fold CV is a better technique than Holdout CV to determine A and B parameters. CV is used to calibrate the model in the learning step as demonstrated in [222]. The optimized parameters are then used on test data. These optimization techniques are presented in detail in Chapter. 5.

3.5.3 Probabilistic estimation for Random forests

Probability estimation using regression Random forests has been extensively used in several applications, such as, in sports to predict outcomes to estimate win probability [226], prediction of shot effectiveness in golf [11], in medicine to predict anti-cancer drug sensitivity [209], to predict receipt of transfusion [227], for non-elective re-hospitalization and post-discharge mortality [228], in vehicle safety [212] and numerous other applications. In fact, Random forests using regression for probability estimations were found to be appropriate in terms of performance according to the studies conducted in [229, 224, 230]. Thus, regression Random forests was studied in this thesis to estimate the probable occurrence of debondings.

Probabilistic Random forests are implemented as presented in Chapter. 3.4, Figure. 3.14 and Figure. 3.17, the forest is constructed during the learning stage with L trees. The final step however in case of probability estimation is different from that of classification. While classification uses the concept of 'majority voting' (see Chapter. 3.4), the probability estimation replaces this by averaging the votes for regression [11]. The procedure is hereafter explained.

Principle

As done previously in case of SVM, the probabilities using Random forests can be estimated in two ways as well, namely P_{deb} and P_{ndeb}.

Consider a classification forest of T trees. During the learning step the split is performed at each node using the Mean Prediction Squared Error (MPSE) metric (in contrast to Gini index used earlier). This is because, as mentioned in [231], the metrics presented in Chapter.3.4.2 are used for classification while PSE is used for regression trees.

The probability of occurrence of a debonding at the ith A-scan is given by:

$$P_{deb,i} = \frac{1}{T}\sum_{j=1}^{T}\left\{\frac{1}{N}\sum_{k=1}^{N} card(f_k(deb))\right\} \tag{3.38}$$

- $f_k(deb)$ is the proportion of 1's in each terminal node
- N is the total number of terminal nodes in the tree T_j
- T is the total number of trees in the forest

The probability estimation procedure using Random forests is summarized in Algorithm. 1 of [229].

In Chapter. 6, we present the estimation of debondings in two sets of experimental data using the various feature sets, namely, local and global features (presented later in Chapter. 4), and compare the results with the benchmark obtained using raw GPR data.

3.6 Synthesis

We finally present a concise list of the family of ML methods presented in this chapter. As presented in Table. 3.6, each of the ML methods possess their own advantages.

Table 3.1: *Synthesized comparison of the ML methods*

Category	Two-class SVM	One-class SVM	Random Forests
1. Learning data type	Uses both debonding and non-debonding data	Only one type of learning data (*i.e*, non-debonding [232] is used	Uses both debonding and non-debonding data
2. Learning data size	Requires a large learning data set (at least 50% of the total data) []	OC-SVM does not require a large number of training samples to create a classification model and as such, it has a simple geometric representation with very few parameters to determine the classification model [233]	Repeated testing in RF (at various 'trees') helps to perform well even using a small learning sample set
3. Kernel functions	The use of kernels provide the user an opportunity to build a classification model by engineering each kernel depending on the requirement	OCSVM, as a special case of SVM also implements kernel functions to improve the performance if possible	RF implements a set of various performance metrics but not kernel functions. However, it can be modified to become a kernel function for other ML methods [234, 235]
4. Over-fitting	Is prone to over-fitting; however the use of regularization parameter helps the user to avoid over-fitting	Is prone to over-fitting; can be avoided using regularization parameter	Growing a large number of RF trees does not create a risk of over-fitting since each tree is a completely independent random experiment [236, 237, 238]
5. Outliers in learning data	Slack variable (ξ) is used to control the sensitivity to outliers	Uses a user-designed parameter (ν) to determine the amount of admitted slack thereby controlling its sensitivity to outliers	RF are resistant to outliers in the learning data [238, 239]

Table 3.1: *Synthesized comparison of the ML methods*

Category	Two-class SVM	One-class SVM	Random Forests
6. Cross validation	Uses CV techniques to avoid overfitting and computation of optimal hyper-parameters	Uses CV techniques to avoid overfitting and computation of optimal hyper-parameters	Self testing is based on an extension of cross validation that is repeated several times. This provides highly reliable assessments of the reliability of the RF model [237]
7. Decision making	Uses the two-class classification model to predict the presence or absence of debondings (single prediction step)	Uses the learning data as reference (single prediction step)	Identifies the best predictor automatically through the process of voting [236] (several repetitions)
8. Computational Speed	Learning step is relatively slower; however it can be sped up using feature selection	Due to its simplistic modeling, OCSVM performs relatively faster learning and testing [240]	Trees are grown at high speed because few variables are in use at any one time [237].
9. Accuracy	SVM presents high accuracy by means of regularization and the use of proper kernels, the learning step generates a more robust result	OCSVM has a high accuracy provided that the hyper-parameters chosen are optimal	RF models are often considerably more accurate than a single decision tree. The accuracy achieved is often competitive with the best alternative methods [236, 237]
10. Estimation of probability	Both two-class and One-class SVMs can be used to estimate probability using Platt scaling		RF has a built-in regression that can be used for probability estimation [11]

3.7 Conclusions

In this chapter we introduced four Machine Learning methods to detect the debondings within pavement structures, namely, Random forests, SVM for binary classification (Two-class SVM) and outlier detection (One-class SVM) and k-means clustering technique. They have been categorized into supervised and unsupervised techniques, respectively.

The principle of each method is illustrated through the straightforward processing of time data as a whole (*i.e* raw GPR data). The four methods were applied to process noisy simulated analytic data with simplified assumptions, which are presented in Appendix. A. The methods demonstrated good qualitative results as they were able to detect debondings with various interlayer permittivities.

Due to the limitations of binary SVM, the anomaly detection method, One-class SVM was then presented to demonstrate a ML method that is closer to the operational level measurement and detection. Finally, the third ML method, Random forests method was studied. This method, although underused (as opposed to its real capability), its advantages made it interesting to compare with other supervised machine learning methods.

The conventional binary SVM presented very high debonding detection rate for all noisy simulated data configurations. However, the need for both debonding and non-debonding data to be present in the learning data limits its implementation at an operational level.

Despite its advantages of being close to the operational level, OCSVM was seen to provide the lowest accuracy among the three methods with several false detection (in case of weak dielectric contrast *i.e.* $\varepsilon_{r,deb} = 6$).

Finally, in case of RF, it was observed that once again very high detection rate was observed for all cases.

In the final section of this chapter, we introduced the approach of probabilistic estimation of the occurrence of debondings using the supervised machine learning methods. Each method, with the help of certain post-processing of the GPR data presented the ability to provide a probability of debondings. This estimation will be explored in Chapter. 6 for experimental data.

The processing of raw data is not always acceptable since the raw GPR data may contain redundant information that could reduce the debonding detection rate. As stated by [143], the machine learning methods could be limited in their processing of raw data. In addition, large data size of the raw data can increase the computational time and complexity. To overcome this issue, certain preprocessing techniques can be done.

As observed in Section. 3.2, the unsupervised clustering method presented low detection rate using simulated data. Similar behavior was also observed on experimental SFR data, which was presented by us in [166]. Thus, the next chapter presents the various preprocessing and feature extraction techniques performed to aid the supervised learning learning methods used for debonding survey.

Chapter 4

Signal Feature Analysis For Debonding Survey

Contents

In the previous chapter, we presented the various data processing methods, supervised and unsupervised, that were used in the thesis to detect the presence of thin debondings within pavement structures. These machine learning methods were used in the context of detecting thin debondings within pavement structures. Qualitative results were presented for each ML method using simulated data generated from various models presented in Appendix A.2, Appendix A.3 and Appendix A.4. However these results were obtained using the raw GPR data (as shown in Chapter 3.3.1 for Two-class SVMs, Chapter 3.3.2 for One-class SVMs and Chapter 3.4.3 for Random forests). By using the raw GPR data, the computational complexity may increase leading to increased processing time. Moreover redundant data may either have no effect on the performance or may also reduce the detection rate of a method.

Thus, in order to improve the performance of a method and avoid the effects of redundant signal data, preprocessing of the data is necessary. This can include the data transformation (time to frequency domains and vice-versa) and feature selection/extraction [143]. In the latter case, either a part of the original data are taken, or, new signal characteristics (called features or attributes) are derived from the original data. Feature

extraction aims to remove irrelevant and redundant information leading to better performance [241]. [242] demonstrate that the performance of machine learning methods can be improved by the use of signal features.

In this chapter, we present the preprocessing step of GPR data feature selection techniques using simulated data. This approach has been also implemented in [10] for debonding detection from experimental data. Feature selection for SVM has been extensively used in the literature for multiple medical applications [243, 244, 245], data classification in data mining [246], facial recognition [247] handwriting character recognition [161], text categorization [248] *etc.* One-class SVM has been demonstrated to use feature selection for document classification [181], image segmentation [249] and also for audio detection and classification applications [250].

Signal feature selection can be performed on both spectral (frequency-domain) and temporal (time-domain) data. Temporal features of the signal are studied here as they are easy to implement and avoid complex preprocessing and computations (such as Fourier transformations, filtering *etc.*) [251]. In some cases, as in [252] for the study of EMG signals, the time-domain features even outperform the spectral features (such as PSD, mean power, mean frequency *etc.*) for supervised machine learning method (k-nearest neighbor).

In this chapter, signal feature extraction is performed on temporal data to obtain features globally (over the complete A-scan signal) as well as features localized at the pavement interface (*i.e.* only the second echo of the A-scan). Additionally, a feature reduction technique, namely Principal Component Analysis (PCA) is used. A parametric study will be done wherein the machine learning methods are analyzed *w.r.t* the input GPR data (in the form of raw GPR data, local signal features, global signal features and PCA reduced local and global signal features).

The motive behind the preprocessing is to study (a) adaptation the ML methods for various input data types, (b) reduce the processing data size and complexity, (c) avoid over-learning/over-fitting that may hinder the performance and improve the debonding detection rate.

4.1 Feature engineering

Most GPR data are very large containing thousands of time samples in each A-scan profile. From this huge data set, it is highly possible that a part of the data is redundant and presents negligible or no information at all. In the machine learning classification problems, the first step is then to perform data reduction by identifying and selecting the data subset that provides maximum information.

Feature engineering is the concept of using the known knowledge of the data to extract/select the signal features that can help to improve the performance of a machine learning method. It can be carried out manually based on the experienced understanding of the operator/user, or, automatically by means of certain well-known feature engineering techniques. On a broader scale, the feature engineering can be two-fold: feature selection and feature extraction.

Feature selection refers to the 'selecting' the signal features from a preexisting dataset/feature set. The features obtained by this approach can be either the raw data or, taken from a feature set collected previously using other approaches. Feature extraction on the other hand is the transformation of the raw data into suitable features that can be used for further processing. Obtaining such relevant information using feature selection or extraction can be useful to classify the data [253], which is expected for the GPR data to detect debondings as well.

As mentioned in [254], features should be able to distinguish between the two classes, efficient in computations, limited in number and also insensitive to the changes in the data. The advantages of using features is that they reduce the computational time, possible increase in the accuracy [255] and also avoid using redundant data [256].

Based on the type of GPR data, the signal features can be either from frequency domain data (*i.e*, spectral features) or time-domain data (*i.e*, temporal features). On the other hand, based on the zone-of-interest of the GPR signal, the signal features can be either global or local. Figure 4.1 presents one way of categorization of the signal features.

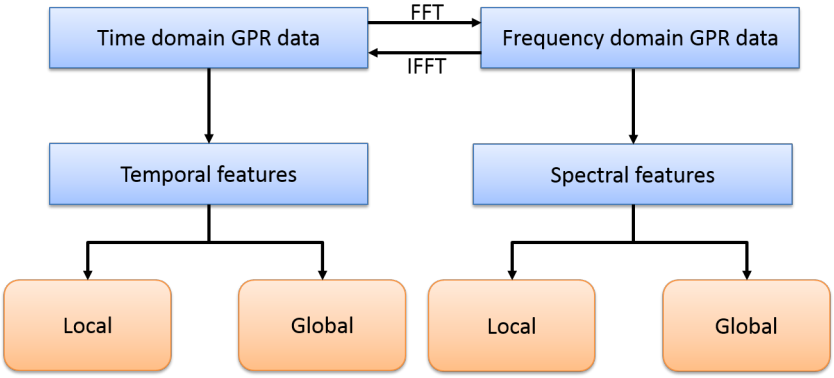

Figure 4.1: *Categorization of signal features*

4.2 Signal features for GPR data

The signal features can be chosen by automatic feature selection as presented in [257, 258, 259] by means of regularization. On the other hand, feature selection can also be done using a physical approach by analyzing a reference data set. In this section, we present the latter approach of feature selection.

Temporal features of the signal are selected here as they are easy to implement and require no transformation. Additionally, the temporal features are sub-categorized into local and global features. Local features are defined as the characteristics extracted from only the second echo of the raw GPR A-scan (*i.e.*, the useful echo from the interlayer pavement interface under survey).

Global features on the other hand are defined as the signal characteristics that are obtained from the complete raw GPR A-scan. Such features are advantageous as they are easier extract and require minimal preprocessing and *a priori* information, as opposed to

the local features. In case of GPR data, global features are usually dominated by the surface clutter and are therefore supposed to be less sensitive to the debonding. Whereas local features are expected to provide more sensitive information about the interface between the first two pavement layers and the debonding that may occur therein.

The two next subsections introduce both local and global temporal features of the signal which have been used for performing SVM classification. The feature selection presented later in Chapter 4.2.5 relies on the prior knowledge about the database (experimental or otherwise) under test.

4.2.1 Local signal features

Local features are expected to provide more sensitive information about the interlayer pavement conditions. They are defined as the signal characteristics of the original raw GPR A-scan over a short time window focused at the pavement interface, whose center and duration are computed using a known non-debonding A-scan as reference. Local features are obtained from this window focused at the second echo only. This approach has been presented in detail in Appendix D.

Figure 4.2 presents the automatic windowing of the second echo used to extract local signal features for simulated data. The same approach is used for experimental data. Figure D.2, Figure D.3 and Figure D.4 respectively present the B-scans before and after the automatic time-gating for experimental SFR data (Appendix D) for Geotextile, Tack-free and Sand-based defects.

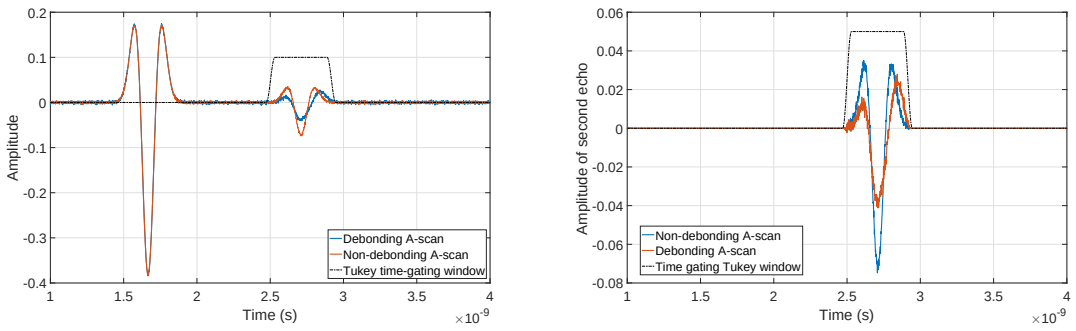

(a) Complete debonding and non-debonding A-scans

(b) Time-gated second echo

Figure 4.2: *Automatic time-gating of the second echo used to extract local signal features (simulated analytic Fresnel data;* $\varepsilon_{r,deb} = 6$, $SNR = 30\,\mathrm{dB}$, $\varepsilon_{r,deb} = 6$, $t_{deb} = 0.3\,\mathrm{cm}$*)*

As presented earlier in Chapter 2, the presence of a debonding layer alters the form of the received signal. This alteration of the signal form is expected to differentiate between the debonding and non-debonding cases. A GPR database is used to analyze the various feature sets that can aid the data processing methods to detect debondings. The probability density functions (PDFs) are then traced for debonding and non-debonding cases for each signal feature. The separation of the distributions is used to decide if the signal feature can be used. The PDFs are displayed after a curve-smoothing technique with moving average is applied to the distributions. We broadly categorize the features

into three subsets: Statistical, Morphological and PQRST features.

The first feature subset, namely statistical feature set, refers to statistical characteristics of the time-gated GPR A-scan. These features have been used in the literature for the detection of abnormal mammograms [260], character recognition [261] and classify external stimuli [262]. As in [263, 264, 265], local statistical features used here are: Standard deviation, Mean absolute deviation (MAD), Kurtosis and Skewness. Standard deviation is the amount of dispersion of the data of the mean. Skewness is the measure of asymmetry while kurtosis measures the 'peakedness' of the given data [266]. We have also used these local features in [10] to detect debondings using SVM.

Figure 4.3 presents the local statistical signal features (*i.e.* for the second echo only). It

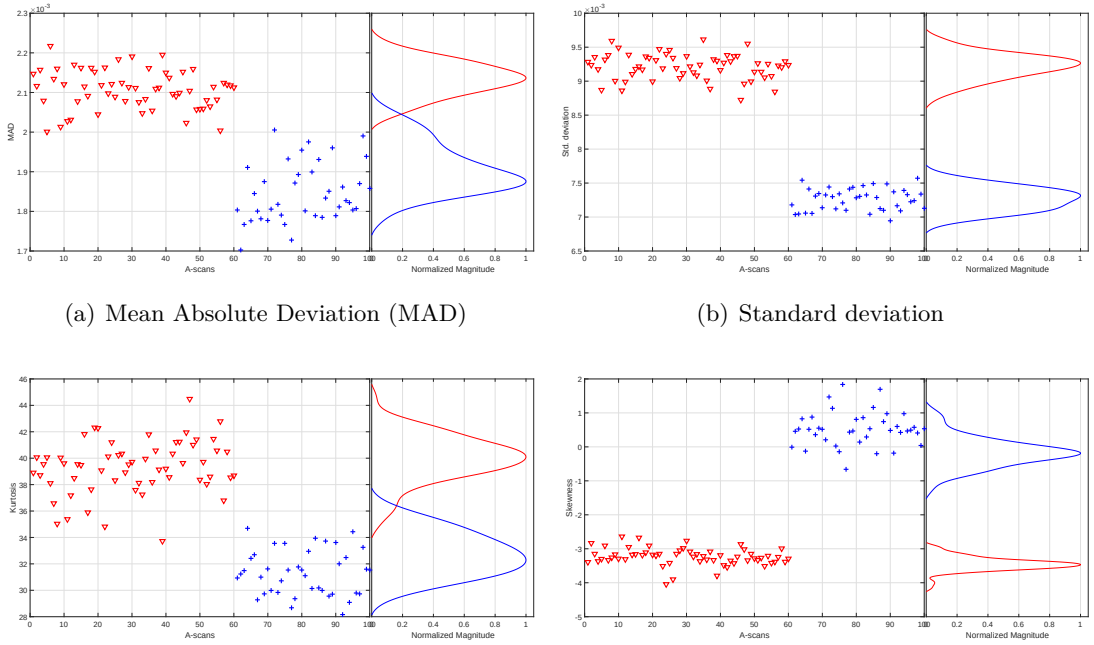

(a) Mean Absolute Deviation (MAD)

(b) Standard deviation

(c) Kurtosis

(d) Skewness

Figure 4.3: *Representation of local statistical features for simulated data (computed from analytic Fresnel data model (Appendix A.2) with added noise ($SNR = 30\,\mathrm{dB}$, $\varepsilon_{r,deb} = 6$, $t_{deb} = 0.3\,\mathrm{cm}$). '$\nabla$' (red) indicate debonding and '+' (blue) indicate non-debonding values*

should be noted that the signal features that do not present sufficient PDF separation are not used. For *e.g*, as mentioned in [10], the mean of a GPR A-scan was found to be centred at zero. As such, the two distributions for debonding and non-debonding cases using mean as the signal feature present very little separation. Additionally, other statistical features such as entropy [260], median [267] were observed to provide any significant PDF separation. Therefore such features are not considered. As illustrations, Figure 4.4 presents the distributions for the rejected statistical features of mean and median.

The second feature subset is named PQRST features. Specific Electrocardiography (ECG) signal features have been used due to the similarity in shape between the GPR A-scan and an ECG signal, namely the PQRST features discussed in [268, 269]. The PQRST signal is the basic pattern of electrical activity (or one cycle) of the heart [270].

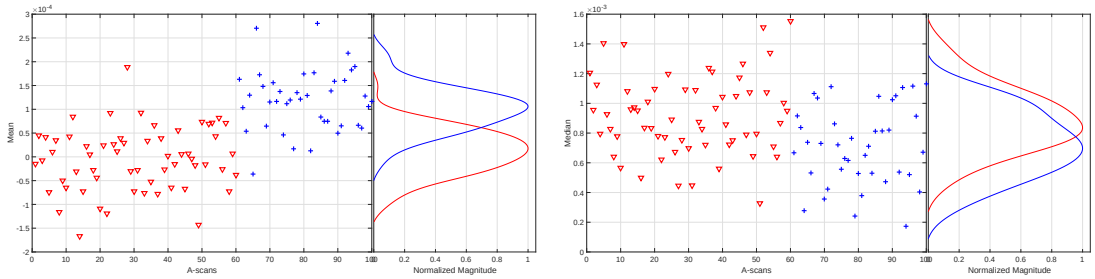

(a) Mean (b) Median

Figure 4.4: *Representation of inseparable unused local statistical features for simulated data (computed from analytic Fresnel data model (Appendix A.2) with added noise ($SNR = 30\,\mathrm{dB}$, $\varepsilon_{r,deb} = 6$, $t_{deb} = 0.3\,\mathrm{cm}$). Due to the faint separation, these features are not used*

Its patterns (shape and/or form) are seen to closely resemble the reflected signal at each interface of the pavement structure (for comparison, see Figure 1 in [271]).

In our application, we propose to assign the points P and T to respectively the first and the last breaks of the second echo while the points Q, R and S respectively represent the first, second and third alterations of the signal. Figure 4.5 shows the PQRST data-points in a GPR signal for debonding and non-debonding for the second echo. The PQRST

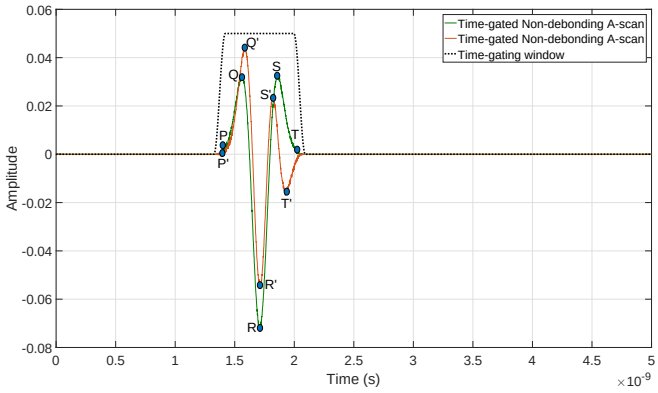

Figure 4.5: *PQRST data-points of time-gated debonding and non-debonding A-scans from simulated data (analytic Fresnel data)*

features were chosen once again on the PDF separation as done for statistical features. Figure 4.6 presents the distributions of the various PQRST feature sets.

Figure 4.7 presents the amplitude at point 'Q' and slope QR from the PQRST features. The PDF for amplitude at point 'Q' does not present a good separation; while that of slope QR is a bimodal PDF as opposed to our assumptions (*i.e*, normal distribution).

The last subset of local features are the Morphological features. These features are related to the 'form' and 'shape' of the GPR signal. The constructive interference of the reflections within the debonding layer results in an observable increase (or decrease depending on the contrast in permittivities) in the characteristics of the second reflection such as amplitude range. As seen in Figure 4.2 the difference between the second echoes of

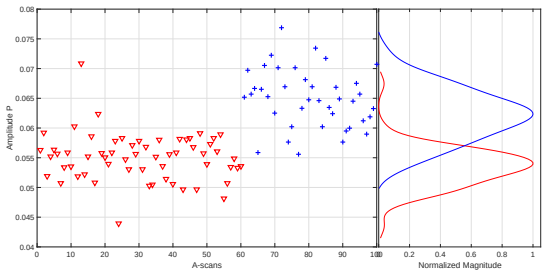

(a) Amplitude at point ‘P’

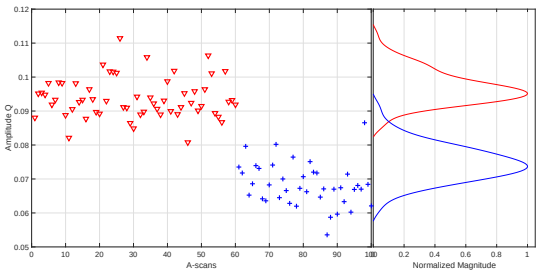

(b) Amplitude at point ‘Q’

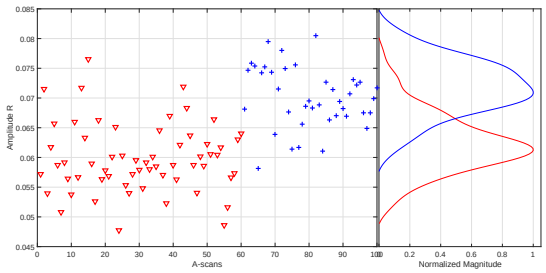

(c) Amplitude at point ‘R’

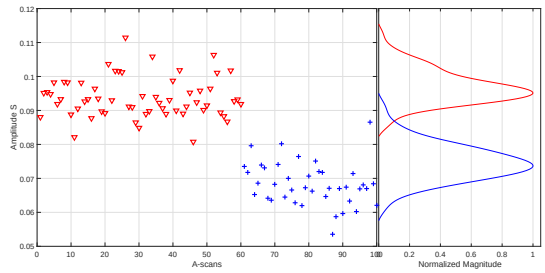

(d) Amplitude at point ‘S’

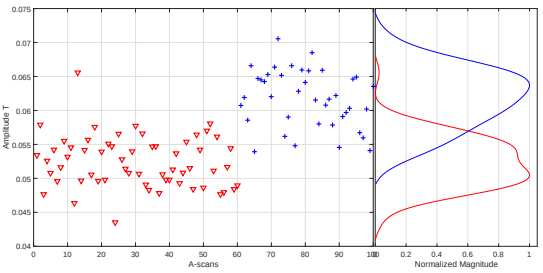

(e) Amplitude at point ‘T’

Figure 4.6: *Representation of local PQRST features for simulated data (computed from analytic Fresnel data model (Appendix A.2) with added noise ($SNR = 30\,\mathrm{dB}$, $\varepsilon_{r,deb} = 6$, $t_{deb} = 0.3\,\mathrm{cm}$). ‘$\nabla$’ (red) indicate debonding and ‘+’ (blue) indicate non-debonding values*

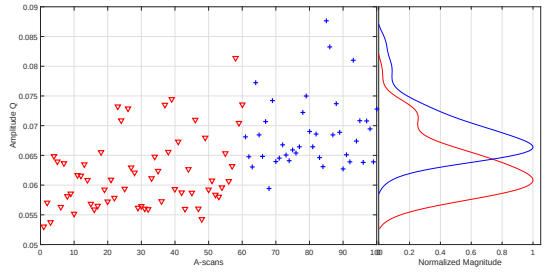

(a) Amplitude at point ‘Q’

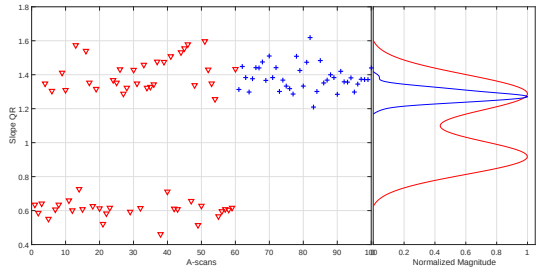

(b) Slope QR

Figure 4.7: *Representation of inseparable unused local PQRST features for simulated data (computed from analytic Fresnel data model (Appendix A.2) with added noise ($SNR = 30\,\mathrm{dB}$). ‘∇’ (red) indicate debonding and ‘+’ (blue) indicate non-debonding values*

debonding and non-debonding cases can be considered to be used as signal feature. Thus, amplitude range and magnitude of the second echo are used as local features. Additionally, the root-mean square (RMS) and inter-quartile range (as in [272]) of the debonding and non-debonding A-scans have been observed to present a significant PDF separation, thereby considered as usable local features. For representation, Figure 4.8 presents the distributions for the usable morphological features.

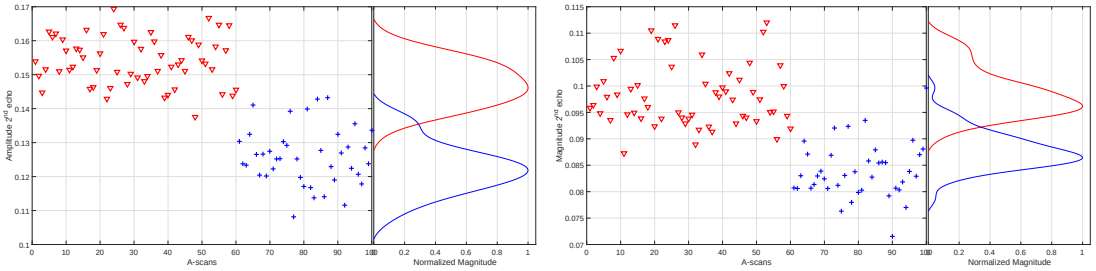

(a) Amplitude range of second echo

(b) Magnitude of second echo

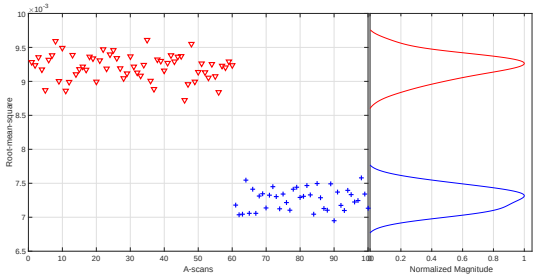

(c) Root-mean square

Figure 4.8: *Representation of local morphological features for simulated data (computed from analytic Fresnel data model (Appendix A.2) with added noise ($SNR = 30\,\mathrm{dB}$, $\varepsilon_{r,deb} = 6$, $t_{deb} = 0.3\,\mathrm{cm}$). '$\nabla$' (red) indicate debonding and '+' (blue) indicate non-debonding values*

4.2.2 Global signal features

Contrary to the local features, the Global signal features are defined as the signal characteristics that are obtained from the raw GPR A-scan. In case of experimental data, the raw GPR data is described as the data after the elimination of clutter, namely the straightforward direct antenna-coupling. These features are relatively easier to extract compared to the local features as they use the raw GPR scans. Additionally, these features do not require any information *a priori* as is the case for local features.

As done for local features, the global features are categorized into two groups, Statistical and Morphological features holding the same definition as for local features.

Each statistical feature was computed for the "raw GPR B-scan". By observing the separation of the PDFs for each feature (debonding *vs.* non-debonding), the best features were chosen. Figure 4.9 presents the usable global statistical features that showed well-separated distributions.

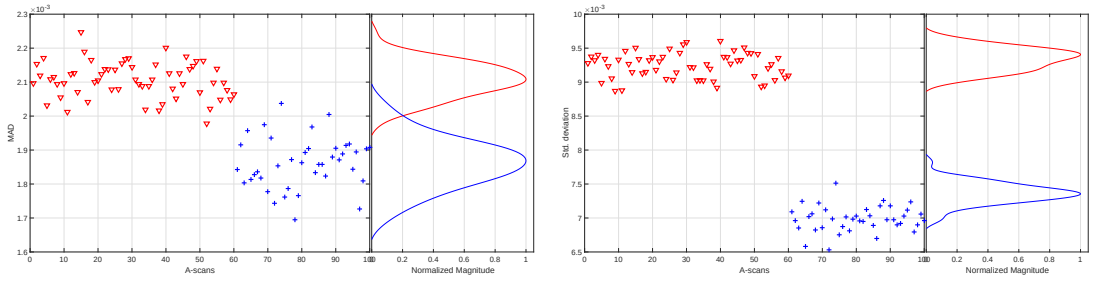

(a) Mean Absolute Deviation (MAD)

(b) Standard deviation

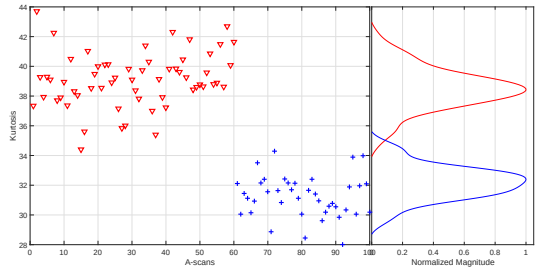

(c) Kurtosis

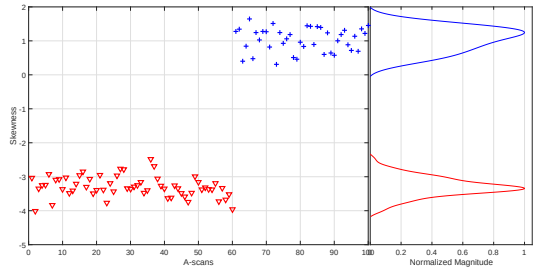

(d) Skewness

Figure 4.9: *Representation of global statistical features for simulated data (computed from analytic Fresnel data model (Appendix A.2) with added noise ($SNR = 30\,\text{dB}$, $\varepsilon_{r,deb} = 6$, $t_{deb} = 0.3\,\text{cm}$). '∇' (red) indicate debonding and '+' (blue) indicate non-debonding values*

The PQRST features are not used in the computation of global features since they are specific to the second echo. In case of morphological features, the RMS and IQR are the two features that were suggested. In addition, a new global feature, namely, Interface Time-Delay (ITD) is introduced. Due to the presence of an additional (debonding) layer in case of a defective pavement, the second echo is an attenuated composite signal usually shifted in time (*w.r.t* the surface echo). ITD is thus defined as the time delay between the maximum magnitudes of the first (surface) echo and the second echo. Figure 4.10 presents the global morphological features that showed well-separated distributions.

4.2.3 Comparison of Local and Global feature sets

Although the signal features chosen in the previous section (local and global) presented 'good' PDF separation; it is necessary to compare the respective features obtained globally and locally. This is done to observe the 'overall goodness of separation'. Since, the rate of classification strongly depends on the separation of the signal features in the feature-space, it is necessary to analyze 'how well are' the chosen signal features separated *w.r.t* each other.

As mentioned in Section 4.2.1, the local features are more accurate than global features (due to their localization at the pavement interface). Thus, they are expected to provide a much better separation compared to their respective global counterparts. For illustration, Figure 4.11(a), Figure 4.11(b), Figure 4.11(c) respectively present the local and global statistical features of standard deviation, signal kurtosis and signal skewness

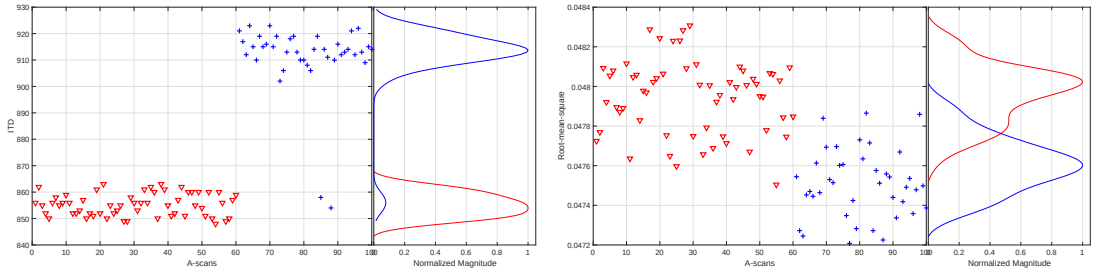

(a) Interface-time delay (b) Root-mean square

Figure 4.10: *Representation of global morphological features for simulated data (computed from analytic Fresnel data model (Appendix A.2) with added noise ($SNR = 30\,\text{dB}$, $\varepsilon_{r,deb} = 6$, $t_{deb} = 0.3\,\text{cm}$). '∇' (red) indicate debonding and '+' (blue) indicate non-debonding values*

and Figure 4.12(a), Figure 4.12(b), Figure 4.12(c) respectively present the same normalized between [0, 1]. As seen in case of Kurtosis and Skewness, the local features clearly demonstrate a more clearer separation between the debonding and non-debonding cases than its counterpart global features.

All signal features listed in Table 4.2 were subsequently analyzed in a similar fashion in order to verify 'how well' are the separations for debonding and non-debonding cases. It was observed that the local signal features always provided better separation than their global counterparts.

Feature reduction using PCA, as presented in the following section, is one approach that can be used to either eliminate the highly correlated features or transform them into uncorrelated features.

4.2.4 Feature reduction using Principal Component Analysis (PCA)

However, in case of both global and local features, since the features were chosen by physical analysis of the GPR data, a threat of correlation between the features may be encountered. Such features, although tend to be different, are influenced by the same parameter. Such features are thus redundant [273] and may lead force the method to 'by-heart' rather than learn. Feature reduction using PCA, as presented here, is one approach that can be used to either eliminate the highly correlated features or transform them into uncorrelated features.

Principal component analysis is a non-supervised transformation technique that is mainly used for feature extraction and dimensionality reduction [274, 275]. Using PCA, it is possible to identify correlation patterns within the data that can be used to find the directions of maximum variance in the higher dimensions and finally project the data on a new space with lesser dimensions than the original one [274]. In other words, PCA is used to transform this larger set of correlated features into a smaller set of uncorrelated principal components [276] while still preserving as much information as possible.

In the literature, PCA has been used for feature extraction with SVM to classify Electroencephalography (EEG) signals [277], ECG signals [278] and pattern identification

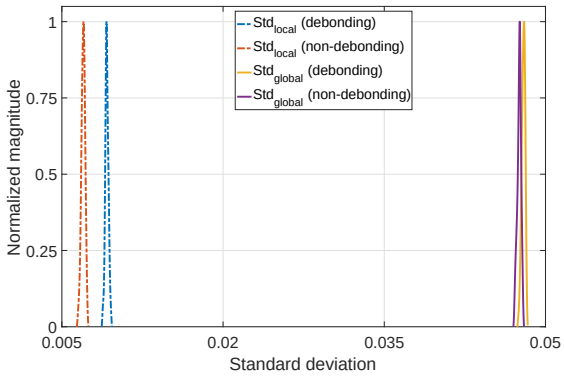

(a) Standard deviation

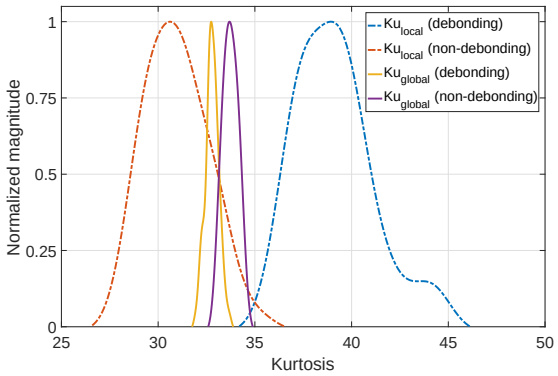

(b) Kurtosis

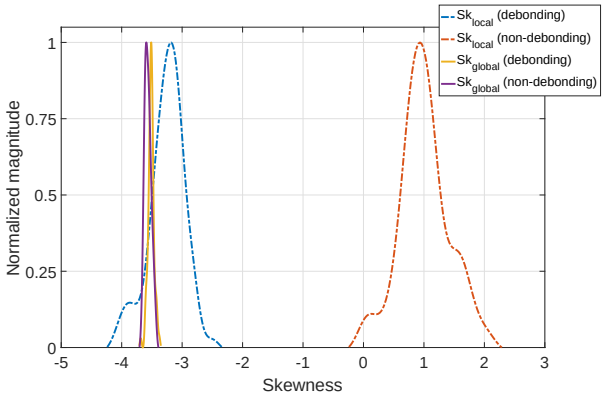

(c) Skewness

Figure 4.11: *Comparison of local and global statistical features for noisy simulated data (computed from analytic Fresnel data mode; Appendix A.2) with added noise ($SNR = 30\,\mathrm{dB}$, $\varepsilon_{r,deb} = 6$, $t_{deb} = 0.3\,\mathrm{cm}$)*

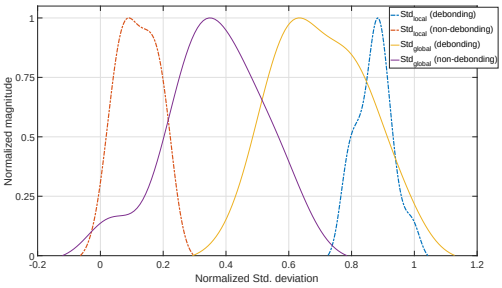

(a) Standard deviation

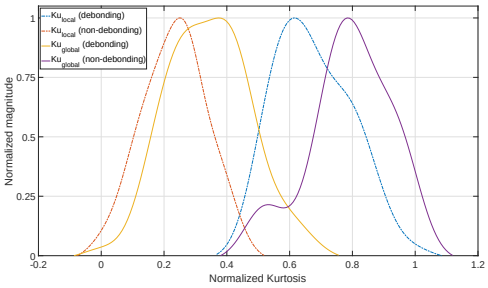

(b) Kurtosis

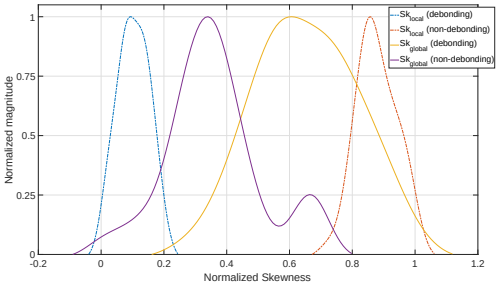

(c) Skewness

Figure 4.12: *Comparison of normalized local and global statistical features for noisy simulated data (computed from analytic Fresnel data mode; Appendix A.2) with added noise ($SNR = 30\,\mathrm{dB}$, $\varepsilon_{r,deb} = 6$, $t_{deb} = 0.3\,\mathrm{cm}$)*

[279].

However, here PCA is used to reduce the dimension of the pre-selected local and global feature data sets. And since we want to reduce the dimensions, a subset of principal components (called *Eigenvectors*) is selected containing the most information. A variance threshold is then used to 'shortlist' the k prominent features that can be used.

Let $\mathbf{X}_{m\times n}$ be a GPR B-scan in time domain (where m is the number of time samples, n is the number of A-scans) whose feature matrix is given by $\mathbf{F}_{p\times n}$ (where p is the number of features). The PCA is computed as follows. In order to assign equal importance to each feature, the feature set is normalized [280] for each feature (*i.e*, row-wise normalization). Then, the covariance matrix $\mathbf{S}$ of the 2D feature matrix is estimated.

As mentioned by [281, 282], the 'importance' of each principal component (or the quality of measure) is indicated by its inertia (or by the proportion of the total inertia). Hence, for a given principal component, the inertia can be expressed as [283, 282]:

$$\pi_j = \frac{\lambda_j}{\sum_{j=1}^{p} \lambda_j} = \frac{\lambda_j}{\mathrm{tr}(\mathbf{S})^T} \tag{4.1}$$

where $\mathrm{tr}(\mathbf{S})$ denotes the trace of the covariance matrix $\mathbf{S}$.

The increment nature of the components means that we can express the total variance of a set of S different principal components as a percentage of total variance accounted for: $\sum_{j\in S} \pi_j \times 100\%$ [282].

Figure 4.13 presents the inertia plots for the global (Figure 4.13(a)) and local (Fig-

ure 4.13(b)) feature sets.

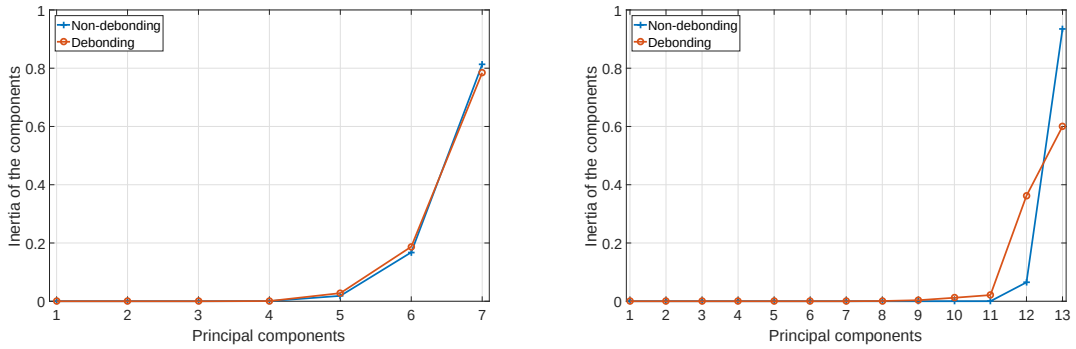

(a) Global feature set

(b) Local feature set

Figure 4.13: *Inertia plot for local and global feature sets on simulated data (analytic Fresnel model; Appendix A.2)*

The principal components that are to be retained are then chosen by using the predetermined threshold. This threshold is user-defined (in percentage). Initially, each of global and local feature sets are extracted. Then, PCA is performed separately on local and global feature sets using the same threshold values for both feature sets.

Initially, the threshold value was set to 100% (considering all the components as new features); allowing us to achieve the same performance as for the original feature set. However by doing so, only transformed features are used but the resulting feature set size remains of the same. At 90% as well, the use of PCA is unnecessary for both, the scope of the application and the feature set as since there is hardly any data/feature reduction. The aim would be to implement a threshold value that can achieve data reduction, but also, at the same time, maintain information within the reduced data for high performance.

By choosing the value of inertia ($\mathcal{I} \in \mathcal{R}\{0, 1\}$ or 0 to 100%), the number of Eigenvectors (and consequently the number of PCs) are controlled. For eg., in case of local features, if threshold = 100%, all 13 components are used; at 80% inertia 10 PCs are used and so on.

As done earlier in our paper [10], PCA is performed independently on local and global feature sets. By initial analysis, it was observed that, at first, the whole set of PCA features (*i.e.* at 100% PC inertia) allows us to achieve the same performance as for the original feature set (as seen for experimental data in our article [10] as well). The inertia was brought down to 90% and similar performance levels were observed. However at 90% PC inertia, the use of PCA is unnecessary for both, the scope of the application and the feature set as since there is hardly any data reduction.

The inertia was reduced step-by-step (steps of 10%) and the finally set to 80%, which gives us 10 components for local signal features and 6 components for global signal features. It should be noted that when the inertia was reduced below 50%, the *DSC* score drastically dropped below 0.5.

4.2.5 Feature selection methodology

The performance of a machine learning method depends on the hyper-parameters, kernel function and also the choice of its input data [284]. As such, a lot of effort is required to design the preprocessing steps for data transformation and feature extraction [284]. Figure 4.14 presents the overall debonding detection approach observed throughout this manuscript.

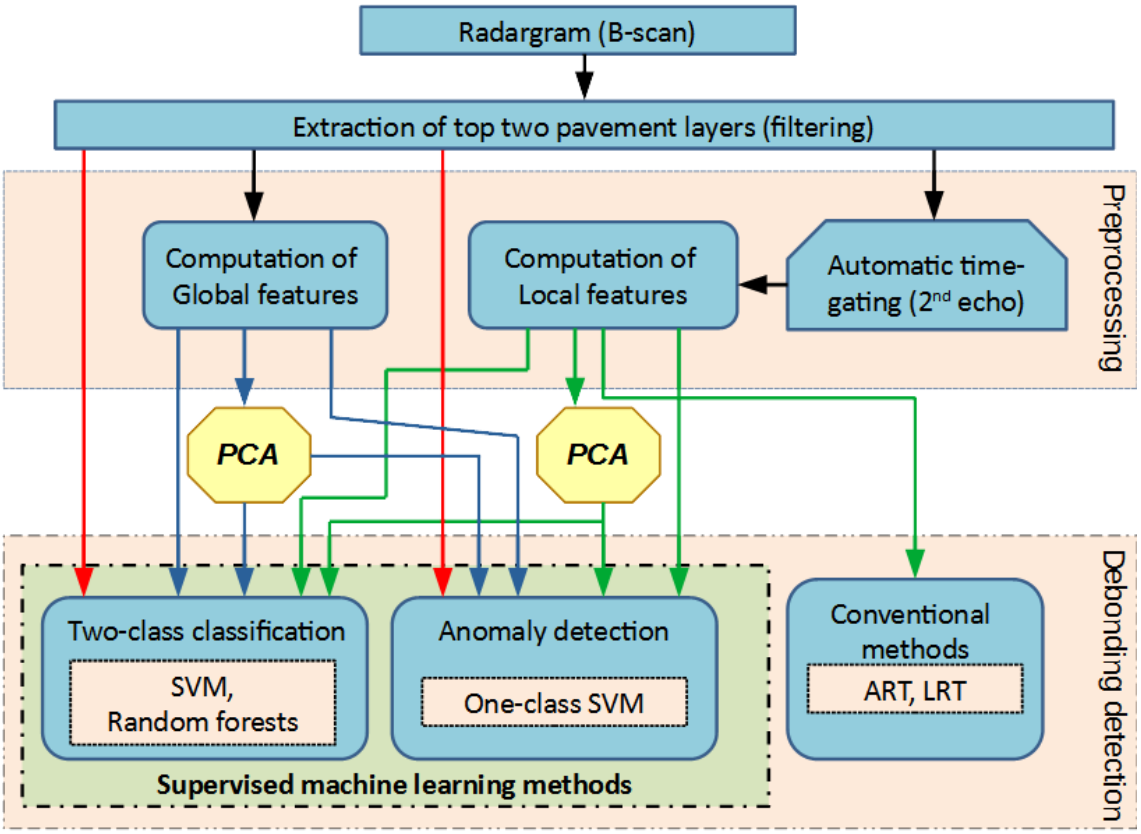

Figure 4.14: *Overall machine learning approach to detect debonding using various input data sets (red, blue and green arrows respectively indicate the detection approach for raw data, global feature set and local feature set)*

Here, we take advantage of the ground truth associated to the data base (see Appendix C.1) to perform the feature selection. The ground truth categorizes the A-scans into two classes, namely debonding and non-debonding cases. The probability density function (PDF) of the features is computed over each class to determine those which are sensitive enough to the pavement conditions.

Initially, a known B-scan with debonding and non-debonding regions is taken. PDFs are traced for each feature listed in Table 4.1 (Global features) and Table 4.2 (Local features) for debonding and non-debonding cases. Figure 4.3 and Figure 4.4 present some of the features to indicate how each feature is able to distinguish between debonding and non-debonding cases. For representation only, a curve-smoothing technique using moving average is applied to the PDFs in Figure 4.3 and Figure 4.4.

The separation between the two curves is used to choose the best features for our ap-

plication. For example, the mean of the signal (represented in Figure 4.4(a), Figure 4.7(a) *etc.*) show minimal/no PDF separation whereas the other features presented in Figure 4.3, Figure 4.6, Figure 4.8, Figure 4.9 and Figure 4.10 provide well-separated distributions and are thus used. The other features are rejected. Additionally, PCA is also used on local and global features to further reduce the data. However, as presented later, it was observed that reduction using PCA did not provide much difference in the detection rate. Finally,

Time domain local signal features
• *Statistical features*: Mean Absolute deviation (MAD), Standard deviation, Skewness and Kurtosis
• *Morphological features*: RMS of the signal, Inter-quartile range, Amplitude of second echo, Magnitude of second echo
• *PQRST features*: Amplitudes at points P, R, S and T, Slope RS

Table 4.1: *List of the local signal features used obtained by analyzing the PDF separations of debonding and non-debonding data*

Time domain global signal features
• *Statistical features*: Mean Absolute deviation (MAD), Standard deviation, Skewness and Kurtosis
• *Morphological features*: RMS of the signal, Inter-quartile range, Interface time-delay of second echo (ITD)

Table 4.2: *List of the global signal features used obtained by analyzing the PDF separations of debonding and non-debonding data*

a total of 13 local features and 7 global features were chosen as input data for further processing by supervised machine learning methods. In case of PCA reduced sets, 10 and 6 components respectively were obtained from local and global feature sets.

We now compare the performance of the three supervised machine learning methods based on the various input feature sets. The results are compared with the benchmark results from Chapter 3 (*i.e.* performance using raw GPR data). These results are obtained using the optimization of each machine learning method (optimization methodologies detailed in the next chapter; Chapter 5).

4.3 Preliminary tests on machine learning methods using GPR signal features

In this section, we perform a preliminary analysis of the supervised machine learning methods by comparing their performances using various input feature sets (*i.e*, local and global features) from simulated analytic data. Additionally, the performance observed

using the raw GPR data (see Chapter 3) is used as the performance benchmark reference for the results.

The analytic Fresnel data model (see Appendix A.2) is used to generate the simulated data with various levels of SNR (*i.e*, SNR = 10 dB, 20 dB, 30 dB, 40 dB, 50 dB and 60 dB). Both global and local feature sets are extracted as discussed in Chapter 4.2.1 and 4.2.2 respectively.

To represent the results, the ROC is traced at all levels of SNR (10 dB, 20 dB, 30 dB, 40 dB, 50 dB and 60 dB) averaged over 100 independent Monte-Carlo realizations.

To illustrate the binary classification of GPR data, we use the ROC curves as the preliminary form of representation. Although the ROC curve does not provide a diagnostic tests in terms of gains and losses, they are still considered to be better in terms of representation at a superficial level. To add more meaning to the results, we use the performance indexes, namely *DSC* and *MCC* scores as well.

4.3.1 Two-Class SVM

Figure 4.15 presents the ROC curves to compare the performance of Two-class SVM using various input data sets discussed in Chapter 4.2 for simulated analytic data at various levels of SNR. These results are obtained using 5-fold cross validation (presented in the next chapter) and non-linear RBF kernel. In case of binary Two-class SVM for simulated

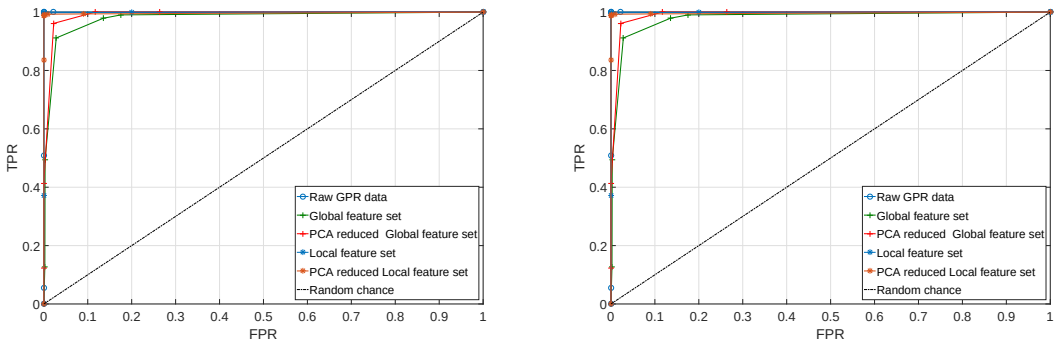

(a) Weak contrast ($\varepsilon_{r,deb} = 6$) (b) Strong contrast ($\varepsilon_{r,deb} = 2$)

Figure 4.15: *ROC curves obtained using Two-class SVM for simulated analytic Fresnel data model (see Appendix A) at various levels of SNR* ($t_{deb} = 0.3$ cm)

data, at low SNR levels the detection is low. However, with the increase in SNR, high detection rate is observed for all types of feature sets, with local features providing results better than global feature sets.

4.3.2 One-Class SVM

Figure 4.16 presents the ROC curves to compare the performance of One-class SVM using various input data sets discussed in Chapter 4.2 for simulated analytic data at various levels of SNR. Learning data size is $T_{learn} = 20$ A-scan/feature vectors of non-debonding case. A linear kernel is used with 5-fold cross validation to obtain an optimal value for the

parameter ν_{opt}. In case of $\varepsilon_{r,deb} = 2$ (strong contrast), $\nu_{opt} = 0.03$ and $\varepsilon_{r,deb} = 6$ (weak contrast), $\nu_{opt} = 0.05$.

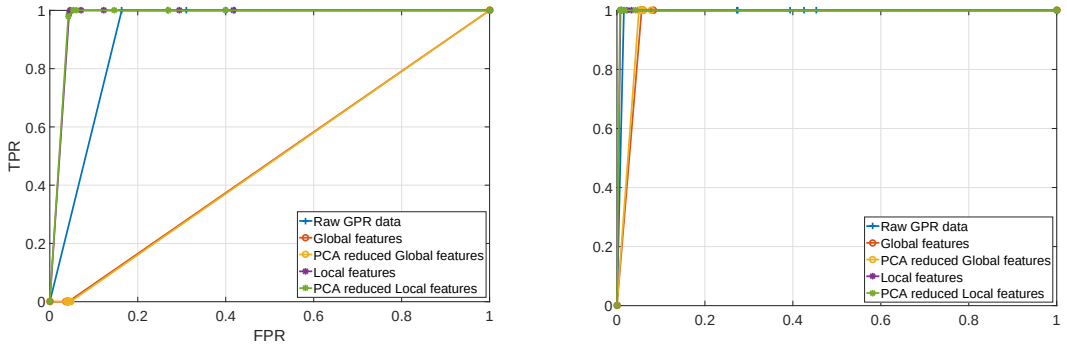

(a) Weak contrast ($\varepsilon_{r,deb} = 6$) (b) Strong contrast ($\varepsilon_{r,deb} = 2$)

Figure 4.16: *ROC curves obtained using One-class SVM for simulated analytic Fresnel data model (see Appendix A) at various levels of SNR ($t_{deb} = 0.3\,\mathrm{cm}$)*

In case of weak contrast ($\varepsilon_{r,deb} = 6$), the performance of the global feature set is very low. However, the local signal features perform well and better than the raw GPR data as well as global features.

4.3.3 Random forests

Figure 4.17 presents the ROC curves to compare the performance of Random forests using various input data sets discussed in Chapter 4.2 for simulated analytic data at various levels of SNR. As done in Chapter 3.4.3 for raw GPR data, we use $T = 100$ trees with each tree having the same number of observation samples. The value for the subset size (p) is fixed as mentioned earlier in Chapter 3.4.3.

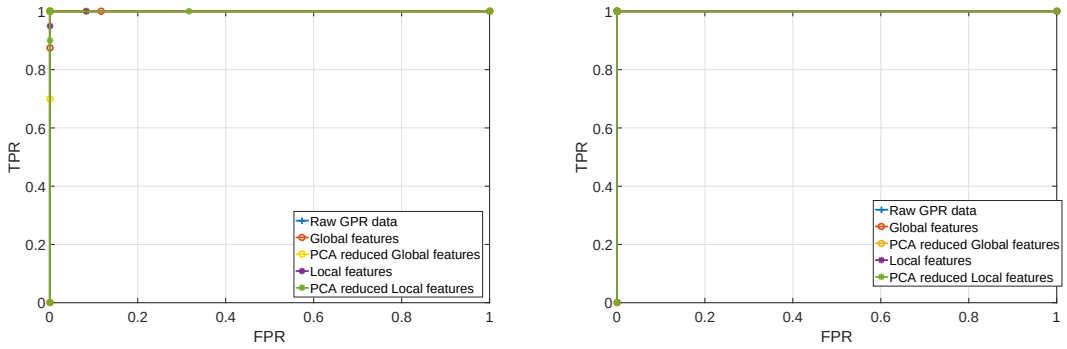

(a) Weak contrast ($\varepsilon_{r,deb} = 6$) (b) Strong contrast ($\varepsilon_{r,deb} = 2$)

Figure 4.17: *ROC curves obtained using RF for simulated analytic Fresnel data model (see Appendix A) at various levels of SNR ($t_{deb} = 0.3\,\mathrm{cm}$)*

It can be seen that, for simulated data, both local and global feature sets demonstrate excellent detection at various levels of SNR.

Table 4.3: *Comparison of DSC scores for machine learning methods with various input data sets obtained using noisy simulated analytic data at SNR* = 30 dB *($\varepsilon_{r,deb} = 2, 6$; t_{deb} = 0.3 cm)*

Input data set	Two-class SVM		One-class SVM		Random forests	
	$\varepsilon_{r,deb} = 2$	$\varepsilon_{r,deb} = 6$	$\varepsilon_{r,deb} = 2$	$\varepsilon_{r,deb} = 6$	$\varepsilon_{r,deb} = 2$	$\varepsilon_{r,deb} = 6$
Raw GPR data	1.00	1.00	0.927	0.91	1.00	1.00
Global features	1.00	1.00	0.97	0.0	1.00	1.00
Global features (PCA)	1.00	1.00	0.97	0.842	1.00	1.00
Local features	1.00	0.84	0.964	0.96	1.00	1.00
Local features (PCA)	1.00	1.00	0.962	0.85	1.00	1.00

In summary, Table 4.3 simply compares the *DSC* similarity index for the three machine learning methods at SNR = 30 dB. It is clear that the Random forests outperform the SVM approaches over all types of input data sets (feature sets or raw GPR data) thereby establishing it as the best debonding detection method amongst the three for our application.

4.4 Conclusion

We begin this chapter by presenting one of the important preprocessing step in debonding detection *i.e*, signal feature selection. The feature selection was categorized into time domain local and global signal features. The local features were focused at the pavement interface where the debonding is expected to occur. These features were expected to present higher efficiency for the purpose of debonding detection. Global features on the other hand used the complete GPR signal with the top two pavement interfaces. A total of 13 local features and 7 global features were chosen by physical analysis of the GPR data. In order to further reduce the data complexity, a well-known data reduction technique (PCA) was introduced. The extracted feature sets were obtained for a simulated data model (analytic Fresnel; see Appendix A.2) and the experimental data collected at IFSTTAR's fatigue carousel (for Geotextile and Tack-free defects; see Appendix B.2).

From Chapter 3, the debonding detection from raw GPR data was used as the basis of performance comparison presented on ROC curves. Although the raw GPR data presented very high detection, this approach is quite cumbersome and not efficient in terms of computational time and complexity. As expected, in case of Two-class SVM for simulated data, it was observed that the local feature set presented better detection results than global features. In case of RF, for simulated data, both local and global feature sets demonstrated very high detection rate inferring that the method is well-suited for various types of input data. Finally, in case of anomaly detection (One-class SVM), the local feature sets presented better detection rate than its counterparts.

In case of each of the machine learning methods, it was observed that the raw GPR

data provided very similar results to that obtained using the local feature sets. However, the preference of using the local feature set over raw data was its smaller data size that reduced the computational burden for the machine learning methods.

The motive behind the comparison of the methods using various input data was to analyze their dependency on the input data for debonding detection and verify if there is a necessity of initial data preprocessing. By observing the results, the overall conclusion is, although the raw GPR data presents high debonding detection rate (in most cases), due to computational complexity and the burden, it is necessary to perform feature selection.

The preliminary results presented for each machine learning method were obtained using optimized hyper-parameters that control the methods. However the optimization of the machine learning methods can be performed on several parameters such as, the learning data size, method hyper-parameters, method kernels, cross validation techniques *etc*. Moreover, from the operator point-of-view, the objective would be to have robust detection methods that are able to perform well despite the lack of knowledge (information regarding pavement permittivity, composition *etc*).

Thus, in the next chapter, we explore this adaptability of machine learning methods to these parameters by means of optimization and parameter tuning.

Part III

DATA PROCESSING FOR DEBONDING DETECTION IN PAVEMENT STRUCTURES

Chapter 5

Machine Learning Model Selection and Validation For Debonding Survey

Contents

In the previous chapter, we presented the pre-processing of GPR data by means of feature extraction and feature reduction. We also presented an initial performance analysis of the machine learning methods by comparing the various input feature sets. These results were obtained using optimized hyper-parameters that govern the methods.

The optimization of a machine learning method is an important part since, by identifying the 'best' parameters, it is possible to achieve high debonding detection rate. In this chapter, we focus on the behavior of various parameters included in the machine learning method in the context of detecting interface debondings. Various optimization techniques for machine learning methods have already been discussed in the literature [285, 286, 287].

One such approach namely, Sensitivity Analysis [255], is studied here in the context of detection of interface debonding. The approach namely, method-based model fitting (Chapter 5.2) is used to study the relationship between the performance of the methods and the input hyper-parameters that control said methods, such as cross-validation techniques, kernel functions, learning data size *etc*). The sensitivity analysis of Two-class SVM was implemented for GPR data in [10] *w.r.t* kernel function, learning data size and input signal feature sets.

On the other hand, in this chapter, we also perform robustness tests (Chapter 5.3) to observe the effect of pavement medium and configurations (such as variations in the debonding thickness, permittivity and effect of noisy data) on the performance of the methods. Finally, a concept of global parameter-optimization, which is suited for practical applications, is also introduced here.

As seen in the previous chapter (Chapter 4), the local signal features were able to provide a higher detection rate to its counterparts (*i.e.* global features). Thus, in this chapter, the optimization of the methods is performed on the local signal features only. The optimization was performed using simulated data (Appendix A) independently on each machine learning method, but over various pavement configurations (*i.e* global optimization).

5.1 Methodology

The standard methodology for debonding detection as we have presented in [10] is implemented in this chapter. The GPR B-scan data is initially generated using simulated analytic Fresnel model (see Appendix A). Initial pre-processing feature selection steps are then carried out as presented in Chapter 4.2.5. The data is then ready for processing using the machine learning methods.

In case of two-class classification (Two-class SVM and Random forests), the data is randomly divided into two disjoint sets: learning and test data. In this case, learning data set contains both debonding as well as non-debonding data. One-class SVM, on the other hand is divides the data in such a way that the learning data contains only one type of data, *i.e.* non-debonding.

In the learning stage, SVM methods then use various cross validation techniques to obtain the optimal hyper-parameters for the specific method. These optimal values are then used with the test data for validation of results. In case of Random forests, the learning data is randomly divided into several subsets to generate a 'forest' as presented in Chapter 3.4.3. The classification for Random forests depends on the number of trees (T) and the number of features (p) in each subset. These values are chosen as mentioned in Chapter 3.4.3.

Representation of results

In the previous chapter, the initial analysis and performance of the machine learning methods for various input feature sets was presented using ROC curves. In this chapter, the ROC and AUC were found not easy to handle to determine the optimal parameters of the machine learning methods [288, 289, 290, 291]. As established in [292], diagnostic tests are better understood when presented in terms of gains and losses, using numeric indicators such as accuracy, error rate *etc.*. We then switch from ROC to performance indexes.

Numeric indicators such as DSC score and MCC *etc.* are more representative and can thus be easily understood and interpretive by the operator with minimum knowledge. As

explained in [288], the advantage of MCC coefficient over the other performance indexes is that it provides a high MCC score *iff* the machine learning method has high percentage of true positives (in this case, *debondings*). The other rates (such as Accuracy, DSC score, Precision, *etc.*) lack in this aspect and as discussed in [288, 289], they can lead to misleading results. For illustration, Figure 5.1 compares the DSC and MCC scores for balanced and imbalanced cases. The value N_{ratio} is the ratio N_{deb}/N_{ndeb} where N_{deb} and N_{ndeb} are respectively number of debonding and non-debonding A-scans.

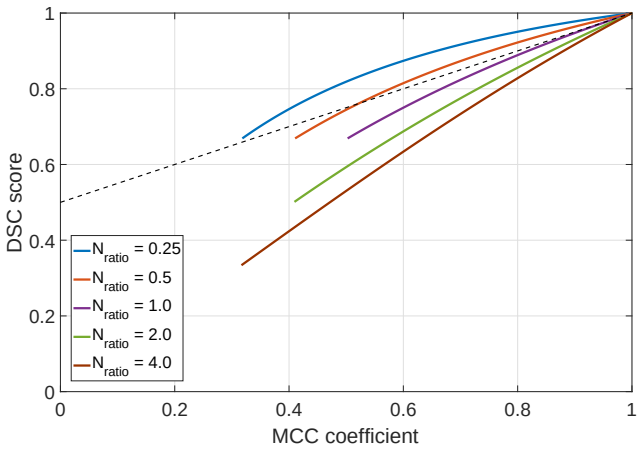

Figure 5.1: *Variation of DSC score and MCC coefficient at different N_{ratio} values*

It can be observed that in case of imbalanced data, *i.e.*, $N_{ratio} < 0.5$, DSC score saturates at higher values presenting very less variation, while MCC demonstrates to be more robust. Conversely, for $N_{ratio} > 1$, DSC would be recommended. Both indicators are almost equivalent for balanced data, *i.e.*, $N_{ratio} \approx 1$. Despite this different behavior, the DSC score is still used for imbalanced data and is widely used to represent the performance in binary classification [293].

However, in this thesis we are dealing with both situations. The tests on simulated data are performed with balanced data, leading to equivalent interpretation with either DSC or MCC. By contrast, we may face the situation of imbalanced experimental data in Chapter 6, for which MCC would lead to a more reliable data interpretation. To avoid the dilemma of choice, we then use both DSC and MCC scores to present the optimization results for the methods.

5.2 Method-based model fitting

Machine learning involves predicting and classifying data and to do so, various machine learning models can be best suited to a given dataset. The machine learning models are parameterized so that they can be 'tuned' in order to suit it to a given situation [286]. Each machine learning model can have various parameters and the goal would be to find the best combination of parameters in order to achieve the highest efficiency and demonstrate its robustness. However, the term 'parameter' and 'hyper-parameter' hold totally different meanings in machine learning. Parameters are simply the input settings that make an

algorithm work; whereas hyper-parameters are the settings of an algorithm that can be adjusted to optimize the machine learning performance [287].

For debonding detection using supervised learning methods presented in Chapter 3, various input method-related parameters can be used. However, all these parameters may or may not yield the desired accuracy solution. So, *to decide what are the optimal values for each parameter that can provide the highest accuracy*, a task most commonly called as Model selection [294]. In the field of data analysis, Sensitivity Analysis (SA) refers to the study of relationship of uncertainties between the input and its outputs [255]. As mentioned in [295], both model selection and sensitivity analysis are similar as they both attempt to analyze the appropriateness of a model. However, while model selection concentrates on the assessment of 'fitting' specific to an application, SA has a more general approach to quantify the uncertainty in a model [295].

Several model-fitting approaches have been discussed in literature [286, 287, 296]. This can be either performed manually by the user or it can also be automatically performed by the machine learning method. In the latter, the machine learning method has the freedom to perform this parameter exploration and select the optimal model architecture automatically governed by certain constraints.

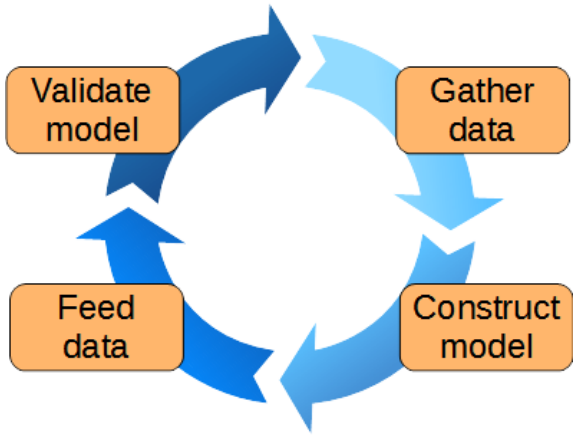

Figure 5.2: *Generic machine learning model fitting/parameter tuning approach*

A model is said to be 'fit' if it is capable of identifying the relationship between the data (or features) and the target detection [297]. In order to fit a model, the input parameters are adjusted in such a manner that the best predictions can be achieved for the data set under study. This process is sometimes also referred to as 'Parameter tuning'. The parameter tuning by the machine learning method is an iterative process wherein the model is continuously tuned to improve the accuracy of the method as shown in Figure 5.2.

Following the conclusions in Chapter 4, the local features presented better results than the global feature sets. Thus, hyper-parameter optimization for model selection and validation in this chapter will be performed using local feature sets.

In this section, we propose the implementation of model-fitting by means of hyper-parameter optimization in the case of pavement debonding detection in two ways: global optimization and $\varepsilon_{r,deb}$-specific optimization.

In case of the $\varepsilon_{r,deb}$-specific optimization, the cross validation techniques (presented later in Chapter 5.2.2) is used to find the optimized hyper-parameters for individual cases of pavement configurations that vary in terms of debonding layer permittivity *etc.* Although this approach may present the best hyper-parameters and achieve may very high efficiency, it is not practically possible due to the limited knowledge possessed by the operators about the pavement configuration.

On the other hand, we define the global approach in which the optimization is performed with respect to all $\varepsilon_{r,deb}$ scenarios. By doing so, the hyper-parameters used in the testing stage are the same regardless of the debonding material under test. This approach is closer to the operational level than the former, since the operators do not possess all the information about the pavement layers. The subsequent sections will discuss these approaches.

Figure 5.3 presents the parameter tuning during the learning stage to obtain the optimal machine learning parameters necessary for 'best-fitting' the model (*i.e.* hyper-parameters).

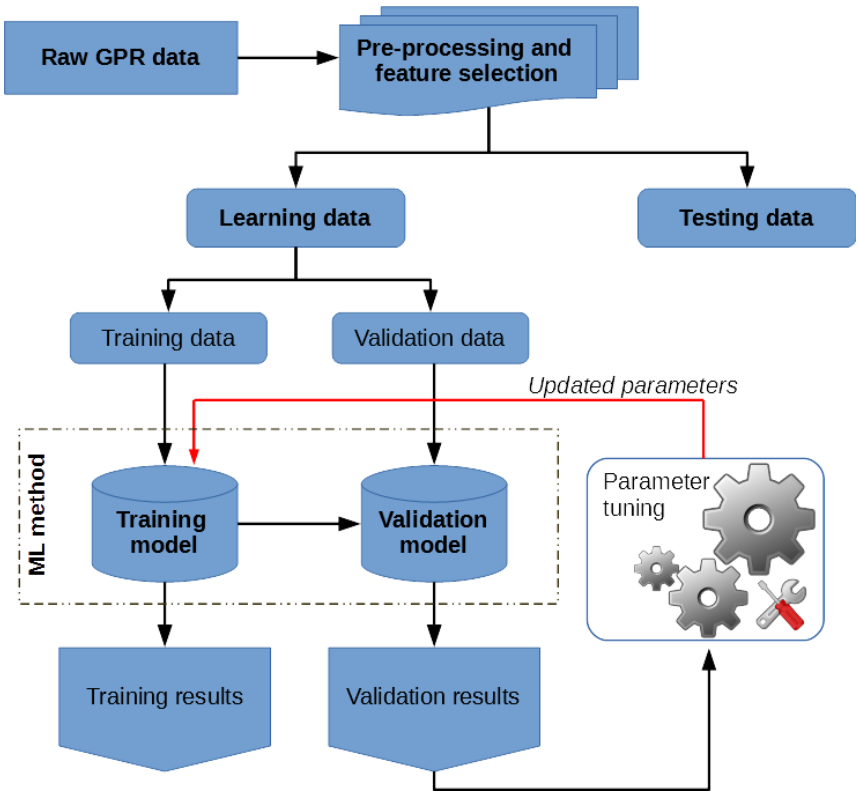

Figure 5.3: *Parameter tuning for supervised machine learning methods*

In general, the model selection involves optimization of criterion, such as cross validation [298]. Some other model selection techniques include the kernel functions and learning data sizes. Figure 5.4 presents the categorization of the method based model fitting approaches presented here. In this section, we explore the model selection approach for the three machine learning methods, SVM, OCSVM and Random forests for noisy analytic simulated databases. For each model-fitting approach, the two remaining categories are optimized beforehand.

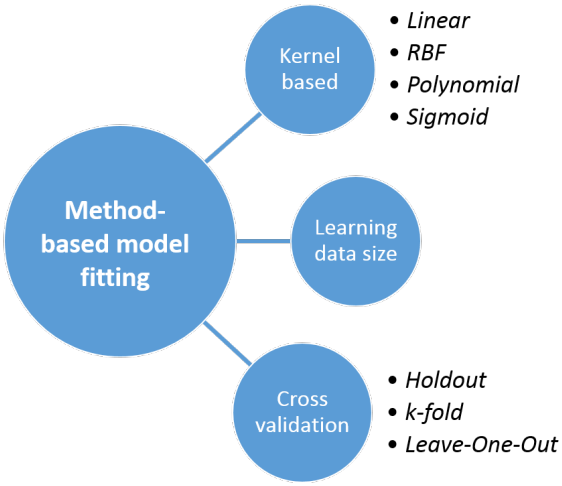

Figure 5.4: *Categorization of method-based model fitting approaches for supervised machine learning methods*

5.2.1 Kernel-based analysis

For classification applications, machine learning methods such as (Two-class and One-classSVM) can use various mathematical functions called '*kernels*'. As discussed in Chapter 3.3, a linear kernel can be used for linearly separable data whereas for non-linearly separable data, there are various kernels. Some of the non-linear SVM kernels include: Gaussian RBF, Sigmoid, Polynomial kernel *etc.* With the help of kernel functions, it is possible to generate a more robust result during the learning step.

In this section, we analyze the performance of SVM for various kernels. Kernel analysis has been already presented in the literature for the diagnosis of respiratory diseases [299], classification of Landsat and QuickBird datasets [300] using Two-class SVMs. A similar study has already been published using SVM by us in our article [10]. One-class SVM has been implemented in the literature using various kernel functions to detect landmines [93, 114].

In case of Random forests, performance metrics (presented in Chapter 3.4.3) are used instead of kernel functions. However, it can be modified to become a kernel function for other ML methods [234, 235].

Figure 5.5(a) compares the DSC score for various simulated data configurations using various SVM (Two-class and One-class) kernel functions. Three values of permittivities were used, $\varepsilon_{r,deb1} = 2$, $\varepsilon_{r,deb2} = 6$ and $\varepsilon_{r,deb3} = 10$ for the debonding layer of thickness t_{deb} = 0.3 cm. The DSC score is averaged over 100 Monte-Carlo independent realizations. A 5-fold cross validation is used to obtain the optimal hyper-parameters required for each kernel functions (the approach is presented later). The strategy for each machine learning method is optimized independent of the $\varepsilon_{r,deb}$ value (detailed in Chapter 5.2.2.1).

We compare the MCC coefficient for Two-class and One-class SVM using various kernel functions in Table 5.1 and Table 5.2 respectively.

For Two-class SVM, it can be observed from Figure 5.5(a) and Table 5.1 that the linear, RBF and Polymonial kernels presented very high detection for all debonding permittivity

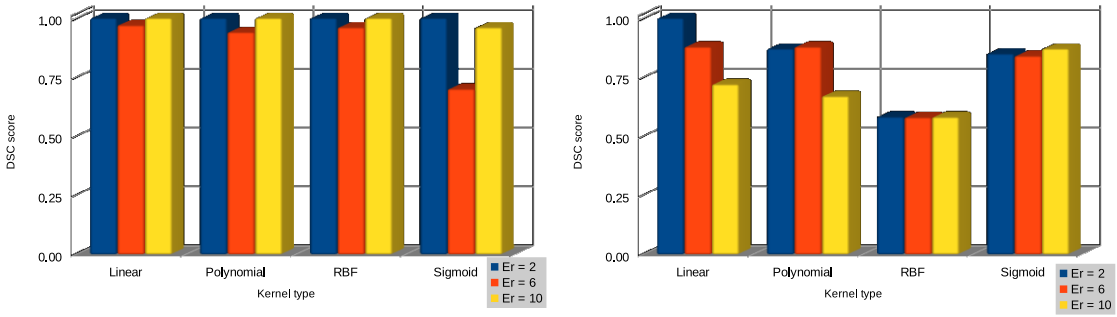

(a) Two-class SVM

(b) One-class SVM

Figure 5.5: *DSC score for the Method-based kernel SA for noisy simulated (analytic Fresnel) data for various values of* $\varepsilon_{r,deb}$

Table 5.1: *MCC coefficient for various kernel functions for noisy simulated (analytic Fresnel) data using Two-class SVM at various values of* $\varepsilon_{r,deb}$

Kernel type	$\varepsilon_{r,deb} = 2$	$\varepsilon_{r,deb} = 6$	$\varepsilon_{r,deb} = 10$
Linear	1.00	0.929	0.993
Polynomial	1.00	0.873	0.998
RBF	**1.00**	**0.933**	**1.00**
Sigmoid	1.00	0.591	0.93

Table 5.2: *MCC coefficient for various kernel functions for noisy simulated (analytic Fresnel) data using One-class SVM at various values of* $\varepsilon_{r,deb}$

Kernel type	$\varepsilon_{r,deb} = 2$	$\varepsilon_{r,deb} = 6$	$\varepsilon_{r,deb} = 10$
Linear	**1.0**	**0.794**	0.48
Polynomial	0.77	0.78	0.38
RBF	0.117	0.12	0.114
Sigmoid	0.74	0.72	**0.77**

values with RBF providing an edge over the two. This observation was found in case of local features for experimental data and published in our article [10]. The sigmoid kernel however, in case of $\varepsilon_{r,deb} = 6$ has false detection leading to $DSC \approx 0.65$.

On the contrary, in case of One-class SVM, it was observed that apart from the RBF kernel, the linear and sigmoid kernels presented better results with $DSC \geq 0.70$.

5.2.2 Cross-validation techniques

Cross validation is a model evaluation method that is better than residuals [301]. The problem with residual evaluations is that they do not give an indication of how well the learner will do when it is asked to make new predictions for data it has not already seen. One way to overcome this problem is to not use the entire data set when training a learner.

Some of the data is removed before training begins. Then when training is done, the data that was removed can be used to test the performance of the learned model on 'new' data. This is the basic idea for a whole class of model evaluation methods called cross validation.

Here, we present and compare three principal cross validation approaches for tuning the machine learning parameters. These CV techniques have been presented in detail in [297], compared in [302] using ROC and AUC curves, in [303, 304] compares the CV techniques for defect prediction models and in [305] to classify medical images.

1. Holdout CV:
The holdout method is one of the simplest approach in cross validation. Here, the learning data is split equally into two exclusive sets, namely, training and validation. The training dataset is used to 'fit' the model and then it is tested using the validation data. Error function is then used to evaluate the model performance and the optimal model is defined as the one with lowest error. Since the training and validation sets are mutually exclusive, the performance of the method completely depends in the samples that end up in each of the sets, thereby resulting in a high variance.

2. k-fold CV:
The k-fold CV is one way to improve the Holdout method. The approach here is to randomly split the learning data into k disjoint subsets (namely, training and validation sets) of identical sizes. The goal is to respect the class distribution in each subdivision. The model is then fit using the $k-1$ folds and validated on the kth fold. This is repeated until each k-fold has served as the validation set. The optimal model is then defined as being the one with the highest score (minimum generalization error) of cross validation.

3. Leave-one-out CV (LOO-CV):
This is a modified version of the k-fold cross validation stretched to its logical extremes *i.e.*, the k-fold are chosen in such a way that $k = N$ where N is the number of data-points (or A-scans). The model training is then carried out the $k-1$ sets and validating using the remaining dataset with simply one data-point. The process is repeated until each data-point has participated as validation data-point. The evaluation given by leave-one-out cross validation seems very expensive to compute at first pass but is efficient as it carries out the modeling with every data-point.

As seen in the literature, the k-fold CV technique is the commonly used method of cross-validation.

5.2.2.1 Choice of optimal hyper-parameters

In this section, the method to obtain the optimal hyper-parameters is presented. In order to have the best classification model and guarantee global optimum, it is necessary to avoid local optimum hyper-parameters as they might seriously affect the learning process of a method [306]. The local optimum is best solution obtained within a small range of hyper-parameter values; whereas, the global optimum is obtained over all the hyper-

parameter values.

With the help of CV techniques, it is possible to improve the SVM's performance (One-class as well as Two-class) in the detection process. These CV techniques can be used to find the optimal hyper-parameters for a machine learning method and by using suitable loss-functions, it is possible to avoid the local minima. One such loss function is the Hinge-loss [307]. For binary classification, Hinge loss function takes values $\in [0, 2]$; *i.e.* non-zero values for misclassified points (or penalized) and is equal to zero for well-classified points. Therefore, the Hinge loss function is suited for classification problems; in contrast to the root-mean square error (RMSE), which is suitable for regression problems.

Since Random forests implements a built-in equivalent of cross validation, namely bootstrapping and bagging, we present the optimization of hyper-parameters using CV for SVM (Two-class and One-class).

Two-class SVM

As seen earlier in Section 5.2.1, the non-linear RBF kernel demonstrated to perform better than the other kernel functions. Thus, the optimization of kernel hyper-parameters for RBF kernel using k-fold CV is presented here. It should be noted that this approach can be used for other kernel functions and the other CV techniques as well. From Equation 3.22, in order to optimize the RBF kernel, two parameters should be controlled, namely, the cost function C and the RBF γ parameter. In addition, a 5-fold CV with the hinge loss function is used.

Two-class SVM model is initially optimized independently for individual pavement configurations (in other words, $\varepsilon_{r,deb}$-specific optimization). Figure 5.6 presents the Hinge-loss as a function of C and γ parameters for the non-linear RBF kernel averaged over 100 independent Monte-Carlo realizations. The optimum hyper-parameters are thus obtained as a pair $[C_{opt}, \gamma_{opt}]$ which can be used on test data.

From Figure 5.6, it can be seen that γ parameter does not have a huge effect on the loss function. This explains the performance of linear SVM kernel being very similar to the RBF kernel in Section. 5.2.1.

Additionally, it can be seen that, within the specific range chosen for C and γ parameters, all three configurations overlap with similar regions. This results in the same optimal hyper-parameters for all configurations. For illustration, Figure 5.7 presents the Hinge-loss as a function of C and γ parameters for global optimization for the three configurations from Figure 5.6. Additionally, it was observed that both locally optimized ($\varepsilon_{r,deb}$-specific optimization) as well as the global optimized results provided very similar results with the former narrowly performing better than the latter approach.

One-class SVM

As seen above in Section. 5.2.1, in case of One-class SVM, the linear kernel provides a better performance than the other kernel functions. We thus present the optimization of this kernel *w.r.t* its input hyper-parameters. Once again, this approach can be used for other kernel functions as well.

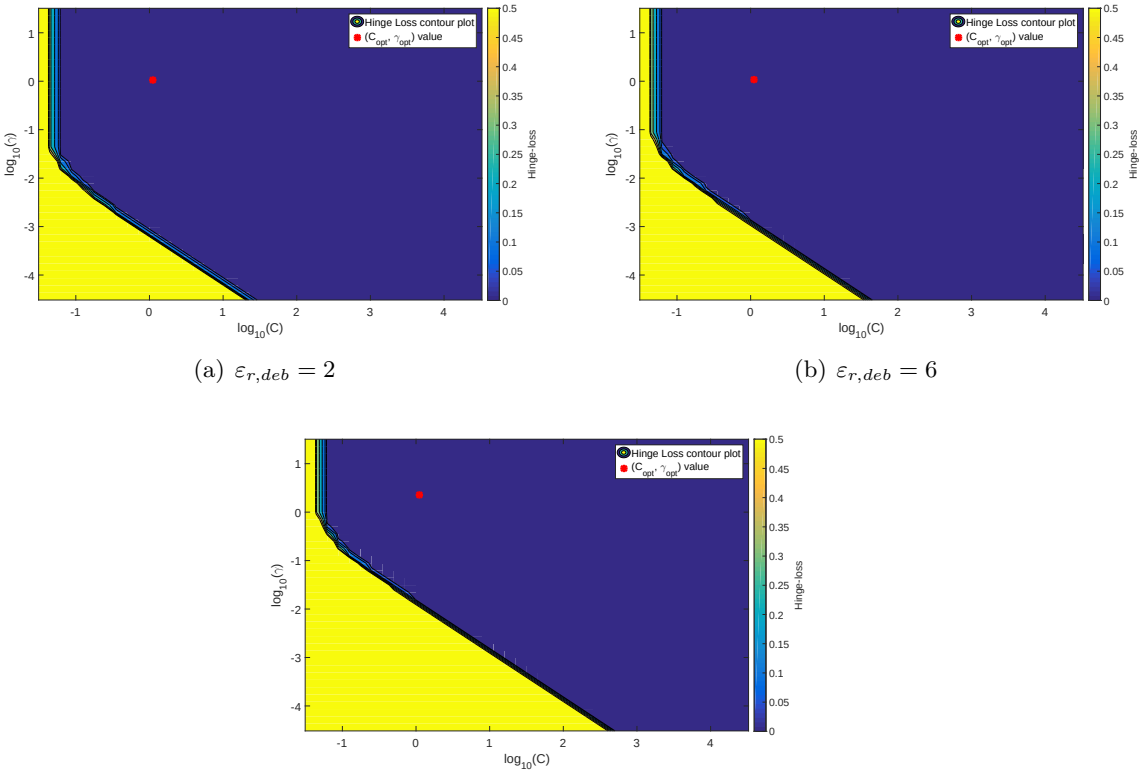

(a) $\varepsilon_{r,deb} = 2$

(b) $\varepsilon_{r,deb} = 6$

(c) $\varepsilon_{r,deb} = 10$

Figure 5.6: *Variation of Hinge-loss function w.r.t. C and γ parameters for noisy simulated analytic data ($\varepsilon_{r,deb}$-specific optimization) for various $\varepsilon_{r,deb}$ and $t_{deb} = 0.3\,\text{cm}$ at 30 dB SNR. The red 'o' indicates the optimal hyper-parameter pair chosen during the CV stage*

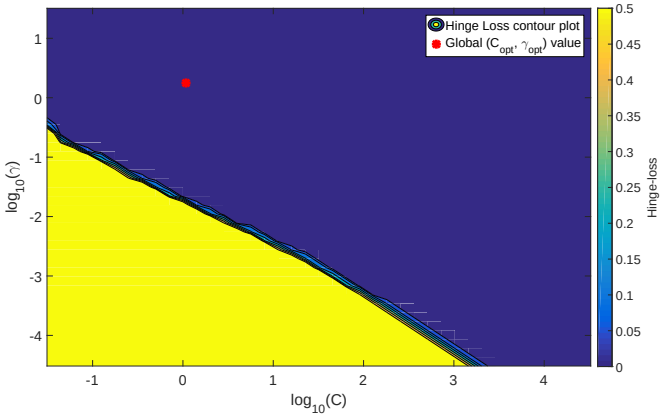

Figure 5.7: *Representation of Hinge-loss function w.r.t. C and γ parameters for noisy simulated analytic data (global optimization approach) over all $\varepsilon_{r,deb}$ values with $t_{deb} = 0.3\,\text{cm}$ at 30 dB SNR. The red 'o' indicates the optimal hyper-parameter pair chosen during the CV stage*

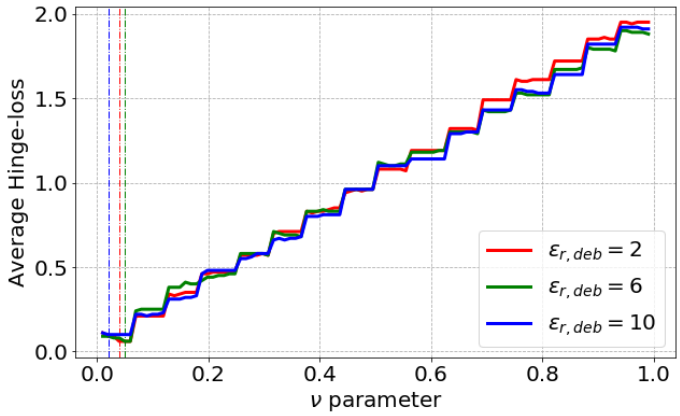

Figure 5.8: *Representation of Hinge-loss function w.r.t. C and γ parameters for noisy simulated analytic data ($\varepsilon_{r,deb}$-specific optimization) for all $\varepsilon_{r,deb}$ values with $t_{deb} = 0.3\,\text{cm}$ at $30\,\text{dB}$ SNR. The solid lines indicate the loss-function curves and the dashed lines represent their respective optimal ν values*

As mentioned in [308], the One-class linear kernel requires the optimization of a single parameter, namely, the user-defined parameter that defines the admitted slack (ν). This parameter decides the amount of outliers (in our case, debondings) present in the learning data [308] and has a value within the range $\nu \in (0, 1]$ [308].

From Equation 3.27, we can see that, the smaller the value of ν, the greater is the possibility to encompass all the learning data within the hyper-sphere and vice versa. Thus, it is imperative to optimize ν in order to obtain the best results.

As done for the Two-class SVM, the hinge loss function is used here. In order to determine the optimal value of ν, a 5-fold CV with the hinge loss function is used. Figure 5.8 presents the Hinge-loss *w.r.t.* ν using the linear kernel averaged over 100 independent Monte-Carlo realizations for $\varepsilon_{r,deb}$-specific optimization.

It can be confirmed that with higher values of ν-parameter, we tend to increase the loss (*i.e* Hinge-loss function) thereby reducing the detection efficiency during the testing stage. Additionally, Figure 5.8 shows that the optimal ν values for the three configurations are very similar to each other ($\nu_{opt} \approx [0.03 - 0.06]$).

On the other hand, as seen in case of Two-class SVM, Figure 5.9 shows the global optimization approach for ν-parameter. This observation however, is seen for simulated data. In the next chapter, we aim to test this behavior in experimental data.

By optimizing each set of hyper-parameters globally irrespective of the material configuration, we aim to provide a more robust and independent methodology that can be implemented in the practical scenarios with minimal changes. Thus, in the subsequent sections, we implement the global optimization for various parametric studies on the machine learning robustness.

NOTE: Since these analyses are averaged over several Monte-Carlo realizations, the Hinge loss functions in Figures. 5.6, 5.7, 5.8 and 5.9 show fractional loss values rather than integer values.

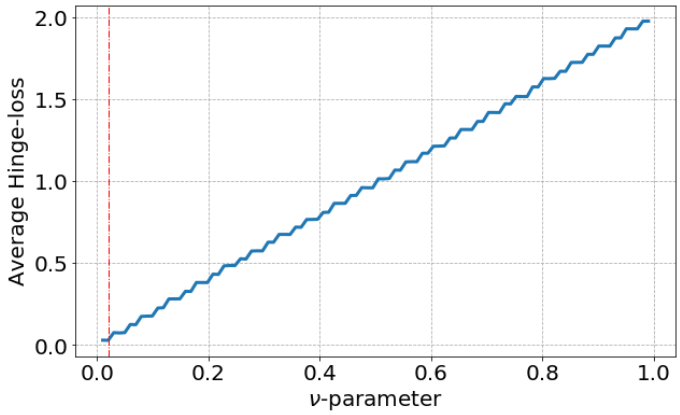

Figure 5.9: *Representation of Hinge-loss function w.r.t ν parameter for noisy simulated analytic data (global optimization approach) over all $\varepsilon_{r,deb}$ and $t_{deb} = 0.3\,\mathrm{cm}$ at 30 dB SNR. The solid line indicate the loss-function curve and the dashed line represent its optimal ν value*

5.2.2.2 Some results

In this section, we compare the various CV techniques and present the performance for simulated analytic data. Each CV technique uses the Hinge-loss function to find the optimal hyper-parameters (global) in the learning stage that are used later on test data.

We implement the CV techniques on both SVMs (Two-class and One-class). However, in case of Random forests, the cross-validation is not implemented here as its process of bootstrapping and bagging is considered as a built-in CV technique.

Figure 5.10(a) and Figure 5.10(b) present the *DSC* curve for noisy simulated analytic Fresnel data for respectively Two-class and One-class SVMs for various CV techniques averaged over 100 independent Monte-Carlo realizations at various permittivity values ($\varepsilon_{r,deb} = 2$, $\varepsilon_{r,deb} = 6$ and $\varepsilon_{r,deb} = 10$).

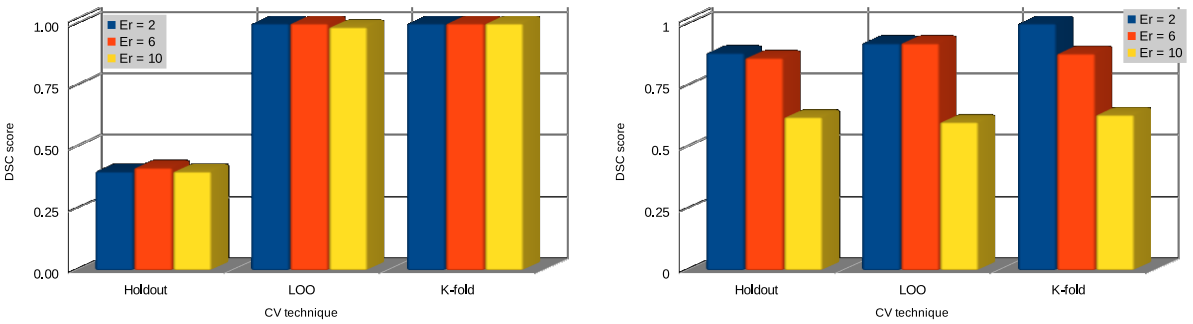

(a) Two-class SVM

(b) One-class SVM

Figure 5.10: *DSC score vs. Cross validation techniques for noisy simulated analytic Fresnel data for various permittivity values on local signal features*

Table 5.3 and Table 5.4 compare the *MCC* coefficient for respectively Two-class and One-class SVM methods at various debonding permittivity values.

In case of Two-class SVM, as seen in Table 5.3 and Figure 5.10(a), the Hold-out CV

Table 5.3: *MCC coefficient for various learning data sizes for noisy simulated (analytic Fresnel) data using Two-class SVM at various values of* $\varepsilon_{r,deb}$

CV type	$\varepsilon_{r,deb} = 2$	$\varepsilon_{r,deb} = 6$	$\varepsilon_{r,deb} = 10$
Holdout	0.07	0.01	0.03
Leave-one out	1.00	0.99	0.97
K-fold	**1.00**	**0.99**	**0.99**

Table 5.4: *MCC coefficient for various learning data sizes for noisy simulated (analytic Fresnel) data using One-class SVM at various values of* $\varepsilon_{r,deb}$

CV type	$\varepsilon_{r,deb} = 2$	$\varepsilon_{r,deb} = 6$	$\varepsilon_{r,deb} = 10$
Holdout	0.8	0.8	0.62
Leave-one out	0.87	0.87	0.625
K-fold	**1.0**	**0.8**	**0.68**

technique provided very low detection rate and was incapable of detecting debondings. However, k-fold CV presented excellent debonding detection with very few (or none) false detection. Since LOO-CV is a special case of k-fold where $k = n$ (number of A-scans), similar results were observed for LOO-CV as well.

In case of One-class SVM (Figure 5.10(b) and Table 5.4), similar conclusions were observed for k-fold CV and LOO-CV techniques. Although Holdout CV presented much better detection rate than that for Two-class, finally the performance of k-fold CV and LOO-CV techniques was better.

5.2.3 Learning data size

A supervised machine learning method relies on the learning data to generate a model that can be used for classification and/or regression. As such, the data size used during the learning step has an impact on the performance of the method. For example, by using a small learning data size, under-fitting may occur leading to improper model fitting (low performance). On the other hand, using a very large learning data set could possibly overfit the model (where the model 'learns' by-heart) which once again affects the performance rate. Thus, it is imperative to find and use an optimal learning to testing data ratio.

In this section, we analyze the effect of learning data size on the debonding detection efficiency of the machine learning methods. Here, we fix the test data size to 100 A-scans (comprising of respectively 60 and 40 A-scans for non-debonding and debonding cases) while the learning data size is varied from a sum of 5 A-scans to 60 A-scans. This implementation is different from [10] where both the learning and test data st sizes are varied to maintain a specific learn-to-test ratio.

Figure 5.11(a), Figure 5.11(b) and Figure 5.11(c), present the *DSC* curves for simulated analytic Fresnel data *w.r.t* various learning data set sizes at various levels of SNR

obtained using respectively Two-class SVM, One-class SVM and Random forests. The *DSC* score in each case is averaged over 100 independent Monte-Carlo realizations.

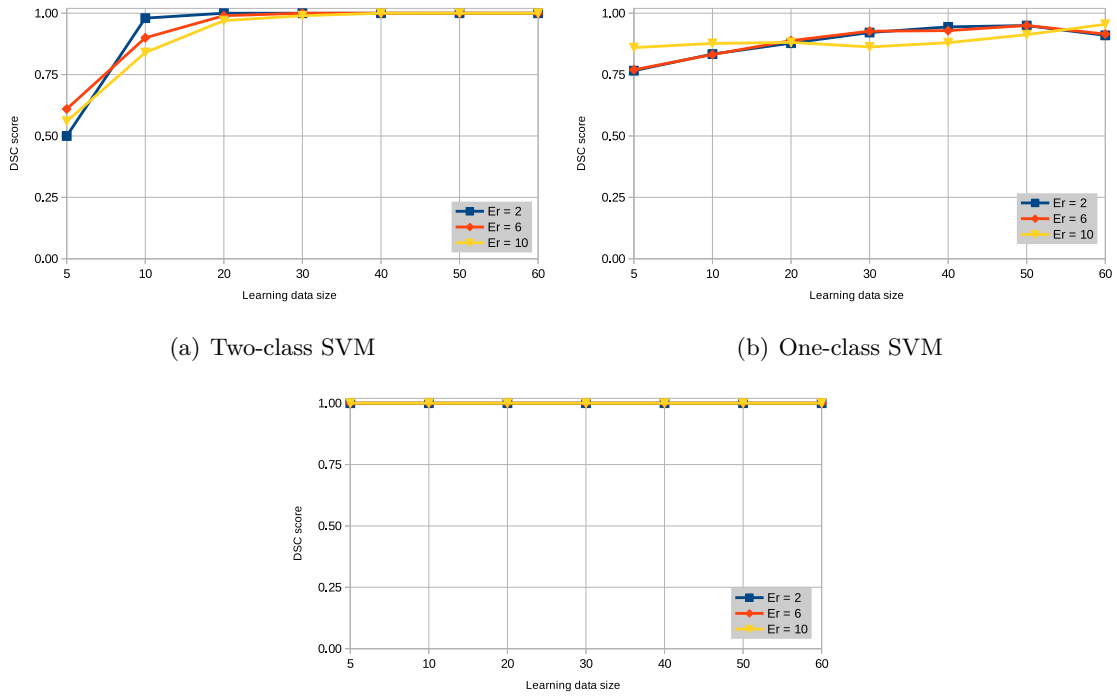

(a) Two-class SVM

(b) One-class SVM

(c) Random forests

Figure 5.11: *DSC score vs. Learning data size curve for noisy simulated analytic Fresnel data for various permittivity values for local signal features*

Table 5.5 and Table 5.6 compare the *MCC* coefficient for Two-class ans One-class SVMs at various sizes of learning data.

Table 5.5: *MCC coefficient for various learning data sizes for noisy simulated (analytic Fresnel) data using Two-class SVM at various values of* $\varepsilon_{r,deb}$

$\varepsilon_{r,deb}$	5	10	20	30	40	50	60
2	0.00	0.84	1.00	1.00	1.00	1.00	1.00
6	0.00	0.8	0.99	1.00	1.00	1.00	1.00
10	0.00	0.56	0.94	0.99	1.00	1.00	1.00

As mentioned extensively in the previous chapters, the Two-class SVM requires the data from both classes (debonding and non-debonding) during the learning step to create a classification model. However, while using a smaller learning data size (*e.g.* Learn size = 5 A-scans), possibilities arise that insufficient data is available. This leads to under-learning resulting in an incomplete/rigid classification model that is unable to consider all possibilities. Therefore, we observe low detection rate at lower learning data set size. As the learning data size is increased, the performance grows rapidly as seen in Figure 5.11(a) and Table 5.5.

Table 5.6: *MCC coefficient for various learning data sizes for noisy simulated (analytic Fresnel) data using One-class SVM at various values of* $\varepsilon_{r,deb}$

$\varepsilon_{r,deb}$	5	10	20	30	40	50	60
2	0.585	0.717	0.796	0.869	0.908	0.916	0.84
6	0.599	0.713	0.815	0.879	0.889	0.918	0.908
10	0.78	0.79	0.8	0.8	0.8	0.84	0.92

In case of One-class SVM, it was observed that the efficiency of detection increases with the increase in the size of the learning data set size. However, at very large learning data size, the efficiency gradually reduces indicating the occurrence of over-learning/over-fitting of the One-class model (see Figure 5.11(b) and Table 5.6).

For Random forests, it was observed that the detection rate over various learning data sizes was excellent with zero false detection. Even by using a larger learning data set, the detection rate does not reduce supporting the claim that RF is immune to over-learning/over-fitting (see Figure 5.11(c)).

5.3 Robustness of machine learning methods *w.r.t* pavement medium

The parameters that define a debonding layer are its physical characteristics such as layer thickness and permittivity, or, the signal characteristics such as noise and scattering effects occurring within the debonding layer as summarized in Figure 5.12. Permittivity and thickness increase (or decrease subject to the $\lambda_{mat}/4$ limit) the signal strength, and therefore have an effect of the detection performance.

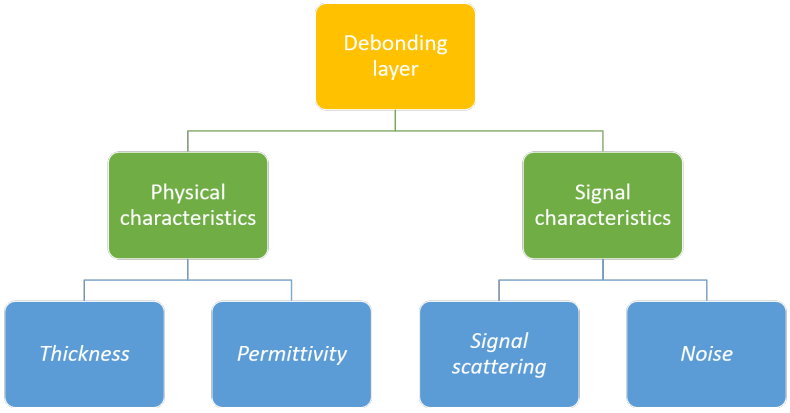

Figure 5.12: *Characteristics that define the echo for the debonding layer*

In this section, we present how well the machine learning methods (SVM, OCSVM and RF) adapt to the changes in characteristics of the medium. To do so, various B-scan configuration images are generated using the analytic Fresnel data model. Since local feature sets presented the detection rate higher (or sometimes closer) than the other

data sets (raw GPR or global), here the robustness of the machine learning methods is performed on the Local feature set. In addition, as done is the previous sections, the $\varepsilon_{r,deb}$-independent (*i.e*, global) optimization is used by the three machine learning methods.

5.3.1 Noise *vs.* permittivity variations

5.3.1.1 Analysis of noisy data

Noise plays an important role in the consistency of a signal and as such, the noise level of a signal may also limit the performance of the debonding detection methods. A machine learning method can be said to be robust enough if it can, with high accuracy, be able to detect debondings regardless of the presence of noise. Thus, an initial analyses of the machine learning methods is performed to observe their behavior at various noise levels.

Two-class SVM

As done in Chapter 5.2.2.1, the non-linear RBF kernel is analyzed here with its two parameters, C and γ. A 5-fold cross validation. The signal-to-noise ratio is varied from 10 dB to 60 dB. The resulting traces for the two hyper-parameters are averaged over 100 independent Monte-Carlo realizations.

Figure 5.13 presents the cost function C and γ hyper-parameters *w.r.t* Hinge-loss at various levels of SNR. The variation of the loss function at higher SNR levels is very low and the hyper-parameters are seen to be stabilized.

At low SNR, the erraticity of the signal and the signal features do not provide the 'best' optimal hyper-parameters. This can be seen by a larger $[C_{opt}, \gamma_{opt}]$ values in Figure 5.13(a). However, the increase in SNR results the signal features are well-separated leading to the generation of 'stable' hyper-parameters with very low loss (errors) in the learning step (as seen in Figure 5.13(b), 5.13(c), the increase in SNR gradually displaces the optimal $[C_{opt}, \gamma_{opt}]$ values).

One-class SVM

In case of One-class SVM, we present the effect of noise on the simulated data configurations with various $\varepsilon_{r,deb} = 2, 6, 10$. The methodology is as mentioned in Chapter 5.1. Figure 5.14 presents the optimization of the ν hyper-parameter at various levels of SNR for $\varepsilon_{r,deb} = 2$ (Figure 5.14(a)), $\varepsilon_{r,deb} = 6$ (Figure 5.14(b)) and $\varepsilon_{r,deb} = 10$ (Figure 5.14(c)). It can be observed that the hinge-loss is slightly dependent on the SNR value, except at SNR = 10 dB, where the loss function is non-zero even at low ν value indicating that due to low SNR, the optimization of the model is not completely accurate. However as the SNR increases, the loss is reduced to zero.

By using the optimization approaches presented above, we now present some results for the effect of noise on the performance of the machine learning methods.

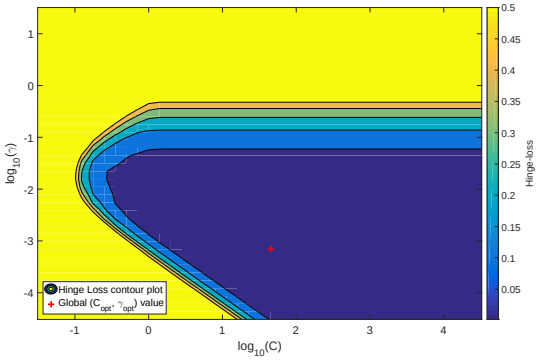

(a) SNR = 20 dB

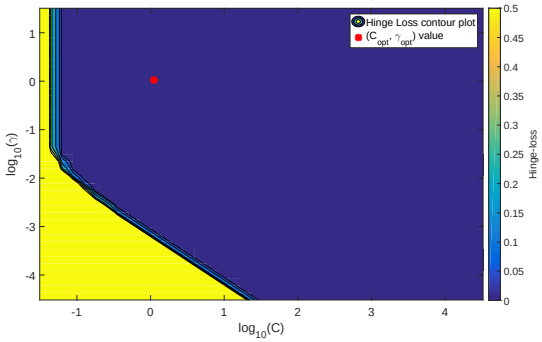

(b) SNR = 30 dB

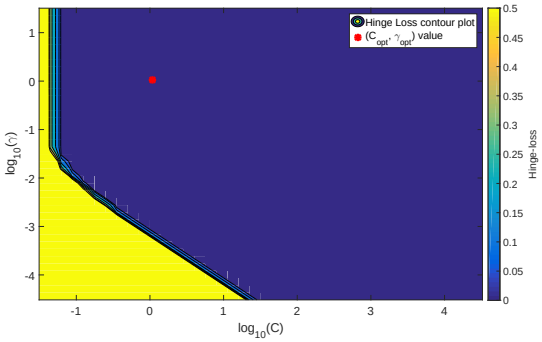

(c) SNR = 50 dB

Figure 5.13: *Representation of Hinge-loss function w.r.t. C and γ parameters for noisy simulated analytic data (see Appendix A) for $\varepsilon_{r,deb} = 2$ and $t_{deb} = 0.3\,\mathrm{cm}$ at different SNR levels. The red 'o' indicates the optimal hyper-parameter pair chosen during the CV stage*

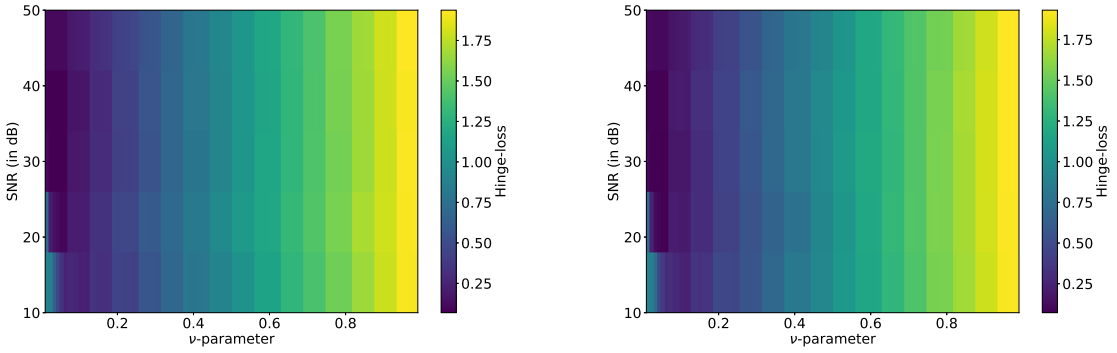

(a) $\varepsilon_{r,deb} = 2$

(b) $\varepsilon_{r,deb} = 6$

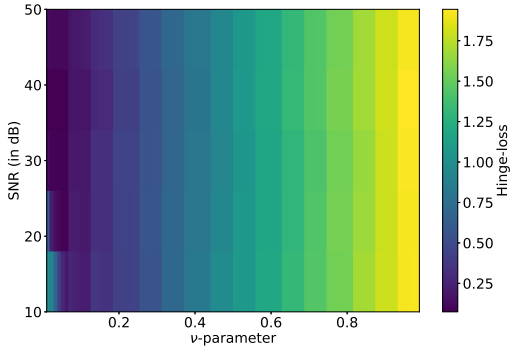

(c) $\varepsilon_{r,deb} = 10$

Figure 5.14: *Representation of Hinge-loss function w.r.t ν parameter for noisy simulated analytic data (see Appendix A) for $\varepsilon_{r,deb} = 2, 6, 10$ and $t_{deb} = 0.3\,\mathrm{cm}$ at various levels of SNR*

5.3.1.2 Some results

Figure 5.15(a), Figure 5.15(b) and Figure 5.15(c) compare the *DSC* score at various levels of SNR (= 10 dB to 60 dB) for $\varepsilon_{r,deb} = 6$ (weak contrast) and $\varepsilon_{r,deb} = 2, 10$ (strong contrast); the debonding thickness is fixed at $t_{deb} = 0.3$ cm for respectively Two-class SVM, One-class SVM and Random forests. These results are averaged over 100 independent Monte-Carlo realizations. Table 5.7, Table 5.8 and Table 5.9 present the *MCC* score for the same.

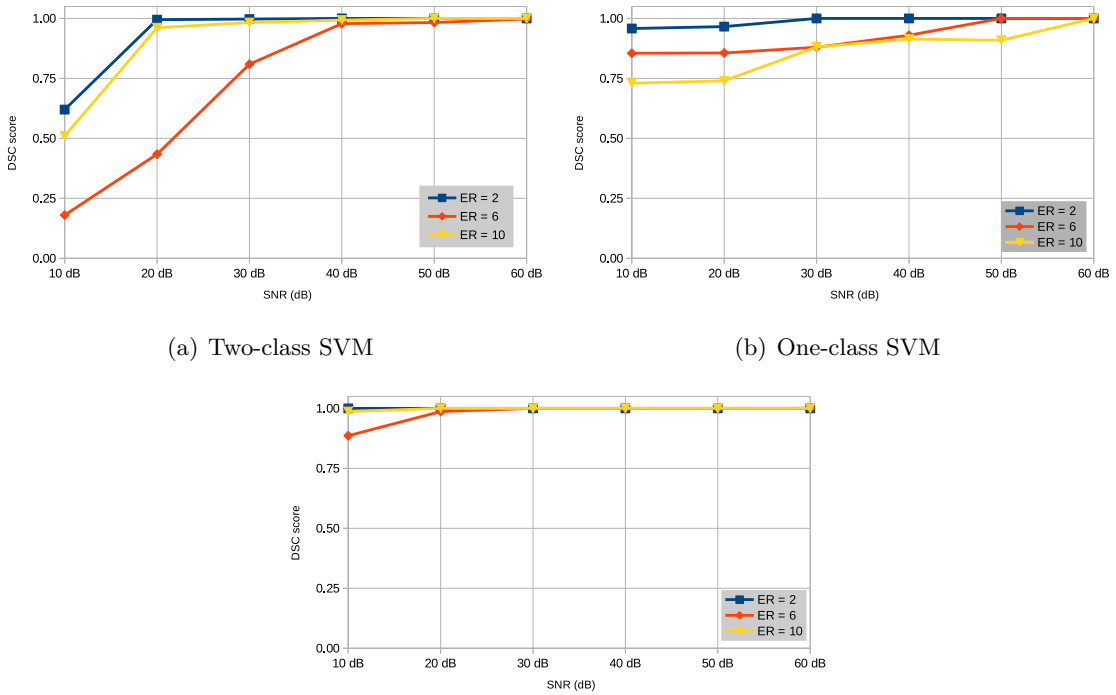

(a) Two-class SVM

(b) One-class SVM

(c) Random forests

Figure 5.15: *Comparison of DSC score vs. Signal-to-noise ratio for simulated analytic Fresnel data model ($\varepsilon_{r,deb} = 2, 6, 10$ and $t_{deb} = 0.3$ cm) using local features*

Table 5.7: *MCC coefficient for various levels of SNR values for noisy simulated (analytic Fresnel) data using Two-class SVM at various values of $\varepsilon_{r,deb}$*

$\varepsilon_{r,deb}$	10 dB	20 dB	30 dB	40 dB	50 dB	60 dB
2	0.61	**0.99**	**1.00**	**1.00**	**1.00**	**1.00**
6	0.05	0.18	0.70	**0.97**	**1.00**	**1.00**
10	0.37	**0.94**	**0.97**	**0.99**	**1.00**	**1.00**

At lower SNR values, due to the randomness in the signal, the signal features being unable to provide a good separation between debonding and non-debonding cases led to low detection rate (≈ 0.4) for Two-class SVMs. However, at stronger signal-to-noise ratios (≥ 30 dB), the efficiency was very high with very less (or none) false detection.

With the increase in SNR, the effect of noise is reduced thereby reducing the erratic

Table 5.8: *MCC coefficient for various levels of SNR values for noisy simulated (analytic Fresnel) data using One-class SVM at various values of* $\varepsilon_{r,deb}$

$\varepsilon_{r,deb}$	10 dB	20 dB	30 dB	40 dB	50 dB	60 dB
2	0.93	0.94	**1.00**	1.00	1.00	1.00
6	0.83	0.83	0.89	0.89	**1.00**	1.00
10	0.55	0.55	0.80	0.86	0.86	1.00

Table 5.9: *MCC coefficient for various levels of SNR for noisy simulated (analytic Fresnel) data using Random forests at various values of* $\varepsilon_{r,deb}$

$\varepsilon_{r,deb}$	10 dB	20 dB	30 dB	40 dB	50 dB	60 dB
2	**1.00**	1.00	1.00	1.00	1.00	1.00
6	0.81	0.98	**1.00**	1.00	1.00	1.00
10	0.98	**1.00**	1.00	1.00	1.00	1.00

signal behavior. Thus, an increase in the detection rate is observed. For SNR values greater than 30 dB, the detection rate is excellent. The case of $\varepsilon_{r,deb} = 10$ presented low detection rate at low SNR values. However, for SNR values ≥ 30 dB, both the *DSC* and *MCC* values indicated increased performance.

In case of Random forests, it can be observed that even at very low SNR values, Random forests has a very high detection rate ($> 80\%$) making it the best performing method among the three machine learning methods studied here. Random forests can thus be seen as a robust method that has a very low effect of noise and permittivity variations on debonding detection.

5.3.2 Debonding thickness and permittivity variations

The robustness of the machine learning methods depends on the capability of not only detection debondings but also the ability to do so for at different debonding characteristics. One such debonding layer characteristic that may change is the thickness.

Figure 5.16(a), Figure 5.16(b) and Figure 5.16(c) compare the *DSC* score for various debonding thicknesses with respective permittivities $\varepsilon_{r,deb1} = 2$ (strong contrast), $\varepsilon_{r,deb2} = 6$ (weak contrast) and $\varepsilon_{r,deb3} = 10$ (strong contrast) obtained using respectively Two-class SVM, One-class SVM and Random forests. The debonding thickness is chosen from $t_{deb} = 0.1$ cm, 0.3 cm, 0.5 cm, 0.7 cm and 0.9 cm, satisfying the $\lambda_{mat}/4$ condition. As done repeatedly in this chapter, we present the results averaged over 100 independent Monte-Carlo realizations. Due to the large dielectric contrast, the case of $\varepsilon_{r,deb1}$ and $\varepsilon_{r,deb3}$ are expected to provide better detection rates. As done in the previous sections, the global (*i.e*, $\varepsilon_{r,deb}$ independent) optimization approach is used here.

Additionally, Tables. 5.10, 5.11 and 5.12 presents the *MCC* score for the Two-class SVM, One-class SVM and Random forests respectively.

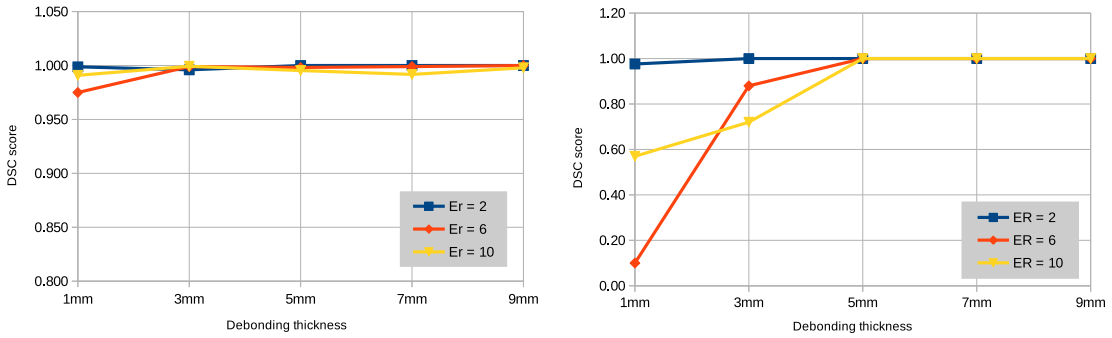

(a) Two-class SVM

(b) One-class SVM

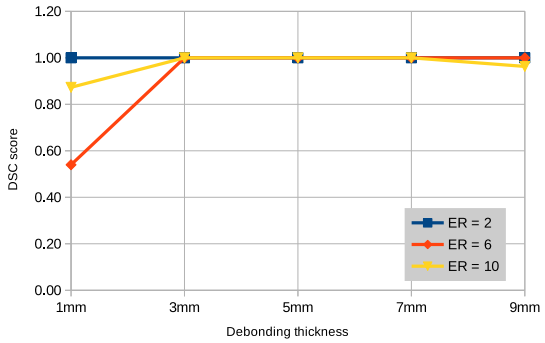

(c) Random forests

Figure 5.16: *DSC scores for the Material-based debonding layer SA for analytic Fresnel data using SVM.* $\varepsilon_{r1} = 5$, $\varepsilon_{r3} = 7$, $\varepsilon_{r,deb} = 2$, *6 and 10,* $t_{deb} = 0.1\,\text{cm}$, $0.3\,\text{cm}$, $0.5\,\text{cm}$, $0.7\,\text{cm}$ *and* $0.9\,\text{cm}$

Table 5.10: *MCC coefficient for various debonding thicknesses at SNR = 30 dB for noisy simulated (analytic Fresnel) data using Two-class SVM at various values of* $\varepsilon_{r,deb}$

$\varepsilon_{r,deb}$	0.1 cm	0.3 cm	0.5 cm	0.7 cm	0.9 cm
2	0.99	0.99	1.00	1.00	1.00
6	0.96	0.0.99	0.99	1.00	1.00
10	0.98	0.99	0.99	0.99	0.99

From the Figure 5.16(a) and Table 5.10, it can be observed that SVM is able to detect the presence of debondings of smaller thickness at various configurations with very high accuracy.

In case of One-class SVM, it was observed that in case of $\varepsilon_{r,deb} = 6$ and 10, the detection of debonding layers with very small thickness (*i.e.* 0.1 cm) was difficult due to the low physical and statistical variations between the debonding and non-debonding signals. For larger thickness ($t_{deb} > 0.1$ cm), the detection rate gradually increased to reach 100% efficiency for debonding over 0.5 cm thickness. On the other hand, $\varepsilon_{r,deb} = 2$ presented very high detection for the small thickness with excellent detection for all debonding thicknesses.

Table 5.11: *MCC coefficient for various debonding thicknesses at SNR = 30 dB for noisy simulated (analytic Fresnel) data using One-class SVM at various values of* $\varepsilon_{r,deb}$

$\varepsilon_{r,deb}$	0.1 cm	0.3 cm	0.5 cm	0.7 cm	0.9 cm
2	0.96	**1.00**	1.00	1.00	1.00
6	0.10	0.89	**1.00**	1.00	1.00
10	0.06	0.48	**1.00**	1.00	1.00

Table 5.12: *MCC coefficient for various debonding thicknesses at SNR = 30 dB for noisy simulated (analytic Fresnel) data using Random forests at various values of* $\varepsilon_{r,deb}$

$\varepsilon_{r,deb}$	0.1 cm	0.3 cm	0.5 cm	0.7 cm	0.9 cm
2	**1.00**	1.00	1.00	1.00	1.00
6	0.30	**1.00**	1.00	1.00	1.00
10	0.785	**1.00**	1.00	1.00	0.94

Random forests presented similar results as those of Two-class SVM. However, at very small debonding thickness *i.e* 0.1 cm, the Two-class SVM performed better than Random forests. For thicknesses $t_{deb} \geq 0.3$ cm both Two-class SVM and Random forests performed excellently.

5.3.3 Single scattering *vs.* Multiple scattering effects

As presented in Appendix A, the analytic Fresnel data model can be expressed as a single scattering model as well as a multiple scattering model. While the single scattered signal is a sum of simple reflections from the top and bottom interface of the debonding layer, in case of multiple scattering the reflected echo from the debonding layer is a composite signal consisting of several reflections occurring within the layer. Figure 5.17 compares two debonding A-scan signals for $\varepsilon_{r,deb} = 2$ at $t_{deb} = 0.3\,\text{cm}$ with single and multiple scattering within the debonding layer.

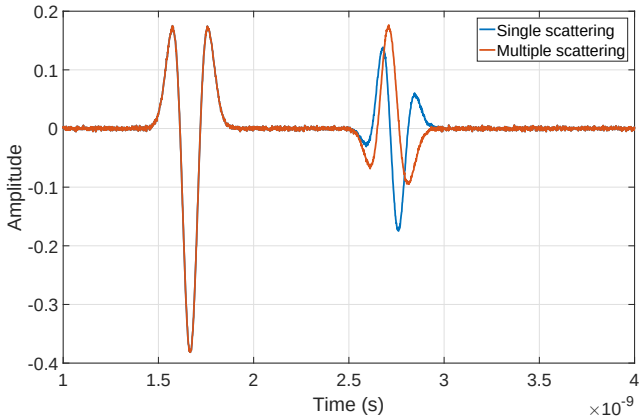

Figure 5.17: *Comparison of debonding A-scan signals with single and multiple scattering within the debonding layer for simulated analytic Fresnel data model ($\varepsilon_{r,deb} = 2$ and $t_{deb} = 0.3\,\text{cm}$)*

Although both single and multiple scattering are theoretical cases, the multiple scattering effect is likely closer to the practical situations for roughless interfaces. In this section, we analyze the effect of signal scattering on the performance of a machine learning method. The methodology is as explained in Chapter 5.1. Local signal feature set with 5-fold cross validation are used.

In case of the Two-class SVM, the non-linear RBF kernel is used. On the contrary, in case of One-class SVM, a linear kernel is used. Figure 5.18, present the *DSC* score variation for the three noisy simulated data configurations for respectively Two-class SVM (Figure 5.18(a)), One-class SVM (Figure 5.18(b)) and Random forests (Figure 5.18(c)). Table 5.13 presents the *MCC* score for the three methods.

It can be observed that in case of Random forests and Two-class SVM, similar performances were observed in for both single and multiple scattering conditions. For both methods, the detection rate observed at SNR $= 30\,\text{dB}$ was ≈ 1 indicating that the two methods are insensitive to the scattering effects of the signal within the debonding layer. On the other hand, in case of One-class SVM, the ideal single scattering scenario presented higher debonding detection rate in comparison to multiple scattering.

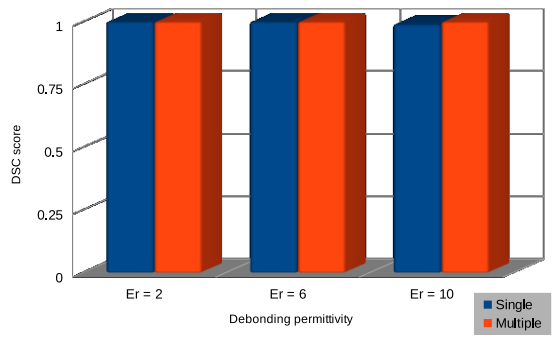

(a) Two-class SVM

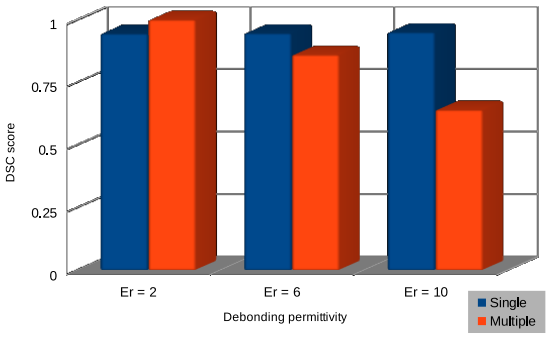

(b) One-class SVM

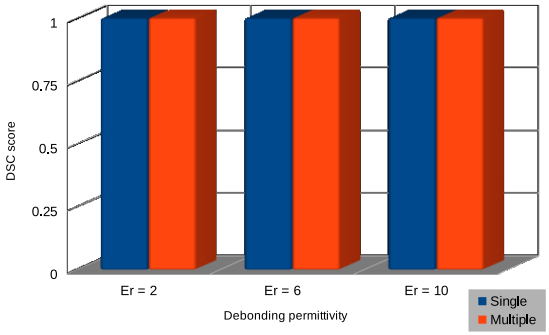

(c) Random forests

Figure 5.18: *Comparison of DSC score for single vs. multiple scattering for simulated analytic Fresnel data model ($t_{deb} = 0.3\,\mathrm{cm}$) using local features at* $30\,\mathrm{dB}$ *SNR value*

Table 5.13: *MCC coefficient for various levels of SNR for noisy simulated (analytic Fresnel) data using Two-class, One-class SVMs and Random forests at various values of* $\varepsilon_{r,deb}$ *with SNR* $= 30\,\mathrm{dB}$ *for* $t_{deb} = 0.3\,\mathrm{cm}$

$\varepsilon_{r,deb}$	**Two-class SVM**		**One-class SVM**		**Random forests**	
	Single	*Multiple*	*Single*	*Multiple*	*Single*	*Multiple*
2	1.00	1.00	0.9	1.00	1.00	1.00
6	1.00	1.00	0.911	0.794	1.00	1.00
10	0.99	1.00	0.92	0.681	1.00	1.00

5.4 Summary

In this chapter, the three supervised machine learning methods were compared and their robustness *w.r.t*, the pavement medium and the model characteristics were studied. Table 5.4 presents a short comparison of the three methods in terms of performance in general.

Table 5.14: *Synthesis of the robustness of supervised machine learning methods*

Category	Two-class SVM	One-class SVM	Random Forests
1. Kernel functions	Overall, for the two-class SVM, all the kernels presented high efficiency	Linear and Polynomial kernels provided the best detection efficiency	*Not applicable*
2. Cross validation	k-fold and LOO-CV presented similar yet excellent results	k-fold CV provided the best results followed by LOO-CV	*Not applicable*
3. Learning data size	Performance affected at smaller learning data; very high efficiency at larger learning data sizes	Did not require a large number of training samples to create a classification model since it depends only on one type of data; better performance at small learning sets	Repeated testing in RF (at various 'trees') provided excellent debonding detection even while using a small learning sample set
4. Debonding thickness	Was easily able to detect debondings of $t_{deb} = 0.1\,\text{cm}$ with very high accuracy	One-class SVM was unable to detect smaller defects in some cases. However, debondings of $t_{deb} \geq 0.1\,\text{cm}$ were detected with ease	Was easily able to detect debondings of $t_{deb} = 0.1\,\text{cm}$ with very high accuracy.
5. Debonding permittivity	In general, all 3 methods were able to detect the presence of debodings at various permittvity values ($\varepsilon_{r,deb} = 2$, 6 and 10)		
6. Effect of noise	At low SNR values, the performance was low with several false detection. However, with the increase in SNR, all the methods showed increased accuracy with very few (or none) false detection		

Table 5.14: *Synthesis of the robustness of supervised machine learning methods*

Category	Two-class SVM	One-class SVM	Random Forests
7. Signal scattering effects	No convincing difference observed for debonding detection for single or multiple scattering	Presented similar results in case of $\varepsilon_{r,deb} = 2,6$. However, for $\varepsilon_{r,deb} = 10$, the multiple scattering effects seem to reduce the detection compared to single scattering	Similar conclusions as Two-class SVM were seen for RF as well
	(**Note**: *This behavior has been seen to be coherent whilst* $t_{deb} \leq \lambda_{mat}/4$*; beyond which, the performance is found to vary for the two cases*)		

5.5 Conclusion

We began this chapter by introducing the optimization of machine learning methods by various approaches. The first approach to optimize the methods included the model-fitting approach using CV technique and kernel functions. The detection was carried out using local signal features since, as presented in Chapter 4, these features are focused at the pavement interface, thus provide more accurate information. The ROC curves (used previously in Chapter 4.3) were replaced with performance indexes of DSC score and MCC (presented in Appendix C.2) since they provided a more representative result. By the use of parameter tuning, it was possible to improve the performance of the methods and also, prevent over-fitting the model. By conducting parameter tuning on simulated as well as experimental data, analysis of various approaches was done.

It was observed that, in case of Two-class SVM, although Holdout was a simple CV technique, the k-fold CV (with $k = 5$) provided the best debonding detection rate. The sigmoid and polynomial kernel functions were the least efficient and although linear kernel was efficient for simulated cases, the RBF kernel function was useful for all types of data. SVM also presented a good robustness to noisy (simulated) data at various levels of SNR and with a suitable learning data size, provided very high detection rate. Finally, the adaptability was tested over various debonding thicknesses. SVM was able to detect debondings with various thicknesses (subject to the $\lambda_{mat}/4$ limit).

In case of Random forests, similar conclusions were drawn. RF provided very high detection rate at SNR over 20 dB for all debonding thickness. Also, it was observed that the performance of RF was immune to the problem of over-learning as it presented an excellent debonding detection for all learning data sizes (simulated data).

In case of the anomaly detection OCSVM method, it was observed that the k-fold CV once again presented better results compared to its counterparts. However, linear kernel presented the best results over all the simulated data. At low levels of SNR ($= 10$ dB), OCSVM presented difficulty in the detection; however, the detection rate increased rapidly with the increase in SNR. Debonding detection with very low false detection was observed for SNR over 30 dB. OCSVM was able to detect debondings with very high accuracy using smaller sets of learning data over various debonding thickness. However, by increasing the learning data size over a specific value resulted in the decrease in the detection rate suggesting the occurrence of overlearning.

Due to its immunity to over-learning, adaptability to various material characteristics (permittivity, debonding thickness and noise), Random forests was observed to provide the best debonding detection compared to SVM (both Two-class and One-class).

By performing parameter tuning and analyzing the robustness of the machine learning methods using analytic data, it is now possible to replicate the similar methodologies on experimental data. In the next chapter, we implement our methodologies and approaches studied in Chapter 4 and Chapter 5 on experimental data. These experimental data are collected using various GPR configurations at two test sites respectively located at Cerema and IFSTTAR.

Chapter 6

Application For Decision Support To Detect Debondings

Contents

In Chapter 3, we presented the supervised machine learning methods that were studied throughout this thesis to detect interlayer debondings. Chapter 4 presented the preprocessing of GPR data by means of signal feature selection. It was observed that the local signal features provided the best debonding detection rate. Finally, in Chapter 5, we demonstrated the optimization of the machine learning methods based on the input parameters (and hyper-parameters) and also the robustness of each method to the pavement medium characteristics.

This chapter incorporates all the studies and analyses performed in the previous chapters to optimize the machine learning methods on real experimental data. Two sets of experimental data collected at two independent sites located respectively at Nantes (IFSTTAR) and Angers (Cerema) will be analyzed in this chapter. The first database is a controlled thickness with air-void debondings of thicknesses 0.5 cm and 1.0 cm using a commercial GSSI radar (see Appendix B.2 for detailed description). On the other hand, the second database is collected at the fatigue carousel at IFSTTAR with artificially induced defects of different characteristics (see Appendix B.3 for detailed description).

The objective of this chapter is two-fold: firstly, we present the detection of debondings as a binary result, as presented in the previous chapters for simulated analytic databases. We then introduce the estimation of probability of debonding occurrences in the pavement structures. Probability estimates is expected to provide a much more efficient and convenient information than its counterpart binary values (*i.e.* -1 or +1). Additionally, these estimates can also be used as a measure of their own errors leading to a more comprehensible result.

6.1 Debonding detection on experimental data

The detection of debondings using simulated analytic data has been presented in Chapter 3 (using raw GPR data) and Chapter 4 (using signal features). In Chapter 5, we presented the optimization of the machine learning methods and the robustness of the methods was studied. In this section, we implement the optimized machine learning models on experimental data collected at two independent test sites.

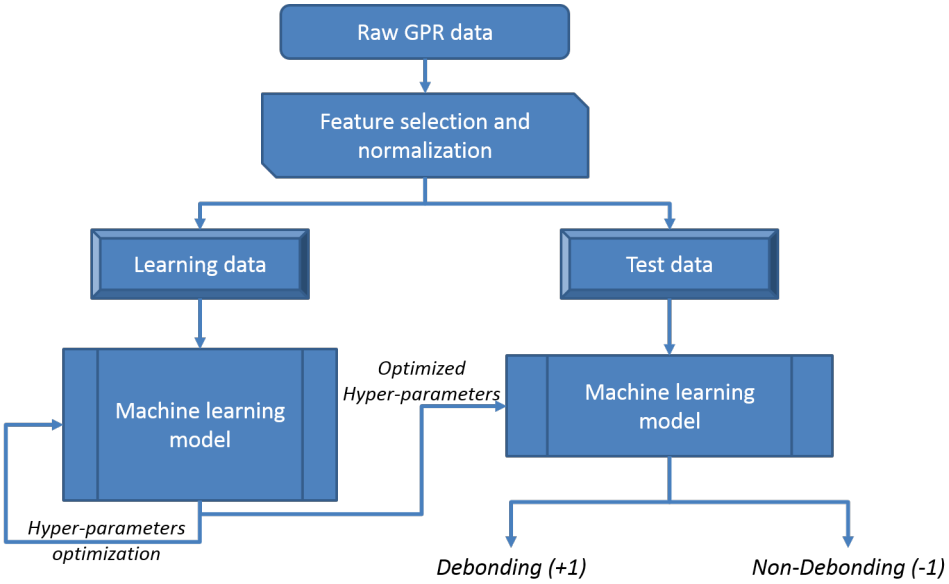

Figure 6.1: *Formulation of machine learning methods for the debonding detection*

The classification results obtained by individual machine learning methods are compared to the benchmarked conventional reference method, namely Amplitude Ratio Test (see Chapter 2.6). The formulation of the machine learning methods shown in Figure 6.1 presents the overall approach of the formulation of machine learning methods for the debonding detection. In case of binary detection, the indexes of DSC and MCC are used to represent the performance numerically, whereas, in case of probabilistic estimation, we use DPR and NPR rates. The performance using the conventional reference method, namely ART, is presented as a benchmark for binary detection).

In case of SF-GPR data, as presented in our article [10], the selected strategies for the machine learning methods have been optimized for individual type of defects separately, namely, Tack-free, Sand and Geotextile.

On the other hand, in case of air-void test slabs (GC-GPR), the machine learning methods are combinedly optimized over both debonding thicknesses, *i.e,* 0.5 cm and 1.0 cm.

6.2 Artificial air-void debonding detection in test slabs

As mentioned in Appendix B, the data collected at the test site in Cerema-Angers using air-void test slabs at two thicknesses, namely $t_{deb} = 0.5$ cm and 1.0 cm. The radar for data acquisition is a commercial ground-coupled GPR, namely GSSI SIR-3000. As mentioned in [13], to avoid the edge/border effect, the A-scans from the central zone of the test slabs are taken into consideration. The main challenge in this section is indirectly to test the sensitivity of the classification methods to the slight time overlapping between the clutter and the interlayer interface echoes.

In this section, we present the results for two test bench configurations each consisting of air-void gaps of 0.5 cm and 1.0 cm:

- **Configuration 1**: Layers in the order (from top to bottom) BBTM, BBSG and GB
- **Configuration 2**: Layers in the order (from top to bottom) BBTM, GB and BBSG

6.2.1 Two-class SVM

Figure 6.2(a) and Figure 6.2(b) compares the binary detection against the probability estimation of the occurrence of debondings from local signal features for two configurations of the test slabs using Two-class SVM with air-void gaps of thickness $t_{deb} = 1.0$ cm. The methodology is as done previously in Chapter 6.1. The data with air-void gap of thickness $t_{deb} = 0.5$ cm is used as learning data and the data of $t_{deb} = 1.0$ cm are used as test data. In case of probability estimation as well, the non-linear RBF kernel is used.

For binary detection, the DSC and MCC coefficients obtained for Configuration 1 were respectively 0.96 and 0.95 for Configuration 2 were respectively 1 and 1. Table 6.1 presents the DPR and NPR for the two configurations and Table 6.4 presents the DSC and MCC for the two configurations.

Table 6.1: *DPR and NPR coefficients for probability estimation from local signal features for various air-void thicknesses of the test bench using Two-class SVM*

Debonding thickness	Configuration 1		Configuration 2	
	DPR	NPR	DPR	NPR
$t_{deb} = 1.0$ cm	0.88	0.92	0.93	0.98

6.2.2 One-class SVM

Figure 6.3(a), Figure 6.3(b) , Figure 6.3(c) and Figure 6.3(d) compares the binary detection against the probability estimation of the occurrence of debondings from local

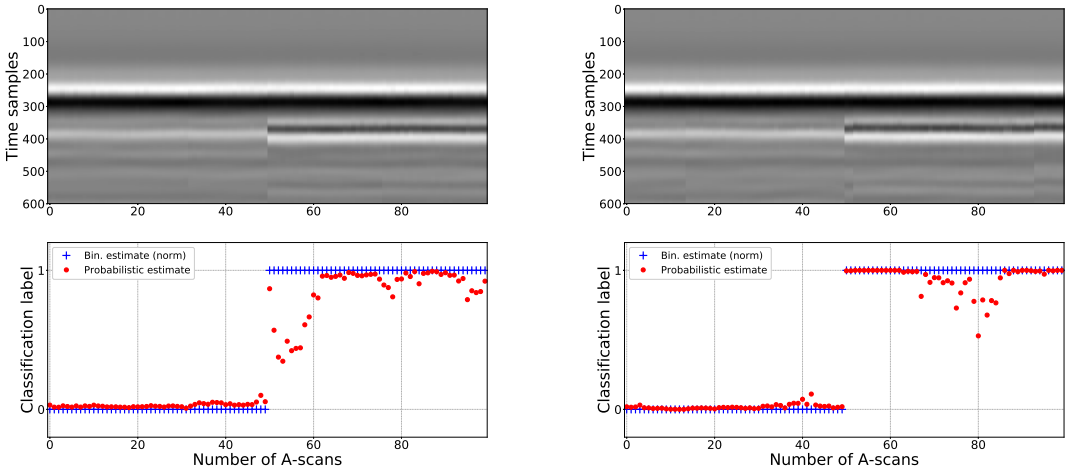

(a) Configuration 1

(b) Configuration 2

Figure 6.2: *Two-class SVM Probabilistic estimate for GSSI-GPR data using local features for various test bench configurations*

signal features for various test bench configurations and air-void thicknesses using One-class SVM. The vertical dashed lines indicate the learning data set which is devoid of debondings. For the sake of comparison, each figure also presents the binary estimation of debondings using One-class SVM.

To have a convenient form of representing the results, Table 6.2 compares the DPR and NPR coefficients (see Appendix C for details) for the results from Figure 6.2. From Table 6.2, it can be seen that in both configurations, the DPR and NPR rates are very high. Table 6.4 presents the DSC and MCC for the two configurations using One-class SVM.

Table 6.2: *DPR and NPR coefficients for probability estimation from local signal features for various air-void thicknesses of the test bench using One-class SVM*

Debonding thickness	Configuration 1		Configuration 2	
	DPR	NPR	DPR	NPR
$t_{deb} = 0.5\,\text{cm}$	0.99	0.92	0.99	0.99
$t_{deb} = 1.0\,\text{cm}$	0.98	0.92	0.98	0.88

6.2.3 Random forests

Figure 6.4(a) and Figure 6.4(b) compare the binary detection against the probability estimation of the debonding occurrence from local signal features for the two configurations of the test slabs using Random forests with air-void gaps of thickness $t_{deb} = 1.0\,\text{cm}$. The methodology is as done previously in Chapter 6.1 for two-class SVM results. The data

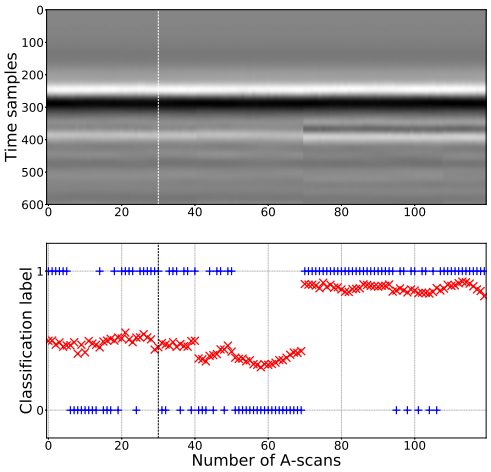

(a) Configuration 1; $t_{deb} = 0.5\,\text{cm}$

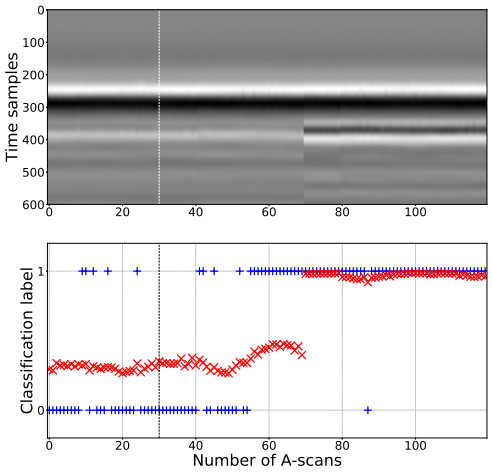

(b) Configuration 1; $t_{deb} = 1.0\,\text{cm}$

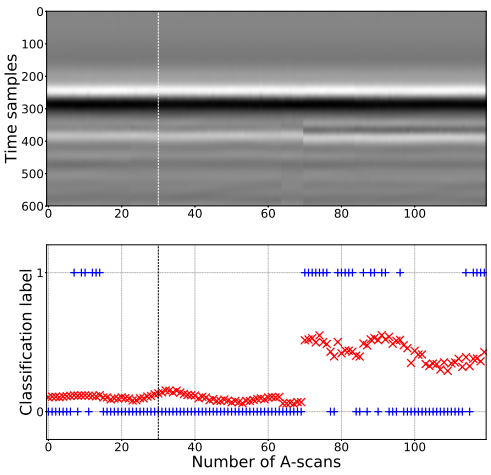

(c) Configuration 2; $t_{deb} = 0.5\,\text{cm}$

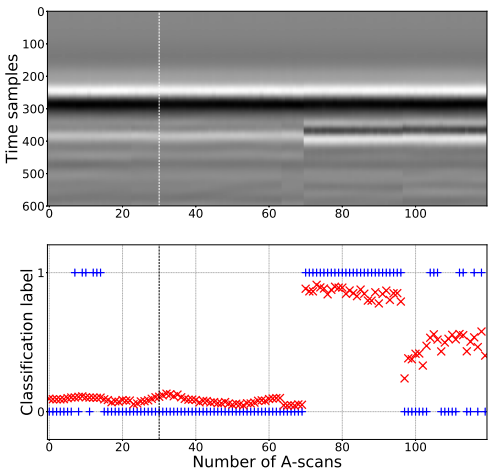

(d) Configuration 2; $t_{deb} = 1.0\,\text{cm}$

Figure 6.3: *One-class SVM Probabilistic estimate for GSSI-GPR data using local features for various test bench configurations*

with air-void gap of thickness $t_{deb} = 0.5\,\text{cm}$ is used as learning data and $t_{deb} = 1.0\,\text{cm}$ are used as test data. In case of probability estimation, Gini impurity is used with the values for the optimal data size for each subset (p) and number of trees (T) as mentioned in Chapter 4 and Chapter 5.

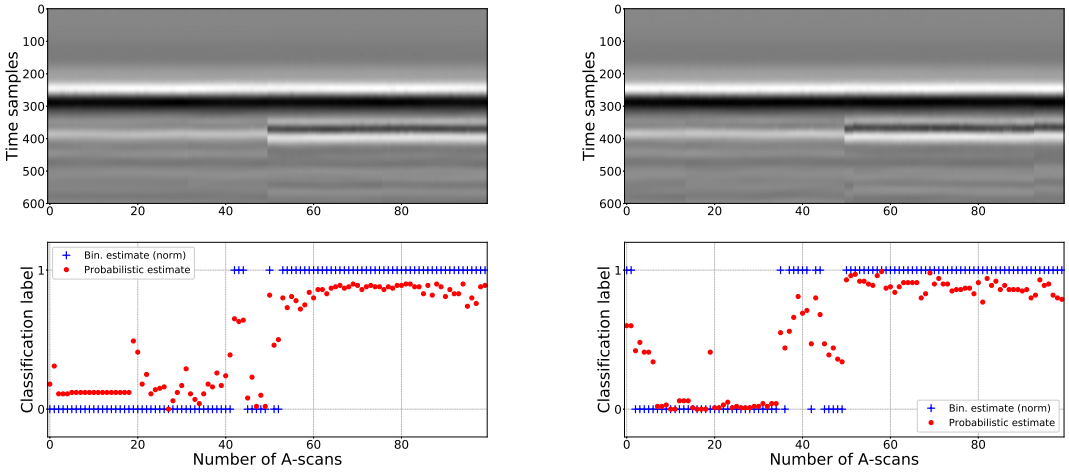

(a) Configuration 1

(b) Configuration 2

Figure 6.4: *Random forests Probabilistic estimate for GSSI-GPR data using local features for various test bench configurations*

For binary detection, the DSC and MCC coefficients obtained for Configuration 1 were respectively 0.96 and 0.92 for Configuration 2 were respectively 0.94 and 0.92. Table 6.3 presents the DPR and NPR rates obtained for Configuration 1 and 2 for the test data *i.e*, $t_{deb} = 1.0\,\text{cm}$ and Table 6.4 presents the DSC and MCC for the same.

Table 6.3: *DPR and NPR coefficients for probability estimation from local signal features for various air-void thicknesses of the test bench using Random forests*

Debonding thickness	Configuration 1		Configuration 2	
	DPR	NPR	DPR	NPR
$t_{deb} = 1.0\,\text{cm}$	0.83	0.82	0.82	0.82

6.2.4 Benchmark comparison with reference method

In order to assess the performance of binary debonding detection of each method on experimental data from Cerema, we compare the results with the reference method, namely ART. Table 6.4 compares the MCC coefficient and the DSC score of the three methods *w.r.t* ART.

Table 6.4: *Comparison of DSC ([..]) and MCC ((..)) scores for debonding detection from local signal features for various methods at* $t_{deb} = 1.0\,\text{cm}$ *at two test bench configurations*

Method	Configuration 1	Configuration 2
ART (reference method)	[0.94], (0.97)	[0.93], (0.97)
Two-class SVM	[0.95], (0.96)	[1.00], (1.00)
One-class SVM	[0.79], (0.66)	[0.87], (0.77)
Random forests	[0.96], (0.92)	[0.94], (0.92)

We can see that the performance is not as high as observed in simulated databases, specially in case of One-class SVM. It is also seen that the reference method has a good performance for both configurations. However, such performance cannot be guaranteed for all cases of ground coupled GPR since in case of wideband ground-coupled GPR (such as GSSI-GPR used in our experiments), the second echo almost always overlaps with the clutter/first echo (see Figure B.6) and thus, it is difficult to isolate of second echo (see Figure B.6). On the other hand, both Two-class SVM and Random forests have very high performance as well in both configurations despite the difficulty in obtaining the second echo for local signal features. Besides, we observe that the feature-based results of Two-Class SVM have an improved debonding detection rate compared to the raw-data-based results in [13].

6.3 Artificial debonding detection from embedded in pavements

In this section, we present the debonding detection from the second experimental database collected at IFSTTAR's fatigue carousel (presented in detail in Appendix B). The radar for data acquisition is an experimental air-launched stepped-frequency radar operating in UWB.

It should be noted that, as mentioned in Appendix B, a certain zone of the data is sectioned as 'transition zone' since the this zone contains ambiguous data and it is ignored during the computation of performance indexes.

In case of Two class SVMs, the initial loading data (*i.e*, 10K loading) is used as learning data to create the Two-class model. The remainder of the data are subsequently used for testing. This approach is already used and has been adapted in [10]. The same approach is used for Random forests as well for coherence. In case of Geotextile defects at 10K cycles loading, due to the bad quality of the data collected over the pavement, most of the data is lost in the transition zone. Thus, both Two-class SVM and Random forests use 50K cycles loading as learning data and the remaining loading as test data.

On the other hand, in case of One-class SVMs, the approach is as adapted in our article [309]. At each K-loading stage, a known zone of healthy data (consisting of 20 A-scans) is used for learning to generate the One-class model. The remainder of the data is used for testing.

A transition zone is indicated in each figure for the B-scan images as a blue dashed box. This zone is excluded while computing the performance indexes for both binary and probability estimations.

6.3.1 Two-class SVM

Figure 6.5, Figure 6.6 and Figure 6.7 compares the binary detection against the probability estimation of the occurrence of debondings from local signal features at 10K and 300K loading stages for respectively Geotextile, Sand and Tack-free based defects using Two-class SVM. For intermediate loading stages, the figures (Figure E.1, Figure E.2, Figure E.3) are presented in Appendix E. The methodology is as presented in the article [10]. The 10K cycles loading stage data is used as learning data and the remainder of the data are used as test data. In case of probability estimation as well, the non-linear RBF kernel is used.

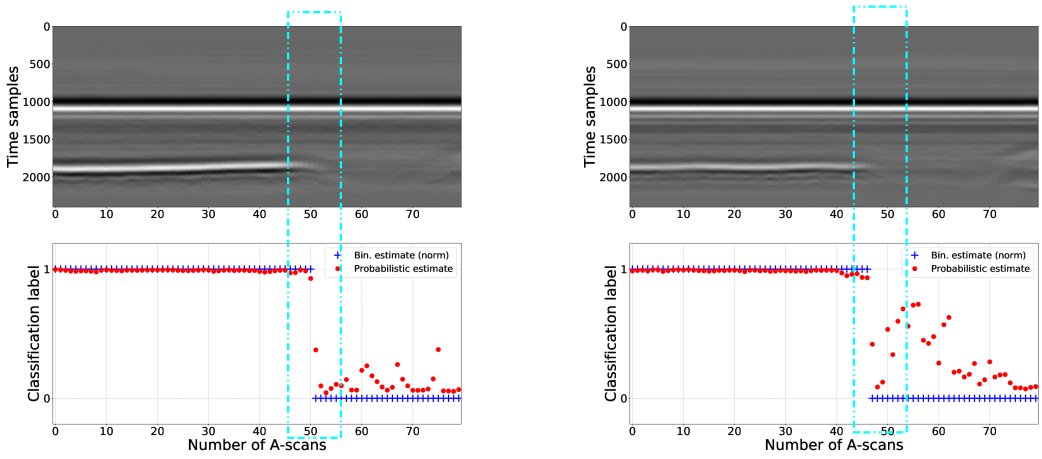

(a) 50K loading (learning data)

(b) 300K loading

Figure 6.5: *Two-class SVM debonding detection estimates for SF-GPR data using local features at initial and final loading stages for Geotextile-based defects (strong debonding permittivity contrast)*

Table 6.5 presents the DPR and NPR rates for the three types of defects over initial and final loading stages using local features for Two-class SVM. Table E.1 in Appendix E presents the for the intermediate loading stages.

6.3.2 One-class SVM

Figure 6.8, Figure 6.9 and Figure 6.10 present the probability estimation of the occurrence of debondings from local signal features at 10K and 300K loading stages for respectively Geotextile, Sand and Tack-free based defects using One-class SVM. For intermediate loading stages, the figures (Figure E.4, Figure E.5, Figure E.6) are presented in Appendix E. The vertical dashed lines indicate the learning data set which is devoid of

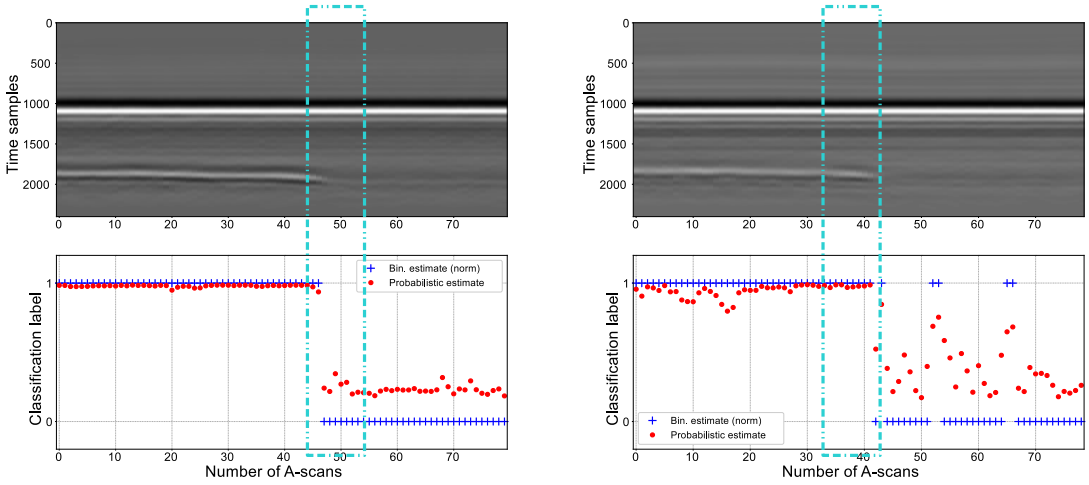

(a) 10K loading (learning data) (b) 300K loading

Figure 6.6: *Two-class SVM debonding detection estimates for SF-GPR data using local features at initial and final loading stages for Sand-based defects (average debonding permittivity contrast)*

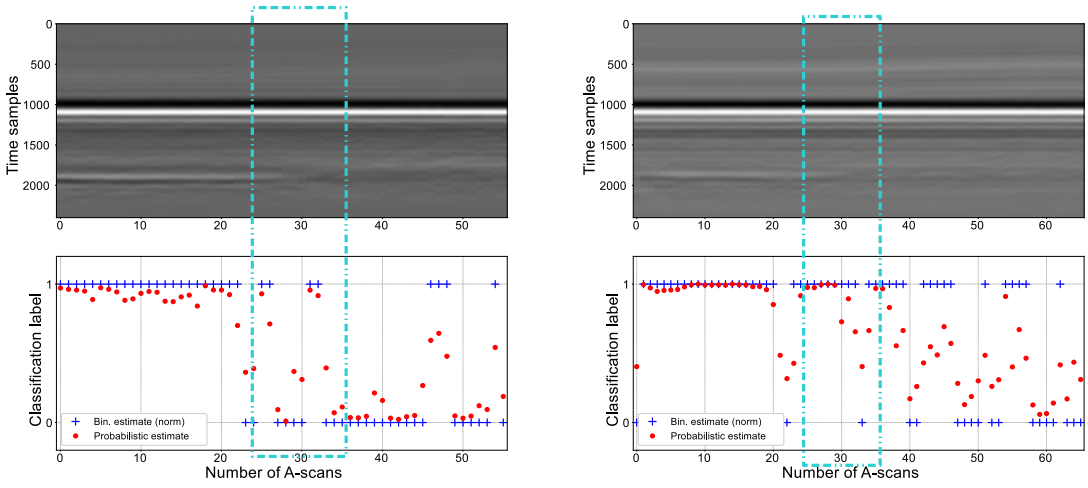

(a) 10K loading (learning data) (b) 300K loading

Figure 6.7: *Two-class SVM debonding detection estimates for SF-GPR data using local features at initial and final loading stages for Tack free-based defects (weak debonding permittivity contrast)*

Table 6.5: *DPR and NPR coefficients for probability estimation from local signal features at 10K (initial stage) and 300K (final stage) loading for respectively Geotextile, Sand and Tack-free based defects using Two-class SVM*

Loading stage	Geotextile		Sand		Tack-free	
	DPR	*NPR*	*DPR*	*NPR*	*DPR*	*NPR*
50K cycles	0.98	0.58	0.99	0.62	0.63	0.51
300K cycles	0.99	0.53	0.74	0.63	0.84	0.82

debondings. For the sake of comparison, each figure also presents the binary estimation of debondings using One-class SVM.

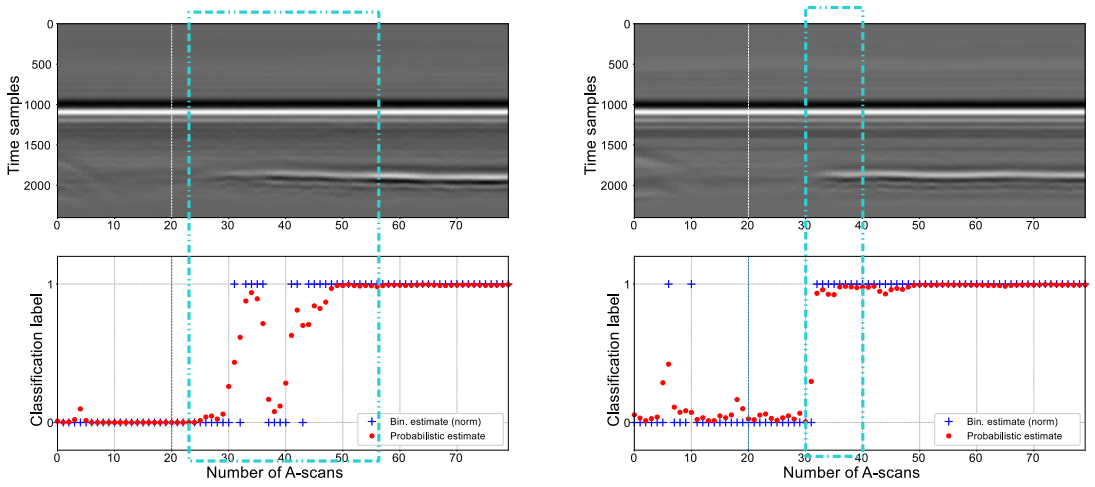

(a) 10K loading

(b) 300K loading

Figure 6.8: *One-class SVM debonding detection estimates for SF-GPR data using local features at initial and final loading stages for Geotextile-based defects (strong debonding permittivity contrast)*

Table 6.6: *DPR and NPR coefficients for probability estimation from local signal features at 10K (initial stage) and 300K (final stage) loading for respectively Geotextile, Sand and Tack-free based defects using One-class SVM*

Loading stage	Geotextile		Sand		Tack-free	
	DPR	*NPR*	*DPR*	*NPR*	*DPR*	*NPR*
10K cycles	0.99	0.92	0.99	0.99	0.98	0.92
300K cycles	0.98	0.86	0.99	0.93	0.84	0.85

To provide a more convenient from of representation of results, Table 6.6 compares the *DPR* and *NPR* coefficients (see Appendix C for details) for the three defects at the initial

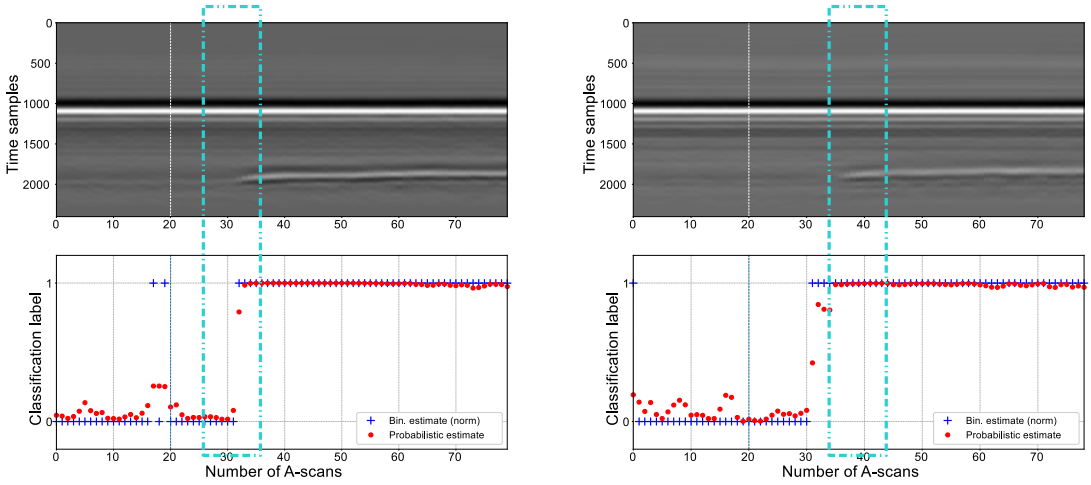

(a) 10K loading (b) 300K loading

Figure 6.9: *One-class SVM debonding detection estimates for SF-GPR data using local features at initial and final loading stages for Sand-based defects (average debonding permittivity contrast)*

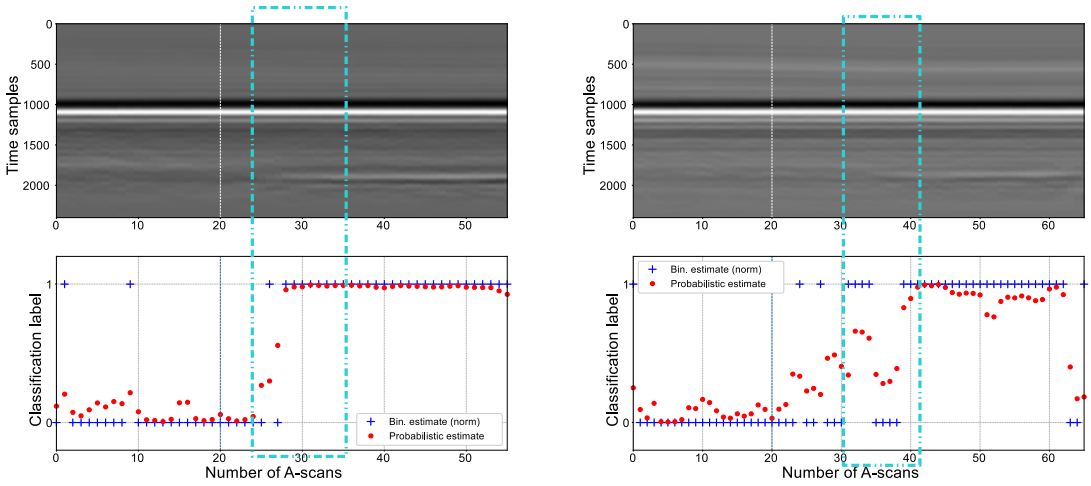

(a) 10K loading (b) 300K loading

Figure 6.10: *One-class SVM debonding detection estimates for SF-GPR data using local features at initial and final loading stages for Tack free-based defects (weak debonding permittivity contrast)*

and final loading stages. Table E.2 in Appendix E presents the same for the intermediate loading stages.

From the tables, it can be seen that, in case of Geotextile and Sand (strong defects), the prediction rates for both debonding and non-debonding (respectively DPR and NPR) are very high. In case of Tack-free defects as well, similar observations are seen.

6.3.3 Random forests

Figure 6.11, Figure 6.12 and Figure 6.13 present the probability estimation of the occurrence of debondings from local signal features at 10K and 300K loading stages for respectively Geotextile, Sand and Tack-free based defects using Random forests. For intermediate loading stages, the figures (Figure E.7, Figure E.8, Figure E.9) are presented in Appendix E. The methodology is as done previously in Chapter 6.1. The 10K loading stage data is used as learning data and the remainder of the data are used as test data.

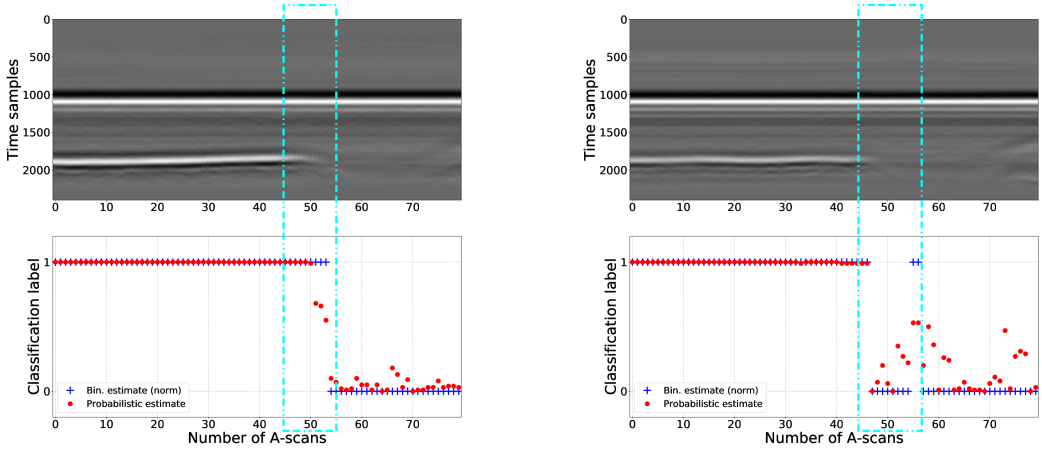

(a) 50K loading (learning data)

(b) 300K loading

Figure 6.11: *Random forests debonding detection estimates for SF-GPR data using local features at initial and final loading stages for Geotextile-based defects (strong debonding permittivity contrast)*

Table 6.7: *DPR and NPR coefficients for probability estimation from local signal features at 10K (initial stage) and 300K (final stage) loading for respectively Geotextile, Sand and Tack-free based defects using Random forests*

Loading stage	Geotextile		Sand		Tack-free	
	DPR	NPR	DPR	NPR	DPR	NPR
50K cycles	1.00	0.66	1.00	0.52	0.84	0.91
300K cycles	1.00	0.68	0.98	0.86	0.88	0.68

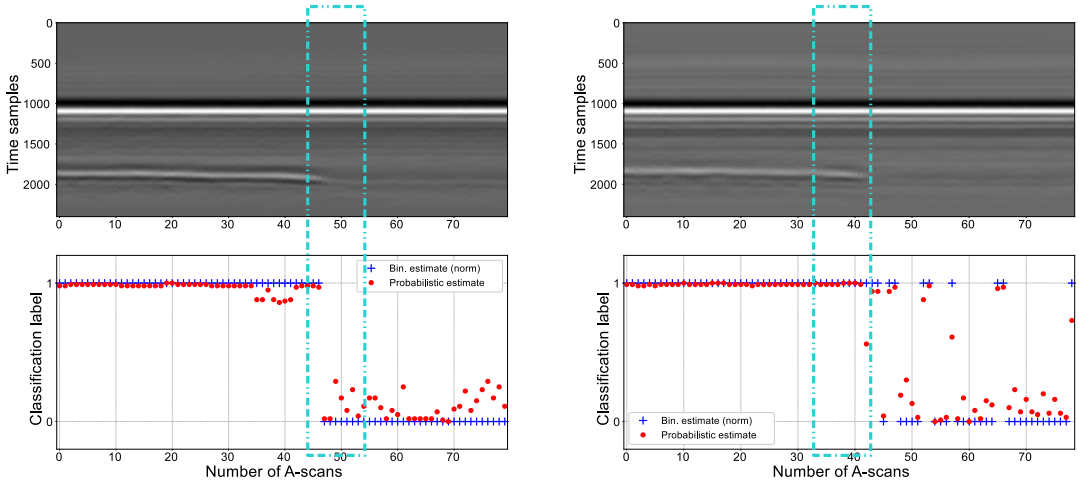

(a) 10K loading (learning data) (b) 300K loading

Figure 6.12: *Random forests debonding detection estimates for SF-GPR data using local features at initial and final loading stages for Sand-based defects (average debonding permittivity contrast)*

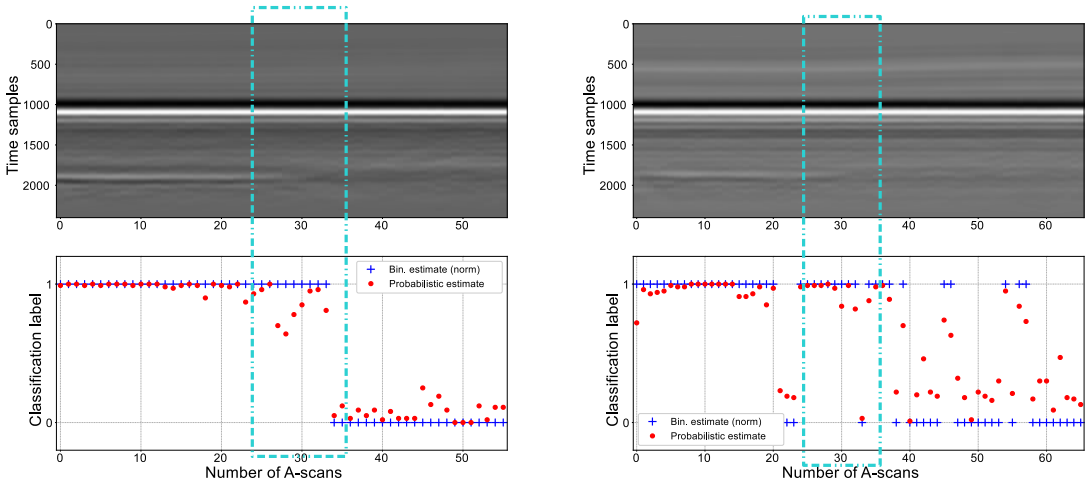

(a) 10K loading (learning data) (b) 300K loading

Figure 6.13: *Random forests debonding detection estimates for SF-GPR data using local features at initial and final loading stages for Tack free-based defects (weak debonding permittivity contrast)*

For qualitative representation of results, Table 6.7 compares the DPR and NPR coefficients (see Appendix C for details) for the three defects at the initial and final loading stages. Table E.3 in Appendix E presents the same for the intermediate loading stages.

It can be observed that in case of all the three defects, the debonding detection rate is excellent. However, in case of Tack-free based defects at 200K loading, the DPR rate was found to be low ($DPR \approx 0.65$)

In the following section, we compare the performance of each method against the reference method, namely ART.

6.3.4 Benchmark comparison with reference method

As done previously in Chapter 6.2.4 for GSSI-GPR air-void debondings database, here, we once again compare the performance of SF-GPR data at various loading stages against the reference ART method.

Table 6.8, Table 6.9, and Table 6.10 present the DSC and MCC rates for respectively Two-class SVM, One-class SVM and Random forests for various defects at the initial and final loading stages. Tables. E.4, Table E.5, and Table E.6 (see Appendix E) provide the same for intermediate loading levels.

Table 6.8: *Comparison of DSC ([..]) and MCC ((..)) coefficients for binary debonding detection from local signal features at initial and final loading stages for Geotextile based defects*

Loading stage	ART (reference)	Two-class SVM	One-class SVM	Random forests
10K cycles	[1.00], (1.00)	[1.00], (1.00)	[0.88], (0.79)	[1.00], (1.00)
300K cycles	[0.91], (0.86)	[0.99], (0.97)	[0.88], (0.74)	[1.00], (1.00)

Table 6.9: *Comparison of DSC ([..]) and MCC ((..)) coefficients for binary debonding detection from local signal features at initial and final loading stages for Sand based defects*

Loading stage	ART (reference)	Two-class SVM	One-class SVM	Random forests
10K cycles	[1.00], (1.00)	[1.00], (1.00)	[0.98], (0.94)	[1.00], (1.00)
300K cycles	[0.9], (0.86)	[1.00], (1.00)	[1.00], (1.00)	[0.88], (0.78)

Table 6.10: *Comparison of DSC ([..]) and MCC ((..)) coefficients for binary debonding detection from local signal features at initial and final loading stages for Tack-free based defects*

Loading stage	ART (reference)	Two-class SVM	One-class SVM	Random forests
10K cycles	[0.98], (0.96)	[1.00], (1.00)	[0.95], (0.91)	[1.00], (1.00)
300K cycles	[0.86], (0.8)	[0.87], (0.85)	[0.85], (0.72)	[0.88], (0.85)

It was observed that in case of both Two-class SVMs and Random forests, the performance rates were very high for all the three types of defects. In case of One-class SVM as well, similar conclusions were drawn.

6.4 Conclusion

This chapter concentrated on the application of machine learning methods on the detection of debondings from experimental data. The detection was carried out in two ways: binary detection by representing the results as 0 or 1 and secondly, as a probability estimation of the occurrence of debondings.

In the first part, the debonding detection was carried out on the experimental test bench under controlled environment with air-void debondings at Cerema. A wideband commercial GPR (GSSI SIR-3000) was used here. The debondings were set for thicknesses 0.5 cm and 1.0 cm. It was observed that, Two-class SVM and Random forests provided the best detection rate, both in case of binary as well as probabilistic. One-class SVM on the other hand performed averagely having the least accuracy among the three.

The second part concentrated on the experimental data collected at the fatigue carousel at IFSTTAR where three defect types were monitored over various loading stages. It was observed that, in cases of strong defects (Geotextile and Sand-based), the three methods (Two-class, One-class SVM and Random forests) performed with very high accuracy rate. The estimation of probability of the occurrence of defects was very high as well ($DPR \geq 0.95$) in all cases. In case of Tack-free based defects, apart from 200K and 250K cycles loading stage, the three methods were once again able to detect debondings with high accuracy at the same time estimate the occurrence at $DPR \geq 0.8$.

The reference method ART, was used as a benchmark for comparison in both experimental results and it was observed that ART was able to provide good results for strong defects; however, its efficiency reduced for weaker defects (such as Tack-free defects). In case of 100K and 250K loading for Geotextile and Sand defects, $DSC_{ART} \approx 0.96$; while Two-class SVM and Random forests provided near perfect detection with $DSC \approx 1.00$ (Table E.4). On the other hand, in case of Tack-free, ART provided very similar results to SVM and Random forests at 50K, 100 and 250K loading *i.e*, $DSC \in 0.9 - 0.95$; however, for 10K and 200K, the DSC for ART was less than that of SVM and Random forests (Table E.6).

In addition, it should be noted that ART relies on the time domain data to obtain its features (namely MAD or $MAAG$; refer Chapter 2.6.2). However, the machine learning methods can process temporal as well as frequential data. The final drawback using ART is that, unlike the machine learning methods, ART cannot be used for probability estimation.

However, despite its drawbacks, in most cases, ART debonding detection was very close to that observed using the machine learning methods. Thus, in perspective, we aim to take advantage of the efficiency of the ART method by including ART as a feature into the machine learning approach for improved performance.

Chapter 7

Conclusions and Perspectives

Contents

7.1 Conclusions

In this thesis, we primarily focused on the detection of thin interlayer debondings within pavement structures as described introduction chapter. The first chapter presented an overview of the thesis by introducing the problem statement and the goals of the thesis.

Various research has already been done in the field of debonding and delamination detection. Most of this research focuses on pavement engineering and monitoring is by means of Destructive Testing. Due to the limited capability of destructive testing, we dive into the field of Non-destructive testing (NDT). In Chapter 2, we discuss the State of the art and the progress in the field of NDT. The focus is on the NDT radar imaging on pavement structures. To support the work in this thesis, some available research was found to implement NDT techniques to detect delaminations within pavement interfaces. The data interpretation of most of these methods require human skills. In addition, some papers also presented the detection of interface debondings; however they were limited to the detection in the order of a few centimeters. The objective in this thesis was the detection of millimetric interlayer debondings using UWB systems for better time resolution. To achieve this objective, the 2D GPR imaging technique is carried out to map the pavement subsurface structure. Besides, we aimed to achieve improved debonding detection with the help of suitable data processing techniques.

It was also seen that despite their advantages, the implementation of machine learning (ML) methods in the field of interlayer debonding detection has not been explored to its full potential by the NDT community. A comparative study of various ML methods, both unsupervised and supervised methods, was carried out. Finally, the performance of each method was compared to ART, which is a benchmark technique to assess the pavement subsurface conditions and sealing screeds over bridges in the GPR community. The subsequent chapters discussed in detail the various data processing methods studied during the thesis.

In Chapter 3, we introduce the machine learning methods studied during the thesis. An unsupervised conventional clustering method was modified in order to improve the initial seed-point selection for better performance. A parameterized supervised machine learning method, namely SVM was then presented. This method was used to detect debondings in two ways: as of classification into two classes (Two-class SVM) and as anomaly detection (One-class SVM). Finally a non-parameterized method, Random forests, was introduced. The principle of each method is illustrated through the straightforward processing of time data in its raw form. The four methods were applied to process noisy analytic data, which were presented in the appendices. The methods demonstrated good qualitative results as they were able to detect debondings with various interlayer permittivities in noisy data.

However, the processing of raw data is not always acceptable since the raw GPR data may contain redundant information that could reduce the debonding detection rate. Additionally, as stated in the literature, the machine learning methods could be limited in their processing of raw data signals. The processing of a large databases affect the computational time and complexity of a supervised machine learning method. To overcome this issue, feature engineering techniques were proposed.

Chapter 4 began by presenting one of the important preprocessing step in debonding detection *i.e*, signal feature selection. The feature selection was categorized into time domain local and global signal features. The local features were focused at the pavement interface where the debonding is expected to occur. These features were expected to present higher efficiency due to their time localization. Global features on the other hand used the complete GPR signal with the top two pavement interfaces. Feature sets were selected by the 'goodness of separation' of their associated PDF distributions for debonding and non-debonding cases. In order to further reduce the data complexity, PCA was also used.

As a part of initial tests, the performance of the supervised machine learning methods were tested using various input feature sets. These results were compared with the performance observed in Chapter 3 on temporal raw GPR data as a benchmark. Although the raw GPR data presented very high detection, this approach was seen to be quite cumbersome and not efficient in terms of computational time and complexity. As expected, in case of SVM for simulated data, it was observed that the local feature set presented better detection results than global features. The PCA reduced global and local feature sets provided little-to-none difference in performance of the unreduced data.

However, the study of robustness of supervised machine learning methods is not just limited by the input data but several other parameters such as the learning data size, method hyper-parameters, method kernels, cross validation techniques *etc*. This makes it necessary to identify the 'best' parameters that could be used to achieve high detection rate in the context of detection of interface debondings.

Therefore, in Chapter 5, we presented the optimization of ML methods by these approaches. Following the conclusions of the previous chapter, the local signal features were used in Chapter 5 for optimization. The first approach to optimize the methods included the model-fitting approach using CV techniques and kernel functions. Optimization of the methods was also conducted on the basis of the pavement medium. The parameters

such as debonding thickness, relative permittivity of the debonding layer were used and the methods were adapted to match various configurations of the pavement medium.

Chapter 6 concentrated on the application of optimized machine learning methods on the detection of debondings from experimental data. This chapter presented the debonding detection for experimental data collected at two independent sites located respectively at Nantes (IFSTTAR) and Angers (Cerema). The site at Cerema was set up using pavement test benches and was focused on the detection of artificially induced air-void debonding of thickness 0.5 cm and 1.0 cm using a commercial ground-coupled GPR. The test site at IFSTTAR focused on the detection of artificially induced defects of three types (Geotextile, Sand and Tack-free) using a commercial GPR and an experimental ultra-wide-band air-coupled SF-GPR. The results were presented using the optimized parameters for each machine learning method determined in the Chapters 4 and 5. Chapter 6 also presented a final decision making step wherein the results were presented as an estimate determined as the probability of occurrence of a defect.

In case of ground-coupled GPR (Cerema test bench), it was observed that, Two-class SVM and Random forests provided the best detection rate, both in case of binary as well as probabilistic. One-class SVM on the other hand performed averagely having the least accuracy among the three.

On the other hand, for the air-coupled radar data from IFSTTAR's fatigue carousel, it was observed that, in cases of strong defects (Geotextile and Sand-based), the three methods (Two-class, One-class SVMs and Random forests) performed with very high accuracy rate. The extimation of probability of the occurrence of defects was very high as well ($DPR \geq 0.95$) in all cases. In case of Tack-free based defects, apart from 200K and 250K cycles loading stage, the three methods were once again able to detect debondings with high accuracy at the same time estimate the occurrence excellently ($DPR \geq 0.8$).

Finally, the performance of the machine learning methods was compared to the ART method, which was used as a benchmark in both experimental results. It was observed that ART, although relying on two signal features, was able to provide equivalent results for strong defects. However, its efficiency was reduced for weaker defects (such as Tack-free defects).

In conclusion, it was seen that the three machine learning methods, despite certain drawbacks, presented the ability to detect debondings and also estimate their occurrence with very high efficiency by means of probability estimates. The use of local signal features and optimized hyper-parameter computation proved to improve the performance of the methods.

7.2 Perspectives

The objective of this thesis was to to detect the presence of thin interlayer debondings within pavement structures. Although we were able to achieve the goals foreseen as objectives for this thesis, some improvements are open to discussions that we can attempt to answer by further research in the fields of NDT, GPR and machine learning. Following are some of the future works from the point of preprocessing for machine learning methods:

Multi-class classification: The study for the detection of thin interface debondings in this thesis was performed as a binary classification (Two-class SVM, Random forests, k-means clustering) or as an outlier anomaly detection (One-class SVM). The presence of various other types of defects (based on material composing the debonding layer, debonding layer thickness *etc.*) can be explored to perform multi-class classification.

Spectral signal features: As mentioned in Chapter 4, the detection of debondings was carried out by using various time domain signal features (global and local) extracted from the GPR A-scan time signatures. It is proposed to explore in the future the performance of frequency domain signal features, and eventually to mix both domain features for improved performance in classification.

In addition, we aim to take advantage of the efficiency of the ART method by including ART as a feature into the machine learning approach for improved performance.

Feature selection: PDF-based feature selection method was implemented in the thesis along with a feature reduction technique (PCA). However, as presented in the literature, various automatic feature selection methods can be used. Among others, it is proposed to substitute the qualitative "goodness of separation" in Chapter 4 by a quantitative index.

Estimation of debonding layer characteristics: This thesis focused mainly on detecting the presence/absence of debondings in pavements. This however leaves the determination of other debonding characteristics such as debonding layer thickness, length, permittivity *etc.*

Exploring Deep learning methods: The use of deep learning methods such as Neural Networks has not yet been conducted in the field of NDT for the detection of interlayer debondings. We aim to explore the possibility to implement deep learning methods in NDT for both classification and regression related problems.

Future work: One of the final goals would be to implement and continue the research from this thesis useful in WP3 of **ACIMP** project.

Appendices

Appendix A

Simulated Databases

Contents

The detection methods studied during the thesis were initially validated using the simulated data models which are presented in this appendix. Each data model simulates the noiseless backscattered radar signal from the layered pavement structure assuming (quasi-)vertical incidence. It provides B-scan air-coupled radar data over a simplified synthetic layered pavement structure with either k = 2 or k = 3 layers, corresponding to healthy and debonded areas respectively.

Three techniques were used to create the simulated databases, namely, Analytic Fresnel data model, Numeric 2D FDTD model and Numeric MoM data model. In brief, the analytic and the numeric MoM data models rely on simplified 1D wave propagation. By contrast, the numeric FDTD model accounts for the wave propagation in 2D, *e.g.*, a diffraction hyperbola is visible on simulated data at the frontier between healthy and debonded areas. Besides, the antenna effect are approximately accounted for in these three models. For the FDTD model, antennas are supposed to be dipole antennas. For analytic model, the frequency antenna response is accounted for through the radar pulse to be introduced hereafter.

A.1 Radar pulse

In this section, we present, in brief, the 1D radar pulse used in data modeling to provide more realistic radar vertical profiles using simulations. For the sake of comparison, we also present the experimental radar pulse and the procedure to extract the emitted pulse from the GPR data.

A.1.1 Analytic GPR pulse

The radar pulse used for the analytical data models in the ricker (or commonly known as the Mexican hat) pulse as it is often used in seismic analysis of thin beds [310]. It can be defined as the negative normalized second derivative of the Gaussian waveform obtained by solving the Stokes' differential equation [311, 310].

The ricker wavelet ($w(t)$) in time domain is defined as [310]:

$$w(t) = \left(1 - \frac{1}{2}\omega_c^2 t^2\right) exp\left\{ - \frac{1}{4}\omega_c^2 t^2 \right\} \tag{A.1}$$

where,

- $\omega_c = 2\pi f_c$ with f_c being the dominant frequency
- t is the time (in seconds)

The pulse is symmetric in time domain and has zero mean *i.e*, $\int_{-\infty}^{\infty} W(t)dt = 0$ [310]. In frequency domain, it is expressed as [310]:

$$W(\omega) = \frac{2\omega^2}{\sqrt{\pi}\omega_c^3} exp\left\{ - \frac{\omega^2}{\omega_c^2} \right\} \tag{A.2}$$

where ω is the angular frequency at a given frequency f.

Figure. A.1 presents the ricker pulse used to generate the simulated model in time domain and its respective frequency spectrum.

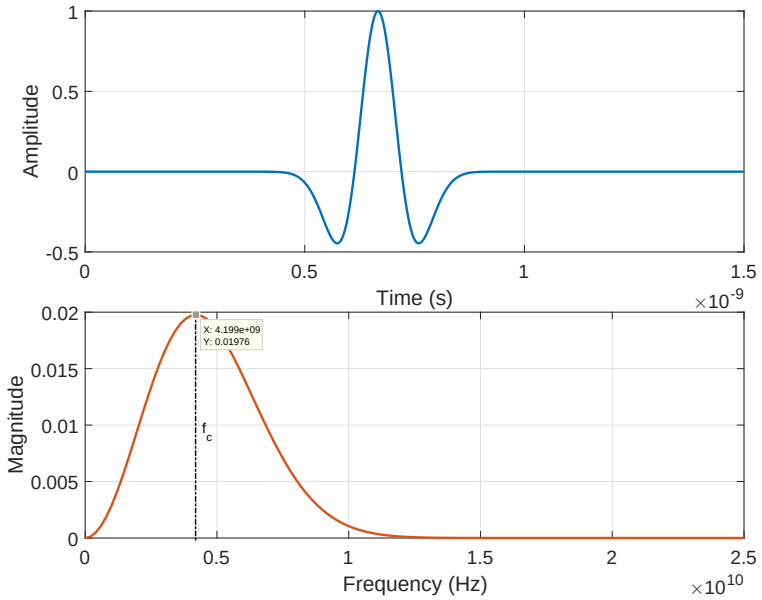

Figure A.1: *Illustration of the Ricker pulse in time and frequency domain used to generate the simulated models with* $f_c = 4.2\,\mathrm{GHz}$

This radar pulse will be used subsequently in Appendix. A.2 in the generation of simulated databases.

A.1.2 Experimental GPR pulse

In order to extract the GPR pulse from the radar data, the following process is used. The emitted GPR pulse can be recovered by placing the metallic plate (sufficiently large so that the edge and scattering effects are avoided) underneath the antenna. As mentioned in [312], this plate could be made of copper. The antennas are initially arranged in the designated form (see Appendix. B.2.3.1 for details) and the metallic plate is placed underneath as shown in Figure. A.2.

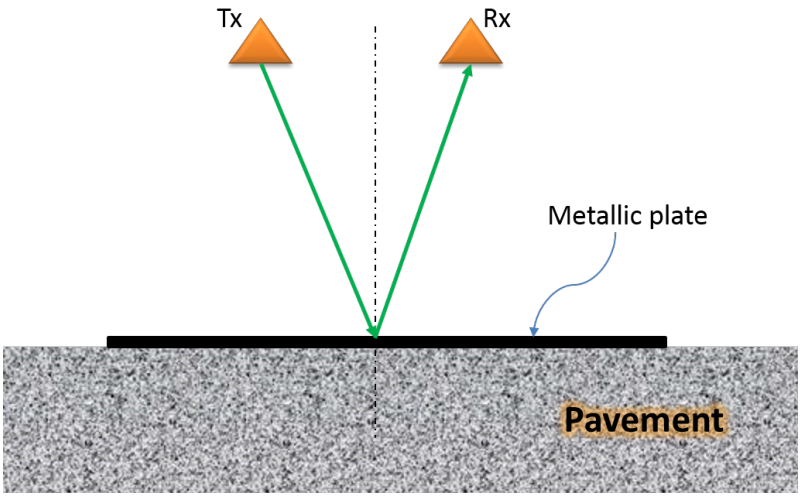

Figure A.2: *Illustration of the setup used to experimentally extract GPR pulse*

The reflected signal from the plate is an inverted signal (since the reflection coeffi-

cient of copper is -1). The signal is thus multiplied by -1 and after removing the direct coupling between the transmitter and receiver, the emitted GPR pulse is obtained. Figure. A.3 presents the extracted ricker pulse from experimental data in time domain and its respective frequency spectrum.

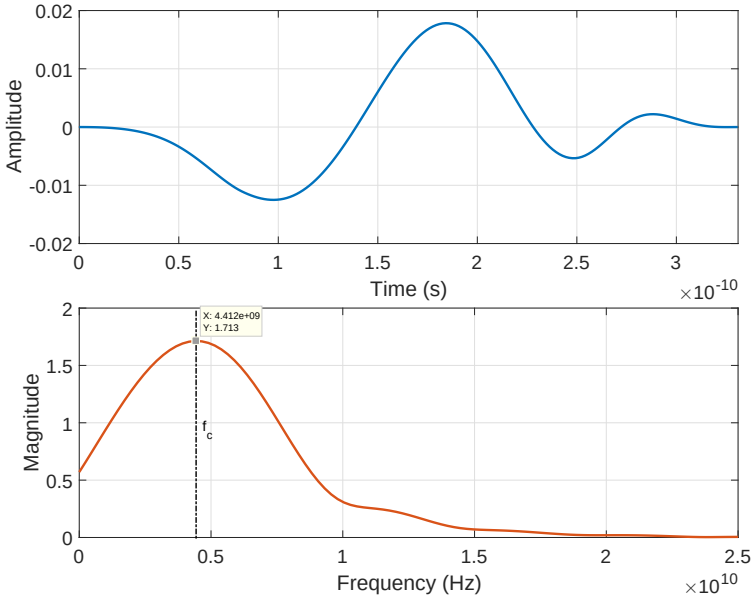

Figure A.3: *Illustration of the Ricker pulse in time and frequency domain used in experiments*

This pulse is used to collect the pavement data using the SF-GPR as detailed in Appendix. B.2.

A.2 Analytic GPR modeling

A.2.1 Basics and hypothesis

The analytic GPR data model has been widely used for processing purpose. It relies on the following conventional assumptions:

1. Wave propagation : Plane waves impinging on the pavement surface (far field assumption);

2. Wave interaction vs. medium : single scattering within (thick enough) layers, *i.e.*, each interface provides a single echo in the data model.

3. Medium: Lateral and vertical homogeneity; roughless layers interfaces; dispersion-free medium, *i.e.*, constant material permittivity *w.r.t.* frequency; lossless medium.

4. Antenna effects are ignored

Within this scope, the received time signal $r(t)$ which is backscattered by the k layered pavement structure is the sum of attenuated and shifted copies of the radar pulse, $s(t)$, as

follows:

$$r(t) = \sum_{i=1}^{k'} A_i s(t - T_i) + n(t) \tag{A.3}$$

where,

- A_i is the amplitude of the received echo from the ith interface,
- T_i is the time delay attached to the ith echo; it is the sum of the propagation time shift through each layer; it is given by $T_i = \sum_{n=1}^{i} \frac{2d_n}{\nu_n}$ where d_n is the thickness and ν_n the wave speed within the nth layer.
- k is the amount of layers; within the scope of the thesis, $k = 2$ for healthy pavement structure and $k = 3$ for disbonded structure.
- k' is the total amount of echoes accounted for in the data model; it is equal to the amount of layers providing single scattering assumption (see Appendix. A.2.3.1), and larger in case of multiple scattering (see Appendix. A.2.3.2).
- $n(t)$ is the additive noise, which SNR is discussed in Appendix. A.5.

The amplitude of echoes relies on the well-known Fresnel reflection and transmission coefficients. At vertical incidence, the Fresnel coefficients for reflection and transmission at the interface ij can be expressed in terms of the permittivity of the two materials as:

$$R_{ij} = \frac{\sqrt{\varepsilon_{r,i}} - \sqrt{\varepsilon_{r,j}}}{\sqrt{\varepsilon_{r,i}} + \sqrt{\varepsilon_{r,j}}} \tag{A.4}$$

$$T_{ij} = \frac{2\sqrt{\varepsilon_{r,j}}}{\sqrt{\varepsilon_{r,i}} + \sqrt{\varepsilon_{r,j}}} \tag{A.5}$$

where, $\varepsilon_{r,i}$ is the relative permittivity of the material layer i. Since the materials of each layer are considered to be lossless, the transmission and reflection coefficients are related as $R_{ij} + T_{ij} = 1$.

For later use in this Appendix, we also introduce the received signal in the frequency domain, as follows:

$$\tilde{r}(f) = \left\{ \sum_{i=1}^{k'} A_i z(T_i) \right\} \tilde{s}(f) + \tilde{n}(f) \tag{A.6}$$

where $z(T) = exp(-2i\pi fT)$ represent the complex phasor associated to the time delay T; $\tilde{s}(f)$ and $\tilde{n}(f)$ are the Fourier transform of the radar pulse $s(t)$ and the noise $n(t)$, respectively.

Within the scope of the thesis, a two-layered structure is created with each layer governed by physical parameters such as thickness, material permittivity, antenna height according to the parameters in Table. A.1. To create a defective pavement section, a debonding layer is introduced between the two pavement layers. The debonding layer is

assumed to be a thin-bed structure satisfying the following condition [313, 314, 315]:

$$\frac{\lambda_{deb}}{4} > d \tag{A.7}$$

where λ_{deb} is the dominant wavelength within the debonding layer of thickness d given by $\lambda_{deb} = c/f_c\sqrt{\varepsilon_{r,deb}}$. The latter condition limits to $\pi/2$ the phase shift between the two successive echoes, namely, the condition for in-phase summation.

Figure. A.4 presents the simplified pavement model with the defect-free and defective zones. To create the analytic GPR data model, MATLAB was used.

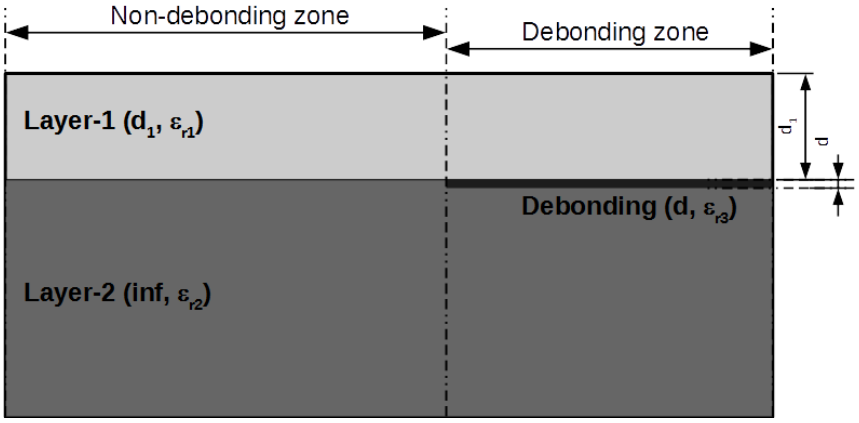

Figure A.4: *Simplified pavement structure to create the Analytic data model*

A.2.2 Non-debonding case

For a two-layered structure ($k = 2$) as shown in Figure. A.5, the received signal in eq. A.3 can be expressed as:

$$r(t) = A_0 s(t - T_0) + A_1 s(t - T_1) + n(t) \tag{A.8}$$

where, - A_0 is the amplitude of the surface echo defined as $A_0 \propto R_{01}$ with the time delay $T_0 = \frac{2h}{c}$ as a function of the antenna height (h) in air.

- A_1 is the amplitude of the second echo, *i.e.*, the interface to be surveyed; in case of non-debonding, $A_1 \propto T_{01} \times R_{12} \times T_{10}$ with the time delay $T_1 = T_0 + \frac{2d_1}{\nu_1}$ as a function of the thickness of top layer d_1 (where the wave speed is $\nu_1 = c/\sqrt{\varepsilon_{r1}}$).

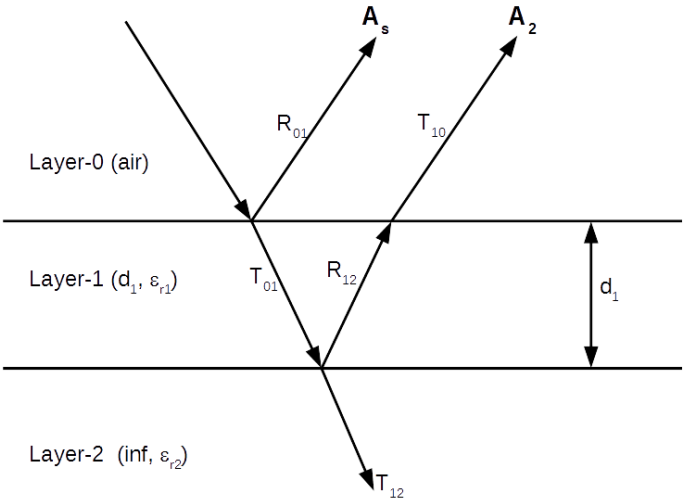

Figure A.5: *Fresnel coefficients for a two-layered structure*

Table A.1: *Parameters used to create a GPR B-scan using the analytic data model*

Layer	Label	Value
Top layer	ε_{r1}	5
	t_1	5 cm
	ρ_1	0 S m^{-1}
Base layer	ε_{r2}	7
	t_2	40 cm
	ρ_2	0 S m^{-1}
Debonding layer	$\varepsilon_{r,deb}$	2 (air-void), 6 (weak contrast), 10 (strong contrast)
	t_{deb}	0.3 cm
	ρ_d	0 S m^{-1}
Center frequency	f_c	2 GHz
Antenna height	h_{ant}	46 cm
Observation time	T_{obs}	10 ns
Time resolution	Δt	2.44 ps
Sampling frequency	f_s	409.6 GHz

A.2.3 Debonding case

As indicated in Figure. A.4, in case of a disbonded zone, a thin layer is sandwiched between the two pavement layers, namely, a thin-bed structure which thickness d satisfying the condition in Eq. A.7.

Two data models have been used in the literature to interpret the backscattering data from a thin bed structure. They rely on two opposite assumptions regarding the wave

interaction within the thin-bed structure, namely, single scattering vs. multiple scattering.

A.2.3.1 *Single scattering model*

The conventional data model assumes single scattering within the thin-bed structure, *e.g.*, see Chung and Lawton [316]. Then, the signal backscattered from the three-layered structure shown in Figure. A.6 can be rewritten following Eq. A.3 as the sum of three primary echoes:

$$r(t) = A_0 s(t - T_0) + \{A_1 s(t - T_1) + A_3 s(t - T_3)\} + n(t) \tag{A.9}$$

where $T_3 = T_1 + \frac{2d_3}{\nu_3}$ is the time delay from the debonding layer as a function of debonding layer thickness d_3 and the wave speed ν_3.

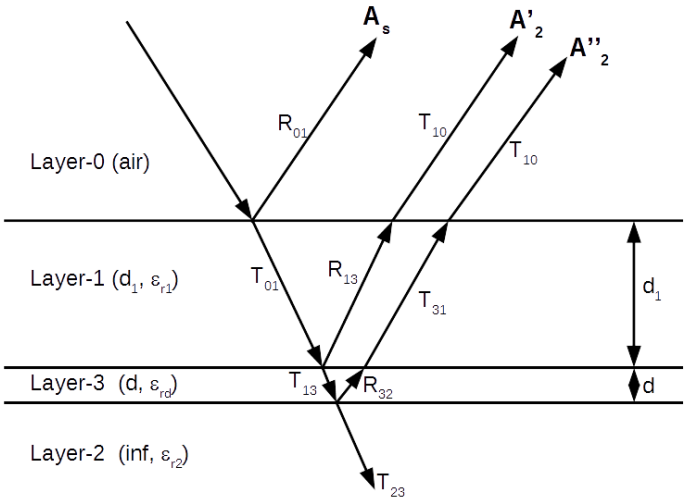

Figure A.6: *Fresnel coefficients for a three-layered structure (two layers with a sandwiched debonding layer as a thin bed structure)*

Using Fresnel coefficients, the respective amplitudes A_1 and A_3 can be expressed as:

$$A_1 \propto T_{01} \times R_{13} \times T_{10} \tag{A.10}$$

$$A_3 \propto T_{01} \times T_{13} \times R_{32} \times T_{31} \times T_{10} \tag{A.11}$$

In the frequency domain, introducing $A_1^{eq,s}$ for the backscattered signal amplitude by the interlayer interface to be surveyed, the signal can be written as:

$$\tilde{r}(f) = \tilde{s}(f)\Big\{A_0 z(T_0) + A_1^{eq,s} T_{01} T_{10} z(T_1)\Big\} + \tilde{n}(f) \tag{A.12}$$

$$\text{where: } A_1^{eq,s} = R_{13} + T_{13} R_{32} T_{31} z(2d_3/\nu_3) \tag{A.13}$$

$$\text{and: } z(T) = exp(-2i\pi f T) \tag{A.14}$$

The second and third echoes, *i.e.*, $s(t-T_1)$ and $s(t-T_3)$ in Equation. A.9, represent the reflected signal from the top and bottom interfaces of the debonding layer, respectively.

Providing the thickness condition in Equation. A.7, the two latter echoes overlap to each other in time and shape as a single composite echo.

A.2.3.2 *Multiple scattering model*

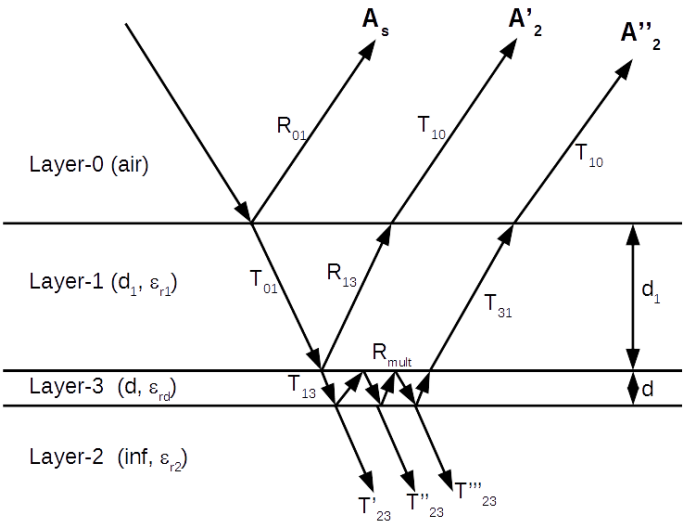

Figure A.7: *Fresnel coefficients for a three-layered structure (two layers with a sandwiched debonding layer as a thin bed structure) with multiple internal reflections within the debonding layer*

Multiple scattering is assumed to be limited to the thin-bed structure only. Equation. A.9 then becomes:

$$r(t) = A_0 s(t - T_0) + \left\{ A_1 s(t - T_1) + \sum_m A'_{3,m} s(t - T_3 - 2(m-1)\frac{d_3}{\nu_3}) \right\} + n(t) \quad \text{(A.15)}$$

where $\sum_i$ operator indicates the sum of all the multiple scattering echoes occurring within the thin debonding layer with the following diminishing amplitude $A'_{3,i}$:

$$A'_{3,m} \propto T_{01} \times T_{13} \times R_{32}^m \times R_{31}^{m-1} \times T_{31} \times T_{10} \quad \text{(A.16)}$$

In practice, the contribution of multiple scattering to the data model is usually formulated in the frequency domain, in order to achieve the analytic solution to the sum in Equation. A.15. The data model in the frequency domain is expressed as:

$$\tilde{r}(f) = \tilde{s}(f) A_0 z(T_0) + \tilde{s}(f) \left\{ A_1 z(T_1) + z(T_1) \sum_m A'_{3,m} z(2m\frac{d_3}{\nu_3}) \right\} + \tilde{n}(f) \quad \text{(A.17)}$$

$$\text{with: } z(T_m) = exp(-2i\pi f T_m) \quad \text{(A.18)}$$

The backscattered signal from the thin-bed structure with multiple scattering accounted for, has been formulated by Rayleigh [317, 318] for seismic waves, and by Annan [72] for GPR waves, providing that layers surrounding the thin-debonding possess the same material characteristics (*i.e.* $\varepsilon_{r1} = \varepsilon_{r2}$). More recent formulation is given by Arosio

[319] and Shakas [320, 321].

Within the scope of the thesis, [322] provides the general solution for the thin-bed structure with different surrounding permittivity values (*i.e.* $\varepsilon_{r1} \neq \varepsilon_{r2} \neq \varepsilon_{r3}$), as follows:

$$A_1^{eq,m} = \left\{ A_1 z(T_1) + z(T_1) \sum_m A'_{3,m} z(2m\frac{d_3}{\nu_3}) \right\} = \frac{R_{13}(1 - Gz)}{1 - GR_{13}^2 z} \tag{A.19}$$

where,

$$z = z(2d_3/\nu_3) = exp(-4i\pi f d_3/\nu_3) \tag{A.20}$$

$$G = \frac{\sqrt{\varepsilon_{r1}} + \sqrt{\varepsilon_{r3}}}{\sqrt{\varepsilon_{r2}} + \sqrt{\varepsilon_{r3}}} \left\{ 1 - \frac{R_{12}}{R_{13}} \frac{\sqrt{\varepsilon_{r1}} + \sqrt{\varepsilon_{r2}}}{\sqrt{\varepsilon_{r1}} + \sqrt{\varepsilon_{r3}}} \right\} \tag{A.21}$$

For a conventional thin-bed structure, for which $\varepsilon_{r1} = \varepsilon_{r2}$, the parameter $G = 1$, and Equation. A.19 simplifies to the existing reflection coefficient shown in [319].

Finally, the data model in the frequency domain can be expressed as:

$$\tilde{r}(f) = \tilde{s}(f) \left\{ A_0 z(T_0) + A_1^{eq,m} T_{01} T_{10} z(T_1) \right\} + \tilde{n}(f) \tag{A.22}$$

The data were generated in the frequency domain, and a inverse Fast Fourier Transform allowed to compute the final B-scan data in the time domain. For illustration, Figure. A.8 shows the simulated B-scan using the parameters from Table A.1.

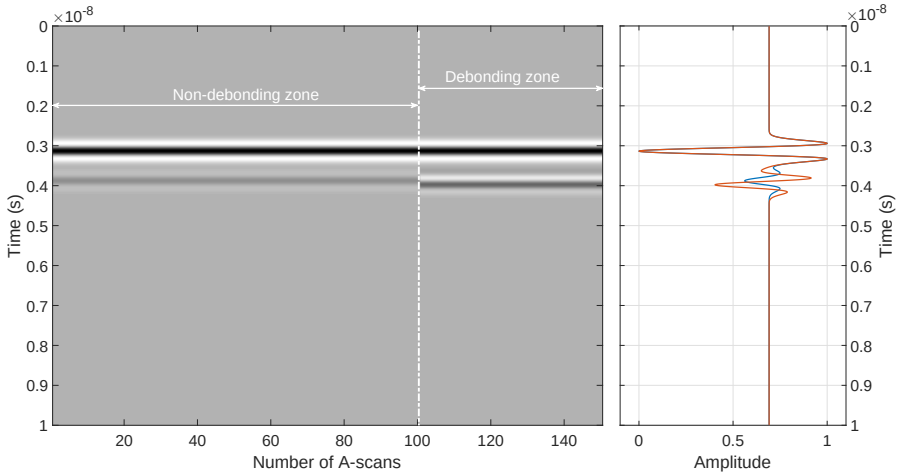

Figure A.8: *Example of a noiseless B-scan generated with multiple scattering accounted for and the following parameters :* $\varepsilon_{r1} = 5$, $\varepsilon_{r2} = 7$, $\varepsilon_{r,deb} = 2$ *and* $t_{deb} = 0.3\,\text{cm}$. *On the right, the two A-scans represent respectively non-debonding and debonding cases*

A.3 Numeric database: Pavement modeling using MoM

One major drawback of the Fresnel data model is that it assumes a smooth surface and smooth interface across the model. To obtain a more realistic model, the numeric GPILE was used.

Propagation-Inside-Layer Expansion (PILE) is a 1D numerical approach based on the

Method of Moment (MoM) proposed in [323]. PILE is an efficient numerical model that can be used to compute the scattering fields by the rough pavement interfaces for both reflection and transmission. By introducing the roughness at each interface, the complexity of the model is increased due to the increased number of unknowns.

The major advantage of the PILE method relies on its ability to calculate the echoes scattered by each interface with both the multiple scattering and the accounted inter-layer surface roughness. PILE is also capable of performing faster and efficient computations. Additionally, PILE focuses on rigorous but simple formulation and straightforward physical interpretation of the pavement model.

GPILE or Generalized PILE is the extension of PILE for three or more pavement layers. The method has been extensively discussed in [12]. Since GPILE can be used to simulate more than two layers, a three-layered GPILE model can be used to simulate a defective pavement structure as shown in Figure. A.9.

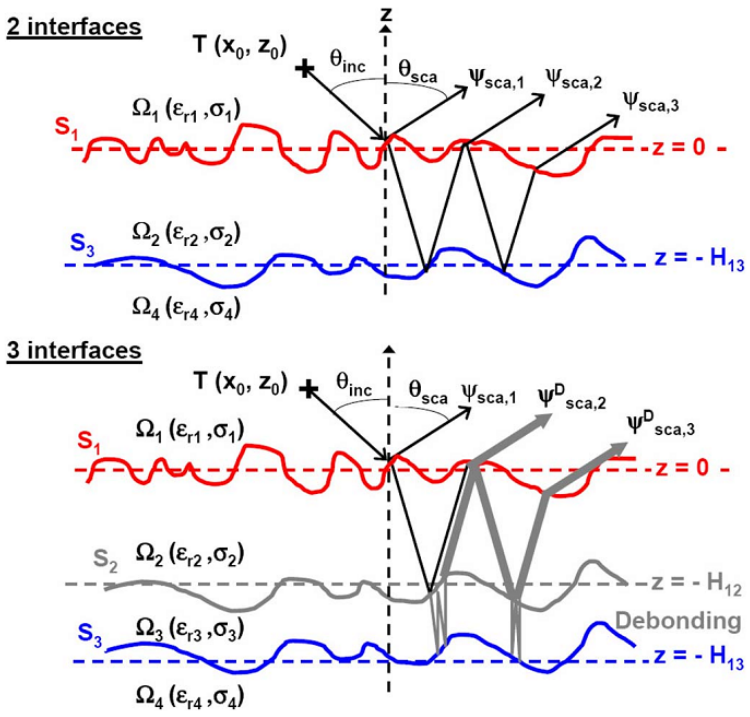

Figure A.9: *EM scattering from a 1-D random rough layer with two rough surfaces i.e. Non-debonding case (top) and scattering from 1-D three rough interfaces i.e. debonding case (bottom) [12]*

The 2D GPILE B-scan is generated by repeating the the 1D propagation for N_{ndeb} times for non-debonding case and N_{deb} times for debonding case. This is a 2D image obtained in frequency domain. Using Inverse Fourier transforms, the B-scan image in time domain is obtained. In addition to the parameters presented in Table. A.1, the additional parameters used to generate the numerical model are given in Table. A.2.

Table A.2: *Parameters used to create a GPR B-scan using the numerical GPILE model*

Layer	Label	Value
Center frequency	f_c	2 GHz
Bandwidth	BW	0.1 GHz to 5.1 GHz
Antenna height	h_{ant}	46 cm
Conductivity	$Layer-1$	1×10^{-3} S m^{-1}
	$Layer-2$	1×10^{-3} S m^{-1}
	$Debonding$	1×10^{-3} S m^{-1}
Roughness	$topsurface$	0×10^{-3} m
	$interlayerinterface$	0×10^{-3} m

Figure. A.9 shows the 2D image generated using the parameters from Table. A.1 and Table. A.2.

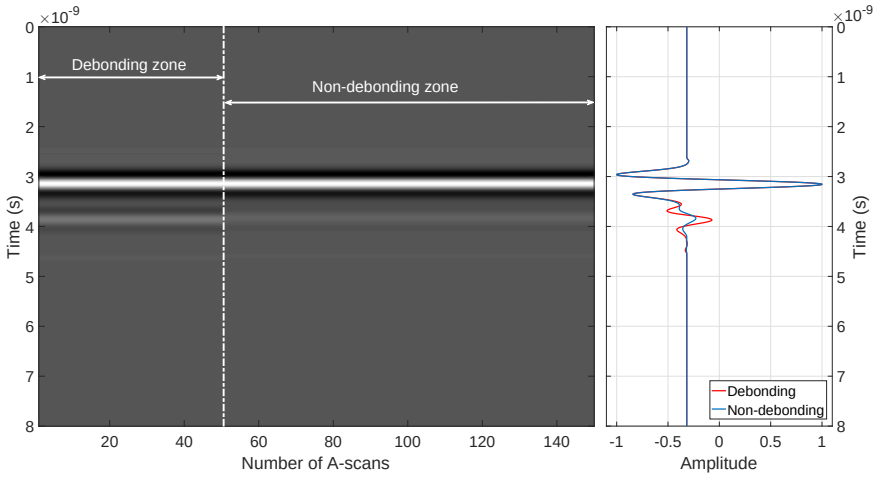

Figure A.10: *Example of GPILE B-scan generated with* $\varepsilon_{r1} = 5$, $\varepsilon_{r2} = 7$, $\varepsilon_{r,deb} = 2$ *and* $t_{deb} = 0.3$ cm *(left). A-scans representing respectively non-debonding and debonding cases (right)*

A.4 Numeric database: Pavement modeling using FDTD

gprMax is an open source tool used to simulate the electromagnetic wave propagation within a material (and multiple materials as well). With the help of Maxwell's equations projected in 3D using the Finite-Difference Time-Domain (FDTD) method [324, 325], gprMax is capable of creating various pavement models for different radar configurations operating at ultra-wideband frequency.

Developed in 1995 [326, 327], gprMax was first openly distributed by Giannopoulos and Giannakis [328] in 2015. It uses both Python and Cython for background programming whereas the user interface is a high-level programming unique to gprMax. Extensive user manuals on gprMax are available in [329, 328, 330, 331].

A.4.1 Creating a 2D gprMax model of a pavement structure

A right-handed Cartesian coordinate system is used with the origin of space coordinates in the lower left corner at (0,0,0). The FDTD approach to the numerical solution of Maxwells equations is to discretize both the space and time domains. Thus, the spatial discretization plays a very important role in the performance of the modeling method.

The 3D gprMax model is discretized in the three axes as Δx (spatial discretization), Δy (temporal discretization) and Δz (lateral discretization). In order to observe a good resolution of the time domain GPR signal, the discretization size (mesh size) in the time axis can be defined as:

$$\Delta y = \frac{\lambda}{10} \tag{A.23}$$

The pavement model created using gprMax consists of: two layers for the healthy zone and, three layers for the defective zone as depicted in Figure. A.11.

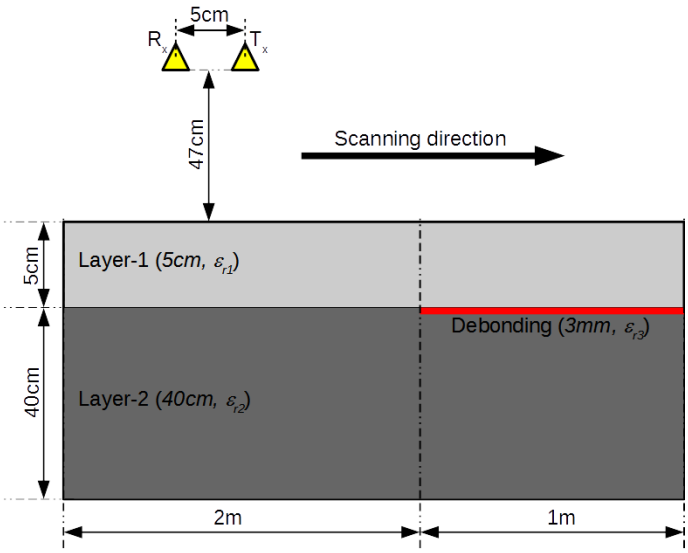

Figure A.11: *Two-layered pavement model created using gprMax. R_x, T_x and represent the antenna positioning*

Let λ_1, λ_2 and λ_{deb} be respectively the wavelength of the impulse within the top layer, base layer and debonding layer of permittivities respectively ε_{r1}, ε_{r2} and ε_{rdeb}. Then, from Eq. A.23, the optimal temporal discretization can be obtained from:

$$\Delta y = \min\left\{\frac{\lambda_1}{10}, \frac{\lambda_2}{10}, \frac{\lambda_{deb}}{10}\right\} \tag{A.24}$$

In order to maintain regularity, we use $\Delta x = \Delta y = \Delta z$.

Using the pavement layer parameters presented in Table. A.1, B-scan images were generated in gprMax. A dipole as a hard-source is used as the signal source.

Firstly, the GPR domain is defined along with the total acquisition time and the domain discretization defined previously (Listing. A.1).

```
#domain: 3.0 0.98 0.002
#dx_dy_dz: 0.001 0.001 0.002
#time_window: 10e-9
```

Listing A.1: gprMax modeling: Specifying the domain parameters

The material characteristics of each pavement layer such as permittivity, conductivity and permeability are defined (Listing. A.2).

```
#material: 5 0.001 1 0 asphalt_layer_1
#material: 7 0.001 1 0 asphalt_layer_2
#material: 2 0.001 1 0 debonding_layer
```

Listing A.2: gprMax modeling: Initializing material characteristics

Each material is assigned a unique identifier that can be used to associate a layer with the material characteristic. Listing. A.3 presents the code to generate the three pavement layers with specified thicknesses and are associated to the material defined previously using the identifier.

```
#box: 0.0 0.4 0.0 2.0 0.45 0.002 asphalt_layer_1
#box: 0.0 0.0 0.0 2.0 0.4 0.002 asphalt_layer_2
#box: 0.0 0.39 0.0 2.0 0.4 0.002 debonding_layer
```

Listing A.3: gprMax modeling: Modeling pavement layers

Once the design is complete, the source of the signals is defined. Characterized by the frequency of operation and the type of waveform used. A voltage source is used as the signal source that emits the impulse (Listing. A.4). The source is specified to be a 'hard source' (*i.e.*, source internal resistance $R = 0\,\Omega$). This is done in order to make the source completely reflecting and prescribe the value of the electric field component.

```
#waveform: gaussiandotnorm 1 2e9 my_pulse_1
#hertzian_dipole: z 0.97 0.92 0 my_pulse_1
#rx: 1.02 0.92 0
```

Listing A.4: gprMax modeling: Creating waveform source

In order to acquire data over a zone (in 2D) to create a B-scan image, the antennae are displaced spatially step-by-step. Listing. A.5 presents the antenna displacement.

```
#src_steps: 0.01 0 0
#rx_steps: 0.01 0 0
```

Listing A.5: gprMax modeling: Displacing the source and receiver spatially

Using the code presented above, various gprMax data models were created to generate the 2D B-scan images. Figure. A.12 presents one such B-scan.

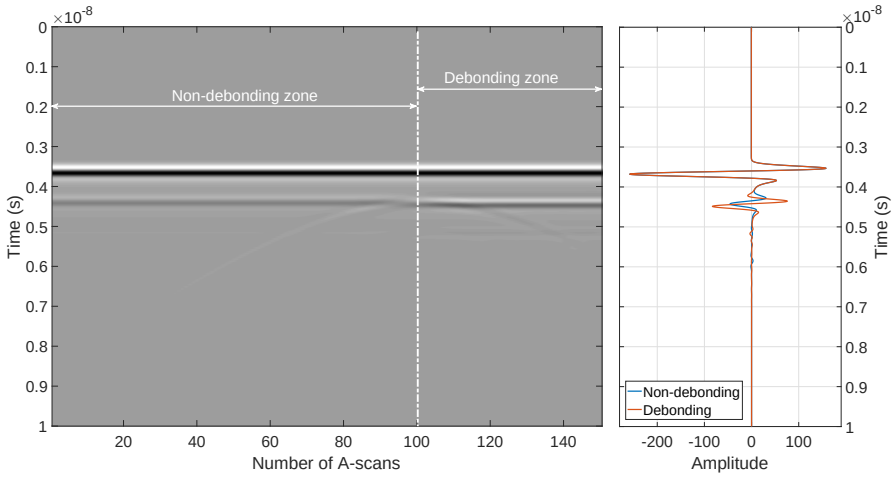

Figure A.12: *gprMax B-scan generated using Figure. A.11*

A.5 Noisy data

In order to test the performance sensitivity of the detection methods against noise, we associate to each simulated noiseless database noisy datasets at different selected signal-to-noise ratio (SNR) values.

A.5.1 SNR definition

In this section, the conventional additive noise model is assumed, as formulated by Equation. A.25 on each radar profile. The noise is usually a White Gaussian Noise (WGN) with zero mean $\mu = 0$ and standard deviation $\sigma = \sigma_n$. It is assumed to be decorrelated to the useful signal, and decorrelated between successive A-scan radar profiles.

The SNR is defined in the time domain with respect to the signal to detect, i.e., the second echo from the healthy interlayer interface, according to :

$$SNR_{dB} = 20log_{10}\frac{M}{\sigma_N} \tag{A.25}$$

where,

- M is the maximum magnitude of the second echo of the non-debonding A-scan,
- σ_N is the standard deviation of the noise added.

Owing to this definition, a stronger SNR is likely observed over the debonding areas. Inversely, for a selected SNR, the standard deviation of the noise to add to the noiseless simulated data is given b:

$$\sigma_N = M \times 10^{-\frac{SNR}{20}} \tag{A.26}$$

A.5.2 Illustrative results

The noise matrix is then added to each simulated B-scan images to obtain the respective noisy data. The result is illustrated in this section for the same SNR and the same subsurface parameters as input for each data model.

Figure. A.13 to A.13 present the noisy B-scans with $SNR = 20\,\text{dB}$ associated to the noiseless B-scans images from Figure. A.8 to Figure. A.8.

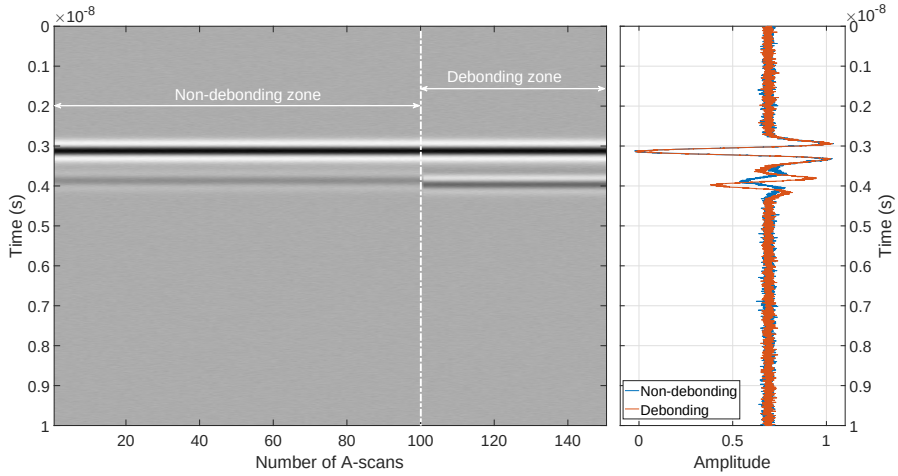

Figure A.13: *Example of a noisy analytic B-scan for Figure. A.8 generated with* $SNR = 20\,\text{dB}$ *(left). A-scans represent respectively non-debonding and debonding cases (right)*

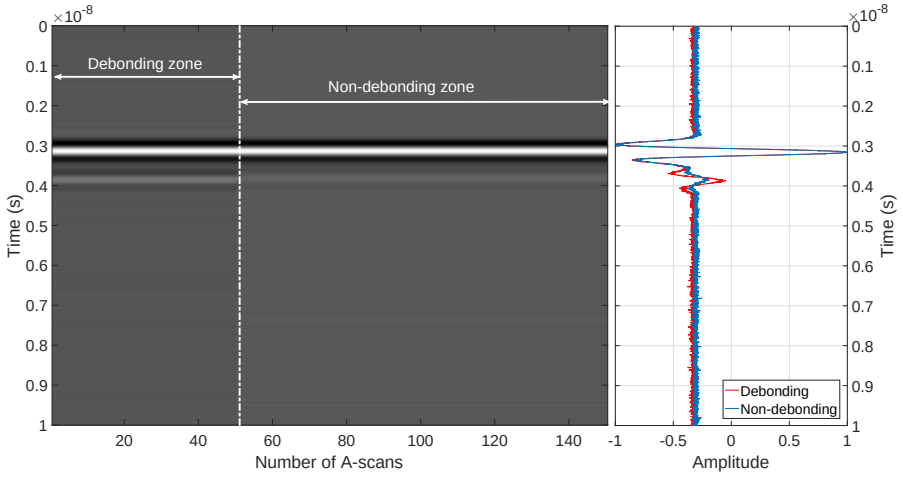

Figure A.14: *Example of a noisy GPILE B-scan for Figure. A.9 generated with* $SNR = 20\,\text{dB}$ *(left). A-scans represent respectively non-debonding and debonding cases (right)*

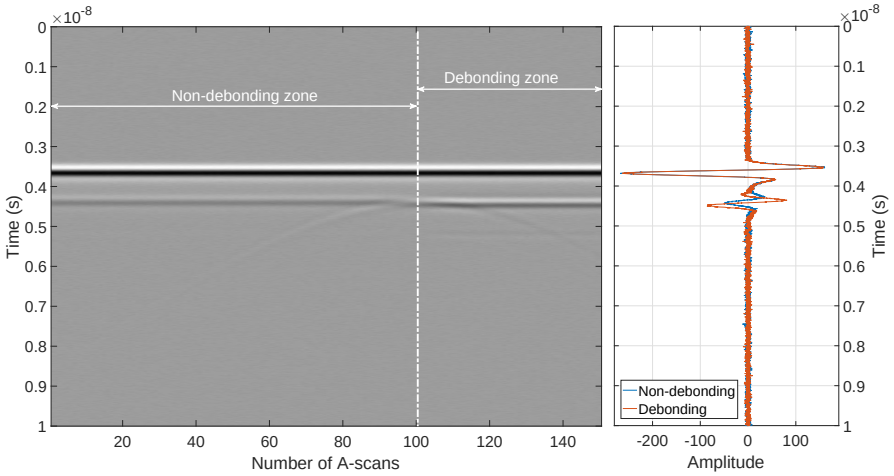

Figure A.15: *Example of a noisy gprMax B-scan for Figure. A.12 generated with* $SNR = 20\,\mathrm{dB}$ *(left). A-scans represent respectively non-debonding and debonding cases (right)*

Appendix B

Experimental Databases

Contents

The experimental databases used during the thesis were obtained from the test sites at both Cerema and IFSTTAR. At Cerema, an artificial test bench was created under controlled environment to simulate the effect of debondings between the top and the base layers. At IFSTTAR, on the other hand, a fatigue carousel test track was used to perform the experiments.

B.1 Test slabs database with controlled air-void debondings at Cerema

The test setup at Cerema uses a commercial ground-coupled GPR, namely, GSSI SIR-3000. This GPR is a hand-held portable radar used extensively in GPR imagery for civil engineering applications.

B.1.1 Experimental setup

The setup was composed of four layers as shown in Figure B.1. The top layer is an ultra-thin bituminous layer followed by the debonding layer. The two base layers are made of either semi-coarse HMA or bituminous gravel.

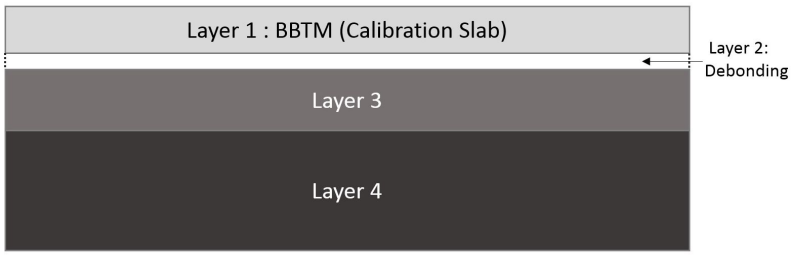

Figure B.1: *Depiction of the test bench setup [13]*

The layer nomenclature is as follows:

- BBTM (*Béton Bitumineux Très Mince* in French): This is an Ultra-thin Asphalt Surface (UTAS), a very thin Bituminous concrete layer with an average thickness of 2.0 cm to 2.5 cm. BBTM is the top layer and is also used to calibrate the GPR.
- Air-void: The second layer is a thickness-controlled air void that acts as a debonding layer between the top and the subsequent layers. The thickness of this air gap is between 0.5 cm to 1.0 cm.
- BBSG (*Béton Bitumineux Semi-Grossier* in French): The third layer is a semi-coarse hot-mix asphalt (HMA) used for surface layers in roadways with medium to high traffic. This layer is between 5.5 cm to 6.0 cm thick.
- GB (*Gravier Bitumineux* in French): The final base layer is the coarse bituminous gravel with average thickness ranging from 10.5 cm to 11.5 cm.

During the experiments, 32 pavement configurations were used. Bituminous concrete test slabs were manufactured under controlled environment for each configuration with variations in the degrees of freedom (*i.e.* thickness, aggregate size, compaction levels *etc.*) were used. Table. B.1 presents the degrees of freedom and their individual threshold values.

Table B.1: *Degrees of freedom for each pavement layer*

Degrees of freedom	**BBTM**	**BBSG**	**GB**
Thickness	2.5 cm to 3 cm	5.5 cm to 6 cm	10.5 cm to 11.5 cm
Binder content	5.5%	5.2%	4.0%
Aggregate size fraction	0/10 mm	0/10 mm	0/14 mm
Compaction level	75% - 96%		
Emulsion quality	$0\,g\,m^{-2}$, $200\,g\,m^{-2}$, $400\,g\,m^{-2}$ and $600\,g\,m^{-2}$		

One such configuration of the test slab is shown in Figure. B.2 (*Config. 28*). The top layer made of BBTM and the bottom layer made of BBSG each having an emulsion quantity of $400\,g\,m^{-2}$.

Figure B.2: *A bituminous concrete test slab used during the experiments [13]*

B.1.2 Ground-coupled WB GPR: GSSI SIR-3000

The GSSI SIR-3000 is a GPR of the SIR family of antennae that operate at a wide range of frequencies varying between 0.016 GHz to 2.6 GHz. During the controlled tests, a wideband ground-coupled radar, namely, the GSSI SIR-3000 was used, which operates at 2.6 GHz (bandwidth 0.4 GHz to 5.0 GHz). The SIR-3000 implements smart antennae with a high-frequency ground-coupled quasi mono-static configuration. The GPR has a maximum time range of 8 ns. Figure. B.3 presents the SIR-3000 transmitter-receiver system.

Figure B.3: *GSSI SIR-3000 trans-receiver system [14]*

Table. B.2 lists the system settings of the GPR for data acquisition.

Table B.2: *System settings used for data acquisition during the controlled tests*

Parameter	Value
Samples per scan	512
Time range	8 ns
A-scans per meter	150
Transmission rate	200 kHz

B.1.3 Data Acquisition

The GSSI GPR is coupled to the test slab and the measurements are made longitudinally (longer end of the test slab). Six B-scans were collected for each configuration with each B-scan equidistantly placed (5 cm apart) at the central section of the slabs. Each B-scan further consist of 120 A-scans, of which, 50 A-scans were considered for further processing. The extremities were discarded as they presented stray reflections from the slab edges. Figure. B.4 shows one such setup with the data acquisition process.

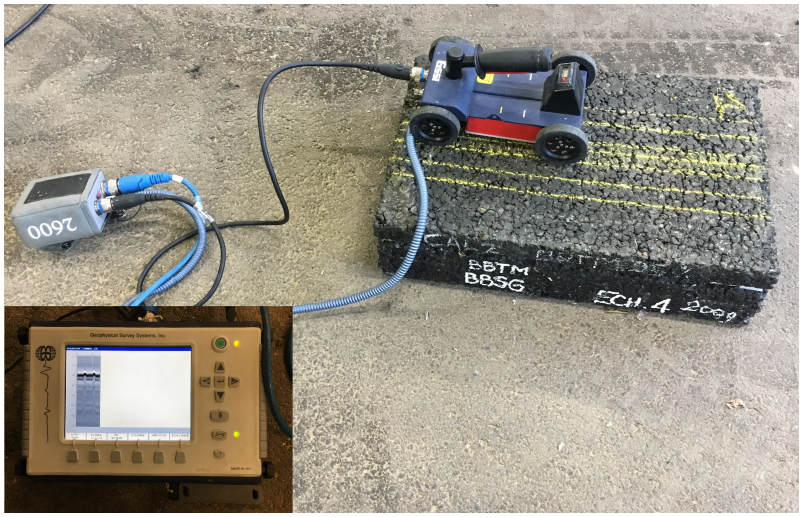

Figure B.4: *Experimental Setup for GSSI SIR-3000 [13]*

Figures B.5(a), B.5(b) and B.5(c) respectively show the test slab configurations for non-debonding and debonding with thickness 0.5 cm and 1 cm.

(a) Non-debonding

(b) Debonding with $t_{deb} = 0.5\,\text{cm}$

(c) Debonding with $t_{deb} = 1\,\text{cm}$

Figure B.5: *Test slab configurations for data acquisition [13]. The unraised slab (Figure. B.5(a)) is assumed to represent non-debonding case*

To demonstrate the GSSI data, Figure. B.6 presents the B-scan radargram along with the individual A-scans for non-debonding zone and debonding zone with thickness 0.5 cm and 1.0 cm.

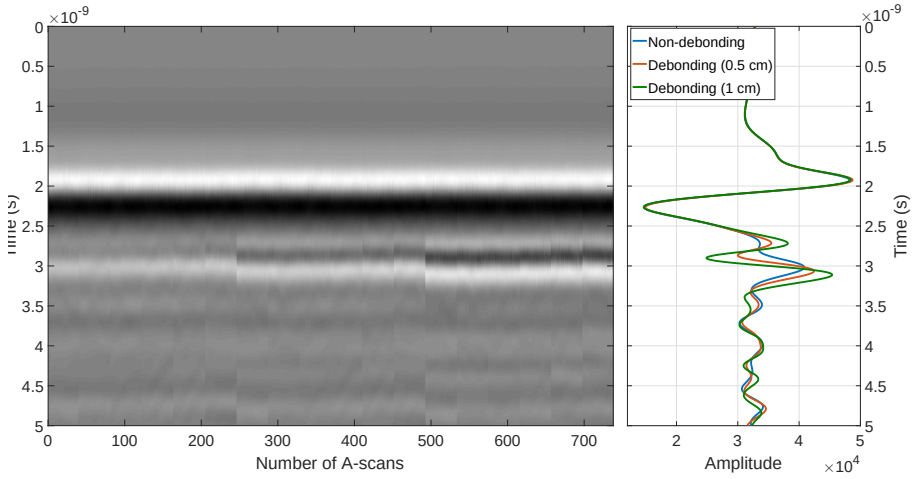

Figure B.6: *Radargrams obtained using the WB GSSI-GPR for the artificial air-void debonding test slabs at Cerema (left) along with each of the A-scans are presented (right)*

B.2 Fatigue Carousel database over embedded artificial debondings at IFSTTAR

The fatigue carousel at IFSTTAR is a unique road traffic simulator that allows Accelerated Pavement Testing (APT) (Figure. B.7). This test site is composed of a rotating carousel and a pavement test track. The 6 m wide test pavement track is divided into different sections and subjected to represent an altered pavement design for a comparative study of pavement condition. The carousel is off-circular with four arms movable heavy loads up to 65 kN on a single wheel, twin wheel tandem and tridem axles (Figure. B.8). The carousel is capable of rotating at different speeds (up to 100 km h^{-1}) at different radii (between 15.5 m to 19.5 m).

Figure B.7: *Fatigue carousel at IFSTTAR, Nantes site [15, 16]*

Figure B.8: *Carousel loading arm configurations at the fatigue carousel at IFSTTAR*

Table B.3: *Debonding zone characteristics at the pavement test site [18, 17]*

Defect type	**Label**	**Length** (m)	**Width** (m)
Sand	a	0.5	2.0
	A	1.5	2.0
Geotextile	b	0.5	2.0
	B	1.5	2.0
	D	3.0	0.5
Tack-free	c	0.5	2.0
	C	1.5	2.0

B.2.1 Experimental setup

A quarter section of the track (approximately 25 m) is dedicated to study the detection and monitoring of artificial subsurface defects by NDT methods. The pavement structure consists of two layers of bituminous concrete. The top layer is of thickness 6 cm and the base layer is 8 cm thick which is laid on a granular sub-base bed. Rectangular patches of materials were embedded between the top layer and the base layer to create artificial debondings as shown in Figure. B.9.

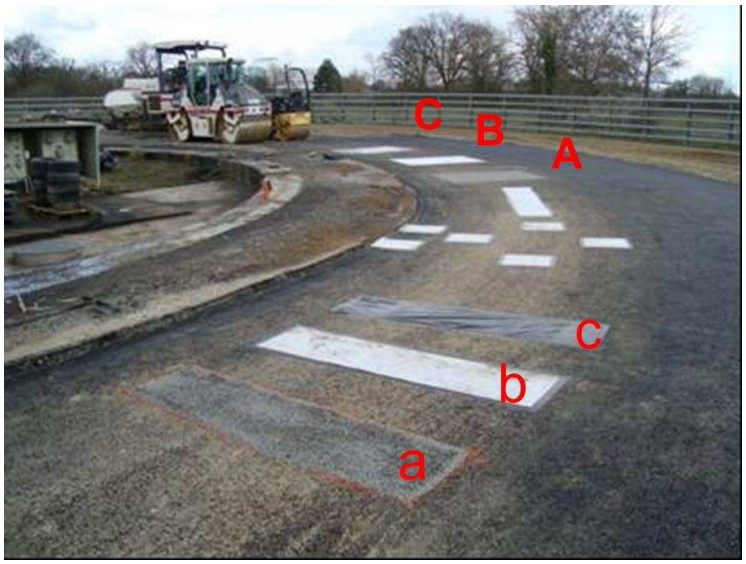

Figure B.9: *Fatigue carousel at IFSTTAR, Nantes site [15, 17]*

Each patch differs from the other by their size, location, thickness and the material embedded (namely, Geotextile, Sand and Tack-free). Table. B.3 summarizes the material characteristics based from Figure. B.9.

B.2.2 GPR used

Two GPR configurations were used for data acquisition. The first GPR is a ground coupled wideband GPR (GSSI SIR-3000) discussed in Appendix B.1.2. The parameter setting for the GSSI is as given in Table. B.2. The second GPR used during the experiments is an air-coupled ultra-wideband stepped-frequency GPR.

B.2.2.1 Air-coupled UWB Stepped-frequency GPR

An experimental air-coupled Ultra Wide-Band (UWB) stepped-frequency GPR is used for data acquisition. Data are acquired in frequency domain within the bandwidth 0.8 GHz to 10.8 GHz using a Vector Network Analyzer (VNA) [332]. Inverse Fourier Transform is conventionally used to provide radar data in time domain.

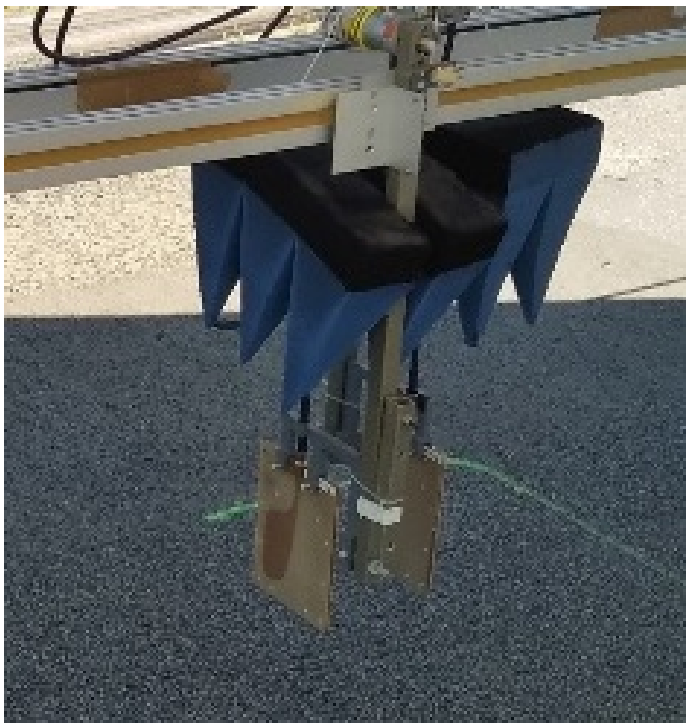

Figure B.10: *ETSA antenna configuration*

The transmitter and receiver are exponentially tapered slot antennas (ETSA) [333] positioned in bi-static configuration with $dist_{TR} = 20\,\text{cm}$, and offset at a height $h_{ant} = 40\,\text{cm}$ above the pavement surface. Fig. B.10 shows the configuration scheme for SFR during the experiments.

B.2.3 Data acquisition

A small section of the fatigue carousel has been set up to monitor the growth of defects over time and traffic (aptly referred to as APT). The data is collected repeatedly over a specific zone; that comprises of a defect-free region and a debonding region (already known to the operator) at several carousel revolutions.

To analyze the 'state' of the pavement structure and observe the growth of defects over time and traffic, the data is collected at several stages. The measurements are taken at various rotations of the carousel, namely, at 10 Kcycles, 50 Kcycles, 100 Kcycles, 200 Kcycles, 250 Kcycles and 300 Kcycles (where Kcycles denoting thousands of loading charges) using two radar configurations, namely, Air-coupled UWB SF-GPR and Ground-coupled WB GSSI-GPR. The carousel is controlled by a programmable automatic tool where the number of rotations can be started and stopped automatically. [15] provides an exhaustive description of the test site and the mechanical behavior of the bituminous material using various models.

B.2.3.1 Air-coupled UWB Stepped-frequency GPR

The transmitter and receiver are exponentially tapered slot antennas (ETSA) [333] positioned in bi-static configuration with $dist_{TR} = 20\,\text{cm}$, and offset at a height $h_{ant} = 40\,\text{cm}$ above the pavement surface.

In Fig. B.11, an automatic bench which is controlled by a computer can move the Tx and Rx antennas in both X (scanning direction) and Y axes (elevation). The scanning direction along the X-axis is about 1.50 m at the most. The bench moves the antennas stepwise every 1 cm to 2 cm to collect data vectors, namely, A-scan profiles over the pavement. Dampeners on either sides on the Tx-Rx shield the receiver from the surrounding stray reflections from the bench.

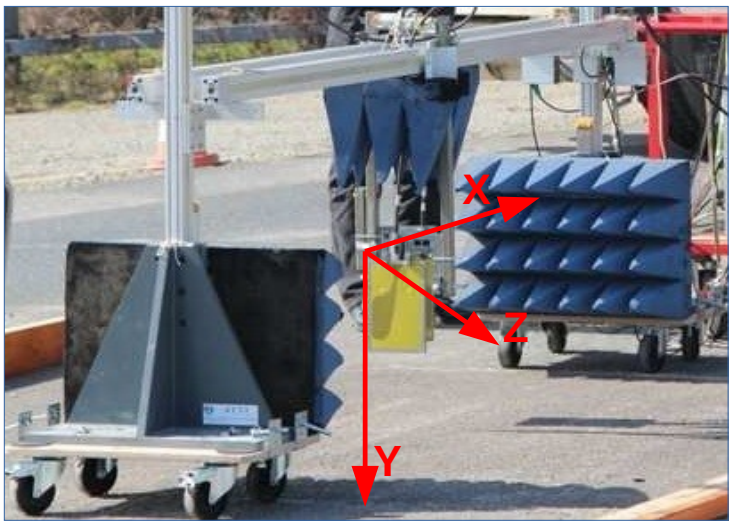

Figure B.11: *Experimental setup for data collection (surrounding blue cones are dampeners to avoid stray reflections) [10, 18]. The axes 'X', 'Y' and 'Z' respectively denote spatial, temporal and axial scanning directions*

The B-scan images were taken at each loading stage over each defective patch, each B-scan having 80 to 160 traces (A-scans) per image straddling between the two areas, namely, healthy *vs.* debonding, to ensure a visual control on data. Finally, the free space antenna response is eliminated from the data to provide the radar signal to be analyzed.

Preprocessing SF-GPR data

The SFR collects the data in frequency domain at limited speed thanks to a vector network analyzer (VNA). The frequency data is then converted to time domain data using inverse Fourier transform (IFT) for further processing. The temporal data is processed to extract signal features that well express the data without losing any significant information to perform the detection of debondings using the ML methods presented in Chapter. 3. This process is discussed extensively in Chapter. 4.

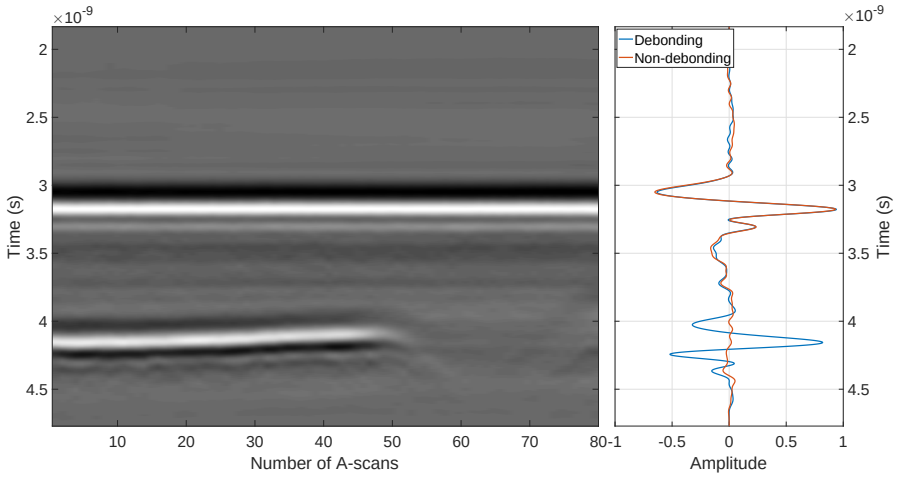

Figure B.12: *Radargram obtained for Geotextile based defects using the UWB SF-GPR at the APT site at 50 kcycles loading stage (left) along with each of debonding and non-debonding A-scans are presented (right)*

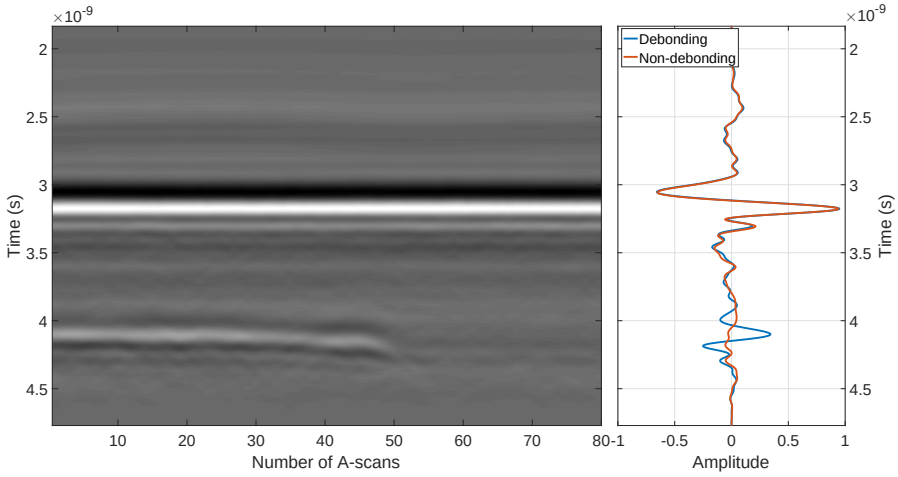

Figure B.13: *Radargram obtained for Sand based defects using the UWB SF-GPR at the APT site at 50 kcycles loading stage (left) along with each of debonding and non-debonding A-scans are presented (right)*

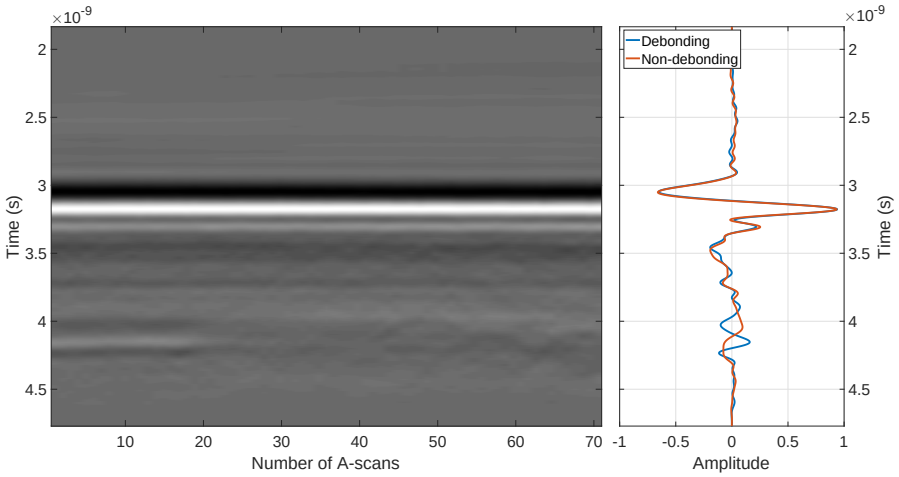

Figure B.14: *Radargram obtained for Tack-free based defects using the UWB SF-GPR at the APT site at 50 kcycles loading stage (left) along with each of debonding and non-debonding A-scans are presented (right)*

To present the temporal radar data obtained after (IFT), Figure. B.12, Figure. B.13 and Figure. B.14 depict the B-scan radargrams along with the individual A-scans for both debonding and non-debonding zones for respectively Geotextile, Sand and Tack-free based defects.

B.2.3.2 Ground-coupled WB GPR: GSSI SIR-3000

The data is acquired over the debonded zones for each loading stage using the GSSI SIR-3000 as done for the UWB SF-GPR. Figure. B.15 shows the data acquisition setup for the pavement section at the fatigue carousel using GSSI SIR-3000.

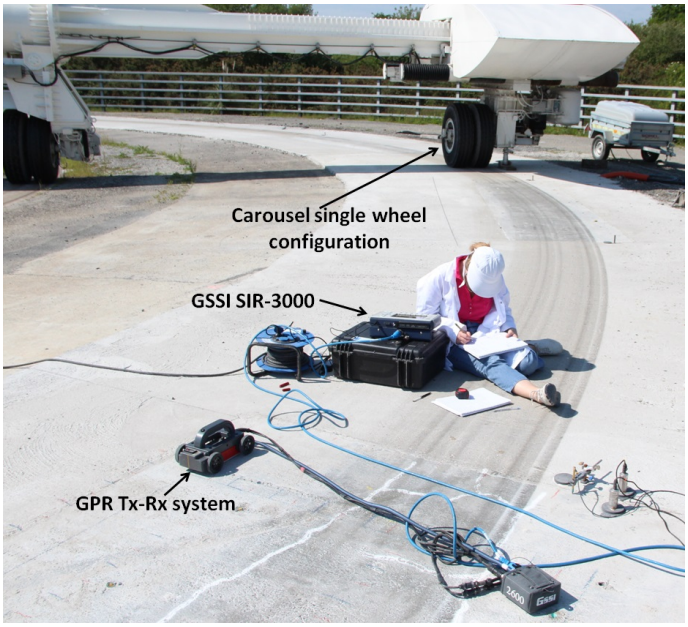

Figure B.15: *GSSI SIR-3000 for data acquisition at the fatigue carousel, IFSTTAR*

Since the GSSI acquires the data in time domain, the initial preprocessing step (*i.e*,

IFT) is avoided. The further preprocessing is carried out as discussed extensively in Chapter. 4.

To demonstrate the GSSI data, Figure. B.16, Figure. B.17 and Figure. B.18 present the B-scan radargrams along with the individual A-scans for both debonding and non-debonding zones for respectively Geotextile, Sand and Tack-free based defects.

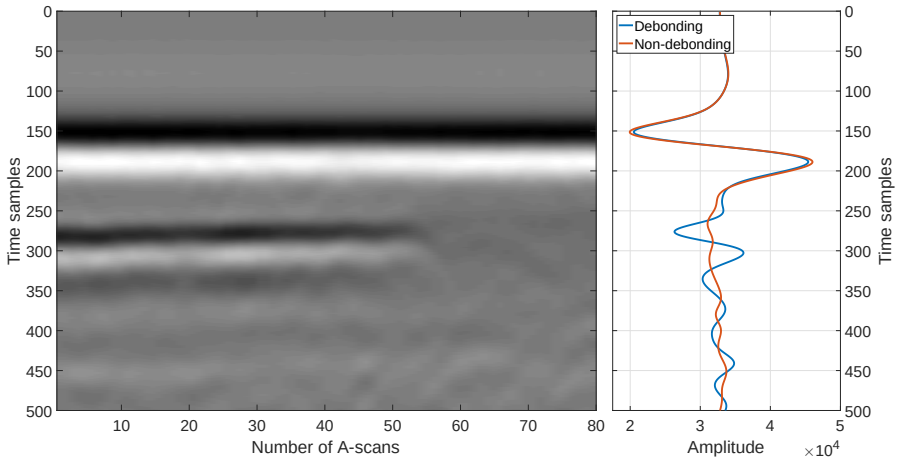

Figure B.16: *Radargram obtained for Geotextile based defects using the WB GSSI-GPR at the APT site at 50K cycles loading stage (left) along with each of debonding and non-debonding A-scans are presented (right)*

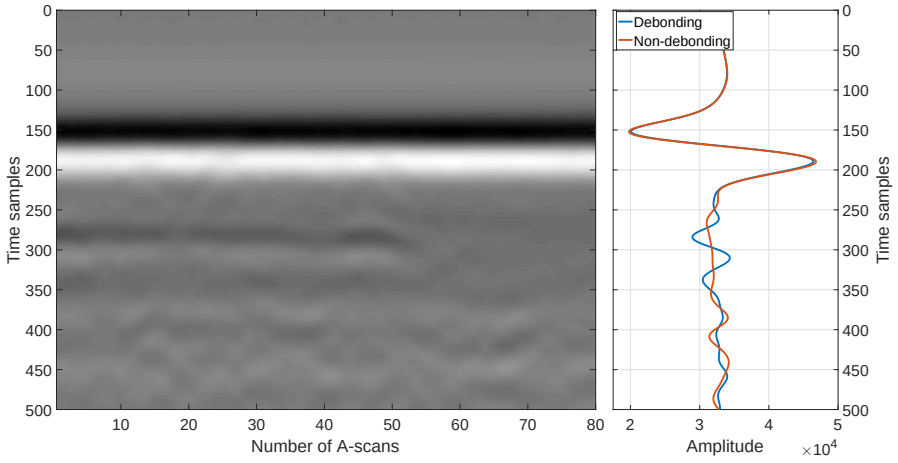

Figure B.17: *Radargram obtained for Sand based defects using the WB GSSI-GPR at the APT site at 50K cycles loading stage (left) along with each of debonding and non-debonding A-scans are presented (right)*

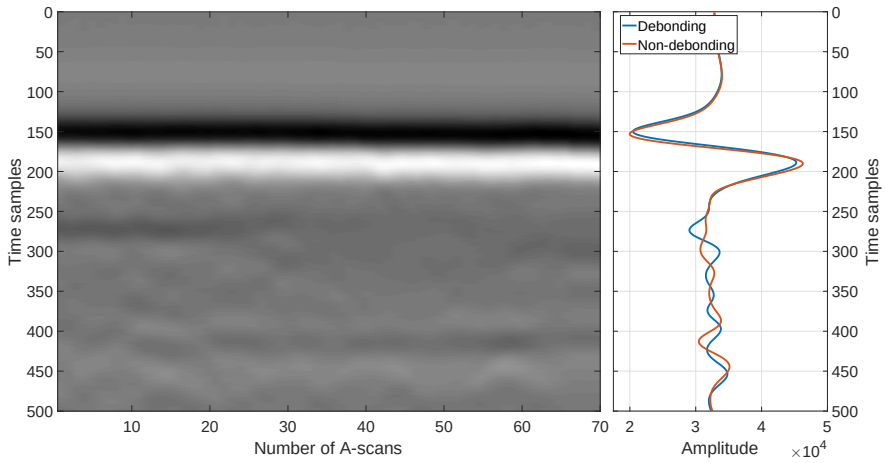

Figure B.18: *Radargram obtained for Tack-free based defects using the WB GSSI-GPR at the APT site at 50K cycles loading stage (left) along with each of debonding and non-debonding A-scans are presented (right)*

Appendix C

Performance benchmarks and Performance metrics

Contents

The performance of a ML method is judged by the amount of accurate predictions it makes. Higher the right predictions, higher is its performance. However, it is necessary to have certain benchmark with which the predictions made by the ML method can be compared to. Such benchmarks are called Performance benchmarks as they are used to analyze the performance of said methods. In this annexe, we present the various benchmarks and their creation. Further, the performance metrics are presented for each of binary classification, multi-class classification and probabilistic debonding estimation.

C.1 Performance benchmark

The performance of a ML method is judged by the amount of accurate predictions it makes. Higher the right predictions, higher is its performance. However, it is necessary to have certain benchmark with which the predictions made by the ML method can be compared to. Such benchmarks are called Performance benchmarks as they are used to analyze the performance of said methods. Performance benchmarks are estimates that we '**want**' the ML method to predict in an ideal scenario (*i.e*, 100% efficient method). Two types of benchmarks are typically used:

- Ground truth (GT)
- Pseudo-ground truth (PGT)

C.1.1 Ground truth (GT)

In case of controlled tests, the operator mostly possesses complete information about the material under test (MUT); or in this case, bituminous HMA test slabs. As such, the operator is completely aware of the MUTs containing debondings and those without any such defects.

Ground truth (GT) refers to the accurate interpretation and labeling of the pavement conditions under controlled tests. Due to the lack of any misinformation, the GT is almost always accurate and does not require any special expertise on the operator's side. This information can easily be obtained by simple observations of the pavement structure to indicate the debonding and non-debonding regions.

GT can be generated in several ways. Some of them are discussed in [334, 335] as:

1. *Synthetically produced*: GT generated from computer models

2. *Real produced*: a video or image sequence is designed and produced

3. *Real Selected*: real images selected from existing data sources

4. *Machine-automated annotation*: GT generated from the data using feature analysis and learning methods.

5. *Human annotated*: GT is defined by an operator based on his observations

The advantage of GT is that it presents a perfect representation of the MUT for benchmarking. Moreover, GT does not require high expertise. However, such type of benchmarking is suitable when the operator has all the information, which, is practically not possible.

GT has been used to create the benchmark for the experimental data collected for the test slabs with controlled air void debondings (presented in Appendix. B.1). Figure. C.1 shows two test slab configurations along with the assigned GT.

(a) Test bench: Non-debonding (b) Test bench: Debonding with $t_{deb} = 0.5\,\text{cm}$

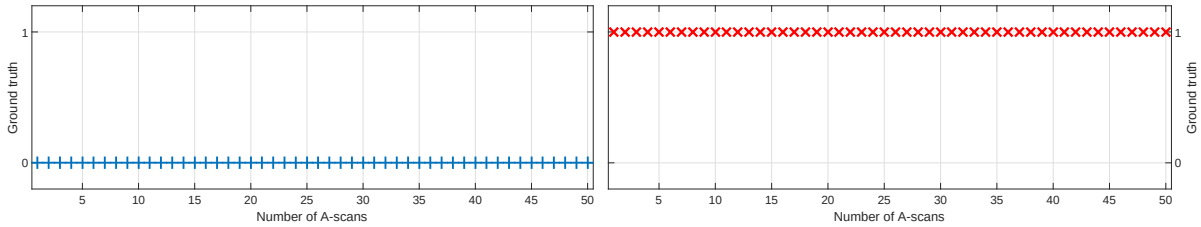

(c) Ground truth: Non-debonding (d) Ground truth: Debonding with $t_{deb} = 0.5\,\text{cm}$

Figure C.1: *Example of the GT assignment for two test slab configurations presented in Appendix. B.1. '0' indicates non-debonding and '1' indicates debonding*

C.1.2 Pseudo-ground truth (PGT)

Pseudo-ground truth (PGT) on the other hand is a roughly estimated benchmark of the MUT. In contrast to GT, PGT is an estimate of the image that would have been acquired without being affected by motion or noise during acquisition.

The primary difference between GT and PGT is that, while GT is generated from the MUT, the PGT is generated using the data collected from the MUT. The efficiency of PGT primarily depends on the level of expertness of the operator. Nevertheless, [336] presents a manual and a semi-automatic method to determine the PGT for pavement images.

For the experimental data used during the thesis, the 'measured' zone is initially divided into sections that are already known by the operator. The acquired data in the specific zones (namely, debonding and non-debonding) are respectively assigned. In order to reaffirm the assigned PGT values, the operator uses the signal magnitude as explained below (Algorithm. C.1).

The *threshold* used in Algorithm. C.1 is manually chosen by the operator based on his experience in pavement survey.

ALGORITHM C.1: Steps to determine the PGT for a B-scan image

if *Spectral data* **then**
  Data: Take Inverse Fourier Transform of the data
else
  continue;
end
while *Repeat for 'N' A-scans* **do**
  Identify the second echo (interface echo)
  Find the magnitude (*magn*) of the second echo
  if *magn* < *threshold* **then**
    Assign A-scan '0' (Non-debonding)
  else
    Assign A-scan '1' (Debonding)
  end
end

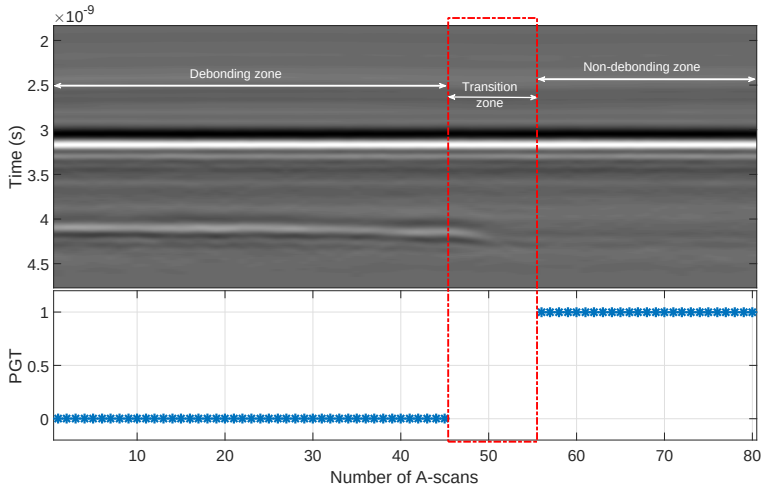

Figure C.2: *Pseudo-ground truth for experimental data collected at IFSTTAR's fatigue carousel; sand-based defects at 50 kcycles loading. The boxed region is the transition zone and is not assigned a classification label*

Transition zone

The measured pavement is divided into two zones: Healthy (Non-debonding) and Defective (Debonding). In certain pavement conditions, the operator is unable to 'decide' if a specific zone can be classified as a defective or not. During such cases, the operator defines a new class of data, namely the 'Transition zone' data. This data is ambiguous and is avoided during the classification steps in ML.

Figure. C.2 presents an example of a PGT defined for the experimental data collected at IFSTTAR's fatigue carousel (sand-based defects at 50 kcycles loading).

C.2 Performance assessment of detection methods

In order to evaluate the performance of debonding detection methods, certain metrics are used quantitatively. Such metrics are in general termed as Performance metrics. In case of debonding detection, we propose to use various metrics suitable for each type of classification:

- Metrics for Binary classification
- Metrics for Probabilistic estimation

C.2.1 Performance assessment for Binary classification

In case of binary classifications (*i.e*, {0, 1} or {-1, +1}), the detection of a ML method can result in four possible outcomes namely [10],

1. Debonding detected as a Debonding (or **TP**)
2. Debonding detected as a Non-debonding (or **FN**)
3. Non-debonding detected as a Debonding (or **FP**)
4. Non-debonding detected as a Non-debonding (or **TN**)

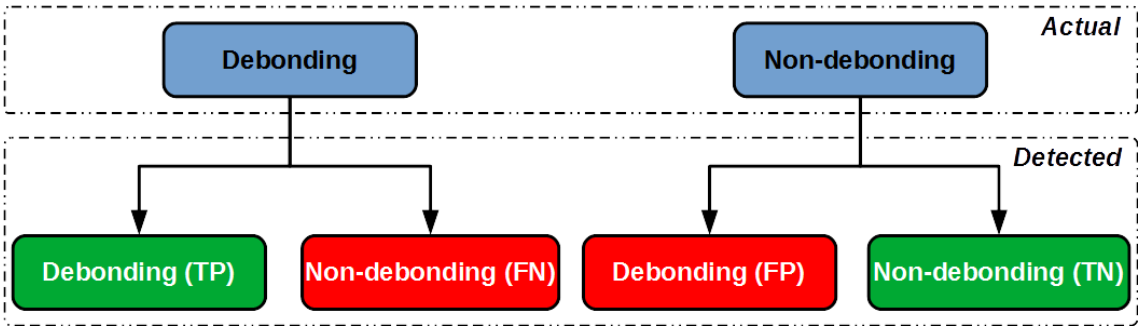

Figure C.3: *Representation of Confusion matrix in case of binary classification*

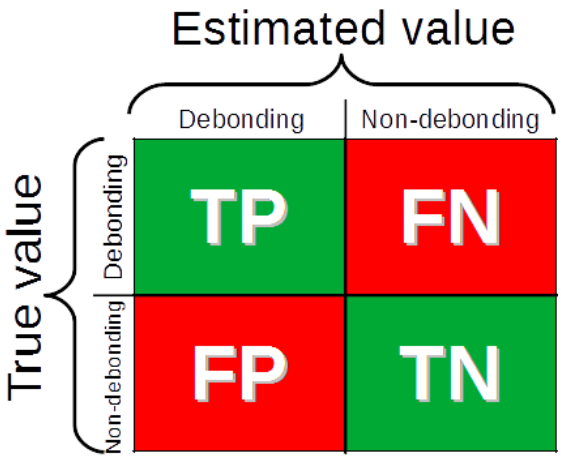

Figure C.4: *Confusion matrix in case of binary classification*

Figure. C.3 represents the possible detection outcomes and Figure. C.4 presents the confusion matrix in case of binary classification. These outcomes together form the basis of the criterion for performance assessment called as 'Confusion Matrix'. The values are complementary and can be related as:

- $TP + FN = N_{deb}$
- $TN + FP = N_{ndeb}$

where, N_{deb} and N_{deb} are respectively number of debonding and non-debonding A-scans in the B-scan.

To exploit the confusion matrix and elaborate the information presented by the results, four performance indexes were proposed for binary classification, namely,

- Sensitivity (S)
- Precision (P)
- Dice score (DSC)
- Matthew's correlation coefficient (MCC)

Sensitivity (S), also called the True Positive Rate (TPR) measures the proportion of correctly identified positives. In other words, S defines the percentage of debondings that were correctly identified by the ML method. Using the confusion matrix, S can be given as:

$$S = \frac{TP}{TP + FN} \tag{C.1}$$

Precision P, also called the Positive Predictive Value (PPV) is the fraction of the positive data that is actually positive. In other words, P can be defined as the fraction of 'detected' debondings that are 'actually' debondings. It can be expressed as:

$$P = \frac{TP}{TP + FP} \tag{C.2}$$

Finally, the harmonic mean of P and S coefficients [13, 10] is used to evaluate the performance of the detection methods; it is called the Dice coefficient (DSC) or the F1-score, equivalently [337, 338]. The DSC can be written as:

$$DSC = \frac{2 \times TP}{2 \times TP + FP + FN} = \left(\frac{1}{2}\left\{\frac{1}{P} + \frac{1}{S}\right\}\right)^{-1} \tag{C.3}$$

Matthew's correlation coefficient (MCC): While P, S and DSC take only the rate of debonding detection into consideration, the MCC is a metric that considers the rate of non-debonding detection as well. Introduced in 1975, MCC is the correlation between the observed and the predicted classifications and is computed using the confusion matrix. The MCC coefficient is sensitive to imbalanced data [339]. It is expressed as:

$$MCC = \frac{(TP \times TN) - (FP \times FN)}{\sqrt{(TP + FP)(TP + FN)(TN + FP)(TN + FN)}} \tag{C.4}$$

These performance metrics are used in Chapter. 4, 5 and 6 for decision support to detect debondings as a binary problem.

C.2.2 Performance assessment for probabilistic estimation

Since the confusion matrix can be implemented from only integral outputs, it is unsuitable for probabilistic outputs. Thus, we introduce two new performance indexes for probabilistic estimates that use the ground truth (or pseudo ground truth based on the implementation) and the predicted probabilities.

In the context of pavement monitoring, the probabilities expressed by the machine learning method can be done in two ways:

- Probability of occurrence of a debonding (P_d)
- Probability of occurrence of a non-debonding (P_n)

In order to assess the probabilistic estimation of debondings, we introduce two new metrics namely, Debonding Prediction Rate (DPR) and Non-debonding Prediction Rate (NPR) expressed as:

$$DPR = 1 - \left\{ \frac{1}{N} \sum_{i=1}^{N} |p_i - d_i| \right\} \tag{C.5}$$

$$NPR = 1 - \left\{ \frac{1}{N} \sum_{i=1}^{N} |p_i - n_i| \right\} \tag{C.6}$$

where,

N is the total number of A-scans,

p_i is the GT (or PGT) and $p_i \in \mathbb{N}\{0, 1\}$

d_i is the probability of detection of a debonding and $d_i \in \mathbb{R}\{0, 1\}$

n_i is the probability of detection of a non-debonding and $n_i \in \mathbb{R}\{0, 1\}$

These metrics are used in Chapter. 6 for decision support to present a probabilistic estimate of the occurrence of debonding or non-debonding.

Appendix D

Time-gating of a GPR A-scan

In this appendix, we present the automatic time gating of the second echo from a GPR A-scan. This windowing step is necessary in order to obtain the information localized at the interface between the two pavement layers.

The time-gating step is used in Chapter. 2 in the ART and LRT methods to determine the second amplitude. In addition, it is also used in Chapter. 4 to extract the local signal features in time domain.

Principle

Let $\mathbf{x}$ be a non-debonding A-scan signal in time domain with n time samples for the time interval t. Let the dominant operating frequency of the emitted pulse be f_c.

We define the window size (W_x) for the A-scan $\mathbf{x}$ as a function of t_w (pulse width of the emitted pulse) and f_{samp} as:

$$W_x = 2 \times f_{samp} \times t_w \tag{D.1}$$

where t_w is related to the f_c as: $t_w = \frac{1}{f_c}$.

As discussed extensively throughout the thesis, in case of a debonding, an additional signal is observed that interferes constructively with the second echo (of course, limited by the $\lambda_{mat}/4$ criteria for constructive interference). Beyond this, the two signals begin to separate until $\lambda_{mat}/2$. Thus, the pulse width of the second echo is expected to be greater than t_w, but, at the same time, less than or equal to $2 \times t_w$.

To perform the windowing, the position of a the second maximum (M_2) magnitude is obtained. This is because the first maximum corresponds to the surface echo, and the second maximum is expected to occur at the interface of the pavement layers. The window W is evenly distributed on either sides of M_2. A Tukey cosine-tapering window [340] with a taper ratio of 25% is used. The taper ratio is manually chosen by the operator such that the unwanted noise and parasitic signal around the second echo is avoided but, at the same time the important information within the window is preserved. Figure. D.1 shows an example of an A-scan with its designated time-gating window.

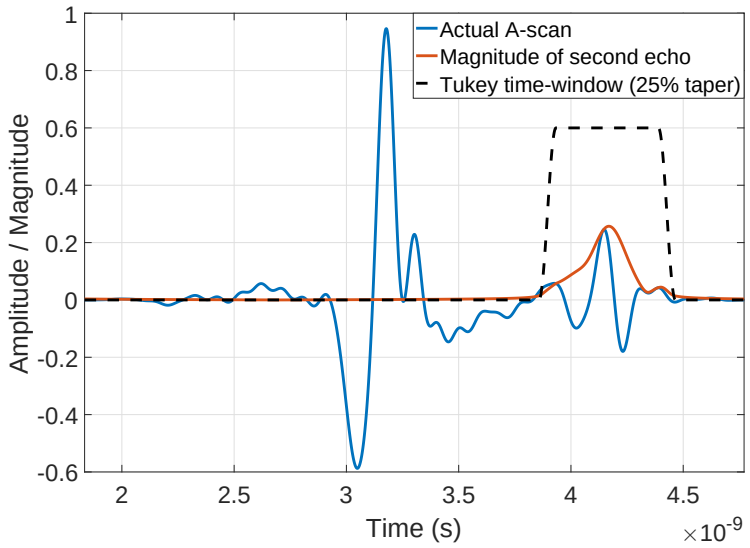

Figure D.1: *Example of an A-scan from experimental data collected using the UWB SF-GPR at IFSTTAR's fatigue carousel (Appendix. B.2.1); Tack-free defect type at 10k cycles loading stage and the time-gating window used to isolate the second echo*

Figure. D.2, Figure. D.3 and Figure. D.4 present B-scan image before windowing and compares it with the time-gated B-scan obtained after windowing for respectively Geotextile, Tack-free and Sand based defects at 10K loading.

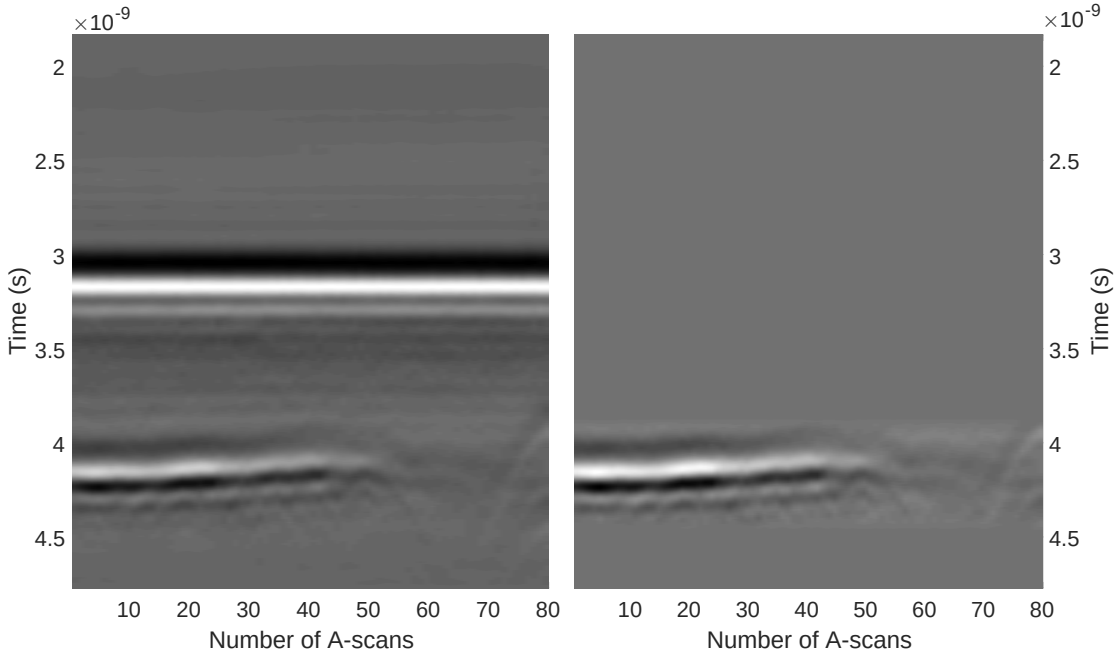

Figure D.2: *B-scan images for experimental data collected using the UWB SF-GPR at IFSTTAR's fatigue carousel (Appendix. B.2.1); Geotextile defect type at 10K cycles loading stage (left) and its respective the B-scan obtained after time gating (right)*

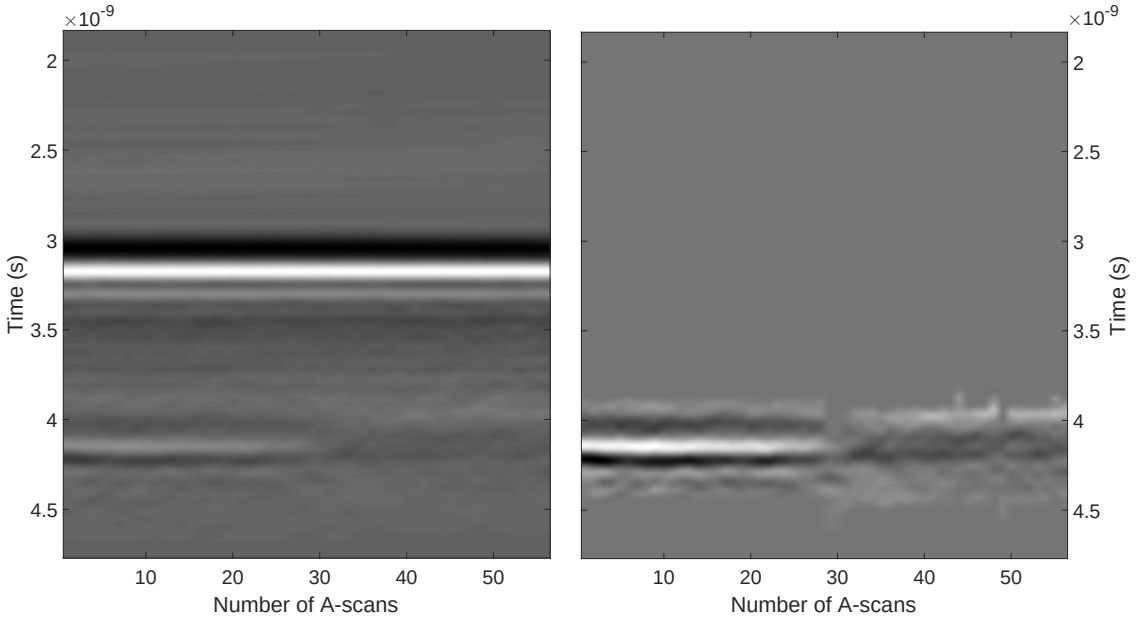

Figure D.3: *B-scan images for experimental data collected using the UWB SF-GPR at IFSTTAR's fatigue carousel (Appendix. B.2.1); Tack-free defect type at 10K cycles loading stage (left) and its respective the B-scan obtained after time gating (right)*

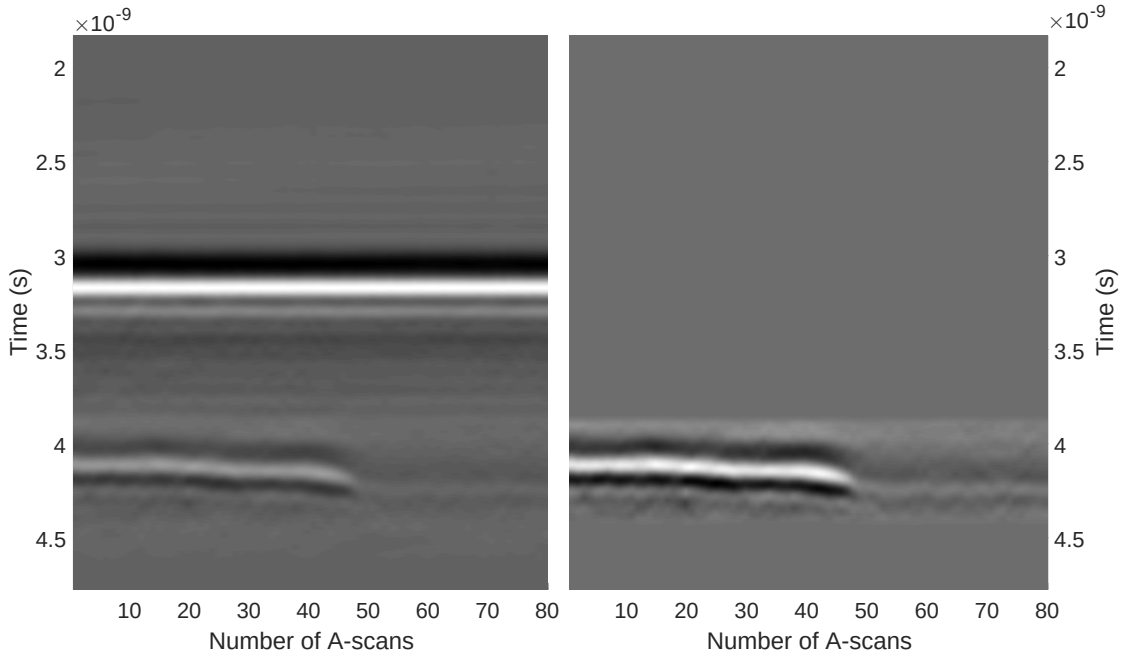

Figure D.4: *B-scan images for experimental data collected using the UWB SF-GPR at IFSTTAR's fatigue carousel (Appendix. B.2.1); Sand defect type at 10K cycles loading stage (left) and its respective the B-scan obtained after time gating (right)*

Appendix E

Additional illustrations for Chapter. 6

In this appendix, we present the debonding detection results for the intermediate loading stages of the fatigue carousel experiments for Chapter. 6. Each figure indicates the transition zone in a dashed blue box.

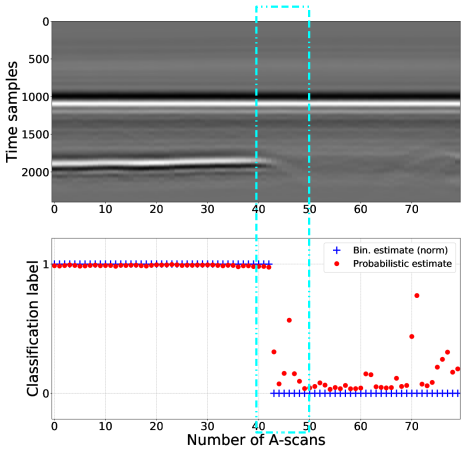

(a) 100K loading

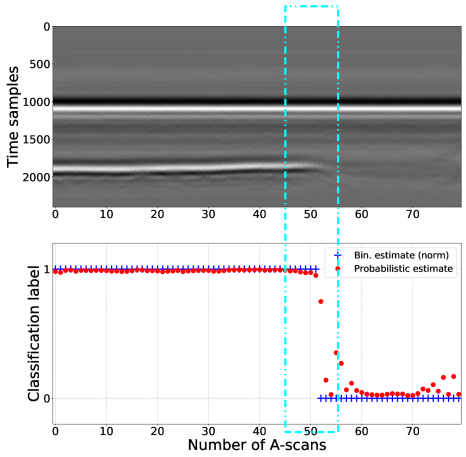

(b) 200K loading

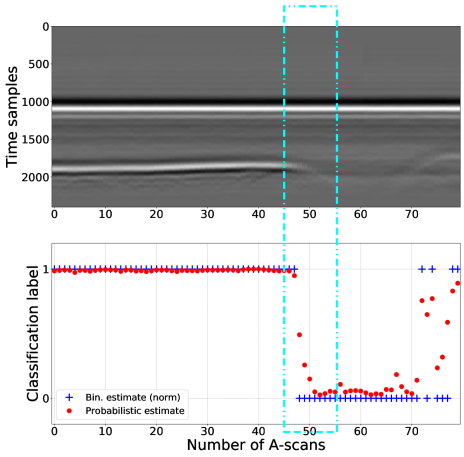

(c) 250K loading

Figure E.1: *Two-class SVM debonding detection estimates for SF-GPR data using local features at intermediate loading stages for Geotextile-based defects (strong debonding permittivity contrast)*

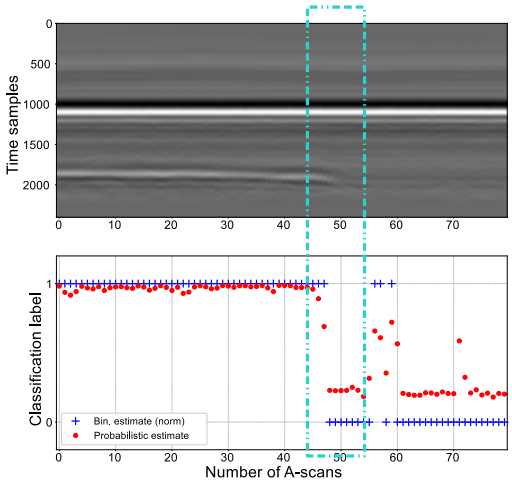

(a) 50K loading

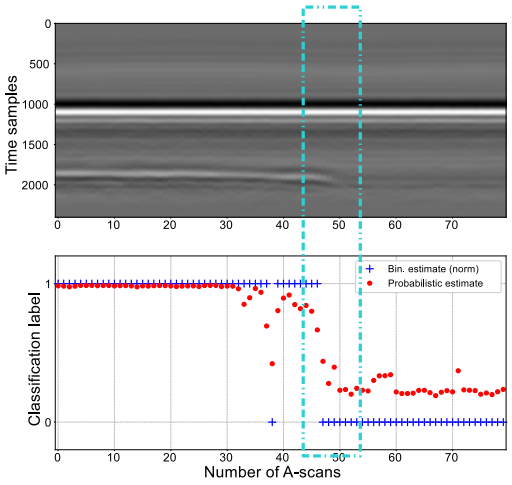

(b) 100K loading

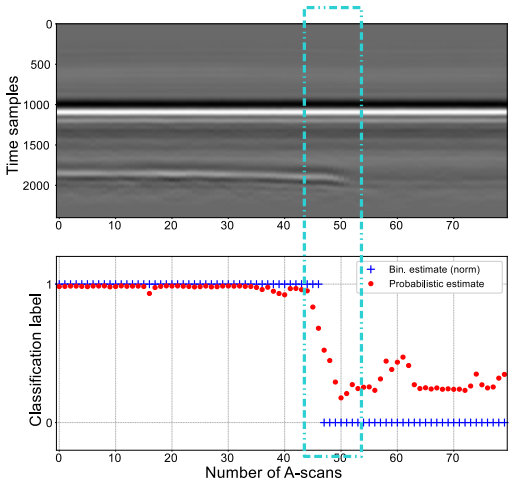

(c) 200K loading

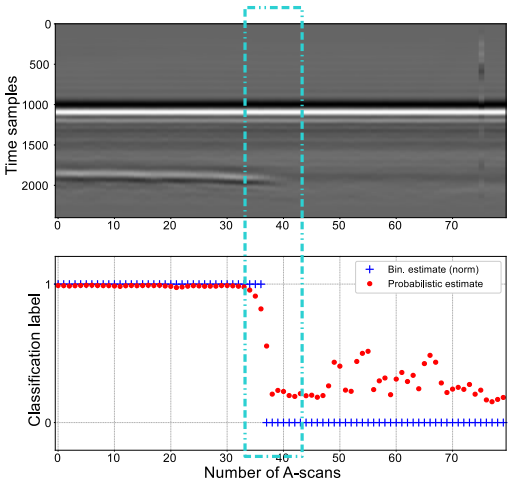

(d) 250K loading

Figure E.2: *Two-class SVM debonding detection estimates for SF-GPR data using local features at intermediate loading stages for Sand-based defects (average debonding permittivity contrast)*

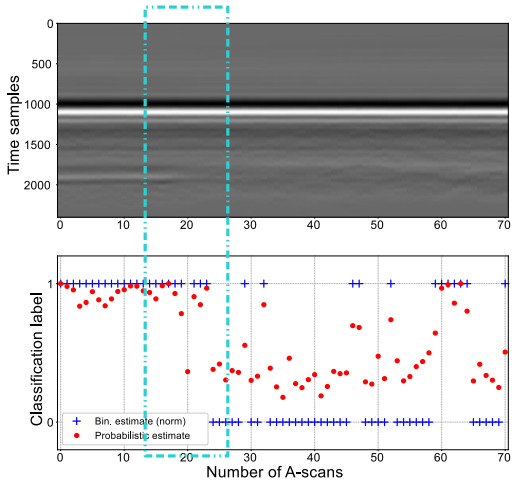

(a) 50K loading

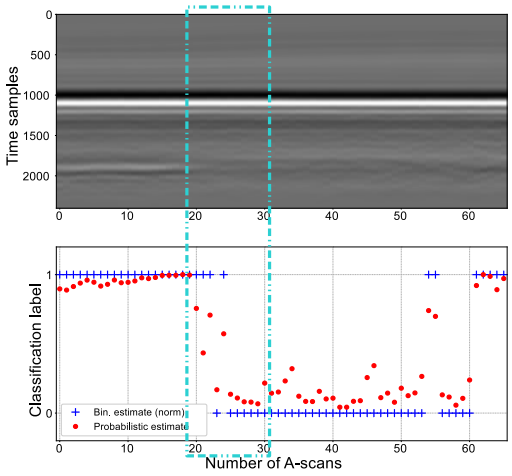

(b) 100K loading

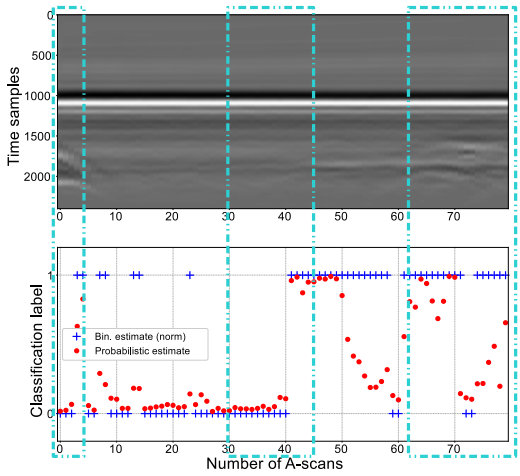

(c) 200K loading

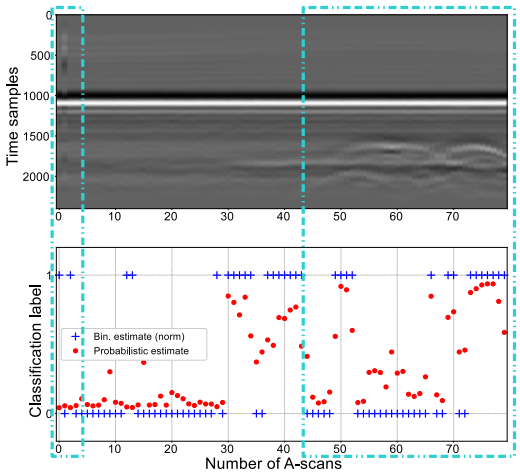

(d) 250K loading

Figure E.3: *Two-class SVM debonding detection estimates for SF-GPR data using local features at intermediate loading stages for Tack free-based defects (weak debonding permittivity contrast)*

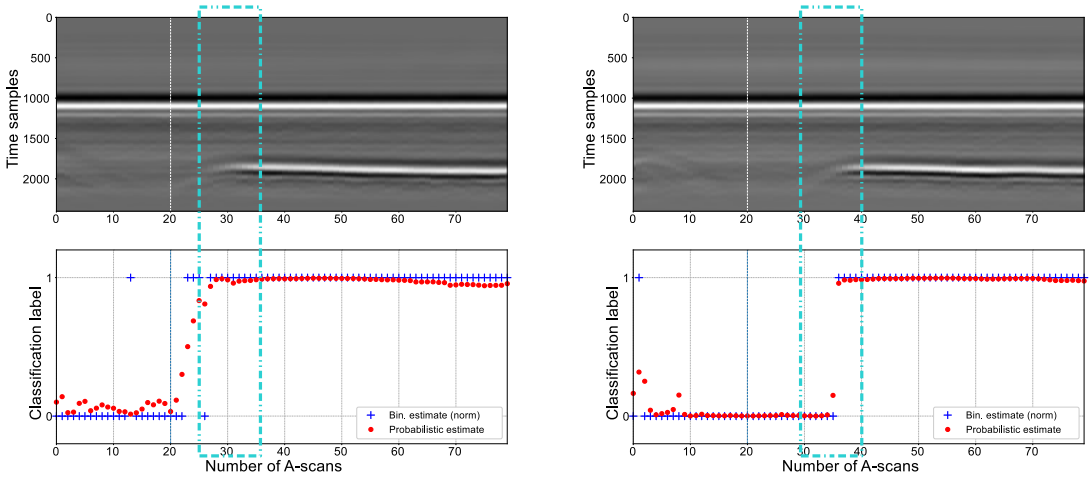

(a) 50K loading

(b) 100K loading

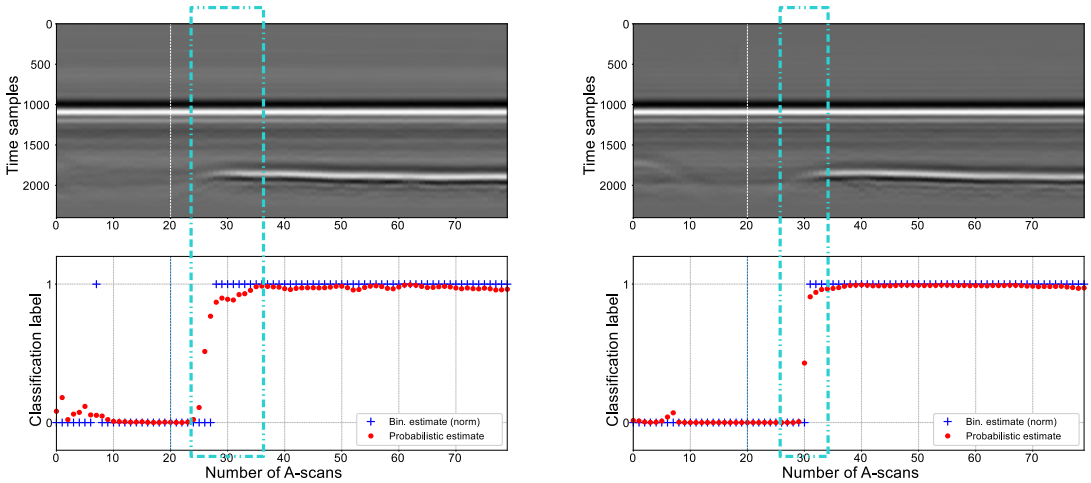

(c) 200K loading

(d) 250K loading

Figure E.4: *One-class SVM debonding detection estimates for SF-GPR data using local features at intermediate loading stages for Geotextile-based defects (strong debonding permittivity contrast)*

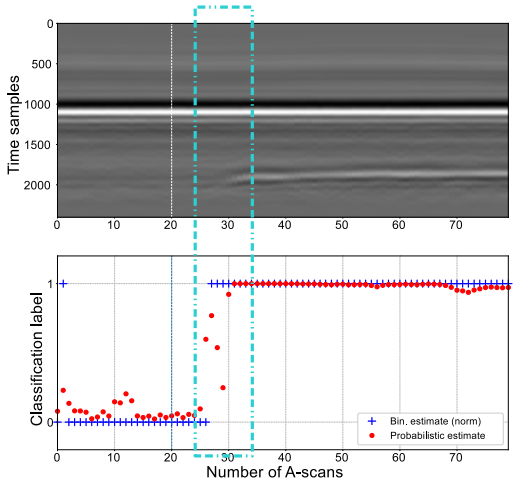

(a) 50K loading

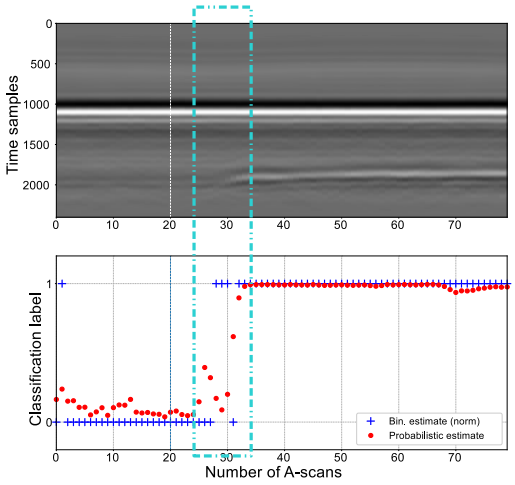

(b) 100K loading

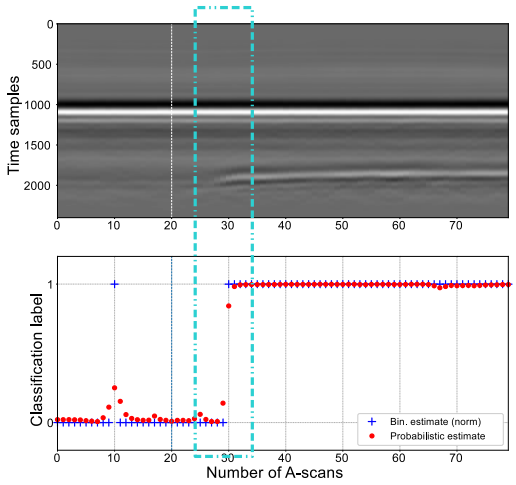

(c) 200K loading

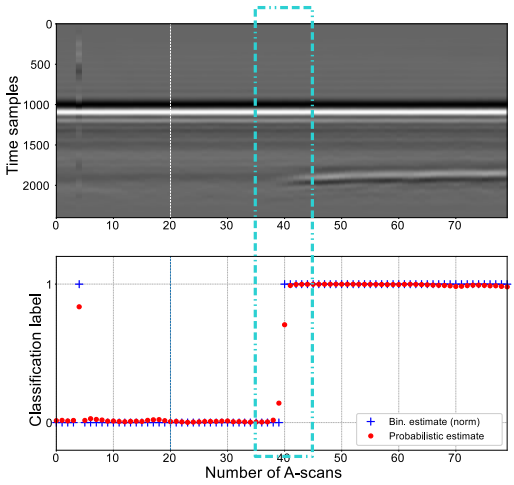

(d) 250K loading

Figure E.5: *One-class SVM debonding detection estimates for SF-GPR data using local features at intermediate loading stages for Sand-based defects (average debonding permittivity contrast)*

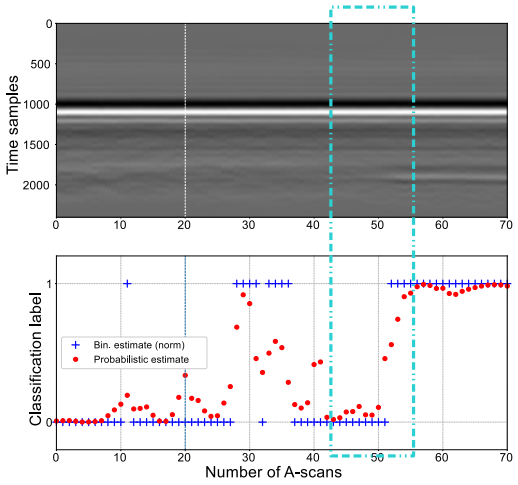

(a) 50K loading

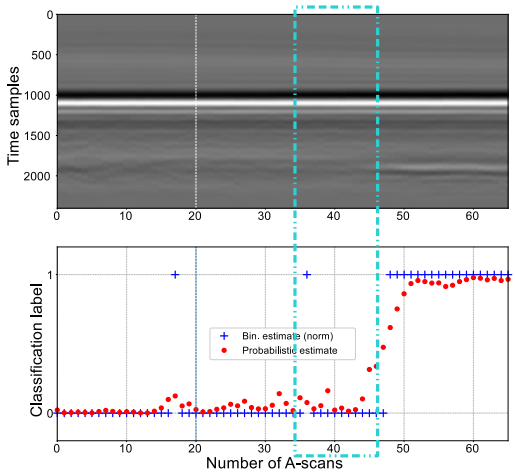

(b) 100K loading

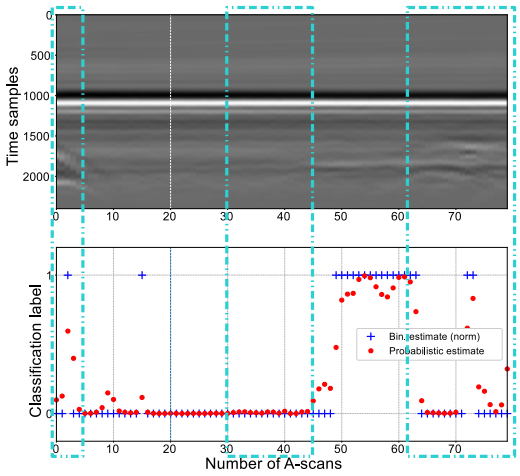

(c) 200K loading

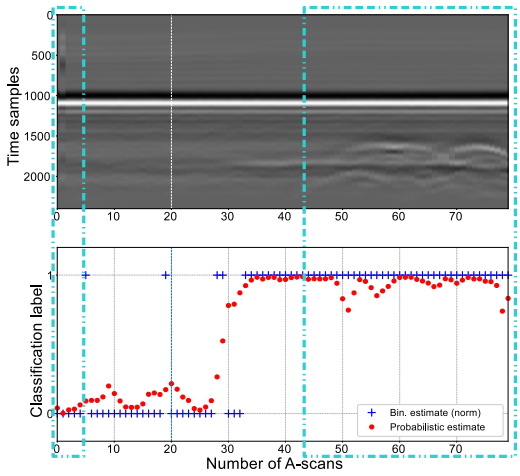

(d) 250K loading

Figure E.6: *One-class SVM debonding detection estimates for SF-GPR data using local features at intermediate loading stages for Tack free-based defects (weak debonding permittivity contrast)*

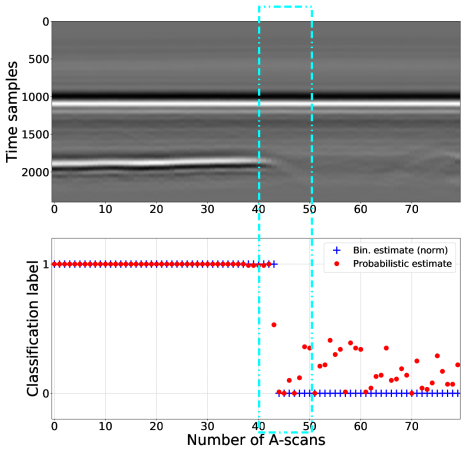

(a) 100K loading

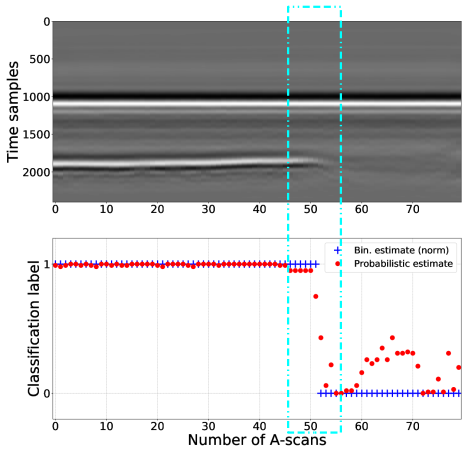

(b) 200K loading

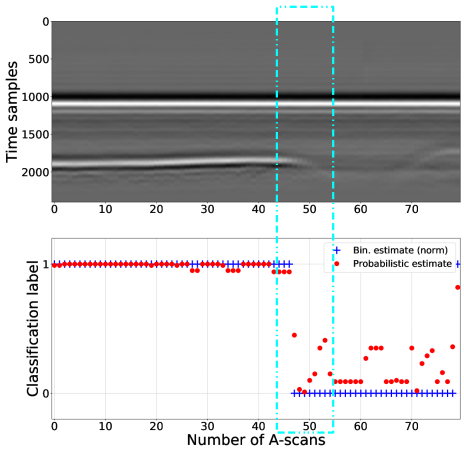

(c) 250K loading

Figure E.7: *Random forests debonding detection estimates for SF-GPR data using local features at intermediate loading stages for Geotextile-based defects (strong debonding permittivity contrast)*

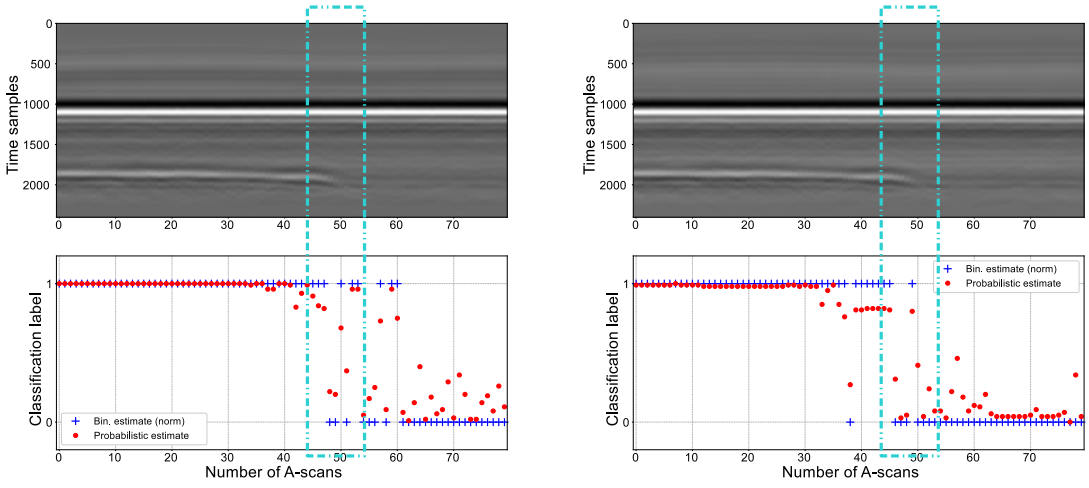

(a) 50K loading

(b) 100K loading

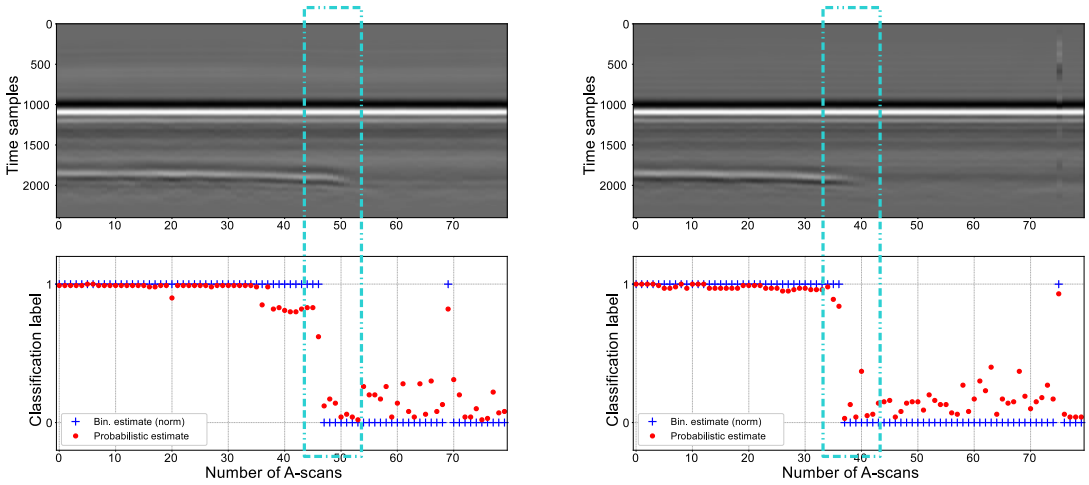

(c) 200K loading

(d) 250K loading

Figure E.8: *Random forests debonding detection estimates for SF-GPR data using local features at intermediate loading stages for Sand-based defects (average debonding permittivity contrast)*

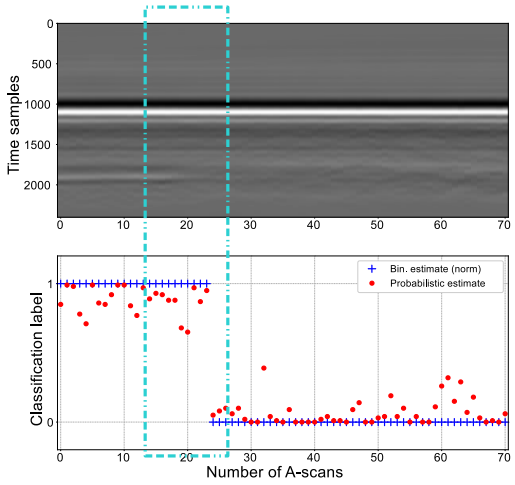

(a) 50K loading

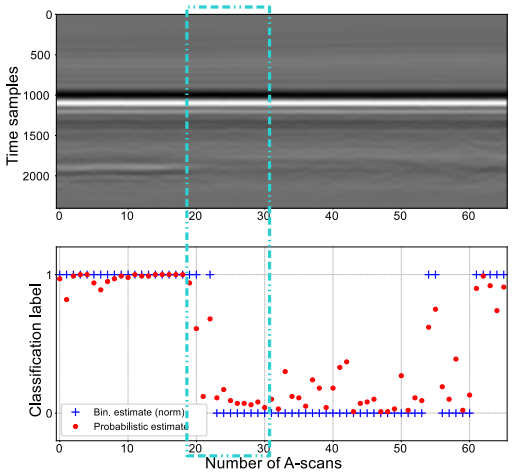

(b) 100K loading

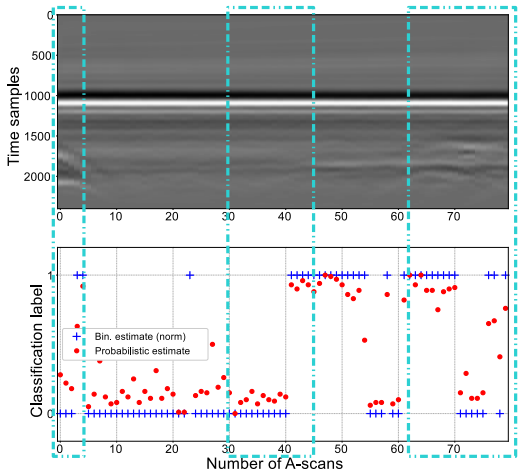

(c) 200K loading

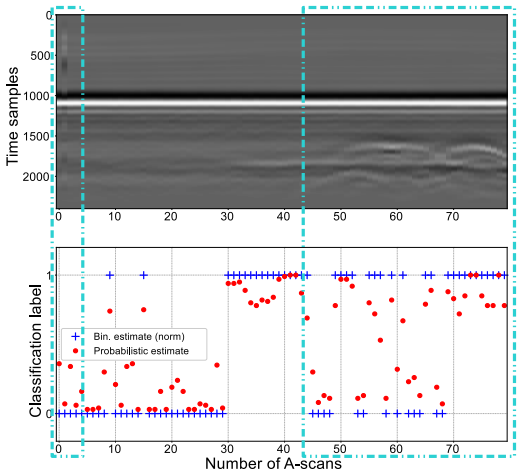

(d) 250K loading

Figure E.9: *Random forests debonding detection estimates for SF-GPR data using local features at intermediate loading stages for Tack free-based defects (weak debonding permittivity contrast)*

Table E.1: *DPR and NPR coefficients for probability estimation from local signal features at* 50 K *to* 250 K *loading for respectively Geotextile, Sand and Tack-free based defects using Two-class SVM*

Loading stage	Geotextile		Sand		Tack-free	
	DPR	NPR	DPR	NPR	DPR	NPR
100K cycles	0.99	0.87	0.98	0.76	0.52	0.72
200K cycles	0.98	0.58	0.98	0.71	0.59	0.94
250K cycles	0.98	0.68	0.77	0.75	0.39	0.46

Table E.2: *DPR and NPR coefficients for probability estimation from local signal features at* 50 K *to* 250 K *loading for respectively Geotextile, Sand and Tack-free based defects using One-class SVM*

Loading stage	Geotextile		Sand		Tack-free	
	DPR	NPR	DPR	NPR	DPR	NPR
50K cycles	0.98	0.92	0.98	0.88	0.97	0.81
100K cycles	0.98	0.87	0.99	0.96	0.83	0.92
200K cycles	0.99	0.87	0.98	0.91	0.82	0.93
250K cycles	0.99	0.81	0.99	0.99	0.89	0.99

Table E.3: *DPR and NPR coefficients for probability estimation from local signal features at* 50 K *to* 250 K *loading for respectively Geotextile, Sand and Tack-free based defects using Random forests*

Loading stage	Geotextile		Sand		Tack-free	
	DPR	NPR	DPR	NPR	DPR	NPR
100K cycles	1.00	0.78	0.99	0.7	0.62	0.65
200K cycles	0.99	0.58	0.99	0.65	0.66	0.81
250K cycles	0.99	0.68	0.98	0.83	0.73	0.7

Table E.4: *Comparison of DSC ([..]) and MCC ((..)) coefficients for binary debonding detection from local signal features at intermediate loading stages for Geotextile based defects*

Loading stage	ART (reference)	Two-class SVM	One-class SVM	Random forests
50K cycles	[1.00], (1.00)	[1.00], (1.00)	[1.00], (1.00)	[1.00], (1.00)
100K cycles	[0.98], (0.96)	[1.00], (1.00)	[0.85], (0.65)	[1.00], (1.00)
200K cycles	[1.00], (1.00)	[1.00], (1.00)	[0.91], (0.79)	[1.00]. (1.00)
250K cycles	[1.00], (1.00)	[1.00], (1.00)	[1.00], (1.00)	[0.99], (0.97)

Table E.5: *Comparison of DSC ([..]) and MCC ((..)) coefficients for binary debonding detection from local signal features at intermediate loading stages for Sand based defects*

Loading stage	ART (reference)	Two-class SVM	One-class SVM	Random forests
50K cycles	[1.00], (1.00)	[1.00], (1.00)	[0.94], (0.82)	[0.9], (0.8)
100K cycles	[1.00], (1.00)	[0.98], (0.95)	[0.94], (0.82)	[0.91], (0.85)
200K cycles	[1.00], (1.00)	[1.00], (1.00)	[1.00], (1.00)	[0.95], (0.82)
250K cycles	[0.95], (0.91)	[1.00], (1.00)	[1.00], (1.00)	[0.88], (0.77)

Table E.6: *Comparison of DSC ([..]) and MCC ((..)) coefficients for binary debonding detection from local signal features at intermediate loading stages for Tack-free based defects*

Loading stage	ART (reference)	Two-class SVM	One-class SVM	Random forests
50K cycles	[0.96], (0.95)	[0.92], (0.89)	[0.84], (0.77)	[0.90], (0.87)
100K cycles	[0.93], (0.89)	[0.88], (0.85)	[0.96], (0.94)	[0.92], (0.88)
200K cycles	[0.90], (0.86)	[0.9], (0.86)	[0.84], (0.81)	[0.95], (0.92)
250K cycles	[0.95], (0.93)	[0.86], (0.82)	[0.88], (0.82)	[0.88], (0.84)

Nomenclature

Data processing method related

α, β	Lagrangian multipliers	
$\mathcal{H}$	Hilbert transform	
ν	Admitted slack (One-class SVM)	
$\mathbf{y}$	Multi-class classifier labels	$\{0, 1, 2, 3\}$
$\mathbf{y}$	Two-class classifier labels	$\{-1, +1\}$
ξ	Admitted slack (Two-class SVM)	
R	Radius of the hyper-sphere (One-class SVM)	
sgn	Sign function	$\{-, +\}$

Physical constants

c	Speed of the EM wave in air	$3 \times 10^8\,\mathrm{m\,s^{-1}}$

Material related

ρ	Material permeability
σ	Material conductivity
ε_r	Relative permittivity

Operators

$*$	Convolution
$\mathbf{A}^T$	Transpose of the matrix $\mathbf{A}$
$\mathbf{A}^{-1}$	Inverse of the matrix $\mathbf{A}$
$\times$	Multiplication
$card(N)$	cardinality of a number N
$det(\mathbf{A})$	Determinant of the matrix $\mathbf{A}$

GPR data related

$\mathbf{F}$	2D B-scan feature matrix in time/frequency domain
$\mathbf{f}$	1D A-scan feature vector in time/frequency domain
$\mathbf{X}$	2D B-scan matrix in time/frequency domain
$\mathbf{x}$	1D A-scan vector in time/frequency domain
f	One signal feature
M, m	Number of time samples; temporal resolution
N, n	Number of A-scans; spatial resolution
x	Amplitude at an instance t

Abbreviations

EMR	Electromagnetic Radiation
GPR	Ground Penetrating Radar
MLM	Machine Learning Methods
LRT	Likelihood Ratio Test
ART	Amplitude Ratio Test
RF	Random Forests
OC-SVM	One-Class Support Vector Machines
SVM	Support Vector Machines
APT	Accelerated Pavement Test
NDT	Non-Destructive Testing
DT	Destructive testing
SHM	Structural Health Monitoring
FDTD	Finite Difference Time Domain
MoM	Method of Moment
GPILE	Generalized Propagation Inside Layer Expansion
MCC	Matthew's Correlation Coefficient
CV	Cross validation techniques
MAG	Signal Magnitude
MAAD	Maximum Absolute Amplitude Deviation
TDE	Time Delay Estimation
BW	Bandwidth
FFT, IFFT	Finite Fourier Transform, Inverse Finite Fourier Transform
AC-GPR	Air-coupled/Air-launched GPR
GC-GPR	Ground-coupled GPR

Part IV

BIBLIOGRAPHY

Bibliography

[1] Q. You, N. Zheng, and J. Ma, "Study of ravelling failure on dense graded asphalt pavement," *Proceedings of the Institution of Civil Engineers - Transport*, vol. 171, pp. 1–24, 01 2018.

[2] A. Shaat, "Pavement structural analysis based on non-destructive test measurements," *WIT Transactions on Modelling and Simulation*, vol. 12, 1970.

[3] K. Chatti, M. E. Kutay, N. Lajnef, I. Zaabar, S. Varma, H. S. Lee *et al.*, "Enhanced analysis of falling weight deflectometer data for use with mechanistic-empirical flexible pavement design and analysis and recommendations for improvements to falling weight deflectometers," Turner-Fairbank Highway Research Center, Tech. Rep., 2017.

[4] B. Guan, "Characterization of building materials by electromagnetic non-destructive methods: application to limestone," Ph.D. dissertation, Nantes, 2018.

[5] N. Diamanti and A. P. Annan, "Air-launched and ground-coupled gpr data," in *2017 11th European Conference on Antennas and Propagation (EUCAP)*, March 2017, pp. 1694–1698.

[6] H. Larsen, "Strategic highway research program," *STATENS VEJLABORATORIUM NOTAT*, no. 209, 1988. [Online]. Available: http://www.ndtoolbox.org/content/bridge/gpr-equipment

[7] A. Benedetto, F. Tosti, L. B. Ciampoli, and F. D'Amico, "An overview of ground-penetrating radar signal processing techniques for road inspections," *Signal Processing*, vol. 132, pp. 201–209, 2017.

[8] B. Scheers, "Ultra-wideband ground penetrating radar with application to the detection of anti personnel landmines," Ph.D. dissertation, 2001.

[9] M. Duman and A. C. Gürbüz, "3 d imaging for ground-penetrating radars via dictionary dimension reduction," 2015.

[10] S. S. Todkar, C. L. Bastard, V. Baltazart, A. Ihamouten, and X. Dérobert, "Performance assessment of svm-based classification techniques for the detection of artificial debondings within pavement structures from stepped-frequency a-scan radar data," *NDT & E International*, vol. 107, p. 102128, 2019. [Online]. Available: http://www.sciencedirect.com/science/article/pii/S0963869518306960

[11] A. Verikas, E. Vaiciukynas, A. Gelzinis, J. Parker, and M. C. Olsson, "Electromyographic patterns during golf swing: Activation sequence profiling and prediction of shot effectiveness," *Sensors*, vol. 16, no. 4, 2016. [Online]. Available: https://www.mdpi.com/1424-8220/16/4/592

[12] C. Bourlier, C. Le Bastard, and V. Baltazart, "Generalization of pile method to the em scattering from stratified subsurface with rough interlayers: Application to the detection of debondings within pavement structure," *IEEE Transactions on Geoscience and Remote Sensing*, vol. 53, no. 7, pp. 4104–4115, July 2015.

[13] S. S. Todkar, C. Le Bastard, A. Ihamouten, V. Baltazart, X. Dérobert, C. Fauchard, D. Guilbert, and F. Bosc, "Detection of debondings with ground penetrating radar using a machine learning method," in *2017 9th International Workshop on Advanced Ground Penetrating Radar (IWAGPR)*, June 2017, pp. 1–6.

[14] G. A. Manual, "Geophysical survey systems, inc," *Salem, NH, MN30-903 Rev. E, 99ápp*, 2014.

[15] J.-M. Simonin and G. Villain, "Detection and survey of interface defects within a pavement structure with ultrasonic pulse echo," in *8th RILEM International Conference on Mechanisms of Cracking and Debonding in Pavements*, A. Chabot, W. G. Buttlar, E. V. Dave, C. Petit, and G. Tebaldi, Eds. Dordrecht: Springer Netherlands, 2016, pp. 673–678.

[16] X. Dérobert, C. Fauchard, P. Côte, E. L. Brusq, E. Guillanton, J. Dauvignac, and C. Pichot, "Step-frequency radar applied on thin road layers," *Journal of Applied Geophysics*, vol. 47, no. 3, pp. 317 – 325, 2001, ground Penetrating Radar. [Online]. Available: http://www.sciencedirect.com/science/article/pii/S0926985101000751

[17] J. Simonin, V. Baltazart, P. Hornych, X. Dérobert, E. Thibaut, J. Sala, and V. Utsi, "Case study of detection of artificial defects in an experimental pavement structure using 3d gpr systems," in *Proceedings of the 15th International Conference on Ground Penetrating Radar*, June 2014, pp. 847–851.

[18] J. M. Simonin, V. Baltazart, C. Le Bastard, and X. Dérobert, "Progress in Monitoring the Debonding Within Pavement Structures During Accelerated Pavement Testing on the Fatigue Carousel," in *MCD2016, 8th International conference on Mechanisms of Cracking and Debonding in Pavements*, NANTES, France, Jun. 2016, p. 6p, mCD2016, 8th International conference on Mechanisms of Cracking and Debonding in Pavements, NANTES, FRANCE, 07-/06/2016 - 09/06/2016. [Online]. Available: https://hal.archives-ouvertes.fr/hal-01364065

[19] A. W.-C. Chan, "Economic and environmental evaluations of life-cycle cost analysis practice: A case study of michigan dot pavement projects," Ph.D. dissertation, 2007.

[20] K. E. Cooper, P. S. Pell, Transport, and R. R. Laboratory, "The effect of mix variables on the fatigue strength of bituminous materials," 1974, includes bibliographic references.

[21] I. L. Al-Qadi, K. I. Hasiba, A. S. Cortina, H. Ozer, Z. Leng, D. C. Parish, and S. J. Worsfold, "Best practices for implementation of tack coat: Part 1, laboratory study," 2012.

[22] A. Szydo and K. Malicki, "Analysis of the correlation between the static and fatigue test results of the interlayer bondings of asphalt layers," *Archives of Civil Engineering*, vol. 62, 03 2016.

[23] P. Jaskula and D. Rys, "Effect of interlayer bonding quality of asphalt layers on pavement performance," *IOP Conference Series: Materials Science and Engineering*, vol. 236, p. 012005, sep 2017. [Online]. Available: https://doi.org/10.1088%2F1757-899x%2F236%2F1%2F012005

[24] E. Özgan, "Determining the stability of asphalt concrete at varying temperatures and exposure times using destructive and non-destructive methods," 2007.

[25] R. Y. Liang and J. Zhou, "Prediction of fatigue life of asphalt concrete beams," *International Journal of Fatigue*, vol. 19, no. 2, pp. 117 – 124, 1997. [Online]. Available: http://www.sciencedirect.com/science/article/pii/S0142112396000667

[26] R. A. Livingston, "Nondestructive testing of historic structures," *Archives and Museum Informatics*, vol. 13, no. 3, pp. 249–271, Sep 1999. [Online]. Available: https://doi.org/10.1023/A:1012416309607

[27] X. Wang, Q. Guo, S. Yang, D. Zhang, and Y. Wang, "Nondestructive testing and assessment of consolidation effects of earthen sites," *Journal of Rock Mechanics and Geotechnical Engineering*, vol. 8, no. 5, pp. 726 – 733, 2016. [Online]. Available: http://www.sciencedirect.com/science/article/pii/S1674775516300701

[28] M. Andrzej and M. Marta, "Modern ndt systems for structural integrity examination of concrete bridge structures," *Procedia Engineering*, vol. 91, pp. 418 – 423, 2014, xXIII R-S-P Seminar, Theoretical Foundation of Civil Engineering (23RSP) (TFoCE 2014). [Online]. Available: http://www.sciencedirect.com/science/article/pii/S187770581403104X

[29] B. Hankes and D. Couse, "Condition monitoring and non-destructive testing of mechanical equipment," in *2007 IEEE Cement Industry Technical Conference Record*, April 2007, pp. 160–167.

[30] A. Tedeschi and F. Benedetto, "A real-time automatic pavement crack and pothole recognition system for mobile android-based devices," *Advanced Engineering Informatics*, vol. 32, pp. 11–25, 2017.

[31] P. Wang, Y. Hu, Y. Dai, and M. Tian, "Asphalt pavement pothole detection and segmentation based on wavelet energy field," *Mathematical Problems in Engineering*, vol. 2017, pp. 1–13, 02 2017.

[32] A. Dhivya and M. Hemalatha, "Structural health monitoring system - an embedded sensor approach," *International Journal of Engineering and Technology*, vol. 5, pp. 273–281, 02 2013.

[33] G. Song, H. Gu, Y. Mo, T. Hsu, and H. Dhonde, "Concrete structural health monitoring using embedded piezoceramic transducers," *Smart Mater. Struct*, vol. 16, pp. 959–968, 08 2007.

[34] L. Gallucci, C. Menna, L. Angrisani, D. Asprone, R. S. L. Moriello, F. Bonavolontà, and F. Fabbrocino, "An embedded wireless sensor network with wireless power transmission capability for the structural health monitoring of reinforced concrete structures," *Sensors*, vol. 17, no. 11, 2017. [Online]. Available: https://www.mdpi.com/1424-8220/17/11/2566

[35] M. F. Rad and L. Shafai, "A wireless embedded sensor for structural health monitoring applications," in *2009 13th International Symposium on Antenna Technology and Applied Electromagnetics and the Canadian Radio Science Meeting*, Feb 2009, pp. 1–4.

[36] M. Al-Saddique, G. Hamada, and M. N. Al-Awad, "State of the art: Review of coring and core analysis technology," *Journal of King Saud University - Engineering Sciences*, vol. 12, no. 1, pp. 117 – 137, 2000. [Online]. Available: http://www.sciencedirect.com/science/article/pii/S1018363918307098

[37] L. McGrath, K. Maser, and J. Puccinelli, "Determining asphalt thickness using ground penetrating radar," in *Proceedings of the international conferences on the bearing capacity of roads, railways and airfields*, 2013, pp. 199–208.

[38] R. C. West, J. Zhang, J. Moore *et al.*, "Evaluation of bond strength between pavement layers." Auburn University. National Center for Asphalt Technology, Tech. Rep., 2005.

[39] M. Kruntcheva, A. Collop, and N. Thom, "Properties of asphalt concrete layer interfaces," *Journal of Materials in Civil Engineering*, vol. 18, pp. 467–471, 06 2006.

[40] D.-H. Chen, J.-N. Wang, and J. Bilyeu, "Application of dynamic cone penetrometer in evaluation of base and subgrade layers," *Transportation Research Record*, vol. 1764, pp. 1–10, 01 2001.

[41] R. Salgado and S. Yoon, "Dynamic cone penetration test (dcpt) for subgrade assessment," *Joint Transportation Research Program*, p. 73, 2003.

[42] S. Shankar and Y. Ravi, "In-situ strength evaluation of pavement layers of low volume road using dynamic cone penetrometer (dcp)," 2014.

[43] A. Das, "Interpretation of falling weight deflectometer data," *Indian Institute of Technology Kanpur, Kanpur, India*, 1994.

[44] R. K. Dhir, J. de Brito, R. V. Silva, and C. Q. Lye, "12 - use of recycled aggregates in road pavement applications," in *Sustainable Construction Materials*, ser. Woodhead Publishing Series in Civil and Structural Engineering, R. K. Dhir, J. de Brito, R. V. Silva, and C. Q. Lye, Eds. Woodhead Publishing, 2019, pp. 451 – 494. [Online]. Available: http://www.sciencedirect.com/science/article/pii/B9780081009857000121

[45] D. Stolle and F. Peiravian, "Falling weight deflectometer data interpretation using dynamic impedance," *Canadian Journal of Civil Engineering*, vol. 23, pp. 1–8, 02 2011.

[46] S. Gupta, "Comparison of non-destructive and destructive testing on concrete: A review," *Trends in Civil Engineering and its Architecture*, vol. 3, no. 1, sep 2018. [Online]. Available: https://doi.org/10.32474%2Ftceia.2018.03.000154

[47] A. Quansah and D. Atuah, "Evaluation of pavement structural life using dynamic cone penetrometer," 08 2017.

[48] J. W. Jewett and R. A. Serway, *Physics for scientists and engineers with modern physics*. Cengage Learning EMEA, 2008.

[49] J. F. Mcnulty, "Ultrasonic testing apparatus and method," Jul. 12 1966, uS Patent 3,260,105.

[50] W.-h. Pan, X.-d. Sun, L.-m. Wu, K.-k. Yang, and N. Tang, "Damage detection of asphalt concrete using piezo-ultrasonic wave technology," *Materials*, vol. 12, no. 3, 2019. [Online]. Available: https://www.mdpi.com/1996-1944/12/3/443

[51] Y.-c. Cheng, P. Zhang, Y. Jiao, Y.-d. Wang, and J. Tao, "Damage simulation and ultrasonic detection of asphalt mixture under the coupling effects of water-temperature-radiation," *Advances in Materials Science and Engineering*, vol. 2013, pp. 1–9, 12 2013.

[52] G. Concu and N. Trulli, "Concrete defects sizing by means of ultrasonic velocity maps," *Buildings*, vol. 8, no. 12, 2018. [Online]. Available: https://www.mdpi.com/2075-5309/8/12/176

[53] V. Krstelj, J. Stepani, and D. Markui, "Ultrasonic method of materials characterization for recognition buried objects," vol. 3, pp. 6157–129, 01 2000.

[54] T. Sugimoto and T. Abe, "Study on the buried object detection method using optimum frequency range method in extremely shallow underground," in *2011 IEEE International Ultrasonics Symposium*, Oct 2011, pp. 752–755.

[55] T. Arakawa, S. Hirose, and T. Senda, "The detection of weld cracks using ultrasonic testing," *NDT International*, vol. 18, no. 1, pp. 9 – 16, 1985. [Online]. Available: http://www.sciencedirect.com/science/article/pii/0308912685900379

[56] S. Djili, F. Boukazouha, R. Halimi, and A. B. Bouda, "Defects detection in welds using ultrasonic analysis," 2006.

[57] H. Hogan, "Non-destructive technology," *Aviation Aftermarket Defence*, vol. 11, p. 35, 2015.

[58] Y. Teoh, M. Bruka, N. Idris, N. Ismail, and N. Muztaza, "Introduction of a ground penetrating radar system for subsurface investigation in balik pulau, penang island," *Journal of Physics: Conference Series*, vol. 995, p. 012098, apr 2018. [Online]. Available: https://doi.org/10.1088%2F1742-6596%2F995%2F1%2F012098

[59] M. Sato, "Gpr and its application to environmental study," *Center for Northeast Asia Studies (CNEAS), Tohoku University*, 2001.

[60] D. J. Daniels, "Ground penetrating radar," *Encyclopedia of RF and Microwave Engineering*, 2005.

[61] E. Fisher, G. A. McMechan, and A. P. Annan, "Acquisition and processing of wide-aperture ground-penetrating radar data," *Geophysics*, vol. 57, no. 3, pp. 495–504, 1992.

[62] M. I. Skolnik, "An analysis of bistatic radar," *IRE Transactions on Aerospace and Navigational Electronics*, vol. ANE-8, no. 1, pp. 19–27, March 1961.

[63] A. Saintenoy and J. Hopmans, "Ground penetrating radar: Water table detection sensitivity to soil water retention properties," *Selected Topics in Applied Earth Observations and Remote Sensing, IEEE Journal of*, vol. 4, pp. 748–753, 12 2011.

[64] A. P. Annan, S. W. Cosway, and J. D. Redman, *Water table detection with ground penetrating radar*, 2005, pp. 494–496. [Online]. Available: https://library.seg.org/doi/abs/10.1190/1.1888793

[65] M. C. Diallo, L. Z. Cheng, E. Rosa, C. Gunther, and M. Chouteau, "Integrated gpr and ert data interpretation for bedrock identification at cléricy, québec, canada," *Engineering Geology*, vol. 248, pp. 230 – 241, 2019. [Online]. Available: http://www.sciencedirect.com/science/article/pii/S0013795218301327

[66] J. Hager and M. Carnevale, "Gpr as a cost effective bedrock mapping tool for large areas," 01 2001, pp. GP13–GP13.

[67] S.-H. Ni, Y.-H. Huang, K.-F. Lo, and D.-C. Lin, "Buried pipe detection by ground penetrating radar using the discrete wavelet transform," *Computers and Geotechnics*, vol. 37, no. 4, pp. 440 – 448, 2010. [Online]. Available: http://www.sciencedirect.com/science/article/pii/S0266352X10000078

[68] J. J. Bowders, R. M. Koerner, and A. E. Lord, "Buried container detection using ground-probing radar," *Journal of Hazardous Materials*, vol. 7, no. 1, pp. 1 – 17, 1982. [Online]. Available: http://www.sciencedirect.com/science/article/pii/0304389482870015

[69] D. J. Daniels, D. J. Gunton, and H. F. Scott, "Introduction to subsurface radar," *IEE Proceedings F - Communications, Radar and Signal Processing*, vol. 135, no. 4, pp. 278–320, August 1988.

[70] G. Kino, *Acoustic Waves: Devices, Imaging, and Analog Signal Processing*, ser. Prentice-Hall Contemporary Topics in Accounting Series. Prentice-Hall, 1987. [Online]. Available: https://books.google.fr/books?id=hcsYAQAAIAAJ

[71] N. Diamanti, A. P. Annan, and J. D. Redman, "Concrete Bridge Deck Deterioration Assessment Using Ground Penetrating Radar (GPR)," *Journal of Environmental and Engineering Geophysics*, vol. 22, no. 2, pp. 121–132, 06 2017. [Online]. Available: https://doi.org/10.2113/JEEG22.2.121

[72] P. Annan, N. Diamanti, J. Redman, and S. Jackson, "Ground-penetrating radar for assessing winter roads," *Geophysics*, vol. 81, pp. WA101–WA109, 01 2016.

[73] T. Saarenketo and T. Scullion, "Road evaluation with ground penetrating radar," *Journal of Applied Geophysics*, vol. 43, no. 2, pp. 119 – 138, 2000. [Online]. Available: http://www.sciencedirect.com/science/article/pii/S092698519900052X

[74] M. Sun, N. Pinel, C. Le Bastard, V. Baltazart, A. Ihamouten, and Y. Wang, "Time delay and interface roughness estimation by gpr for pavement survey," *Near Surface Geophysics*, 06 2015.

[75] L. Bianchini Ciampoli, F. Tosti, N. Economou, and F. Benedetto, "Signal processing of gpr data for road surveys," *Geosciences*, vol. 9, no. 2, 2019. [Online]. Available: https://www.mdpi.com/2076-3263/9/2/96

[76] *GPR modelling applied to vertical and horizontal resolution of buried objects.* IEEE, 2011.

[77] A. Annan, "Ground penetrating radar principles, procedures, and applications: Sensors & software inc," *Mississauga, ON, Canada*, 2003.

[78] T. Ziani, D. Teguig, M. A. Takkouche, X. Dérobert, and M. Benslama, "Gpr modelling applied to vertical and horizontal resolution of buried objects," in *2011 International Conference on Electromagnetics in Advanced Applications*, Sep. 2011, pp. 1–4.

[79] R. Knight, P. Tercier, and H. Jol, "Multi-frequency ground penetrating radar data to characterize spatial variability," in *SEG Technical Program Expanded Abstracts 1999*. Society of Exploration Geophysicists, 1999, pp. 559–562.

[80] R. Knight, P. Tercier, and J. Irving, "The effect of vertical measurement resolution on the correlation structure of a ground penetrating radar reflection image," *Geophysical Research Letters*, vol. 31, no. 21, 2004. [Online]. Available: https://agupubs.onlinelibrary.wiley.com/doi/abs/10.1029/2004GL021112

[81] Lanbo Liu and Lieyuan Zhu, "Gpr signal analysis: can we get deep-penetration and high-resolution simultaneously?" in *Proceedings of the Tenth International Conference on Grounds Penetrating Radar, 2004. GPR 2004.*, vol. 1, June 2004, pp. 263–265.

[82] H. Jol, "Ground penetrating radar antenna frequencies and transmitter powers compared for penetration depth, resolution and reflection continuity," *Geophysical Prospecting*, vol. 43, pp. 693 – 709, 04 2006.

[83] E. Tebchrany, F. Sagnard, V. Baltazart, J. Tarel, and X. Dérobert, "Assessment of statistical-based clutter reduction techniques on ground-coupled gpr data for the detection of buried objects in soils," in *Proceedings of the 15th International Conference on Ground Penetrating Radar*, June 2014, pp. 604–609.

[84] W. Bi, Y. Zhao, C. An, and S. Hu, "Clutter elimination and random-noise denoising of gpr signals using an svd method based on the hankel matrix in the local frequency domain," *Sensors*, vol. 18, no. 10, 2018. [Online]. Available: https://www.mdpi.com/1424-8220/18/10/3422

[85] X. Song, T. Liu, D. Xiang, and Y. Su, "Gpr antipersonnel mine detection based on tensor robust principal analysis," *Remote Sensing*, vol. 11, no. 8, 2019. [Online]. Available: https://www.mdpi.com/2072-4292/11/8/984

[86] J. F. Roulette and K. A. Skrivseth, "Coherent data collection and analysis capability for the an/sps-48e radar," 1997.

[87] F. Sagnard, E. Tebchrany, and V. Baltazart, "Evaluation of an uwb ground-coupled radar in the detection of discontinuities using polarization diversity: Fdtd modeling and experiments," in *2013 7th International Workshop on Advanced Ground Penetrating Radar*, July 2013, pp. 1–6.

[88] J. Huh, H. Pham Van, S. Han, H.-J. Choi, and S.-K. Choi, "A data-driven approach for the diagnosis of mechanical systems using trained subtracted signal spectrograms," *Sensors*, vol. 19, no. 5, 2019. [Online]. Available: https://www.mdpi.com/1424-8220/19/5/1055

[89] X. Xie, P. Li, and L. Liu, "Gpr identification of voids inside concrete based on support vector machine (svm) algorithm," in *2012 14th International Conference on Ground Penetrating Radar (GPR)*, June 2012, pp. 381–386.

[90] X. Xie, P. Li, H. Qin, L. Liu, and D. C. Nobes, "GPR identification of voids inside concrete based on the support vector machine algorithm," *Journal of Geophysics and Engineering*, vol. 10, no. 3, 06 2013, 034002. [Online]. Available: https://doi.org/10.1088/1742-2132/10/3/034002

[91] J. Zhang, Q. Liu, and B. Nath, "Landmine feature extraction and classification of gpr data based on svm method," in *Advances in Neural Networks – ISNN 2004*, F.-

L. Yin, J. Wang, and C. Guo, Eds. Berlin, Heidelberg: Springer Berlin Heidelberg, 2004, pp. 636–641.

[92] K. Tbarki, S. Ben Said, R. Ksantini, and Z. Lachiri, "Rbf kernel based svm classification for landmine detection and discrimination," in *2016 International Image Processing, Applications and Systems (IPAS)*, Nov 2016, pp. 1–6.

[93] ——, "Landmine detection improvement using one-class svm for unbalanced data," in *2017 International Conference on Advanced Technologies for Signal and Image Processing (ATSIP)*, May 2017, pp. 1–6.

[94] K. Tbarki, S. B. Said, R. Ksantini, and Z. Lachiri, "Covariance-guided landmine detection and discrimination using ground-penetrating radar data," *International Journal of Remote Sensing*, vol. 39, no. 2, pp. 289–314, 2018. [Online]. Available: https://doi.org/10.1080/01431161.2017.1382746

[95] E. Pasolli, F. Melgani, M. Donelli, R. Attoui, and M. de Vos, "Automatic detection and classification of buried objects in gpr images using genetic algorithms and support vector machines," in *IGARSS 2008 - 2008 IEEE International Geoscience and Remote Sensing Symposium*, vol. 2, July 2008, pp. II–525–II–528.

[96] N. Muniappan, A. Hebsur, E. Rao, G. Venkatachalam, and D. Balasubramani, "3d subsurface mapping and classification using gpr and support vector machines for cylindrical object identification," 02 2011.

[97] Q. Lu, J. Pu, and Z. Liu, "Feature extraction and automatic material classification of underground objects from ground penetrating radar data," *JECE*, vol. 2014, pp. 28:28–28:28, Jan. 2014. [Online]. Available: http://dx.doi.org/10.1155/2014/347307

[98] M. S. El-Mahallawy and M. Hashim, "Material classification of underground utilities from gpr images using dct-based svm approach," *IEEE Geoscience and Remote Sensing Letters*, vol. 10, no. 6, pp. 1542–1546, Nov 2013.

[99] C. Le Bastard, Y. Wang, V. Baltazart, and X. Derobert, "Time delay and permittivity estimation by ground penetrating radar with support vector regression," *IEEE Geoscience and Remote Sensing Letters*, vol. 11, no. 4, pp. 873–877, 2014. [Online]. Available: https://hal.archives-ouvertes.fr/hal-00844482

[100] Z. Dong, S. Ye, Y. Gao, G. Fang, X. Zhang, Z. Xue, and T. Zhang, "Rapid detection methods for asphalt pavement thicknesses and defects by a vehicle-mounted ground penetrating radar (gpr) system," *Sensors*, vol. 16, no. 12, 2016. [Online]. Available: https://www.mdpi.com/1424-8220/16/12/2067

[101] J. Pan, C. L. Bastard, Y. Wang, and M. Sun, "Time-delay estimation using ground-penetrating radar with a support vector regression-based linear prediction method," *IEEE Transactions on Geoscience and Remote Sensing*, vol. 56, pp. 2833–2840, 2018.

[102] C. Le Bastard, V. Baltazart, Y. Wang, and J. Saillard, "Thin-pavement thickness estimation using gpr with high-resolution and superresolution methods," *IEEE Transactions on Geoscience and Remote Sensing*, vol. 45, no. 8, pp. 2511–2519, Aug 2007.

[103] V. Baltazart, J.-M. Moliard, R. Amhaz, L.-M. Cottineau, A. Wright, D. Wright, and M. Jethwa, "Automatic crack detection on pavement images for monitoring road surface conditions—some results from the collaborative fp7 trimm project," in *8th RILEM International Conference on Mechanisms of Cracking and Debonding in Pavements*, A. Chabot, W. G. Buttlar, E. V. Dave, C. Petit, and G. Tebaldi, Eds. Dordrecht: Springer Netherlands, 2016, pp. 719–724.

[104] A. Kwietniak, "Spectral decomposition of a seismic signal: Thin bed thickness estimation and analysis of attenuating zones," Ph.D. dissertation, 2016.

[105] N. Grobbe and E. C. Slob, "Seismo-electromagnetic thin-bed responses: Natural signal enhancements?" *Journal of Geophysical Research: Solid Earth*, vol. 121, no. 4, pp. 2460–2479, 2016. [Online]. Available: https://agupubs.onlinelibrary.wiley.com/doi/abs/10.1002/2015JB012381

[106] C. Duan, R. Wu, and J. Liu, "Estimation of airfield pavement void thickness using gpr," in *2011 3rd International Asia-Pacific Conference on Synthetic Aperture Radar (APSAR)*, Sep. 2011, pp. 1–4.

[107] J. H. Bradford and J. C. Deeds, "Ground-penetrating radar theory and application of thin-bed offset-dependent reflectivity," *GEOPHYSICS*, vol. 71, no. 3, pp. K47–K57, 2006. [Online]. Available: https://doi.org/10.1190/1.2194524

[108] J.-M. Simonin, C. Fauchard, P. Hornych, V. Guilbert, J.-P. Kerzrého, and S. Trichet, "Detecting unbounded interface with non destructive techniques," in *7th RILEM International Conference on Cracking in Pavements*, A. Scarpas, N. Kringos, I. Al-Qadi, and L. A., Eds. Dordrecht: Springer Netherlands, 2012, pp. 179–190.

[109] S. Angra and S. Ahuja, "Machine learning and its applications: A review," in *2017 International Conference on Big Data Analytics and Computational Intelligence (ICBDAC)*, March 2017, pp. 57–60.

[110] R. D. Shirwaikar, N. Mago, Dinesh Acharya U, K. Makkithaya, and Govardhan Hegde K, "Supervised learning techniques for analysis of neonatal data," in *2016 2nd International Conference on Applied and Theoretical Computing and Communication Technology (iCATccT)*, July 2016, pp. 25–31.

[111] O. Simeone, "A very brief introduction to machine learning with applications to communication systems," 2018.

[112] T. Wuest, D. Weimer, C. Irgens, and K.-D. Thoben, "Machine learning in manufacturing: advantages, challenges, and applications," *Production & Manufacturing Research*, vol. 4, no. 1, pp. 23–45, 2016. [Online]. Available: https://doi.org/10.1080/21693277.2016.1192517

[113] W. Shao, A. Bouzerdoum, S. L. Phung, L. Su, B. Indraratna, and C. Rujikiatkamjorn, "Automatic classification of ground-penetrating-radar signals for railway-ballast assessment," *IEEE Transactions on Geoscience and Remote Sensing*, vol. 49, no. 10, Oct 2011.

[114] K. Tbarki, S. B. Said, R. Ksantini, and Z. Lachiri, "One-class svm for landmine detection and discrimination," in *2017 International Conference on Control, Automation and Diagnosis (ICCAD)*, Jan 2017, pp. 309–313.

[115] L. KrysiÅski and J. Sudyka, "Gpr abilities in investigation of the pavement transversal cracks," *Journal of Applied Geophysics*, vol. 97, pp. 27 – 36, 2013, ground Penetrating Radar. [Online]. Available: http://www.sciencedirect.com/science/article/pii/S0926985113000669

[116] M. Solla, S. LagÃijela, H. GonzÃąlez-Jorge, and P. Arias, "Approach to identify cracking in asphalt pavement using gpr and infrared thermographic methods: Preliminary findings," *NDT & E International*, vol. 62, pp. 55 – 65, 2014. [Online]. Available: http://www.sciencedirect.com/science/article/pii/S0963869513001515

[117] R. Forest and V. Utsi, "Non destructive crack depth measurements with ground penetrating radar," vol. 2, 02 2004, pp. 799 – 802.

[118] P. Louridas and C. Ebert, "Machine learning," *IEEE Software*, vol. 33, no. 5, pp. 110–115, Sep. 2016.

[119] J. MacQueen, "Some methods for classification and analysis of multivariate observations," in *Proceedings of the Fifth Berkeley Symposium on Mathematical Statistics and Probability, Volume 1: Statistics*. Berkeley, Calif.: University of California Press, 1967, pp. 281–297. [Online]. Available: https://projecteuclid.org/euclid.bsmsp/1200512992

[120] C. Cortes and V. Vapnik, "Support-vector networks," *Machine Learning*, vol. 20, no. 3, pp. 273–297, Sep 1995. [Online]. Available: https://doi.org/10.1023/A:1022627411411

[121] Tin Kam Ho, "Random decision forests," in *Proceedings of 3rd International Conference on Document Analysis and Recognition*, vol. 1, Aug 1995, pp. 278–282 vol.1.

[122] A. Oliver, A. Odena, C. Raffel, E. D. Cubuk, and I. J. Goodfellow, "Realistic evaluation of deep semi-supervised learning algorithms," 2018.

[123] O. Chapelle, B. Schlkopf, and A. Zien, *Semi-Supervised Learning*, 1st ed. The MIT Press, 2010.

[124] T. T. Lu, "Fundamental limitations of semi-supervised learning," Master's thesis, University of Waterloo, 2009.

[125] D. A. J. Amrita Sadarangani *, "A survey of semi-supervised learning," *INTERNATIONAL JOURNAL OF ENGINEERING SCIENCES & RESEARCH TECHNOLOGY*, vol. 5, no. 10, pp. 138–143, Oct. 2016. [Online]. Available: https://doi.org/10.5281/zenodo.159333

[126] J. Bagherzadeh and H. Asil, "A review of various semi-supervised learning models with a deep learning and memory approach," *Iran Journal of Computer Science*, vol. 2, no. 2, pp. 65–80, Jun 2019. [Online]. Available: https://doi.org/10.1007/s42044-018-00027-6

[127] A. Singh, R. Nowak, and J. Zhu, "Unlabeled data: Now it helps, now it doesn't," in *Advances in Neural Information Processing Systems 21*, D. Koller, D. Schuurmans, Y. Bengio, and L. Bottou, Eds. Curran Associates, Inc., 2009, pp. 1513–1520. [Online]. Available: http://papers.nips.cc/paper/3551-unlabeled-data-now-it-helps-now-it-doesnt.pdf

[128] P. Wittek, *Quantum Machine Learning: What Quantum Computing Means to Data Mining*, 08 2014.

[129] O. Bousquet, U. Luxburg, and G. Rätsch, "Advanced lectures on machine learning, ml summer schools 2003, canberra, australia, february 2-14, 2003, tübingen, germany, august 4-16, 2003, revised lectures," 01 2004.

[130] P. Tamilselvi and K. A. Kumar, "Unsupervised machine learning for clustering the infected leaves based on the leaf-colours," in *2017 Third International Conference on Science Technology Engineering Management (ICONSTEM)*, March 2017, pp. 106–110.

[131] N. Amruthnath and T. Gupta, "A research study on unsupervised machine learning algorithms for early fault detection in predictive maintenance," in *2018 5th International Conference on Industrial Engineering and Applications (ICIEA)*, April 2018, pp. 355–361.

[132] A. Wosiak, A. Zamecznik, and K. Niewiadomska-Jarosik, "Supervised and unsupervised machine learning for improved identification of intrauterine growth restriction types," in *2016 Federated Conference on Computer Science and Information Systems (FedCSIS)*, Sep. 2016, pp. 323–329.

[133] P. Mehta, H. Shah, V. Kori, V. Vikani, S. Shukla, and M. Shenoy, "Survey of unsupervised machine learning algorithms on precision agricultural data," in *2015 International Conference on Innovations in Information, Embedded and Communication Systems (ICIIECS)*, March 2015, pp. 1–8.

[134] D. Sonagara and S. Badheka, "Comparison of basic clustering algorithms," 2014.

[135] Y. Yang, "Unsupervised ensemble learning and its application to temporal data clustering," Ph.D. dissertation, The University of Manchester (United Kingdom), 2011.

[136] I. Bekkouche and F. Hadria, "A new image clustering method based on the fuzzy harmony search algorithm and fourier transform," *JIPS*, vol. 12, no. 4, pp. 555–576, 2016. [Online]. Available: https://doi.org/10.3745/JIPS.02.0047

[137] G. Amit, N. Gavriely, and N. Intrator, "Cluster analysis and classification of heart sounds," *Biomedical Signal Processing and Control*, vol. 4, no. 1, pp. 26 – 36, 2009. [Online]. Available: http://www.sciencedirect.com/science/article/pii/S1746809408000530

[138] Z. Di, M. Chang, P. Guo, Y. Li, and Y. Chang, "Using real-time data and unsupervised machine learning techniques to study large-scale spatiotemporal characteristics of wastewater discharges and their influence on surface water quality in the yangtze river basin," *Water*, vol. 11, no. 6, 2019. [Online]. Available: https://www.mdpi.com/2073-4441/11/6/1268

[139] J. Dromard, G. Roudière, and P. Owezarski, "Unsupervised network anomaly detection in real-time on big data," in *New Trends in Databases and Information Systems*, T. Morzy, P. Valduriez, and L. Bellatreche, Eds. Cham: Springer International Publishing, 2015, pp. 197–206.

[140] F. Saki and N. Kehtarnavaz, "Real-time unsupervised classification of environmental noise signals," *IEEE/ACM Transactions on Audio, Speech, and Language Processing*, vol. 25, no. 8, pp. 1657–1667, Aug 2017.

[141] T. Maruyama, "Real-time k-means clustering for color images on reconfigurable hardware," in *18th International Conference on Pattern Recognition (ICPR'06)*, vol. 2, Aug 2006, pp. 816–819.

[142] S. Theodoridis and K. Koutroumbas, *Pattern Recognition*, 01 2009.

[143] Y. LeCun, Y. Bengio, and G. Hinton, "Deep learning," *nature*, vol. 521, no. 7553, p. 436, 2015.

[144] A. E. Maxwell, T. A. Warner, and F. Fang, "Implementation of machine-learning classification in remote sensing: an applied review," *International Journal of Remote Sensing*, vol. 39, no. 9, pp. 2784–2817, 2018. [Online]. Available: https://doi.org/10.1080/01431161.2018.1433343

[145] S. Yadav and S. Shukla, "Analysis of k-fold cross-validation over hold-out validation on colossal datasets for quality classification," in *2016 IEEE 6th International Conference on Advanced Computing (IACC)*, Feb 2016, pp. 78–83.

[146] J. Hubbard, A. Hund, I. Levin, K. McGraw, M. Wilkins, and R. Safran, "The importance of cross-validation, accuracy, and precision for measuring plumage color: A comment on vaquero-alba et al. (2016)," *Auk*, vol. 134, no. 1, pp. 34–38, 1 2017.

[147] M. Wang, Y. Cui, X. Wang, S. Xiao, and J. Jiang, "Machine learning for networking: Workflow, advances and opportunities," *IEEE Network*, vol. 32, no. 2, p. 9299, Mar 2018. [Online]. Available: http://dx.doi.org/10.1109/MNET.2017.1700200

[148] W. Yu and Y. Shun-Zheng, "Supervised learning real-time traffic classifiers," *Journal of Networks*, vol. 4, 09 2009.

[149] G. A. Carpenter, S. Grossberg, and J. H. Reynolds, "Artmap: Supervised real-time learning and classification of nonstationary data by a self-organizing neural network," *Neural Networks*, vol. 4, no. 5, pp. 565 – 588, 1991. [Online]. Available: http://www.sciencedirect.com/science/article/pii/089360809190012T

[150] D. MadroÃśal, R. Lazcano, R. Salvador, H. Fabelo, S. Ortega, G. Callico, E. Juarez, and C. Sanz, "Svm-based real-time hyperspectral image classifier on a manycore architecture," *Journal of Systems Architecture*, vol. 80, pp. 30 – 40, 2017. [Online]. Available: http://www.sciencedirect.com/science/article/pii/S1383762116302910

[151] W. Swinkels, L. Claesen, F. Xiao, and H. Shen, "Real-time svm-based emotion recognition algorithm," in *2017 10th International Congress on Image and Signal Processing, BioMedical Engineering and Informatics (CISP-BMEI)*, Oct 2017, pp. 1–6.

[152] A. Kulkarni, Y. Pino, and T. Mohsenin, "Svm-based real-time hardware trojan detection for many-core platform," in *2016 17th International Symposium on Quality Electronic Design (ISQED)*, March 2016, pp. 362–367.

[153] A. E. Maxwell, T. A. Warner, and F. Fang, "Implementation of machine-learning classification in remote sensing: an applied review," *International Journal of Remote Sensing*, vol. 39, no. 9, pp. 2784–2817, 2018. [Online]. Available: https://doi.org/10.1080/01431161.2018.1433343

[154] G. R. Humphries, D. R. Magness, and F. Huettmann, *Machine learning for ecology and sustainable natural resource management.* Springer, 2018.

[155] D. A. Pados and P. Papantoni-Kazakos, "A note on the estimation of the generalization error and the prevention of overfitting [machine learning]," in *Proceedings of 1994 IEEE International Conference on Neural Networks (ICNN'94)*, vol. 1, June 1994, pp. 321–326 vol.1.

[156] S. Whiteson, B. Tanner, M. E. Taylor, and P. Stone, "Protecting against evaluation overfitting in empirical reinforcement learning," in *2011 IEEE Symposium on Adaptive Dynamic Programming and Reinforcement Learning (ADPRL)*, April 2011, pp. 120–127.

[157] G. Bonaccorso, *Mastering Machine Learning Algorithms: Expert techniques to implement popular machine learning algorithms and fine-tune your models.* Packt Publishing Ltd, 2018.

[158] ——, *Machine learning algorithms.* Packt Publishing Ltd, 2017.

[159] O. Obulesu, M. Mahendra, and M. ThrilokReddy, "Machine learning techniques and tools: A survey," in *2018 International Conference on Inventive Research in Computing Applications (ICIRCA)*, July 2018, pp. 605–611.

[160] P. Tan, M. Steinbach, and V. Kumar, "Cluster analysis: Basic concepts and algorithms," *Introduction to Data Mining*, pp. 487–568, 01 2005.

[161] H. Angadi, "Structural features for recognition of hand written kannada character based on svm," 2015.

[162] N. A. Hamid and N. N. A. Sjarif, "Handwritten recognition using svm, knn and neural network," 2017.

[163] J. Yeh, Y.-C. Pai, C.-W. Wang, F.-W. Yang, and H.-J. Lin, "Face detection using svm-based classification," *Far East Journal of Experimental and Theoretical Artificial Intelligence*, vol. 3, 01 2009.

[164] S. HUANG, N. CAI, P. P. PACHECO, S. NARRANDES, Y. WANG, and W. XU, "Applications of support vector machine (svm) learning in cancer genomics," *Cancer Genomics - Proteomics*, vol. 15, no. 1, pp. 41–51, 2018. [Online]. Available: http://cgp.iiarjournals.org/content/15/1/41.abstract

[165] L. K. Li, "Classification of ground penetrating radar images using histogram of oriented gradients and support vector mechine," Ph.D. dissertation, Universiti Teknologi Malaysia, 2016.

[166] S. S. Todkar, C. Le Bastard, V. Baltazart, A. Ihamouten, and X. Dérobort, "Comparative study of classification algorithms to detect interlayer debondings within pavement structures from step-frequency radar data," in *IGARSS 2018 - 2018 IEEE International Geoscience and Remote Sensing Symposium*, July 2018, pp. 6820–6823.

[167] V. Vapnik, "Pattern recognition using generalized portrait method," 1963.

[168] V. Vapnik and A. Y. Lerner, "Recognition of patterns with help of generalized portraits," *Avtomat. i Telemekh*, vol. 24, no. 6, pp. 774–780, 1963.

[169] B. E. Boser, I. M. Guyon, and V. N. Vapnik, "A training algorithm for optimal margin classifiers," in *Proceedings of the Fifth Annual Workshop on Computational Learning Theory*, ser. COLT '92. New York, NY, USA: ACM, 1992, pp. 144–152. [Online]. Available: http://doi.acm.org/10.1145/130385.130401

[170] H. Yu and S. Kim, "Svm tutorialclassification, regression and ranking," in *Handbook of Natural computing*. Springer, 2012, pp. 479–506.

[171] A. Mammone, M. Turchi, and N. Cristianini, "Support vector machines," *Wiley Interdisciplinary Reviews: Computational Statistics*, vol. 1, no. 3, pp. 283–289, 2009. [Online]. Available: https://onlinelibrary.wiley.com/doi/abs/10.1002/wics.49

[172] A. Ben-Hur and J. Weston, *A User's Guide to Support Vector Machines*. Totowa, NJ: Humana Press, 2010, pp. 223–239. [Online]. Available: https://doi.org/10.1007/978-1-60327-241-4_13

[173] M. Jordan, "Advanced topics in learning & decision making," *Course material available at www. cs. berkeley. edu/˜ jordan/courses/281B-spring01*, 2004.

[174] M. Welling, "Support vector machines," *A note explaining SVM*, 2005.

[175] J. Weston, A. Elisseeff, B. Schölkopf, and M. Tipping, "Use of the zero norm with linear models and kernel methods," *J. Mach. Learn. Res.*, vol. 3, pp. 1439–1461, Mar. 2003. [Online]. Available: http://dl.acm.org/citation.cfm?id=944919.944982

[176] K.-R. Muller, S. Mika, G. Ratsch, K. Tsuda, and B. Scholkopf, "An introduction to kernel-based learning algorithms," *IEEE transactions on neural networks*, vol. 12, no. 2, pp. 181–201, 2001.

[177] B. Yekkehkhany, A. Safari, S. Homayouni, and M. Hasanlou, "A comparison study of different kernel functions for svm-based classification of multi-temporal polarimetry sar data," 2014.

[178] C.-w. Hsu, C.-c. Chang, and C.-J. Lin, "A practical guide to support vector classification chih-wei hsu, chih-chung chang, and chih-jen lin," 11 2003.

[179] B. Schölkopf, R. Williamson, A. Smola, J. Shawe-Taylor, and J. Platt, "Support vector method for novelty detection," in *Proceedings of the 12th International Conference on Neural Information Processing Systems*, ser. NIPS'99. Cambridge, MA, USA: MIT Press, 1999, pp. 582–588. [Online]. Available: http://dl.acm.org/citation.cfm?id=3009657.3009740

[180] Yunqiang Chen, Xiang Sean Zhou, and T. S. Huang, "One-class svm for learning in image retrieval," in *Proceedings 2001 International Conference on Image Processing (Cat. No.01CH37205)*, vol. 1, Oct 2001, pp. 34–37 vol.1.

[181] L. M. Manevitz and M. Yousef, "One-class svms for document classification," *J. Mach. Learn. Res.*, vol. 2, pp. 139–154, Mar. 2002. [Online]. Available: http://dl.acm.org/citation.cfm?id=944790.944808

[182] D. M. Tax and R. P. Duin, "Support vector data description," *Machine Learning*, vol. 54, no. 1, pp. 45–66, Jan 2004. [Online]. Available: https://doi.org/10.1023/B:MACH.0000008084.60811.49

[183] K. Ghiasi-Shirazi, R. Safabakhsh, and M. Shamsi, "Learning translation invariant kernels for classification," *J. Mach. Learn. Res.*, vol. 11, pp. 1353–1390, Aug. 2010. [Online]. Available: http://dl.acm.org/citation.cfm?id=1756006.1859896

[184] X. Solé, A. Ramisa, and C. Torras, "Evaluation of random forests on large-scale classification problems using a bag-of-visual-words representation," vol. 269, pp. 273–276, 01 2014.

[185] A. Navada, A. N. Ansari, S. Patil, and B. A. Sonkamble, "Overview of use of decision tree algorithms in machine learning," in *2011 IEEE Control and System Graduate Research Colloquium*, June 2011, pp. 37–42.

[186] S. Bernard, L. Heutte, and S. Adam, "On the selection of decision trees in random forests," in *2009 International Joint Conference on Neural Networks*, June 2009, pp. 302–307.

[187] P. H. Swain and H. Hauska, "The decision tree classifier: Design and potential," *IEEE Transactions on Geoscience Electronics*, vol. 15, no. 3, pp. 142–147, July 1977.

[188] B. Xu, Y. Ye, and L. Nie, "An improved random forest classifier for image classification," in *2012 IEEE International Conference on Information and Automation*, June 2012, pp. 795–800.

[189] A. Bosch, A. Zisserman, and X. Munoz, "Image classification using random forests and ferns," in *2007 IEEE 11th International Conference on Computer Vision*, Oct 2007, pp. 1–8.

[190] M. Jin, L. N. Govindarajan, and L. Cheng, "A random-forest random field approach for cellular image segmentation," in *2014 IEEE 11th International Symposium on Biomedical Imaging (ISBI)*, April 2014, pp. 1251–1254.

[191] A. Paul, D. P. Mukherjee, P. Das, A. Gangopadhyay, A. R. Chintha, and S. Kundu, "Improved random forest for classification," *IEEE Transactions on Image Processing*, vol. 27, no. 8, pp. 4012–4024, Aug 2018.

[192] A. Lebedev, E. Westman, G. V. Westen, M. Kramberger, A. Lundervold, D. Aarsland, H. Soininen, I. KÅoszewska, P. Mecocci, M. Tsolaki, B. Vellas, S. Lovestone, and A. Simmons, "Random forest ensembles for detection and prediction of alzheimer's disease with a good between-cohort robustness," *NeuroImage: Clinical*, vol. 6, pp. 115 – 125, 2014. [Online]. Available: http://www.sciencedirect.com/science/article/pii/S2213158214001326

[193] U. Aprilliani and Z. Rustam, "Osteoarthritis disease prediction based on random forest," in *2018 International Conference on Advanced Computer Science and Information Systems (ICACSIS)*, Oct 2018, pp. 237–240.

[194] A. Z. Kouzani, S. Nahavandi, and K. Khoshmanesh, "Face classification by a random forest," in *TENCON 2007 - 2007 IEEE Region 10 Conference*, Oct 2007, pp. 1–4.

[195] Y. Shi, L. Cui, Z. Qi, F. Meng, and Z. Chen, "Automatic road crack detection using random structured forests," *IEEE Transactions on Intelligent Transportation Systems*, vol. 17, no. 12, pp. 3434–3445, Dec 2016.

[196] P. jo CHUN and A. IGO, "Crack detection from image using random forest," *Journal of Japan Society of Civil Engineers, Ser. F3 (Civil Engineering Informatics)*, vol. 71, no. 2, pp. I1–I8, 2015.

[197] B. Xu, X. Guo, Y. Ye, and J. Cheng, "An improved random forest classifier for text categorization," *JCP*, vol. 7, pp. 2913–2920, 2012.

[198] S. Patil and M. Ghonge, "Automatic road crack detection techniques: A review," 05 2018.

[199] Tin Kam Ho, "The random subspace method for constructing decision forests," *IEEE Transactions on Pattern Analysis and Machine Intelligence*, vol. 20, no. 8, pp. 832–844, Aug 1998.

[200] T. M. Oshiro, P. S. Perez, and J. A. Baranauskas, "How many trees in a random forest?" in *Machine Learning and Data Mining in Pattern Recognition*, P. Perner, Ed. Berlin, Heidelberg: Springer Berlin Heidelberg, 2012, pp. 154–168.

[201] L. Breiman, "Random forests," *Machine Learning*, vol. 45, no. 1, pp. 5–32, Oct 2001. [Online]. Available: https://doi.org/10.1023/A:1010933404324

[202] C. Kertész, "Rigidity-based surface recognition for a domestic legged robot," *IEEE Robotics and Automation Letters*, vol. 1, no. 1, pp. 309–315, Jan 2016.

[203] V. Franc, A. Zien, and B. Schölkopf, "Support vector machines as probabilistic models," in *Proceedings of the 28th International Conference on International Conference on Machine Learning*, ser. ICML'11. USA: Omnipress, 2011, pp. 665–672. [Online]. Available: http://dl.acm.org/citation.cfm?id=3104482.3104566

[204] Z. Wen, J. Shi, B. He, J. Chen, and Y. Chen, "Efficient multi-class probabilistic svms on gpus," *IEEE Transactions on Knowledge and Data Engineering*, vol. 31, no. 9, pp. 1693–1706, Sep. 2019.

[205] V. Vapnik, "Svm method of estimating density, conditional probability, and conditional density," in *2000 IEEE International Symposium on Circuits and Systems (ISCAS)*, vol. 2, May 2000, pp. 749–752 vol.2.

[206] A. Lambrou, H. Papadopoulos, I. Nouretdinov, and A. Gammerman, "Reliable probability estimates based on support vector machines for large multiclass datasets," in *Artificial Intelligence Applications and Innovations*, L. Iliadis, I. Maglogiannis, H. Papadopoulos, K. Karatzas, and S. Sioutas, Eds. Berlin, Heidelberg: Springer Berlin Heidelberg, 2012, pp. 182–191.

[207] T.-F. Wu, C.-J. Lin, and R. C. Weng, "Probability estimates for multi-class classification by pairwise coupling," *J. Mach. Learn. Res.*, vol. 5, pp. 975–1005, Dec. 2004. [Online]. Available: http://dl.acm.org/citation.cfm?id=1005332.1016791

[208] M. A. Olson and A. J. Wyner, "Making sense of random forest probabilities: a kernel perspective," 2018.

[209] R. Rahman, S. Haider, S. Ghosh, and R. Pal, "Design of probabilistic random forests with applications to anticancer drug sensitivity prediction," *Cancer Informatics*, vol. 14s5, p. CIN.S30794, 2015. [Online]. Available: https://doi.org/10.4137/CIN.S30794

[210] C. Li, "Probability estimation in random forests," 2013.

[211] M. Breitenbach, R. D. Nielsen, and G. Z. Grudic, "Probabilistic random forests: Predicting data point specific misclassification probabilities ; cu-cs-954-03," 2003.

[212] P. Nadarajan and M. Botsch, "Probability estimation for predicted-occupancy grids in vehicle safety applications based on machine learning," in *2016 IEEE Intelligent Vehicles Symposium (IV)*, June 2016, pp. 1285–1292.

[213] H. Boström, "Estimating class probabilities in random forests," 01 2008, pp. 211–216.

[214] V. Leclère, E. Grave, and L. El Ghaoui, "Probabilistic Approach to One-Class Support Vector Machine," Oct. 2016, working paper or preprint. [Online]. Available: https://hal-enpc.archives-ouvertes.fr/hal-01404973

[215] A. Muñoz and J. M. Moguerza, "One-class support vector machines and density estimation: The precise relation," in *Progress in Pattern Recognition, Image Analysis and Applications*, A. Sanfeliu, J. F. Martínez Trinidad, and J. A. Carrasco Ochoa, Eds. Berlin, Heidelberg: Springer Berlin Heidelberg, 2004, pp. 216–223.

[216] K. Hempstalk, E. Frank, and I. H. Witten, "One-class classification by combining density and class probability estimation," in *Machine Learning and Knowledge Discovery in Databases*, W. Daelemans, B. Goethals, and K. Morik, Eds. Berlin, Heidelberg: Springer Berlin Heidelberg, 2008, pp. 505–519.

[217] J. Wang, X. Shen, and Y. Liu, "Probability estimation for large-margin classifiers," *Biometrika*, vol. 95, no. 1, pp. 149–167, 11 2007. [Online]. Available: https://doi.org/10.1093/biomet/asm077

[218] J. Kruppa, A. Ziegler, and I. R. König, "Risk estimation and risk prediction using machine-learning methods," *Human Genetics*, vol. 131, no. 10, pp. 1639–1654, Oct 2012. [Online]. Available: https://doi.org/10.1007/s00439-012-1194-y

[219] J. Milgram, M. Cheriet, and R. Sabourin, ""One Against One" or "One Against All": Which One is Better for Handwriting Recognition with SVMs?" in *Tenth International Workshop on Frontiers in Handwriting Recognition*, G. Lorette, Ed., Université de Rennes 1. La Baule (France): Suvisoft, Oct. 2006, http://www.suvisoft.com. [Online]. Available: https://hal.inria.fr/inria-00103955

[220] H. Drucker, C. J. C. Burges, L. Kaufman, A. J. Smola, and V. Vapnik, "Support vector regression machines," in *Advances in Neural Information Processing Systems 9*, M. C. Mozer, M. I. Jordan, and T. Petsche, Eds. MIT Press, 1997, pp. 155–161. [Online]. Available: http://papers.nips.cc/paper/1238-support-vector-regression-machines.pdf

[221] J. C. Platt, "Probabilistic outputs for support vector machines and comparisons to regularized likelihood methods," in *ADVANCES IN LARGE MARGIN CLASSIFIERS*. MIT Press, 1999, pp. 61–74.

[222] A. Niculescu-Mizil and R. Caruana, "Predicting good probabilities with supervised learning," in *Proceedings of the 22Nd International Conference on Machine Learning*, ser. ICML '05. New York, NY, USA: ACM, 2005, pp. 625–632. [Online]. Available: http://doi.acm.org/10.1145/1102351.1102430

[223] M. Pakdaman Naeini, "Obtaining accurate probabilities using classifier calibration," Ph.D. dissertation, University of Pittsburgh, 2017.

[224] J. D. Malley, J. Kruppa, A. Dasgupta, K. G. Malley, and A. Ziegler, "Probability machines: consistent probability estimation using nonparametric learning machines." *Methods of Information in Medicine*, vol. 51, no. 1, pp. 74–81, 2012. [Online]. Available: https://app.dimensions.ai/details/publication/pub.1071311913andhttps://www.schattauer.de/index.php?id=5236&mid=16692

[225] J. H. Maindonald, "Statistical learning for biomedical data by james d. malley, karen g. malley, sinisa pajevic," *International Statistical Review*, vol. 80, no. 3, pp. 476–478, 2012. [Online]. Available: https://onlinelibrary.wiley.com/doi/abs/10.1111/j.1751-5823.2012.00196_8.x

[226] L. Dennis and N. Dan, "Using random forests to estimate win probability before each play of an NFL game," *Journal of Quantitative Analysis in Sports*, vol. 10, no. 2, pp. 1–9, June 2014. [Online]. Available: https://ideas.repec.org/a/bpj/jqsprt/v10y2014i2p9n10.html

[227] H. S. Gurm, J. Kooiman, T. LaLonde, C. Grines, D. Share, and M. Seth, "A random forest based risk model for reliable and accurate prediction of receipt of transfusion in patients undergoing percutaneous coronary intervention," *PLOS ONE*, vol. 9, no. 5, pp. 1–9, 05 2014. [Online]. Available: https://doi.org/10.1371/journal.pone.0096385

[228] A. Ragins, P. Scheirer, V. Liu, J. Robles, and P. Kipnis, "Nonelective rehospitalizations and postdischarge mortality," *Medical Care*, vol. 53, pp. 916–923, 11 2015.

[229] E. Scornet, G. Biau, and J.-P. Vert, "Consistency of random forests," *The Annals of Statistics*, vol. 43, no. 4, p. 17161741, Aug 2015. [Online]. Available: http://dx.doi.org/10.1214/15-AOS1321

[230] J. Kruppa, Y. Liu, G. Biau, M. Kohler, I. R. KÃűnig, J. D. Malley, and A. Ziegler, "Probability estimation with machine learning methods for dichotomous and multicategory outcome: Theory," *Biometrical Journal*, vol. 56, no. 4, pp. 534–563, 2014. [Online]. Available: https://onlinelibrary.wiley.com/doi/abs/10.1002/bimj.201300068

[231] G. Biau and E. Scornet, "A random forest guided tour," 2015.

[232] A. Senf, X.-w. Chen, and A. Zhang, "Comparison of one-class svm and two-class svm for fold recognition," in *Neural Information Processing*, I. King, J. Wang, L.-W. Chan, and D. Wang, Eds. Berlin, Heidelberg: Springer Berlin Heidelberg, 2006, pp. 140–149.

[233] N. Shahid, I. H. Naqvi, and S. B. Qaisar, "One-class support vector machines: Analysis of outlier detection for wireless sensor networks in harsh environments," *Artif. Intell. Rev.*, vol. 43, no. 4, pp. 515–563, Apr. 2015. [Online]. Available: http://dx.doi.org/10.1007/s10462-013-9395-x

[234] E. Scornet, "Random forests and kernel methods," 2015.

[235] A. Davies and Z. Ghahramani, "The random forest kernel and other kernels for big data from random partitions," 2014.

[236] I. Ahmad, M. Basheri, M. J. Iqbal, and A. Rahim, "Performance comparison of support vector machine, random forest, and extreme learning machine for intrusion detection," *IEEE Access*, vol. 6, pp. 33 789–33 795, 2018.

[237] K. Fawagreh, M. M. Gaber, and E. Elyan, "Random forests: from early developments to recent advancements," *Systems Science & Control Engineering*, vol. 2, no. 1, pp. 602–609, 2014. [Online]. Available: https://doi.org/10.1080/21642583.2014.956265

[238] N. Farnaaz and M. Jabbar, "Random forest modeling for network intrusion detection system," *Procedia Computer Science*, vol. 89, pp. 213 – 217, 2016, twelfth International Conference on Communication Networks, ICCN 2016, August 19â 21, 2016, Bangalore, India Twelfth International Conference on Data Mining and Warehousing, ICDMW 2016, August 19-21, 2016, Bangalore, India Twelfth International Conference on Image and Signal Processing, ICISP 2016, August 19-21, 2016, Bangalore, India. [Online]. Available: http://www.sciencedirect.com/science/article/pii/S1877050916311127

[239] J. Ali, R. Khan, N. Ahmad, and I. Maqsood, "Random forests and decision trees," *International Journal of Computer Science Issues(IJCSI)*, vol. 9, 09 2012.

[240] M. B. Salem and S. J. Stolfo, "A comparison of one-class bag-of-words user behavior modeling techniques for masquerade detection," *Security and Communication Networks*, vol. 5, no. 8, pp. 863–872, 2012. [Online]. Available: https://onlinelibrary.wiley.com/doi/abs/10.1002/sec.311

[241] J. Miao and L. Niu, "A survey on feature selection," *Procedia Computer Science*, vol. 91, pp. 919 – 926, 2016, promoting Business Analytics and Quantitative Management of Technology: 4th International Conference on Information Technology and Quantitative Management (ITQM 2016). [Online]. Available: http://www.sciencedirect.com/science/article/pii/S1877050916313047

[242] J. Suto, S. Oniga, and P. P. Sitar, "Comparison of wrapper and filter feature selection algorithms on human activity recognition," in *2016 6th International Conference on Computers Communications and Control (ICCCC)*, May 2016, pp. 124–129.

[243] J. Gronsbell, J. Minnier, S. Yu, K. Liao, and T. Cai, "Automated feature selection of predictors in electronic medical records data," *Biometrics*, vol. 75, no. 1,

pp. 268–277, 2019. [Online]. Available: https://onlinelibrary.wiley.com/doi/abs/10.1111/biom.12987

[244] S. Shilaskar and A. Ghatol, "Feature selection for medical diagnosis : Evaluation for cardiovascular diseases," *Expert Systems with Applications*, vol. 40, no. 10, pp. 4146 – 4153, 2013. [Online]. Available: http://www.sciencedirect.com/science/article/pii/S0957417413000456

[245] Q. Liu, Q. Gu, and Z. Wu, "Feature selection method based on support vector machine and shape analysis for high-throughput medical data," *Computers in Biology and Medicine*, vol. 91, pp. 103 – 111, 2017. [Online]. Available: http://www.sciencedirect.com/science/article/pii/S0010482517303281

[246] H.-J. Yu, "Data mining via support vector machines: Scalability, applicability, and interpretability," 05 2004.

[247] S.-K. Kim, Y. J. Park, K.-A. Toh, and S. Lee, "Svm-based feature extraction for face recognition," *Pattern Recognition*, vol. 43, no. 8, pp. 2871 – 2881, 2010. [Online]. Available: http://www.sciencedirect.com/science/article/pii/S0031320310001287

[248] J. Brank, M. Grobelnik, N. Milic-Frayling, and D. Mladeni, "Feature selection using linear support vector machines," *Technical report, Microsoft Research*, 01 2002.

[249] X. He, P. Beauseroy, and A. Smolarz, "Feature subspaces selection via one-class svm: Application to textured image segmentation," in *2010 2nd International Conference on Image Processing Theory, Tools and Applications*, July 2010, pp. 21–25.

[250] A. Rabaoui, H. Kadri, Z. Lachiri, and N. Ellouze, "One-class svms challenges in audio detection and classification applications," *EURASIP Journal on Advances in Signal Processing*, vol. 2008, no. 1, p. 834973, May 2008. [Online]. Available: https://doi.org/10.1155/2008/834973

[251] W. Dargie, "Analysis of time and frequency domain features of accelerometer measurements," in *2009 Proceedings of 18th International Conference on Computer Communications and Networks*, Aug 2009, pp. 1–6.

[252] C. AltÄśn and O. Er, "Comparison of Different Time and Frequency Domain Feature Extraction Methods on Elbow Gestureâs EMG," *European Journal of Interdisciplinary Studies Articles*, vol. 5, May-August 2016. [Online]. Available: https://ideas.repec.org/a/eur/ejisjr/125.html

[253] A. B. Gonzalves, J. S. Souza, G. G. d. Silva, M. P. Cereda, A. Pott, M. H. Naka, and H. Pistori, "Feature extraction and machine learning for the classification of brazilian savannah pollen grains," *PLOS ONE*, vol. 11, no. 6, pp. 1–20, 06 2016. [Online]. Available: https://doi.org/10.1371/journal.pone.0157044

[254] G. Kumar and P. K. Bhatia, "A detailed review of feature extraction in image processing systems," in *2014 Fourth International Conference on Advanced Computing Communication Technologies*, Feb 2014, pp. 5–12.

[255] F. Samadzadegan, H. Hasani, and T. Partovi, "Sensitivity analysis of support vector machine in classification of hyperspectral imagery," in *Proceedings of the Canadian Geomatics Conference, Calgary, Canada*, 2010.

[256] H. Liu, H. Motoda, R. Setiono, and Z. Zhao, "Feature selection: An ever evolving frontier in data mining," in *Proceedings of the Fourth International Workshop on Feature Selection in Data Mining*, ser. Proceedings of Machine Learning Research, H. Liu, H. Motoda, R. Setiono, and Z. Zhao, Eds., vol. 10. Hyderabad, India: PMLR, 21 Jun 2010, pp. 4–13.

[257] G. I. Allen, "Automatic feature selection via weighted kernels and regularization," *Journal of Computational and Graphical Statistics*, vol. 22, no. 2, pp. 284–299, 2013. [Online]. Available: https://doi.org/10.1080/10618600.2012.681213

[258] H. Osman, M. Ghafari, and O. Nierstrasz, "Automatic feature selection by regularization to improve bug prediction accuracy," in *2017 IEEE Workshop on Machine Learning Techniques for Software Quality Evaluation (MaLTeSQuE)*, Feb 2017, pp. 27–32.

[259] A. Y. Ng, "Feature selection, l1 vs. l2 regularization, and rotational invariance," in *Proceedings of the Twenty-first International Conference on Machine Learning*, ser. ICML '04. New York, NY, USA: ACM, 2004, pp. 78–. [Online]. Available: http://doi.acm.org/10.1145/1015330.1015435

[260] Y. Ben Youssef, E. h. Abdelmounim, A. Rabeh, J. Zbitou, and A. Belaguid, "Statistical features and classification of normal and abnormal mammograms," in *2014 International Conference on Multimedia Computing and Systems (ICMCS)*, April 2014, pp. 448–452.

[261] S. Arora, D. Bhattacharjee, M. Nasipuri, D. K. Basu, and M. Kundu, "Application of statistical features in handwritten devnagari character recognition," *ArXiv*, vol. abs/1006.5911, 2009.

[262] S. K. Chatterjee, S. Das, K. Maharatna, E. Masi, L. Santopolo, S. Mancuso, and A. Vitaletti, "Exploring strategies for classification of external stimuli using statistical features of the plant electrical response," *Journal of The Royal Society Interface*, vol. 12, no. 104, p. 20141225, 2015. [Online]. Available: https://royalsocietypublishing.org/doi/abs/10.1098/rsif.2014.1225

[263] M. S. El-Mahallawy and M. Hashim, "Material classification of underground utilities from gpr images using dct-based svm approach," *IEEE Geoscience and Remote Sensing Letters*, vol. 10, no. 6, pp. 1542–1546, Nov 2013.

[264] X. Xie, H. Qin, C. Yu, and L. Liu, "An automatic recognition algorithm for gpr images of rc structure voids," *Journal of Applied Geophysics*, vol. 99, pp. 125 – 134, 2013.

[265] S. Shihab, W. Al-Nuaimy, Y. Huang, and A. Eriksen, "Neural network target identifier based on statistical features of GPR signals," in *Society of Photo-Optical Instrumentation Engineers (SPIE) Conference Series*, vol. 4758, Apr. 2002, pp. 135–138.

[266] H.-Y. Kim, "Statistical notes for clinical researchers: Assessing normal distribution (2) using skewness and kurtosis," *Restorative dentistry & endodontics*, vol. 38, pp. 52–54, 02 2013.

[267] A. Kar and L. Das, "A technical review on statistical feature extraction of ecg signal," *IJCA Special Issue on 2nd National Conference- Computing, Communication and Sensor Network (CCSN)*, no. 2, pp. 35– 40, 2011.

[268] K. K. Patro and P. R. Kumar, "Effective feature extraction of ecg for biometric application," *Procedia Computer Science*, vol. 115, pp. 296 – 306, 2017, 7th International Conference on Advances in Computing and Communications, ICACC-2017, 22-24 August 2017, Cochin, India.

[269] W. Lu, H. Hou, and J. Chu, "Feature fusion for imbalanced ecg data analysis," *Biomedical Signal Processing and Control*, vol. 41, pp. 152 – 160, 2018.

[270] S. T. Sanamdikar, S. T. Hamde, and V. G. Asutkar, "Extraction of different features of ecg signal for detection of cardiac arrhythmias by using wavelet transformation db 6," in *2017 International Conference on Energy, Communication, Data Analytics and Soft Computing (ICECDS)*, Aug 2017, pp. 2407–2412.

[271] A. I. Manriquez, Q. Zhang, C. Médigue, Y. Papelier, and M. Sorine, "Multi-lead T wave end detection based on statistical hypothesis testing," in *Modelling and Control in Biomedical Systems*, D. D. Feng, O. Dubois, J. Zaytoon, and E. Carson, Eds. Reims, France: IFAC, Sep. 2006, pp. 93–98. [Online]. Available: https://hal.inria.fr/hal-00854838

[272] R. M. G. Tello, T. Bastos-Filho, A. Frizera-Neto, S. Arjunan, and D. K. Kumar, "Feature extraction and classification of semg signals applied to a virtual hand prosthesis," in *2013 35th Annual International Conference of the IEEE Engineering in Medicine and Biology Society (EMBC)*, July 2013, pp. 1911–1914.

[273] R. Chen, N. Sun, X. Chen, M. Yang, and Q. Wu, "Supervised feature selection with a stratified feature weighting method," *IEEE Access*, vol. 6, pp. 15 087–15 098, 2018.

[274] A. Widodo and B.-S. Yang, "Application of nonlinear feature extraction and support vector machines for fault diagnosis of induction motors," *Expert Systems with Applications*, vol. 33, no. 1, pp. 241 – 250, 2007. [Online]. Available: http://www.sciencedirect.com/science/article/pii/S0957417406001382

[275] V. Kumar, D. Kalitin, and P. Tiwari, "Unsupervised learning dimensionality reduction algorithm pca for face recognition," in *2017 International Conference on Computing, Communication and Automation (ICCCA)*, May 2017, pp. 32–37.

[276] G. Saporta and N. Niang, "Principal component analysis: application to statistical process control," *Data analysis*, pp. 1–23, 2009.

[277] A. Subasi and M. Ismail Gursoy, "Eeg signal classification using pca, ica, lda and support vector machines," *Expert Syst. Appl.*, vol. 37, no. 12, pp. 8659–8666, Dec. 2010. [Online]. Available: http://dx.doi.org/10.1016/j.eswa.2010.06.065

[278] F. Melgani and Y. Bazi, "Classification of electrocardiogram signals with support vector machines and particle swarm optimization," *IEEE Transactions on Information Technology in Biomedicine*, vol. 12, no. 5, pp. 667–677, Sep. 2008.

[279] T.-K. Lin, "Pca/svm-based method for pattern detection in a multisensor system," *Mathematical Problems in Engineering*, vol. 2018, pp. 1–11, 02 2018.

[280] Y. Jain and S. Bhandare, "Min max normalization based data perturbation method for privacy protection," *International Journal of Computer*, vol. 2, 01 2011.

[281] H. Abdi and L. J. Williams, "Principal component analysis," *Wiley Interdisciplinary Reviews: Computational Statistics*, vol. 2, no. 4, pp. 433–459, 2010. [Online]. Available: https://onlinelibrary.wiley.com/doi/abs/10.1002/wics.101

[282] I. T. Jolliffe and J. Cadima, "Principal component analysis: a review and recent developments," *Philosophical Transactions of the Royal Society A: Mathematical, Physical and Engineering Sciences*, vol. 374, no. 2065, p. 20150202, 2016. [Online]. Available: https://royalsocietypublishing.org/doi/abs/10.1098/rsta.2015.0202

[283] B. A. Kostov, "A principal component method to analyse disconnected frequency tables by means of contextual information," Ph.D. dissertation, 2015.

[284] S. Rifai, P. Vincent, X. Muller, X. Glorot, and Y. Bengio, "Contractive auto-encoders: Explicit invariance during feature extraction," in *Proceedings of the 28th International Conference on International Conference on Machine Learning*, ser. ICML'11. USA: Omnipress, 2011, pp. 833–840. [Online]. Available: http://dl.acm.org/citation.cfm?id=3104482.3104587

[285] S. Sun, Z. Cao, H. Zhu, and J. Zhao, "A survey of optimization methods from a machine learning perspective," 2019.

[286] M. Wimmer, F. Stulp, S. Tschechne, and B. Radig, "Learning robust objective functions for model fitting in image understanding applications," 01 2006, pp. 1159–1168.

[287] H. Bertrand, "Hyper-parameter optimization in deep learning and transfer learning: applications to medical imaging," Ph.D. dissertation, 2019.

[288] D. Chicco, "Ten quick tips for machine learning in computational biology," *BioData mining*, vol. 10, no. 1, p. 35, 2017.

[289] R. M. J. Lyra, "Topical subcategory structure in text classification," Ph.D. dissertation, University of Sussex, 2019.

[290] S. Halligan, D. G. Altman, and S. Mallett, "Disadvantages of using the area under the receiver operating characteristic curve to assess imaging tests: A discussion and proposal for an alternative approach," *European Radiology*, vol. 25, no. 4, pp. 932–939, Apr 2015. [Online]. Available: https://doi.org/10.1007/s00330-014-3487-0

[291] F. E. Harrell Jr and J. C. Slaughter, "Introduction to biostatistics for biomedical research," *Retrieved from data. vanderbilt. edu/biosproj/CI2/handouts. pdf*, 2001.

[292] D. Spiegelhalter, M. Pearson, and I. Short, "Visualizing uncertainty about the future," *Science*, vol. 333, no. 6048, pp. 1393–1400, 2011. [Online]. Available: https://science.sciencemag.org/content/333/6048/1393

[293] L. Fidon, W. Li, L. C. Garcia-Peraza-Herrera, J. Ekanayake, N. Kitchen, S. Ourselin, and T. Vercauteren, "Generalised wasserstein dice score for imbalanced multi-class segmentation usingÂăholistic convolutional networks," in *Brainlesion: Glioma, Multiple Sclerosis, Stroke and Traumatic Brain Injuries*, A. Crimi, S. Bakas, H. Kuijf, B. Menze, and M. Reyes, Eds. Cham: Springer International Publishing, 2018, pp. 64–76.

[294] S. Shalev-Shwartz and S. Ben-David, *Understanding machine learning: From theory to algorithms*. Cambridge university press, 2014.

[295] J. D. Salciccioli, Y. Crutain, M. Komorowski, and D. C. Marshall, *Sensitivity Analysis and Model Validation*. Cham: Springer International Publishing, 2016, pp. 263–271. [Online]. Available: https://doi.org/10.1007/978-3-319-43742-2_17

[296] W.-C. Cheung, W. Zhang, Y. Liu, F. Yang, and R.-S.-M. Goh, "Automated hyperparameter tuning for machine learning models in machine health prognostics," 2018.

[297] S. Raschka, "Model evaluation, model selection, and algorithm selection in machine learning," *ArXiv*, vol. abs/1811.12808, 2018.

[298] G. C. Cawley and N. L. Talbot, "On over-fitting in model selection and subsequent selection bias in performance evaluation," *J. Mach. Learn. Res.*, vol. 11, pp. 2079–2107, Aug. 2010. [Online]. Available: http://dl.acm.org/citation.cfm?id=1756006.1859921

[299] R. Palaniappan, K. Sundaraj, and S. Sundaraj, "A comparative study of the svm and k-nn machine learning algorithms for the diagnosis of respiratory pathologies using pulmonary acoustic signals," *BMC bioinformatics*, vol. 15, no. 1, p. 223, 2014.

[300] V. Sharma, D. Baruah, D. Chutia, P. Raju, and D. K. Bhattacharya, "An assessment of support vector machine kernel parameters using remotely sensed satellite data," in *2016 IEEE International Conference on Recent Trends in Electronics, Information Communication Technology (RTEICT)*, May 2016, pp. 1567–1570.

[301] A. Boubezoul, "Système d'aide au diagnostic par apprentissage: application aux systèmes microélectroniques," Ph.D. dissertation, Aix-Marseille 3, 2008.

[302] A. Airola, T. Pahikkala, W. Waegeman, B. D. Baets, and T. Salakoski, "An experimental comparison of cross-validation techniques for estimating the area under the roc curve," *Computational Statistics & Data Analysis*, vol. 55, no. 4, pp. 1828 – 1844, 2011. [Online]. Available: http://www.sciencedirect.com/science/article/pii/S0167947310004469

[303] J. Gardner and C. Brooks, "Statistical approaches to the model comparison task in learning analytics," in *MLA/BLAC@LAK*, 2017.

[304] C. Tantithamthavorn, S. McIntosh, A. E. Hassan, and K. Matsumoto, "An empirical comparison of model validation techniques for defect prediction models," *IEEE Transactions on Software Engineering*, vol. 43, no. 1, pp. 1–18, Jan 2017.

[305] S. Hegenbart, A. Uhl, and A. Vécsei, "Systematic assessment of performance prediction techniques in medical image classification: A case study on celiac disease," in *Proceedings of the 22Nd International Conference on Information Processing in Medical Imaging*, ser. IPMI'11. Berlin, Heidelberg: Springer-Verlag, 2011, pp. 498–509. [Online]. Available: http://dl.acm.org/citation.cfm?id=2029686.2029733

[306] M. Bianchini, M. Gori, and M. Maggini, "On the problem of local minima in recurrent neural networks," *IEEE Transactions on Neural Networks*, vol. 5, no. 2, pp. 167–177, March 1994.

[307] J. D. M. Rennie, "Loss functions for preference levels: Regression with discrete ordered labels," in *Proceedings of the IJCAI Multidisciplinary Workshop on Advances in Preference Handling*, 2005, pp. 180–186.

[308] S. Mei, "A novel one-class svm based negative data sampling method for reconstructing proteome-wide htlv-human protein interaction networks," *Scientific Reports*, vol. 5, p. 8034, 01 2015.

[309] S. S. Todkar, C. Le Bastard, A. Ihamouten, V. Baltazart, and X. Dérobert, "One-class svm based outlier detection strategy to detect thin interlayer debondings within pavement structures using ground penetrating radar data," in *IEEE Journal Of Selected Topics In Applied Earth Observations And Remote Sensing (JSTARS)*, vol. under writing, – –, pp. –.

[310] Y. Wang, "Frequencies of the ricker wavelet," *GEOPHYSICS*, vol. 80, no. 2, pp. A31–A37, 2015. [Online]. Available: https://doi.org/10.1190/geo2014-0441.1

[311] N. Ricker, "Wavelet functions and their polynomials," *GEOPHYSICS*, vol. 9, no. 3, pp. 314–323, 1944. [Online]. Available: https://doi.org/10.1190/1.1445082

[312] S. Lahouar, "Development of data analysis algorithms for interpretation of ground penetrating radar data," Ph.D. dissertation, Virginia Tech, 2003.

[313] H. M. Jol and C. S. Bristow, "GPR in sediments: advice on data collection, basic processing and interpretation, a good practice guide," *Geological Society of London Special Publications*, vol. 211, pp. 9–27, Jan. 2003.

[314] A. Ruffell, J. McKinley, M. Robinson, and C. Bristow, "Ground penetrating radar. geomorphological techniques," pp. 1–26, 3 2013.

[315] P. Huggenberger, "Radar facies: recognition of facies patterns and heterogeneities within pleistocene rhine gravels, ne switzerland," *Geological Society, London, Special Publications*, vol. 75, no. 1, pp. 163–176, 1993.

[316] H.-M. Chung and D. C. Lawton, "Amplitude responses of thin beds; sinusoidal approximation versus Ricker approximation," *Geophysics*, vol. 60, no. 1, pp. 223–230, 02 1995. [Online]. Available: https://doi.org/10.1190/1.1443750

[317] P. M. Shearer, *Chapter 8 - Surface waves and normal modes*, 2nd ed. Cambridge University Press, 2009.

[318] "Chapter 8 - attenuation and scattering of seismic waves," in *An Introduction to Mining Seismology*, ser. International Geophysics, S. J. Gibowicz and A. Kijko, Eds. Academic Press, 1994, vol. 55, pp. 128 – 175. [Online]. Available: http://www.sciencedirect.com/science/article/pii/B9780122821202500121

[319] D. Arosio, "Rock fracture characterization with gpr by means of deterministic deconvolution," *Journal of Applied Geophysics*, vol. 126, pp. 27 – 34, 2016. [Online]. Available: http://www.sciencedirect.com/science/article/pii/S0926985116300064

[320] A. Shakas and N. Linde, "Apparent apertures from ground penetrating radar data and their relation to heterogeneous aperture fields," *Geophysical Journal International*, vol. 209, no. 3, pp. 1418–1430, 03 2017. [Online]. Available: https://doi.org/10.1093/gji/ggx100

[321] ——, "Effective modeling of ground penetrating radar in fractured media using analytic solutions for propagation, thin-bed interaction and dipolar scattering," *Journal of Applied Geophysics*, vol. 116, p. 206214, May 2015. [Online]. Available: http://dx.doi.org/10.1016/j.jappgeo.2015.03.018

[322] V. Baltazart, "Signature temps-fréquence théorique : décalage fréquentiel et temporel des structures thin-beds," 2017.

[323] N. Déchamps, N. de Beaucoudrey, C. Bourlier, and S. Toutain, "Fast numerical method for electromagnetic scattering by rough layered interfaces: Propagation-inside-layer expansion method," *J. Opt. Soc. Am. A*, vol. 23, no. 2, pp. 359–369, Feb 2006. [Online]. Available: http://josaa.osa.org/abstract.cfm?URI=josaa-23-2-359

[324] K. S. Kunz and R. J. Luebbers, *The finite difference time domain method for electromagnetics*. CRC press, 1993.

[325] A. Taflove and S. C. Hagness, *Computational electrodynamics: the finite-difference time-domain method*. Artech house, 2005.

[326] A. Giannopoulos, "Modelling ground penetrating radar by gprmax," *Construction and Building Materials*, vol. 19, no. 10, pp. 755–762, 2005.

[327] ——, "The investigation of transmission-line matrix and finite-difference time-domain methods for the forward problem of ground probing radar," 1998.

[328] C. Warren, A. Giannopoulos, and I. Giannakis, "gprmax: Open source software to simulate electromagnetic wave propagation for ground penetrating radar," *Computer Physics Communications*, vol. 209, pp. 163 – 170, 2016. [Online]. Available: http://www.sciencedirect.com/science/article/pii/S0010465516302533

[329] C. Warren and A. Giannopoulos, "gprmax user guide."

[330] A. Giannopoulos and N. Diamanti, "Numerical modeling of ground penetrating radar response from rough subsurface interfaces," *Near surface geophysics*, vol. 6, pp. 357–369, 12 2008.

[331] I. Giannakis, A. Giannopoulos, and C. Warren, "A realistic fdtd numerical modeling framework of ground penetrating radar for landmine detection," *IEEE Journal of Selected Topics in Applied Earth Observations and Remote Sensing*, vol. 9, no. 1, pp. 37–51, Jan 2016.

[332] D. Seyfried and J. Schoebel, "Stepped-frequency radar signal processing," *Journal of Applied Geophysics*, vol. 112, pp. 42 – 51, 2015. [Online]. Available: http://www.sciencedirect.com/science/article/pii/S092698511400322X

[333] C. Diakité, N. Fortino, and J.-Y. Dauvignac, "Antenne ETSA "Exponential Tapered Slot Antenna" miniature pour radar à pénétration de surface," in *19èmes Journées Nationales Microondes (JNM 2015)*, ser. 19èmes Journées Nationales Microondes (JNM 2015), Bordeaux, France, Jun. 2015, pp. Session Antennes large bande et multibandes C3L–D, papier 9337. [Online]. Available: https://hal.archives-ouvertes.fr/hal-01149096

[334] S. Krig, *Ground Truth Data, Content, Metrics, and Analysis*. Berkeley, CA: Apress, 2014, pp. 283–311. [Online]. Available: https://doi.org/10.1007/978-1-4302-5930-5_7

[335] S. Ahmed, M. I. Malik, M. Z. Afzal, K. Kise, M. Iwamura, A. Dengel, and M. Liwicki, "A generic method for automatic ground truth generation of camera-captured documents," 2016.

[336] V. Baltazart, L. Yang, P. Nicolle, and J. Moliard, "Pseudo-ground truth data collection on pavement images," in *2017 25th European Signal Processing Conference (EUSIPCO)*, Aug 2017, pp. 2021–2025.

[337] M. P. Sampat, Z. Wang, S. Gupta, A. C. Bovik, and M. K. Markey, "Complex wavelet structural similarity: A new image similarity index," *IEEE Transactions on Image Processing*, vol. 18, no. 11, pp. 2385–2401, Nov 2009.

[338] T. Fawcett, "An introduction to roc analysis," *Pattern Recognition Letters*, vol. 27, no. 8, pp. 861 – 874, 2006, rOC Analysis in Pattern Recognition. [Online]. Available: http://www.sciencedirect.com/science/article/pii/S016786550500303X

[339] B. Matthews, "Comparison of the predicted and observed secondary structure of t4 phage lysozyme," *Biochimica et Biophysica Acta (BBA) - Protein Structure*, vol. 405, no. 2, pp. 442 – 451, 1975. [Online]. Available: http://www.sciencedirect.com/science/article/pii/0005279575901099

[340] T. K. Roy and M. Morshed, "Performance analysis of low pass fir filters design using kaiser, gaussian and tukey window function methods," *2013 2nd International Conference on Advances in Electrical Engineering (ICAEE)*, pp. 1–6, 2013.

Titre : **Suivi de l'endommagement des structures de chaussées par technique radar Ultra-large bande**

Mots clés : chaussées, l'essai non-destructif (NDT), radar à impulsions (GPR), détection de décollement, l'apprentissage de machine supervisé, Machine à vecteurs de support (SVM), forêt d'arbres aléatoire (RF)

Résumé : Dans le domaine du génie civil, la détection et la caractérisation de défauts (décollements, fissures non-débouchantes) sont des éléments importants de diagnostic qui influencent la mise en œuvre de politique d'entretien et de gestion. Les défauts sont représentatifs d'un état d'altération de la structure. Les caractéristiques géométriques de ces défauts (forme, largeur et longueur) ainsi que l'étendue et les cheminements d'eau induits par ces défauts est un indicateur de durabilité des ouvrages important. Cette détection permet de localiser une éventuelle pathologie, d'évaluer l'état de santé de la structure et de prédire son évolution.
Dans ce contexte, les systèmes « radar à impulsions », appelé aussi GPR (Ground Penetrating radar) est utilisé depuis une trentaine d'années pour réaliser des opérations de contrôle non destructif dans le flux du trafic. Ils fournissent une mesure en continu de l'épaisseur de la couche de chaussée, mais permettent aussi la détection de décollements significatifs (centimétrique) entre couches, et de déterminer ainsi l'emplacement de contrôles structurels destructifs ultérieurs.
Néanmoins, la résolution temporelle des GPR conventionnels ne permet pas de détecter directement des décollements d'interface millimétriques.
L'objectif de ce travail est donc de réaliser une détection précoce de ce type de défauts. Ainsi, mes travaux se sont focalisés à la fois sur l'utilisation du radar ultra large bande (RSF) et sur le développement de méthodes d'intelligence artificielle (basées sur l'apprentissage supervisé).
Des approches théoriques et expérimentales (dalle de chaussée Cerema et manège de fatigue de l'IFSTTAR) ont été réalisées. Elles ont permis de montrer la faisabilité de détecter des décollements fins dans les chaussées.

Title: **Monitoring subsurface conditions of pavement structures using Ultra-wideband radar technology**

Keywords : pavements, Non-destructive testing (NDT), Ground Penetrating Radar (GPR), debonding detection, Supervised machine learning, Support Vector Machines (SVM), Random Forests (RF)

Abstract: In the field of civil engineering, the detection and characterization of defects (debondings, non-emerging cracks) are important diagnostic elements that influence the maintenance and management of the pavement structure. These defects represent an altered state of the structure. The geometric characteristics of these defects (shape, width and length) as well as their extent and the water seepage induced by these defects are important durability indicators of the structures. This detection makes it possible to locate a possible pathology, to evaluate the state of health of the structure and also predict its evolution.
In this context, "pulse radar" systems, also called Ground Penetrating Radar (GPR) have been used for over thirty years to perform non- destructive testing operations in the traffic flow. They not only provide continuous measurement of the thickness of the pavement layer, but also allow the detection of significant (centimetric) inter-layer detachments, and thus determine the location of subsequent destructive structural controls. However, the temporal resolution of conventional GPRs does not allow direct detection of millimeteric interface debondings.
Therefore, the objective of this work is to realize an early detection of such defects. My work is thus focused on both the use of ultra-wideband radar (SFR) and the development of artificial intelligence methods (based on supervised learning) to detect thin debondings.
Theoretical and experimental approaches (Cerema test pavement slabs and IFSTTAR's fatigue carousel) were realized which have shown the feasibility of detecting fine debondings in pavements.